

Photo-reactive Surfactant and Macromolecular Supramolecular Structures

Matthew P. Cashion

Dissertation submitted to the Faculty of
Virginia Polytechnic Institute and State University
in partial fulfillment of the requirements for the degree of

Doctor of Philosophy

In

Chemistry

Timothy E. Long, Chair
S. Richard Turner
Louis A. Madsen
Richey M. Davis
Robert B. Moore

April 30, 2009

Blacksburg, Virginia

Keywords: photo-curing, gemini surfactants, n-butyl acrylate, 2-hydroxyethyl acrylate,
cinnamate, hydrogen bonding, electrospinning, adhesives, photo-rheology

Photo-reactive Surfactant and Macromolecular Supramolecular Structures

Matthew P. Cashion

Abstract

For the first time nonwoven fibrous scaffolds were electrospun from a low molar mass gemini ammonium surfactant, N,N'-didodecyl-N,N,N',N'-tetramethyl-N,N'-ethanediyl-di-ammonium dibromide (12-2-12). Cryogenic transmission electron microscopy (cryo-TEM) and solution rheological experiments revealed micellar morphological transitions of 12-2-12 in water and water:methanol (1:1 vol). Electrospinning efforts of 12-2-12 from water did not produce fibers at any concentration, however, electrospinning 12-2-12 in water:methanol at concentrations greater than 2C* produced, hydrophilic continuous fibers with diameters between 0.9 and 7 μm .

Photo-reactive surfactants were synthesized to electrospin robust surfactant membranes. Before electrospinning it was important to fundamentally understand the structure-property relationship of gemini surfactants. The thermal and solution properties were explored for a series of ammonium gemini surfactants using differential scanning calorimetry (DSC), polarized light microscopy (PLM), and conductivity experiments. The Kraft temperature (T_k) was measured in water and water:methanol (1:1 vol) to investigate the influence of solvent on the surfactant solution properties.

Other experiments investigate how associated photo-curable architectures are applicable in macromolecular architectures, to gain a fundamental understanding of how hydrogen bonding associations influence the photo-reactivity of functionalized acrylic copolymers. Novel hot melt pressure sensitive adhesives (HMPSAs) were developed

from acrylic terpolymers of 2-ethylhexyl acrylate (EHA), 2-hydroxyethyl acrylate (HEA), and methyl acrylate (MA) functionalized with hydrogen bonding and photo-reactive functionalities. The synergy of hydrogen bonding and photo-reactivity resulted in higher peel values and rates of cinnamate photo-reactivity with increasing urethane concentration.

Random copolymers of poly(n-butyl acrylate (nBA)-*co*-2-hydroxyethyl methacrylate (HEMA)) were functionalized with hydrogen bonding and photo-reactive groups to explore the photo-curing of associated macromolecular architectures. The influence of urethane hydrogen bonding on the photo-reactivity of cinnamate-functionalized acrylics was investigated with photo-rheology and UV-vis spectroscopy. Cinnamate-functionalized samples displayed an increase in modulus with exposure time, and the percentage increase in modulus decreased as the urethane content increased. The synergy of hydrogen bonding and photo-reactive groups resulted in higher rates of cinnamate photo-reactivity with increasing urethane concentration.

Electrospun fibers were *in situ* photo-crosslinked to develop fibrous membranes from cinnamate functionalized low T_g acrylics. Electrospinning was conducted approximately 55 °C above the T_g of the cinnamate acrylate and the electrospun fibers did not retain their fibrous morphology without photo-curing. However, electrospun fibers were collected that retained their fibrous morphology and resisted flow when *in situ* photo-cured during electrospinning. The intermolecular photo-dimerization of cinnamates resulted in a network formation that prevented the low T_g cinnamate acrylate from flowing.

Acknowledgements

I would like to thank my advisor, Dr. Tim Long, for his guidance during my graduate career, and his willingness to allow me the freedom to pursue my scientific endeavors. I appreciate his patience and flexibility in allowing me to pursue research and experiments that I found interesting. I would also like to thank Dr. Richard Turner who supported and helped me develop a deep scientific curiosity. He has helped me immensely during my graduate career and I have genuinely enjoyed our sports discussions. I would also like to thank Dr. Rick Davis for his insightful discussions in helping me learn and understand various topics in colloidal chemistry, and equal thanks goes to the rest of my committee: Dr. Lou Madsen and Dr. Bob Moore for their valuable time and critical input.

I would like to thank Avery Dennison for providing financial support. Laurie Good and Millie Ryan deserve a big thanks for all their immense help. I would like to thank Kathy Lowe and Steve McCartney for all their knowledge of microscopy. I would like to acknowledge our collaborators Dr. Yan Geng and Dr. Xiaolin Li of the University of Georgia for the cryogenic-TEM images and helpful discussions. I have really appreciated the patience and skill of Jim Hall and Larry Jackson of Technology Services who helped me out with many computer issues. Thanks to Tom Glass formerly of Analytical Services for the excellent job and Tom Wertalik for his skilled glassblowing craftsmanship.

Thanks to all the graduate students I spent time with in the Long Labs, particularly those in Davidson 124A and 113. First off, thanks to Matt McKee and Ann Fornof for teaching the ropes of the Long Group and their happy hour discussions. A

special thanks to John Layman, my roommate of two years, for always providing entertainment and making everyday in and out of the lab an adventure. All of my good VT stories involve John Layman in some facet. Another special thanks to Rebecca H. Brown for providing excellent advice and for having a great sense of humor. Thanks to Matt Hunley for keeping me up to date on Hokie sports and for his ability to make things a lot more tolerable in the lab. I would like to acknowledge Tianyu Wu for his enthusiasm and scientific curiosity that never grew tired of discussing science. Thanks to Erika Borgerding, Min Mao, and Andy Duncan for their willingness to help me with any scientific or non-science related problem. Another special thanks to Dr. Taigyoo Park for teaching me so much in the lab and to Dr. Eugene G. Joseph for his helpful insight. A big thanks to the rest of the undergraduates, graduate students, and post docs I had the opportunity to work with in the Long Group: Brian Mohns, Dr. Brian Mather, Dr. Sharlene Williams, Dr. Takeo Suga, Dr. Tomonori Saito, Dr. Bill Heath, Dr. Sean Ramirez, Gozde Ozturk, Emily Anderson, Mana Tamami, and Shijing Cheng.

Where would I be without my wife, Jennifer. She has made extraordinary sacrifices and supported me unconditionally. I could not have survived graduate school without her. She has made this experience and all the others in my life something worth doing. I can not begin to thank her for being so understanding and for her support.

I owe a huge debt of gratitude to my Pop and Mom, Joe and Sandy Cashion, for their guidance and unwavering support throughout my life. They allowed me to make right and wrong decisions in my life, and supported me unconditionally in every endeavor I pursued. My parents have inspired me and this achievement is for them as much as it is for me.

I would like to give a special thanks to my In-Laws, Ned and Rita Hart. They have supported Jennifer and me unconditionally and welcomed me into their family whole-heartedly. They are truly generous people and I appreciate the sacrifices they have made for Jennifer and me.

Table of Contents

Chapter 1: Introduction	1
1.1 Scientific rationale and perspective.....	1
1.2 References.....	2
Chapter 2: Review of the Literature	4
2.1 Photo-reactivity in preorganized assemblies and associated macromolecular architectures.....	4
2.1.1 Introduction to photochemistry.....	4
2.1.2 Photopolymerization	4
2.1.3 Photo-reactive groups.....	8
2.1.4 Photo-reactive preorganized assemblies.....	10
2.2 Photo-reactive associated macromolecular architectures.....	19
2.2.1 Photo-curable multilayer films.....	19
2.2.2 Photo-reactive self-assembled nanostructures.....	24
2.3 References.....	26
Chapter 3: Biomimetic design and performance of polymerizable lipids	29
3.1 Conspectus.....	29
3.2 Introduction.....	32
3.3 Origin and self-assembly of lipid membranes.....	32
3.4 Polymerizable hydrophobic regions in lipid membranes.....	37
3.5 Polymerizable hydrophilic regions in lipid membranes.....	43
3.6 Polymerization of nonlamellar lipid-cubic phases.....	47
3.7 Characterizing the efficiency of lipid membrane polymerization.....	51
3.8 Biomimetic properties of polymerized lipids.....	54

3.9 Perspective.....	57
3.10 Acknowledgements.....	59
3.11 References.....	59
Chapter 4: Gemini surfactant electrospun membranes.....	63
4.1 Abstract.....	63
4.2 Introduction.....	64
4.3 Materials and methods.....	68
4.3.1 Materials.....	68
4.3.2 Instrumentation.....	69
4.3.3 Synthesis of N,N'-didodecyl-N,N,N',N'-tetramethyl-N,N'-ethanediyl-di-ammonium dibromide (12-2-12).....	69
4.3.4 Cryogenic-TEM.....	71
4.3.5 Electrospinning process.....	73
4.4 Results and discussion.....	74
4.4.1 12-2-12 solution microstructure in water.....	74
4.4.2 12-2-12 solution microstructure in water:methanol.....	82
4.4.3 Electrospinning gemini surfactants.....	86
4.5 Conclusions.....	90
4.6 Acknowledgments.....	91
4.7 References.....	91
Chapter 5: Structure-property elucidation of photo-polymerizable gemini surfactants.....	94
5.1 Abstract.....	94
5.2 Introduction.....	95

5.3 Materials and methods.....	99
5.3.1 Materials.....	99
5.3.2 Instrumentation.....	99
5.3.3 <i>In situ</i> FTIR spectroscopy monitoring the synthesis of N,N'-didodecyl-N,N,N',N'-tetramethyl-N,N'-ethanediyl-di-ammonium dibromide (12-2-12)....	100
5.3.4 <i>In situ</i> FTIR spectroscopy monitoring the synthesis of N,N'-didodecyl-N,N,N',N'-tetramethyl-N,N'-hexanediyl-di-ammonium dibromide (12-6-12)...	100
5.3.5 Synthesis of N,N'-didodecyl-N,N,N',N'-tetramethyl-N,N'-ethanediyl-di-ammonium dibromide (12-2-12).....	102
5.3.6 Synthesis of N,N'-dihexadecyl-N,N,N',N'-tetramethyl-N,N'-ethanediyl-di-ammonium dibromide (16-2-16), and N,N'-dioctadecyl-N,N,N',N'-tetramethyl-N,N'-ethanediyl-di-ammonium dibromide (18-2-18).....	102
5.3.7 Synthesis of N,N'-di-(11-(acryloyloxy)undecyl)-N,N,N',N'-tetramethyl-N,N'-ethanediyl-di-ammonium dibromide (Acry-2-Acry).....	102
5.3.8 Synthesis of N,N'-di-(11-(cinnamoyloxy)undecyl)-N,N,N',N'-tetramethyl-N,N'-ethanediyl-di-ammonium dibromide (Cinn-2-Cinn).....	105
5.3.9 Polarized light microscopy.....	108
5.3.10 Kraft temperature conductance experiments	108
5.4 Results and discussion.....	110
5.4.1 Monitoring the synthesis of 12-2-12 and 12-6-12 with <i>in situ</i> FTIR.....	110
5.4.2 Differential scanning calorimetry and polarized light microscopy correlation.....	112
5.4.3 Kraft temperature conductance measurements.....	118
5.5 Conclusions.....	122
5.6 Acknowledgements.....	124
5.7 References.....	124

Chapter 6: Influence of hydrogen bonding on the adhesive properties of photo-curable acrylics.....	127
6.1 Abstract.....	127
6.2 Introduction.....	128
6.3 Materials and methods.....	132
6.3.1 Materials.....	132
6.3.2 Instrumentation.....	132
6.3.3 Free radical synthesis of acrylic precursor copolymers.....	133
6.3.4 Synthesis of Cinn1, Cinn2, and Cinn3: cinnamate functionalization of low T _g acrylic precursors.....	134
6.3.5 Synthesis of Ureth2: urethane functionalization of low T _g acrylic precursor 2.....	136
6.3.6 Cinnamate functionalization.....	136
6.3.7 Peel analysis.....	138
6.3.8 Rate of cinnamate photo-dimerization and gel fraction analysis.....	139
6.4 Results and discussion.....	140
6.4.1 Synthesis and peel performance of Cinn1, Cinn2, and Cinn3.....	140
6.4.2 Hydrogen bonding and photo-active sites in low T _g acrylics.....	144
6.4.3 Influence of hydrogen bonding sites on the rate of cinnamate photo-dimerization.....	148
6.5 Conclusions.....	154
6.6 Acknowledgements.....	156
6.7 References.....	156
Chapter 7: Photo-rheology of low T_g acrylics functionalized with hydrogen bonding and photo-reactive groups.....	158
7.1 Abstract.....	158

7.2 Introduction.....	159
7.3 Materials and methods.....	163
7.3.1 Materials.....	163
7.3.2 Instrumentation.....	163
7.3.3 Synthesis of poly(n-butyl acrylate-co-2-hydroxyethyl methacrylate) precursor.....	165
7.3.4 Urethane functionalization of the acrylic precursor.....	165
7.3.5 Cinnamate functionalization of the precursor and urethane functionalized acrylic.....	167
7.3.6 UV-vis characterization of UV-irradiated functionalized acrylic films.....	169
7.4 Results and discussion.....	170
7.4.1 Synthesis and functionalization of the acrylic precursor with hydrogen bonding and photo-reactive groups.....	170
7.4.2 Photo-rheology of the urethane and cinnamate functionalized acrylics.....	175
7.4.3 Influence of composition on the rate of cinnamate photo-reactivity.....	177
7.5 Conclusions.....	180
7.6 Acknowledgements.....	181
7.7 References.....	181
Chapter 8: <i>In situ</i> photo-crosslinking electrospun fibers of cinnamate functionalized low T_g acrylics.....	183
8.1 Abstract.....	183
8.2 Introduction.....	184
8.3 Materials and methods.....	188
8.3.1 Materials.....	188
8.3.2 Instrumentation.....	188

8.3.3 Synthesis of poly(n-butyl acrylate-co-2-hydroxyethyl acrylate) precursor.....	189
8.3.4 Cinnamate functionalization of the acrylic precursor.....	191
8.3.5 <i>In situ</i> photo-curing electrospun fibers.....	193
8.4 Results and Discussion.....	194
8.4.1 Synthesis and functionalization of the acrylic precursor with cinnamate.....	194
8.4.2 Electrospinning cinnamate functionalized low T _g acrylics without photo-curing.....	196
8.4.3 <i>In situ</i> photo-crosslinking electrospun cinnamate functionalized low T _g acrylics fibers.....	197
8.5 Conclusions.....	201
8.6 Acknowledgements.....	203
8.7 References.....	203
Chapter 9: Overall Conclusions.....	206
Chapter 10: Suggested Future Work.....	213
10.1 Photopolymerizable gemini surfactant lyotropic liquid crystals.....	213
10.2 Photo-reactive asolectin electrospun membranes.....	213
10.3 Designer electrospinnable photo-reactive gemini surfactans.....	218
10.4 References.....	222
Appendix A: Scaling relationships of 12-2-12 in water and water:methanol.....	223

List of Figures

Figure 2.1 Carbonyl, azo, and peroxide photosensitizers.....	5
Figure 2.2 Photolytic free radical initiation.....	6
Figure 2.3 Photoinitiation of methyl methacrylate.....	7
Figure 2.4 Maleated natural rubber modified with glycol cinnamate.....	8
Figure 2.5 Acetylene, dienoyl, and diene photo-active groups.....	9
Figure 2.6 Undecyl amide N-ethyl acrylate and pentyl amide N-methyl N-ethyl acrylate.....	11
Figure 2.7 Hydrogen bonding amide, urethane, and urea acrylics and non-hydrogen bonding control acrylic monomers.....	12
Figure 2.8 Diaminotriazine cinnamate and barbituric acid derivative complementary hydrogen bonding associations and the four possible configurations.....	15
Figure 2.9 Configuration of cinnamate diaminotriazine photoproducts.....	17
Figure 2.10 Structure of 4-(6-acryloyloxyhexyloxy)benzoic acid and 4-hexyloxy-4'-cyanobiphenyl.....	18
Figure 2.11 Hydroxyphenyl acrylamide, diazoresin, and proposed hydrogen bonding association.....	20
Figure 2.12 Photolithography of PAA-PAAm LBL films with photo-active top layer.....	22
Figure 2.13 PAA and photo-active acrylate copolymerized with PAA and incorporated in the top film layer.....	23
Figure 2.14 Second generation dendron with a hydrogen bonding urethane and amide core with a photo-reactive diacetylene periphery.....	25
Figure 3.1 Photo-polymerization of a self-assembled lipid bilayer with retention of the bilayer structure.....	31
Figure 3.2 Bilayer lipid membrane (BLM).....	33
Figure 3.3 Phosphatidylcholine (PC) vesicle sterically stabilized with PEG-DDGG copolymer.....	35

Figure 3.4 Diacetylene monoalkyl phosphate (1) and bis-diacetylene phospholipid (DiynePC) (2).....	37
Figure 3.5 Linear π -conjugated polydiacetylene backbone of 1	40
Figure 3.6 π -conjugated polydiacetylene network of 2	40
Figure 3.7 Lithographically micropatterned fluid lipid bilayers.....	42
Figure 3.8 Dicytyldimethylammonium-4-vinyl benzoate (DDVB) and dicytyldimethylammonium-3,5-divinyl benzoate (DDDB).....	43
Figure 3.9 (a) MF particle; (b) PE multilayer-coated MF particle; (c) Si-lipid polysiloxane coated PE-multilayer MF particle. Reprinted with permission from <i>Macromolecules</i> 37, 9947-9953 (2004).....	46
Figure 3.10 Polysiloxane silane-lipid that was deposited onto PE coated monodisperse colloidal particles.....	46
Figure 3.11 Lipid bicontinuous cubic liquid-crystalline phase.....	47
Figure 3.12 Polymerizable monoacylglycerol(3) and crosslinkable 1,2-diacylglycerol(4).....	49
Figure 3.13 1-palmitoyl-2-[1,2-(acryloyloxy)dodecanoyl]-sn-glycero-3-phosphocholine (ARPC).....	51
Figure 3.14 Luminal surface of PTFE vascular graft coated with PEM and ARPC polylipid.....	53
Figure 3.15 1,2-bis[10-(2',4'-hexadienoyloxy)decanoyl]-sn-glycero-3-phosphocholine (bis-SorbPC).....	54
Figure 3.16 The 1,2-, 1,4-, and 3,4-diene addition products of dienoyl polymerization..	55
Figure 4.1 N,N'-didodecyl-N,N,N',N'-tetramethyl-N,N'-ethanediyl-di-ammonium dibromide (12-2-12) ammonium gemini surfactant.....	65
Figure 4.2 Gemini surfactant entangled threadlike micelles in a polar solvent.....	67
Figure 4.3 ^1H NMR of 12-2-12.....	72
Figure 4.4 η_{sp} vs. concentration for 12-2-12 in water. The surfactant microstructure transitioned from linear threadlike micelles to branched threadlike micelles at 1.5 wt%, and into a highly-branched entangled network at 2.7 wt%.....	76

Figure 4.5 Cryo-TEM micrographs of 12-2-12 in water, a) 1.0 wt%, linear entangled threadlike micelles, b) 2.4 wt%, branched threadlike micelles, c) 4.1 wt%, highly-branched, entangled, threadlike micelles.....	77
Figure 4.6 Sliding of “Y” shaped branch point along the threadlike micelle.....	81
Figure 4.7 Surfactant ghost-like crosslinks.....	81
Figure 4.8 η_{sp} vs. concentration for 12-2-12 in water:methanol. Individual globular micelles began to overlap at a surfactant concentration of 11 wt%.....	83
Figure 4.9 Cryo-TEM micrographs of 12-2-12 in water:methanol, a) 10 wt%, individual globular micelles, b) 12 wt%, overlapped micelles.....	84
Figure 4.10 SEM of electrospun fibers of 12-2-12 from water:methanol ($C^*=11$ wt%), electrospun from: a) 20 wt%, b) 22 wt%, c) 28 wt%, d) 30 wt%, e) 42 wt%, d) 44 wt% 12-2-12 gemini surfactant solutions in water:methanol.....	87
Figure 5.1 Gemini surfactants.....	98
Figure 5.2 ^1H NMR of Acry-2-Acry.....	104
Figure 5.3 ^1H NMR of Cinn-2-Cinn.....	107
Figure 5.4 Quaternized ammonium growth profile at 908 cm^{-1} using <i>in situ</i> FTIR to monitor the synthesis of 12-6-12 and 12-2-12.....	111
Figure 5.5 TGA analysis of the gemini surfactant series.....	113
Figure 5.6 DSC of 12-2-12 and PLM images at $90\text{ }^\circ\text{C}$, $100\text{ }^\circ\text{C}$, and $110\text{ }^\circ\text{C}$	115
Figure 5.7 DSC of 16-2-16 and PLM images at $90\text{ }^\circ\text{C}$ and $110\text{ }^\circ\text{C}$	115
Figure 5.8 DSC of 18-2-18 and PLM images at $90\text{ }^\circ\text{C}$ and $110\text{ }^\circ\text{C}$	115
Figure 5.9 DSC of Acry-2-Acry.....	116
Figure 5.10 PLM images of Acry-2-Acry at $80\text{ }^\circ\text{C}$, $90\text{ }^\circ\text{C}$, $95\text{ }^\circ\text{C}$, $97\text{ }^\circ\text{C}$, 100°C , $102\text{ }^\circ\text{C}$, $104\text{ }^\circ\text{C}$, $106\text{ }^\circ\text{C}$, and $110\text{ }^\circ\text{C}$	117
Figure 5.11 DSC of Cinn-2-Cinn and PLM images at $120\text{ }^\circ\text{C}$ and $150\text{ }^\circ\text{C}$	117
Figure 5.12 Determination of T_k , conductance vs. temperature for 12-2-12 in water at 0.005 wt%, 1.0 wt%, and 2.0 wt%.....	119
Figure 6.1 Isothermal melt rheology of $2\text{U}_{21}\text{C}_3$ at $150\text{ }^\circ\text{C}$ for 2 h.....	146

Figure 6.2 Composition and structure of the urethane and control series. Both the urethane and control series contained 60 mol% EHA and 16 mol% MA.....	149
Figure 6.3 UV-vis absorbance of precursor 2 following urethane functionalization (2U₂₁H₃) and cinnamate functionalization (2U₂₁C₃).....	150
Figure 6.4 Kinetic plot investigating the rate of cinnamate photo-dimerization as a function of cinnamate and urethane concentration.....	152
Figure 7.1 Schematic of the photo-rheometer for <i>in situ</i> monitoring UV cross-linking. The incident UV beam is reflected from a mirror through the quartz top plate onto the sample film. Reprinted in part with permission from <i>Macromolecules</i> 29, 5368-5374 (1996). Copyright 2009 American Chemical Society.....	160
Figure 7.2 ¹ H NMR of the poly(nBA- <i>co</i> -HEMA) precursor.....	171
Figure 7.3 ¹ H NMR of U₂₄	171
Figure 7.4 ¹ H NMR of C₂₄	172
Figure 7.5 Photo-rheology of the precursor, urethane- and cinnamate-functionalized copolymers at 25 °C. Films were equilibrated for 420 s, at which point the UV-light was actuated.....	176
Figure 7.6 Decrease in cinnamate UV-absorbance at 275 nm with increasing UV-exposure time for U₂₀C₄	177
Figure 7.7 Kinetic plot investigating the rate of cinnamate dimerization verses UV-exposure time as a function of cinnamate and urethane concentration.....	179
Figure 8.1 Electrospinning setup with <i>in situ</i> photo-curing.....	187
Figure 8.2 UV-vis absorbance of the acrylic precursor and cinnamate functionalized acrylate.....	195
Figure 8.3 SEM of cinnamate functionalized acrylic electrospun without <i>in situ</i> photo-curing, which resulted in an acrylic coating on the collection substrate.....	196
Figure 8.4 SEM of the <i>in situ</i> photo-cured cinnamate acrylate electrospun fibers from concentrations of a) 15 wt% b) 25 wt% c) 35 wt% in DMF/THF (3/1 vol).....	199
Figure 8.5 FTIR spectroscopy of the cinnamate acrylate and <i>in situ</i> photo-cured electrospun membrane. The cinnamate C=C stretch decreased following photo-curing.....	200

Figure 10.1 Mixture of lipids that compose asolectin. Referenced from Sigma-Aldrich.....	214
Figure 10.2 UV-vis characterization of asolectin at 0.1 wt% in chloroform and chloroform.....	215
Figure 10.3 TGA analysis of the UV-irradiated asolectin films with 0 wt%, 0.1 wt%, and 1.0 wt% photoinitiator and a non-irradiated control film.....	216
Figure 10.4 Storage modulus of UV-irradiated asolectin films with 0 wt%, 0.1 wt%, and 1.0 wt% photoinitiator and non-irradiated control film. Melt rheology conditions: 8 mm parallel plates, 2% strain, 110 °C, and 1 mm gap.....	217
Figure 10.5 Solution rheology of Acry-2-Acry in water:methanol (1:1 vol).....	219
Figure 10.6 SEM of Acry-2-Acry electrospun from 70 wt% in water:methanol (1:1 vol), a) without <i>in situ</i> photo-curing, b) <i>in situ</i> photo-cured.....	220
Figure 10.7 Designer polymerizable gemini surfactants.....	221

List of Schemes

Scheme 4.1 Synthesis of 12-2-12.....	70
Scheme 5.1 Synthesis of 12-6-12.....	101
Scheme 5.2 Synthesis of Acry-2-Acry, (i) 0 °C for 16 h, triethylamine, dichloromethane, (ii) 80 °C for 48 h, methanol, hydroquinone.....	103
Scheme 5.3 Synthesis of Cinn-2-Cinn, (i) 0 °C for 16 h, triethylamine, dichloromethane, (ii) 80 °C for 48 h, methanol.....	106
Scheme 6.1 Synthesis of acrylic precursors 1-3	135
Scheme 6.2 Synthesis of UrethCinn2, the urethane and cinnamate functionalization of precursor 2, (i) 0.2 mL of 1 wt% di-n-butyltin-dilaurate in toluene, 40 wt% solids in toluene, 50 °C (ii) triethylamine, 20 wt% solids in dichloromethane, 0 °C.....	137
Scheme 7.1 Synthesis of the poly(nBA- <i>co</i> -HEMA) precursor.....	166
Scheme 7.2 Urethane and cinnamate functionalization of acrylic precursor, (i) 0.2 mL of 1 wt% di-n-butyltin-dilaurate in toluene, 40 wt% solids in toluene, 50 °C, (ii) triethylamine, 20 wt% solids in dichloromethane, 0 °C.....	168
Scheme 8.1 Synthesis of the poly(nBA- <i>co</i> -HEMA) precursor.....	190
Scheme 8.2 Cinnamate functionalization of the acrylic precursor.....	192

List of Tables

Table 5.1 T_k of the ammonium gemini surfactant series in water and water:methanol (1:1 vol).....	121
Table 6.1 Composition, molecular weight, and T_g comparison of precursors 1-3	141
Table 6.2 Composition, molecular weight, and UV-cured 90° peel strength of Cinn1 , Cinn2 , and Cinn3	143
Table 6.3 Composition, molecular weight, and T_g of the urethane series (UEA: 2-(cyclohexylcarbamoyloxy)ethyl acrylate (urethane ethyl acrylate)).....	145
Table 6.4 UV-cured and non-cured 90° peel strength of the urethane series.....	147
Table 7.1 Composition, molecular weight, and T_g comparison of the precursor, urethane- and cinnamate-functionalized copolymers (*EMA: ethyl methacrylate).....	174

Chapter 1: Introduction

1.1 Scientific Rationale and Perspective

Photochemical processes, which harvest and circulate the sun's energy, are the basis for all existence.¹⁻³ Nature absorbs and distributes the sun's energy through photo-biological processes. Electromagnetic radiation emitted from the sun is responsible for very important natural processes such as visual processing of humans and animals, photosynthesis, and seasonal transformations.^{4,5} Photochemistry is the scientific discipline of identifying the chemical and physical response of exposing controlled substances to electromagnetic radiation.⁶⁻¹⁰ Photochemistry is a mature discipline that utilizes controlled experiments to drive molecular changes when a atom or molecule absorbs light. Photochemical processes are easily controlled, affordable, effective, and initiated with light, which is a clean energy.⁷⁻⁹ Applicable technologies that utilize photochemistry encompass photonics, microfluidics, solar energy harvesting, and electrooptics.¹¹⁻¹³ Photochemistry is truly a diverse topic that incorporates a multitude of assorted disciplines.

The study of how small molecules behave in response to radiation is an established field that has evolved over the past century. However, the influence of organizing materials via noncovalent interactions before irradiation is a relatively new field that has emerged over the past 25 years,¹⁴⁻¹⁶ and the irradiation of organized macromolecular architectures is an evolving area of interest.^{8,17} There are many reasons why the interest of researchers has turned to the area of organized assemblies.¹⁸⁻²⁰ Most notably there are applicable technologies in electronics, biomaterials, and liquid crystalline displays.^{21,22} Confinement of molecules through noncovalent interactions

restricts their mobility. This type of confinement is used to promote desirable interactions that offer several advantages over unorganized systems. The limited mobility of organized media affords the opportunity for characterization of species with short life times such as intermediates, free radicals, excited states, and highly strained molecules.⁸ The use of noncovalent interactions to promote photochemical reactions is an emerging field. Chromophore alignment in a proximity that promotes photo-reactivity is achievable through noncovalent interactions. Several methods to achieve the association of chromophores include: ionic interactions, hydrogen bonding, donor-acceptor complexes, and metal ligand complexes.

The major research objective was to design photo-reactive supramolecular structures, focusing around the use of non-covalent interactions to associate molecules in combination with photochemical reactions to covalently confine assembled architectures. Small molecule lipids and surfactants were designed with photo-reactive functionality to polymerize self-assembled structures, for application as biologically compatible membranes and scaffolds. Macromolecular acrylic copolymers were functionalized with hydrogen bonding and photo-curable functionality to covalently crosslink associated macromolecular architectures for the development of *in situ* photo-cured electrospun membranes and novel hot melt adhesives.

1.2 References

1. Bjorn, L. O., *Photobiology: The Science of Light and Life*. Kluwer Academic: Boston, 2002.
2. Ott, J. N., *Health and light: the effects of natural and artificial light on man and other living things*. Devin-Adair Co: Old Greenwich, Conn, 1973.
3. Smith, K. C., *The Science of Photobiology*. Plenum Press: New York, 1977.
4. Coyle, J. D., *Introduction to Organic Photochemistry*. John Wiley & Sons: Chichester, England, 1986.

5. Wolken, J. J., *Light and life processes*. Van Nostrand Reinhold Co.: New York, 1986.
6. Griesbeck, A. G.; Mattay, J., *Synthetic Organic Photochemistry*. Marcel Dekker: New York, 2005.
7. Horspool, W.; Lenci, F., *CRC Handbook of Photochemistry and Photobiology*. CRC Press: Boca Raton, FL, 2004.
8. Ramamurthy, V.; Schanze, K. S., *Organic Molecular Photochemistry*. Marcel Dekker: New York, 1999.
9. Ramamurthy, V.; Schanze, K. S., *Organic, Physical, and Materials Photochemistry*. Marcel Dekker: New York, 2000.
10. Wishart, J. F.; Nocera, D. G., *Photochemistry and Radiation Chemistry: Complementary Methods for the Study of Electron Transfer*. ACS: Washington D.C., 1998; Vol. 254.
11. Allen, N. S., *Photochemistry* **1996**, 27, 303-360.
12. Anpo, M., *Surface Photochemistry*. John Wiley & Sons: New York, 1996.
13. Guldi, D. M., *J. Phys. Chem. B* **2005**, 109 (23), 11432-11441.
14. Gao, X.; Friscic, T.; MacGillivray, L. R., *Angew. Chem., Int. Ed.* **2003**, 43 (2), 232-236.
15. Kaanumalle, L. S.; Nithyanandhan, J.; Pattabiraman, M.; Jayaraman, N.; Ramamurthy, V., *J. Am. Chem. Soc.* **2004**, 126 (29), 8999-9006.
16. Papaefstathiou, G. S.; Zhong, Z.; Geng, L.; MacGillivray, L. R., *J. Am. Chem. Soc.* **2004**, 126 (30), 9158-9159.
17. Huang, C.-H.; Bassani, D. M., *Eur. J. Org. Chem.* **2005**, (19), 4041-4050.
18. Lehn, J.-M., *Polym. Int.* **2002**, 51 (10), 825-839.
19. Lehn, J.-M., *Proc. Natl. Acad. Sci. U. S. A.* **2002**, 99 (8), 4763-4768.
20. Whitesides, G. M.; Simanek, E. E.; Mathias, J. P.; Seto, C. T.; Chin, D.; Mammen, M.; Gordon, D. M., *Acc. Chem. Res.* **1995**, 28 (1), 37-44.
21. Schadt, M.; Seiberle, H.; Schuster, A., *Nature* **1996**, 381 (6579), 212-215.
22. Sung, S.-J.; Cho, K.-Y.; Yoo, J.-H.; Kim, W. S.; Chang, H.-S.; Cho, I.; Park, J.-K., *Chem. Phys. Lett.* **2004**, 394 (4-6), 238-243.

Chapter 2: Review of the Literature

2.1 Photo-reactivity of Preorganized Assemblies and Associated Macromolecular Architectures

2.1.1 Introduction to Photochemistry

Photochemical reactions occur when a molecule absorbs a photon of light. Upon photon absorption, the molecule is activated to an electronically excited state, the increase in energy is equal to the energy of the absorbed photon. Exposure to radiation¹, flame treatment², an electrical current³, or a chemical reaction,⁴ are methods to activate ground state molecules. Irradiation with visible or UV light is the most utilized method to activate ground state molecules.⁵⁻⁹ Absorption of visible or UV radiation promotes the ground state electron into a lower-lying unoccupied excited state. UV and visible light are classified in the optical radiation range of the electromagnetic radiation spectrum. UV radiation is the highest energy of the optical range and is subdivided into three subdivisions: UVC (100-280 nm), UVB (280-315 nm), UVA (315-380 nm).¹⁰ Visible light is detectable to the human eye and ranges from violet (~380 nm) to red (~700 nm).

2.1.2 Photopolymerization

Polymerization initiated with UV-irradiation, visible light or exposure to ionizing radiation is referred to as photoinitiated polymerization.¹¹⁻¹⁴ The mechanism can proceed via the same route as conventional polymerizations including cationic, free radical, and living polymerization. Monomers that undergo chain reaction polymerization have a tendency to undergo photopolymerization. Initiation occurs when the monomer absorbs radiation and generates an activated radical or ionic species. Photosensitizers are used to initiate monomers that do not directly absorb light at the given wavelength.

Photoinitiators produce free radicals or ions upon exposure to UV or visible light. Photoinitiators that produce free radicals include carbonyl compounds, peroxides, and azo compounds to list a few, as shown in Figure 2.1.^{3,15,16}

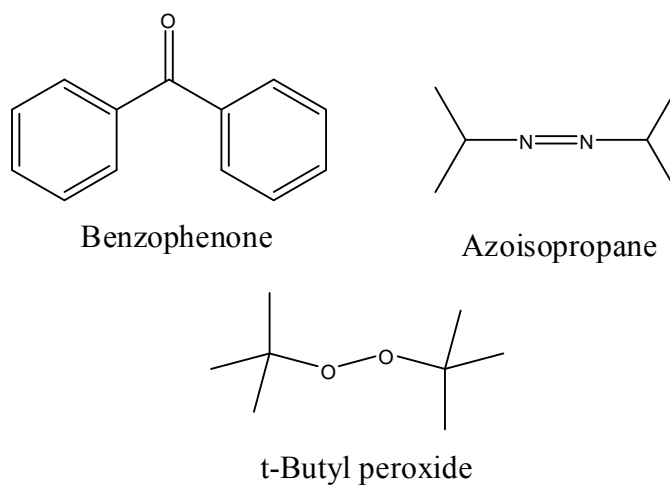


Figure 2.1 Carbonyl, azo, and peroxide photosensitizers.

Photopolymerization offers advantages to thermally initiated chain reaction polymerization. Photoinitiation is less susceptible to reaction conditions, environmentally appealing, and uses a fraction of the energy thermally initiated processes consume. In contrast to thermal initiation, photoinitiated polymerization occurs at lower temperatures at a specific wavelength under mild reaction conditions. Environmentally beneficial reaction conditions and affordable processes make photoinitiated polymerization a directly applicable technology. Photochemistry is utilized in the production of lithography plates, adhesives, protective coatings, biomedical materials, holography technologies, and the manufacturing of integrated circuits.^{3,4,10-17}

Free radical initiated polymerization is the most common and widely used photoinitiation mechanism. Chain propagation, chain transfer, and termination mechanisms are the same for photo-active processes as conventional free radical chain

polymerization. Photoinitiated polymerization generates free radicals through a different mechanism than conventional thermal initiated free radical systems. Photolytic initiation generates an electronically excited initiator or monomer unit (M^*) after light absorption. The excited monomer then dissociates to generate two radical species ($\bullet R_1$ and $\bullet R_2$) that attack other monomer units to propagate polymerization, as shown in Figure 2.2. The efficiency of photolytic free radical generation is proportional to the monomer concentration and independent of temperature. Alkyl vinyl ketones and halogenated vinyls are examples of two monomers which undergo photolytic dissociation.^{18,19}

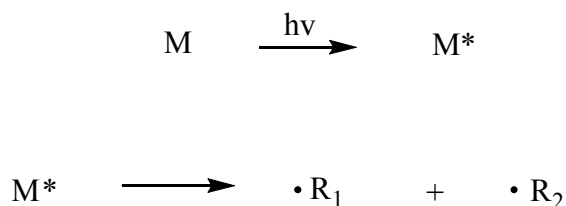


Figure 2.2 Photolytic free radical initiation.

Monomers like styrene and methyl methacrylate require radiation of 300 nm or shorter wavelengths to generate free radicals. The mechanism for radical generation is not completely understood, however, it is known the monomers do not dissociate upon light absorption. When light is absorbed in styrene or methyl methacrylate an excited singlet state is generated which may fluoresce or create an excited triplet state and form a diradical, as shown in Figure 2.3. The diradical then attacks monomer units to propagate polymerization. Other monomers that photopolymerize with or without the use of photosensitizers include acrylonitriles,²⁰ isobutylene,²¹ methyl acrylate,²² and vinyl acetate.²³

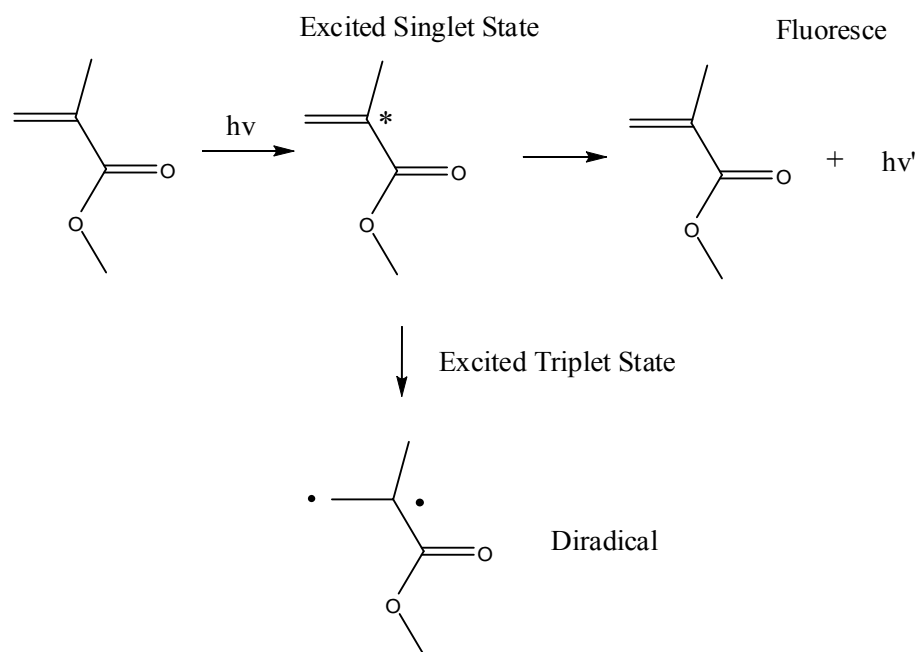


Figure 2.3 Photoinitiated diradical formation of methyl methacrylate.

2.1.3 Photo-reactive Groups

In the 1950's Minsk and coworkers were the first to study the photo-dimerization of cinnamate groups.^{24,25} Minsk and researchers reported the photoinitiated crosslinking reaction of cinnamate groups in poly(vinyl cinnamate). Cinnamates are known to photo-dimerize through $[2\pi + 2\pi]$ cycloaddition to form cyclobutane. Since Minsk's initial discovery the cinnamate functionality has received interest in polymeric and small molecules as a chromophore.²⁶⁻²⁹ Cinnamates are utilized mostly as a crosslinking agent in polymers and liquid crystalline assemblies. Other photo-reactive groups that photo-dimerize in a $[2\pi + 2\pi]$ cycloaddition fashion include furans,^{30,31} maleimides,^{32,33} chalcones,³⁴ and coumarins.^{35,36}

Visconte and coworkers studied the crosslinking efficiency of natural rubber functionalized with cinnamate side chains, and investigated the spatial conformations needed for photo-dimerization to occur.²⁶ Natural rubber was first maleated through reaction with maleic anhydride and then esterified with glycol cinnamate. The glycol spacer unit was varied between 2 to 6 carbons, as shown in Figure 2.4. The study incorporated between 7 and 29 mol % of the cinnamate side chain. The Li^+ , Na^+ , and K^+ carboxylate salt forms were obtained to investigate the salt effects on crosslinking

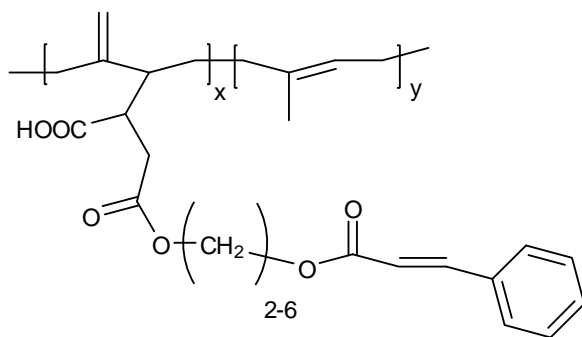


Figure 2.4 Maleated natural rubber modified with glycol cinnamate.

efficiency. The researchers discovered that the spacer unit was strongly dependent for the 7 mol% cinnamate, however, there was no constant trend between the three salt samples. The 15 to 29 mol% cinnamate functionalized samples showed little variation for each of the three cationic salts. The researchers concluded that providing molecular mobility alone and not affording spatial confirmation for the cyclobutane ring to form does not provide sufficient driving force for network formation.

Cinnamates have also received interest as well defined functional end groups in branched polymeric systems. Russell and researchers synthesized PEG based hydrogels from branched PEG macromers.²⁷ Branched PEG end capped with hydroxyl groups was functionalized with cinnamylidene acetyl, to give a water-soluble macromer with only one chromophore per chain end. Exposure to UV irradiation formed an insoluble hydrogel as the branched cinnamylidene macromer exhibited step growth behavior. A pegylated cinnamate containing enzyme was also synthesized and immobilized in the cross-linked hydrogel network. The group studied the uptake, activity, and stability of the enzyme immobilized within the hydrogel.

Examples of photo-active groups that do not form dimers but chain extend are acetylenes,^{37,38} dienoyls or sorbates,³⁹ and dienes,^{40,41} as shown in Figure 2.5. Acetylenic

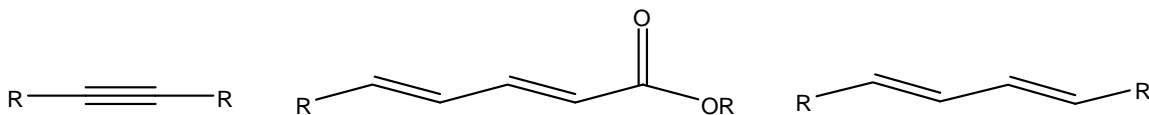


Figure 2.5 Acetylene, dienoyl, and diene photo-active groups.

and dialkene groups UV absorb to generate free radical species that chain extend from propagation of the free radical to other unsaturated groups. Acetylenes, dienoyls, and dienes are photo-active upon UV exposure in the solid state, in the molten state, or in solvating media. Chain extension of the unsaturated photo-active group produces conjugated chains that have generated application in electronics, controlled release, and encapsulation technologies.^{34,36-38} The rate of photopolymerization of chain extenders can benefit from conformational confinement in preorganized assemblies that promote photo-reactivity.

2.1.4 Photo-reactive Preorganized Assemblies

Preorganized assemblies are described as molecular associations that are driven through noncovalent interactions. Hydrogen bonding, ionic interactions, donor-acceptor complexes, and metal ligand complexes are all examples of noncovalent interactions. The prefix pre- is included to indicate the noncovalent molecular associations occur first and photo-curing second. Researchers are interested in gaining a fundamental understanding of how preorganized molecular associations influence the efficiency of photo-reactivity.^{7,42-44} Due to the short life span of an electronically excited state, photochemical processes can benefit from organized assemblies that place reactive groups in close proximity to one another.

Hydrogen bonding is the most widely utilized method to form molecular associations of photo-active assemblies. Jansen and coworkers incorporated hydrogen bonding moieties to enhance photopolymerization of acrylate monomers.⁴⁵ The influence of hydrogen bonding was examined when two acrylate monomers were synthesized, undecyl amide N-ethyl acrylate, which contains hydrogen bonding functionality, and

pentyl amide N-methyl N-ethyl acrylate, which does not contain hydrogen bonding functionality, as shown in Figure 2.6. The samples were exposed to UV irradiation and the photopolymerization was monitored using real time Fourier transform infrared (RT-

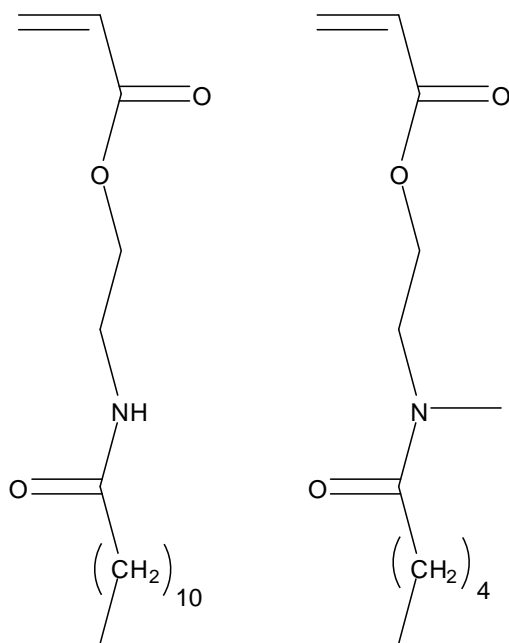


Figure 2.6 Undecyl amide N-ethyl acrylate and pentyl amide N-methyl N-ethyl acrylate.

FTIR) spectroscopy to measure the rate of polymerization (R_p). Initial experiments determined the acrylate capable of hydrogen bonding exhibited an R_p 4.5 times larger than the non-hydrogen bonding control. The apparent influence hydrogen bonding had on the R_p encouraged the researchers to synthesize a series of acrylate monomers, as seen in Figure 2.7, with amid, urethane, and urea functionalities along with non-hydrogen bonding monomers (control) and measure the corresponding R_p . It was evident the

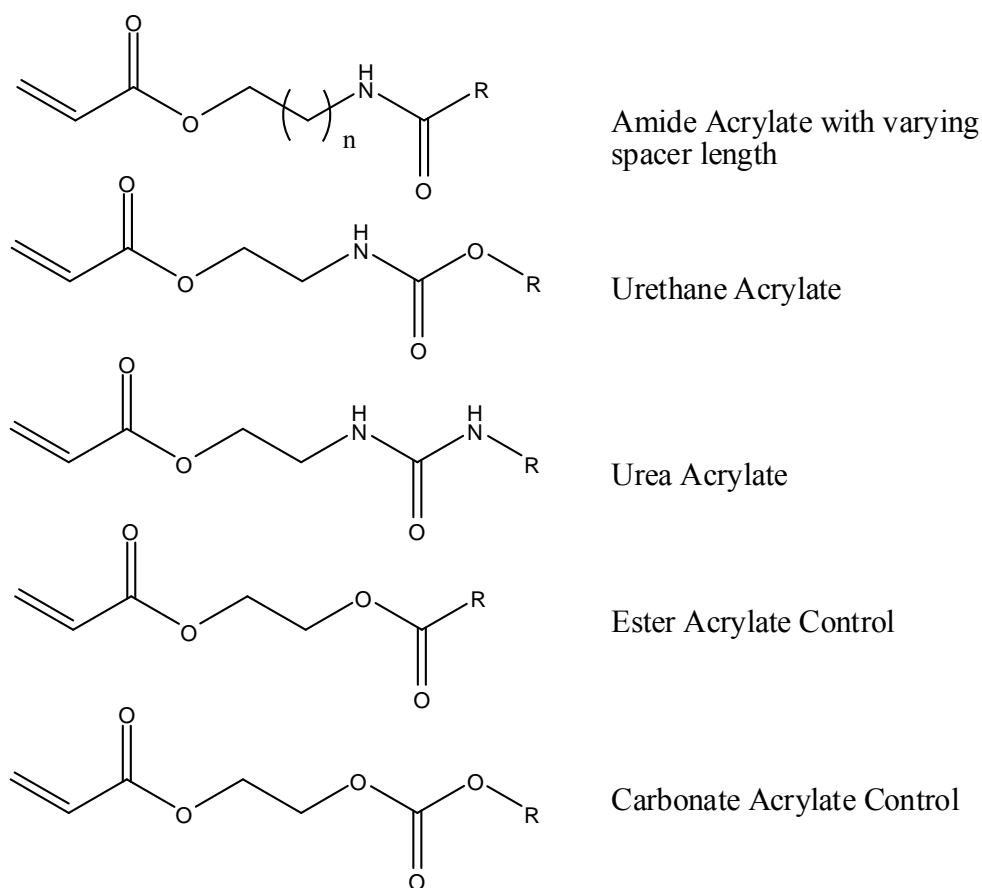


Figure 2.7 Hydrogen bonding amide, urethane, and urea acrylics and non-hydrogen bonding control acrylic monomers.

monomers capable of hydrogen bonding displayed higher R_p . The highest R_p belonged to the strongest hydrogen bonding functionality, the urea acrylate. The rationale for this phenomenon was attributed from two plausible possibilities. One, hydrogen bonding caused the monomers to behave like a difunctional species, similar to methacrylic acid.⁴⁶ The apparent difunctional species did not influence the rate constant of propagation but the rate constant of termination was considerably reduced for methacrylic acid. Secondly, the increase in R_p is a result of the propagation rate enhancement achieved from preorganization of the monomer units. Hydrogen bonding functionality facilitated the organization of acrylate double bonds at a proximity advantageous for propagation. If the preorganized theory was correct, an increase in chain length between the acrylate and hydrogen bonding site would result in a decreased R_p . As the distance between the acrylate and hydrogen bonding moieties increased, the acrylate would have more conformational chain mobility. The reactive acrylate is considered isolated from the hydrogen bonding site at a critical chain length distance. At this distance, the hydrogen bonding site would have no effect on the proximity of the acrylates to one another. The researchers tested their reasoning and synthesized a series in which the alkyl chain of ethyl amide N-alkyl acrylate was varied from ethyl to hexyl and the corresponding R_p determined using RT-FTIR. The chain length influenced the R_p in the manner which the researchers proposed. As the chain length increased to six carbons the R_p decreased to a value comparable to the non-hydrogen bonding controls. The influence of chain length on R_p helped to verify the theory of preorganization.

Preorganization was also applied to associate supramolecular catalyst to enhance photo-dimerization. Cinnamic esters do not give high yields of photo-dimers in the solid

state. Upon irradiation the cinnamates mostly photo-isomerize between the *E*- and *Z*-confirmations and lose their crystalline integrity. The reasoning for low yields of dimerization is not due to the lack of chain mobility but in fact a consequence of crystal packing structures that do not properly align to promote cyclo-dimerization. A C=C center to center distance ≤ 4.2 Å is required to promote photo-dimerization.⁴⁷ Bassani and coworkers covalently attached cinnamate groups to multiple hydrogen bonding groups to combat the reluctance of photo-dimerization and to align reactive groups in a configuration to promote dimerization.^{48,49} Cinnamates were covalently attached to diaminotriazine groups and their association with complementary hydrogen bonding barbituric acid derivatives investigated, as shown in Figure 2.8. There were four possible hydrogen bonded confirmations between barbituric acid and cinnamate functionalized diaminotriazine. Three of the confirmations were trimers with one barbiturate hydrogen bonding with two diaminotriazines with the cinnamates in different proximities to one another. The fourth confirmation was a dimer formed from the association of one barbiturate with one diaminotriazine cinnamate. The photo-reactivity of a diaminotriazine cinnamate with no complementary hydrogen bonding barbiturate (control) was investigated in solution when exposed to 350 nm monochromatic light, and a solution containing a 2:1 molar ratio of diaminotriazine to barbiturate was irradiated under the same conditions.

The irradiation of the control resulted in the presence of a 2:1 mixture of the *Z*- and *E*- confirmations. Only a very small trace of the photo-dimer was detectable after prolonged irradiation. Irradiation of cinnamate diaminotriazine in the presence of a barbiturate resulted in the appearance of three new photoproducts, as shown in Figure

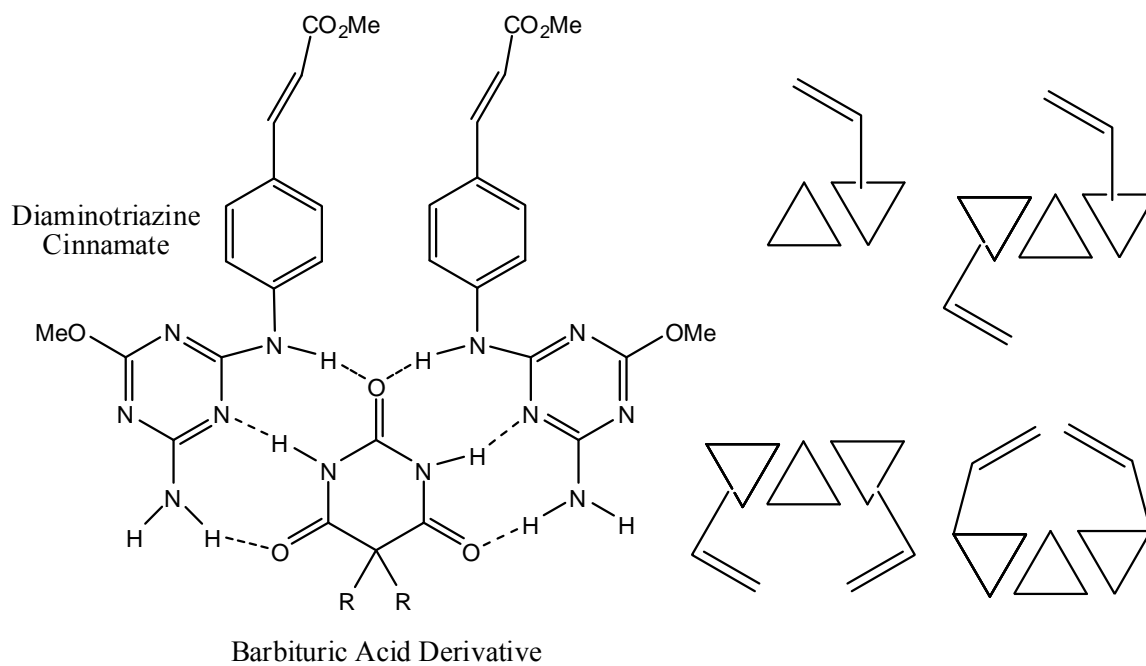


Figure 2.8 Diaminotriazine cinnamate and barbituric acid derivative complementary hydrogen bonding associations and the four possible configurations.

2.9. The major photoproduct was attributed to dimerization of cinnamates in symmetrical head-to-head confirmations with the phenyl groups cis to one another. The second product was attributed to the dimerization of an *E*-cinnamate and a *Z*-cinnamate in an endo head-to-head confirmation. The minor product was associated with the dimerization of two *E*-cinnamates in a head-to-tail configuration. The hydrogen bonding association between a barbiturate and two diaminotriazine cinnamates acted as a supramolecular catalyst. The associations placed the reactive cinnamates in an appropriate template to catalyze photo-dimerization.

Other research groups have exploited different methods to drive associations and enhance photo-reactivity. Lewis and coworkers utilized Lewis acid complexation to catalyze photo-dimerization of cinnamate esters.⁵⁰ Methyl cinnamate and other cinnamate esters were coordinated with SnCl₄ at a ratio of 2:1, cinnamate to SnCl₄. Methyl cinnamate complexation resulted in an 8% increase in photo-dimerization and ethyl cinnamate complexation resulted in a 31% increase in photo-dimerization. The crystal structures of the complexes were not known, however space filling models of the complexation positioned the esters in a closed packed head-to-tail configuration. The head-to-tail configuration positioned the reactive alkene groups within the required 4.2 Å of one another.

In the late 1980's Noonan and coworkers at Eastman Kodak Company realized the potential of incorporating UV-curable cinnamate side chains in novel liquid crystalline (LC) vinyl polymers.⁵¹ The researchers discovered the rate of cinnamate photo-reactivity increased in ordered LC arrays compared to amorphous analogs. The confinement of LC domains is ideal for photoinitiated polymerization. Recently, the

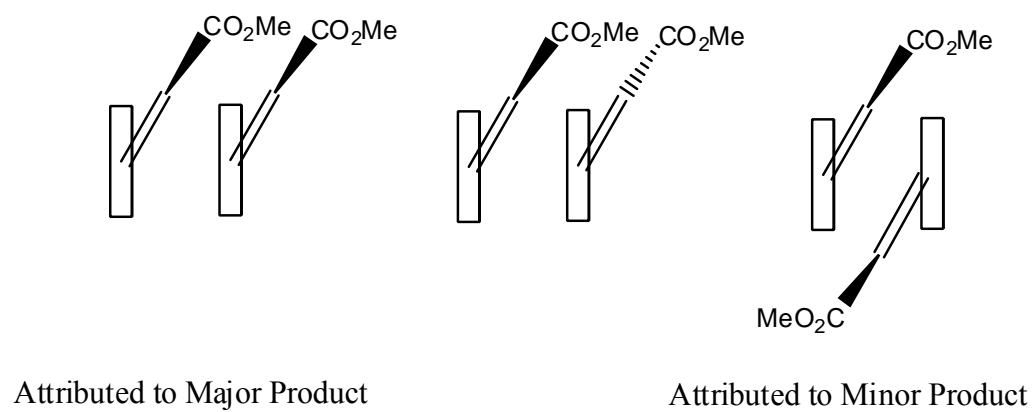


Figure 2.9 Configuration of cinnamate diaminotriazine photoproducts.

photoinitiated polymerization in liquid crystalline (LC) domains facilitated the formation of submicron synthetic polymer fibers.⁵²⁻⁵⁴ Kihara and coworkers⁵⁵ reported the formation of fibers from the photopolymerization of a LC blend of 4-(6-acryloyloxyhexyloxy)benzoic acid and 4-hexyloxy-4'-cyanobiphenyl, as shown in Figure 2.10. The acrylate monomer was miscible in the liquid crystalline field of 4-hexyloxy-4'-cyanobiphenyl, and upon photopolymerization the resulting polymer was immiscible and phase separated to form fibers. The temperature of photopolymerization was varied to investigate how the LC phase behavior influenced the resulting fiber formation. The researchers concluded that fiber formation and organization were optimized at temperatures low enough to facilitate LC formation of the phase separated acrylate polymer.

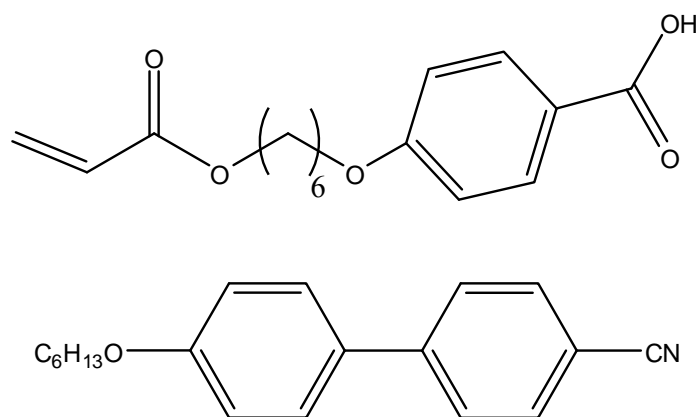


Figure 2.10 Structure of 4-(6-acryloyloxyhexyloxy)benzoic acid and 4-hexyloxy-4'-cyanobiphenyl.

2.2 Photo-reactive Associated Macromolecular Architectures

The association of macromolecules through noncovalent interactions is accomplished through functionality that facilitates the formation of donor-acceptor complexes,⁵⁶⁻⁵⁸ hydrogen bonding,^{59,60} liquid crystalline behavior,⁶¹⁻⁶³ and the self-assembly of polymeric amphiphiles.^{64,65} The capability to associate molecules and photocure the associated structure is a novel scheme that has received significant interest for application as liquid crystalline polymers.⁶⁶⁻⁶⁹ In most cases the LC polymer is formed from the photopolymerization of preassembled LC monomers with photopolymerizable groups. In contrast, layer-by-layer (LBL) assembly technologies utilize the association of macromolecules to form ultra thin multilayer films.⁷⁰ The LBL assembly driven from hydrogen bonding was first reported in 1997 and proved to produce more stable films than Langmuir Blodgett techniques.⁷¹ The hydrogen bonding LBL films exhibited low solvent resistance and were susceptible to deformation at temperatures that disassociated the hydrogen bonding assembly.

2.2.1 Photo-curable Multilayer Films

To increase the solvent resistivity and mechanical strength of hydrogen bonding LBL assemblies, Yang and coworkers⁷² incorporated photo-curable groups. Diazo resin, H-acceptor, and hydroxyphenyl acrylamide, H-donor, are shown in Figure 2.11. The diazo resin and hydroxyphenyl acrylamide were deposited on quartz wafers in an alternating fashion to construct multilayer films. The $-N_2^+$ of diazo resin becomes reactive upon UV-irradiation and the mechanism of crosslinking is facilitated through electrophilic aromatic substitution of the phenyl cation resin with the hydroxyphenyl acrylamide, or the formation of an ether linkage from the nucleophilic attack of the

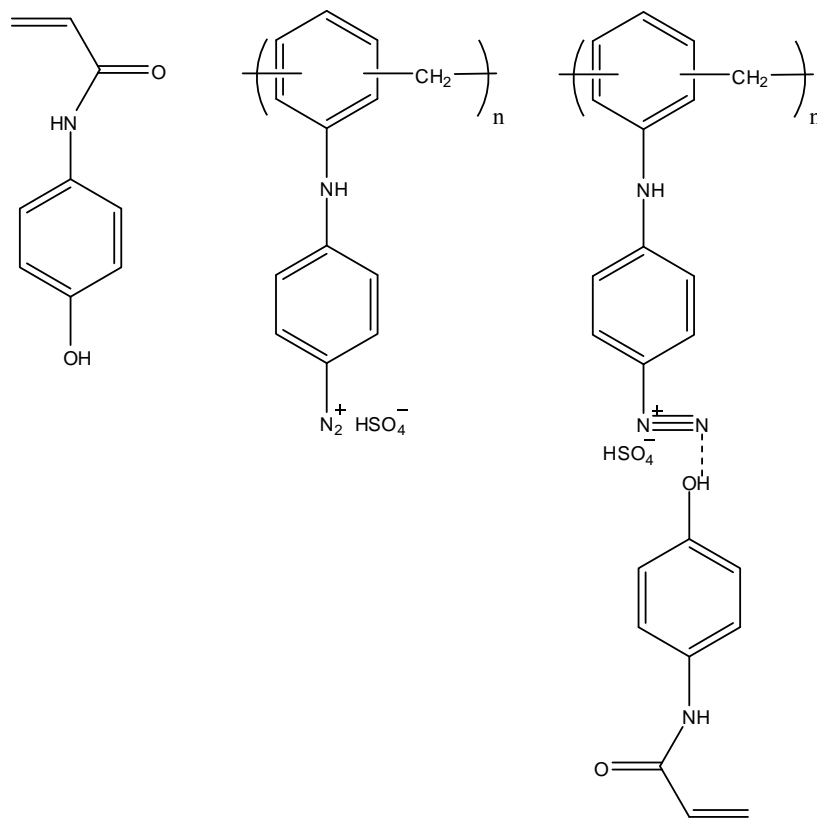


Figure 2.11 Hydroxyphenyl acrylamide, diazoresin, and proposed hydrogen bonding association.

hydroxyphenyl on the diazoresin with N_2 as the leaving group. The irradiated and non-irradiated (control) multilayer films were characterized using IR spectroscopy. Upon irradiation the $-N_2^+$ of the diazoresin, peak disappears along with the peak assigned to the $-OH$ of the hydroxyphenyl participating in hydrogen bonding with the $-N_2^+$. The photo-cured and control multilayer films were immersed in DMF to test their stability towards polar solvents. After 20 min. at room temperature the control was completely dissolved, however, the photo-cured multilayer film remained unetched after immersion for 24 h at room temperature.

Rubner and coworkers⁷³ constructed LBL multilayer films of photo-active hydrogen bonding polymers for application in photolithography. Poly(acrylic acid) (PAA) and polyacrylamide (PAAm) were alternately deposited in a LBL manner, on a variety of substrates as shown in Figure 2.12. LBL assembly was facilitated from dipping the substrate in PAA and PAAm aqueous solutions repeatedly. The cohesive strength of PAA and PAAm was facilitated through hydrogen bonding between the acid and amide groups. The association was restricted to a pH of 3 due to the ionization of the PAA acid groups and the introduction of electrostatic repulsive forces at $pH \geq 5$. Ten percent of the PAA was functionalized with a photoinitiator that induced crosslinking upon UV irradiation, as shown in Figure 2.13. The photo-active PAA was only deposited as the final layer of the film. Upon UV irradiation the entire film became insoluble at a pH greater than 7, indicating the radicals generated on the top layer were capable of diffusing through the film. A control of the LBL film with no photo-active functionalized PAA was irradiated to confirm the crosslinking was attributed to the presence of the photo-active group. The control was completely soluble after UV-

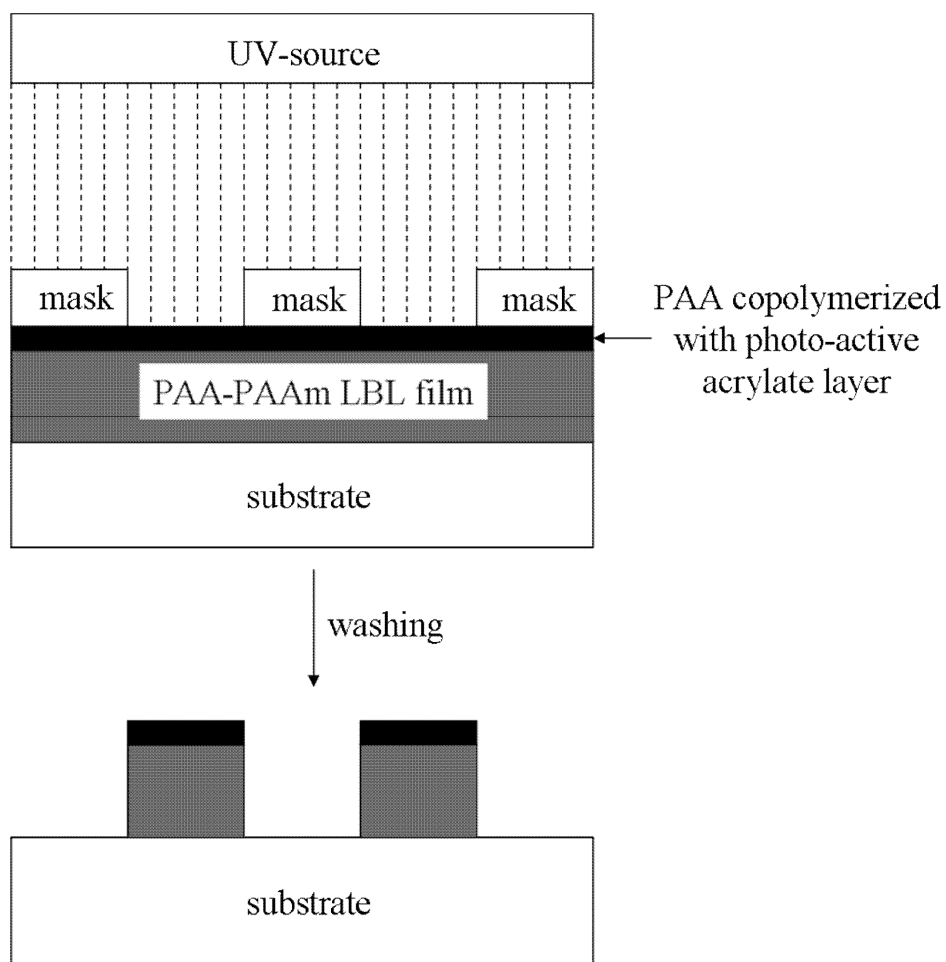


Figure 2.12 Photolithography of PAA-PAAm LBL films with photo-active top layer.

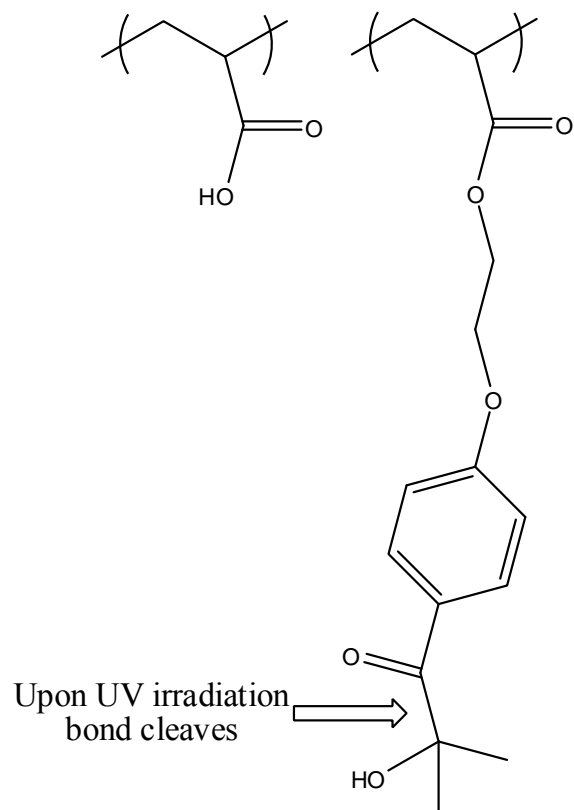


Figure 2.13 Polyacrylic acid (PAA) and photo-active acrylate copolymerized with PAA and incorporated in the top film layer.

treatment. There was no mention of characterizing the irradiated films other than testing their solubility in aqueous solutions. The photo-active hydrogen bonding PAA-PAAm multilayer films were used in photolithography, which placed a grid mask over the film and irradiated with UV light as shown in Figure 2.12. The film was then washed with water to remove the non-irradiated areas and resulted in the production of patterned shapes 100 nm thick and 35 μm wide.

2.2.2 Photo-reactive Self-Assembled Nanostructures

The self-assembly of dendrimers is a technique utilized to assemble supramolecular nanostructures.^{74,75} Inclusion of hydrogen bonding functionality is a method to associate dendrimers for nanostructure formation. If hydrogen bonding is the only interaction, the structure is labile in solvents and at temperatures that dissociate hydrogen bonds. Incorporation of photo-curable groups in the dendrimers periphery is a method to stabilize the self-assembled supramolecular nanostructures.

Kim and coworkers⁷⁶ utilized photo-reactive diacetylenes to photo-cure self-assembled nanostructures of urethane and amide containing dendrimers. The dendrimers were synthesized to the second generation utilizing a convergent method, and contained amid and urethane linkages in the core and diacetylene groups in the periphery, as shown in Figure 2.14. Hydrogen bonding was provided through amide and urethane linkages in the dendrimer core. Hydrogen bonding facilitated the self organization of hexagonal columnar structures which formed fibrous bundles according to transmission electron micrographs. The researchers proposed the columns were constructed from dendrimer stacking, with the dendrimer core inward and the dendrimer periphery outward. The columnar structure oriented the diacetylene groups in a proximity that assisted

photopolymerization. Before irradiation the assemblies did not absorb in the visible range and after UV irradiation the samples absorbed 500-650 nm light indicating the presence of polyene. After photopolymerization the hexagonal columnar structure stayed intact, indicating the hydrogen bonding core network was not disrupted. In fact the hydrogen bonding core was stabilized from the formation of a shell in the periphery, which rendered the fibers insoluble in organic solvents such as chloroform, methylene chloride, THF, DMF, and DMSO.

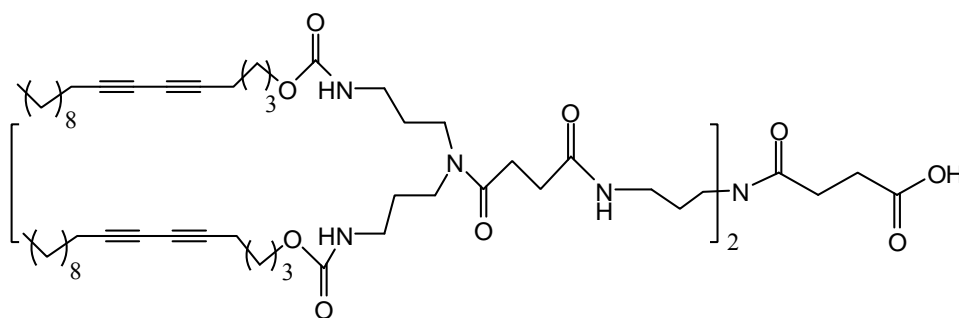


Figure 2.14 Second generation dendron with a hydrogen bonding urethane and amide core with a photo-reactive diacetylene periphery.

2.3 References

1. Butcher, D. J., *Appl. Spectrosc. Rev.* **2005**, *40* (2), 147-164.
2. Winefordner, J. D.; Gornushkin, I. B.; Correll, T.; Gibb, E.; Smith, B. W.; Omenetto, N., *J. Anal. At. Spectrom.* **2004**, *19* (9), 1061-1083.
3. Briand, J. P.; Giardino, G.; Borsoni, G.; Le Roux, V.; Bechu, N.; Dreuil, S.; Tuske, O.; Machicoane, G., *Rev. Sci. Instrum.* **2000**, *71* (2, Pt. 2), 627-630.
4. Pasinszki, T.; Westwood, N. P. C., *J. Electron Spectrosc. Relat. Phenom.* **2000**, *108* (1-3), 63-73.
5. Griesbeck, A. G.; Mattay, J., *Synthetic Organic Photochemistry*. Marcel Dekker: New York, 2005.
6. Horspool, W.; Lenci, F., *CRC Handbook of Photochemistry and Photobiology*. CRC Press: Boca Raton, FL, 2004.
7. Ramamurthy, V.; Schanze, K. S., *Organic Molecular Photochemistry*. Marcel Dekker: New York, 1999.
8. Ramamurthy, V.; Schanze, K. S., *Organic, Physical, and Materials Photochemistry*. Marcel Dekker: New York, 2000.
9. Wishart, J. F.; Nocera, D. G., *Photochemistry and Radiation Chemistry: Complementary Methods for the Study of Electron Transfer*. ACS: Washington D.C., 1998; Vol. 254.
10. Rabek, J. F., *Mechanisms of Photophysical Processes and Photochemical Reactions in Polymers*. John Wiley & Sons: New York, 1987.
11. Fouassier, J. P., *Photoinitiation, Photopolymerization, and Photocuring: Fundamentals and Applications*. Hanser: Munich, 1995.
12. Scranton, A. B.; Bowman, C. N.; Peiffer, R. W.; Editors, *Photopolymerization: Fundamentals and Applications* ACS: Washington D.C., 1997.
13. Belfield, K. D.; Crivello, J. V.; Editors, *Photoinitiated Polymerization*. ACS: Washington D.C., 2003.
14. Corrales, T.; Catalina, F.; Peinado, C.; Allen, N. S., *J. Photochem. Photobiol., A* **2003**, *159* (2), 103-114.
15. Allcock, H. R.; Lampe, F. W.; Mark, J. E., *Contemporary Polymer Chemistry*. 3rd ed.; Pearson Education Inc: New Jersey, 2003.
16. Fisher, J. P.; Dean, D.; Engel, P. S.; Mikos, A. G., *Annu. Rev. Mater. Res.* **2001**, *31*, 171-181.
17. Krongauz, V. V.; Trifunac, A. D., *Processes in Photoreactive Polymers*. Chapman & Hall: New York, 1995.
18. Parsons, B. F.; Szpunar, D. E.; Butler, L. J., *J. Chem. Phys.* **2002**, *117* (17), 7889-7895.
19. Fahr, A.; Braun, W.; Laufer, A. H., *J. Phys. Chem.* **1993**, *97* (8), 1502-1506.
20. Gu, H.; Snavely, D. L., *J. Appl. Polym. Sci.* **2003**, *90* (2), 565-571.
21. Vermeil, C.; Matheson, M.; Leach, S.; Muller, F., *J. Chem. Phys.* **1964**, *61* (4), 596-606.
22. Eskins, K.; Dintzis, F. R.; Friedman, M., *J. Macromol. Sci., Chem.* **1971**, *5* (3), 541-546.
23. De Paoli, M. A.; Tamashito, I.; Galembeck, F., *J. Polym. Sci., Polym. Lett. Ed.* **1979**, *17* (6), 391-394.

24. Robertson, E. M.; Van Deusen, W. P.; Minsk, L. M., *J. Appl. Polym. Sci.* **1959**, 2 (6), 308-311.
25. Minsk, L. M.; Smith, J. G.; Van Deusen, W. P.; Wright, J. F., *J. Appl. Polym. Sci.* **1959**, 2 (6), 302-307.
26. Visconte, L. L. Y.; Andrade, C. T.; Azuma, C., *J. Appl. Polym. Sci.* **1998**, 69 (5), 907-910.
27. Coleman, M. M.; Hu, Y.; Sobkowiak, M.; Painter, P. C., *J. Polym. Sci., Part B Polym. Phys.* **1998**, 36 (9), 1579-1590.
28. Murase, S.; Kinoshita, K.; Horie, K.; Morino, S., *Macromolecules* **1997**, 30 (25), 8088-8090.
29. Andreopoulos, F. M.; Roberts, M. J.; Bentley, M. D.; Harris, J. M.; Beckman, E. J.; Russell, A. J., *Biotechnol. Bioeng.* **1999**, 65 (5), 579-588.
30. Fang, S. W.; Timpe, H. J.; Gandini, A., *Polymer* **2002**, 43 (12), 3505-3510.
31. Gandini, A.; Belgacem, M. N., *Prog. Polym. Sci.* **1997**, 22 (6), 1203-1379.
32. Gheneim, R.; Perez-Berumen, C.; Gandini, A., *Macromolecules* **2002**, 35 (19), 7246-7253.
33. Decker, C.; Bianchi, C., *Polym. Int.* **2003**, 52 (5), 722-732.
34. Zahir, S. A., *J. Appl. Polym. Sci.* **1979**, 23 (5), 1355-1372.
35. Trenor, S. R.; Shultz, A. R.; Love, B. J.; Long, T. E., *Chem. Rev.* **2004**, 104 (6), 3059-3077.
36. Matsuda, T.; Mizutani, M.; Arnold, S. C., *Macromolecules* **2000**, 33 (3), 795-800.
37. Lam, J. W. Y.; Tang, B. Z., *Acc. Chem. Res.* **2005**, 38 (9), 745-754.
38. Cataldo, F., *J. Photochem. Photobiol., A* **1996**, 99 (1), 75-81.
39. Tyminski, P. N.; Ponticello, I. S.; O'Brien, D. F., *J. Am. Chem. Soc.* **1987**, 109 (21), 6541-6542.
40. Kurihara, S.; Ohta, H.; Nonaka, T., *Polymer* **1995**, 36 (4), 849-855.
41. Kurihara, S.; Ohta, H.; Nonaka, T., *J. Appl. Polym. Sci.* **1996**, 61 (2), 279-283.
42. Gao, X.; Friscic, T.; MacGillivray, L. R., *Angew. Chem., Int. Ed.* **2003**, 43 (2), 232-236.
43. Kaanumalle, L. S.; Nithyanandhan, J.; Pattabiraman, M.; Jayaraman, N.; Ramamurthy, V., *J. Am. Chem. Soc.* **2004**, 126 (29), 8999-9006.
44. Papaefstathiou, G. S.; Zhong, Z.; Geng, L.; MacGillivray, L. R., *J. Am. Chem. Soc.* **2004**, 126 (30), 9158-9159.
45. Jansen, J. F. G. A.; Dias, A. A.; Dorsch, M.; Coussens, B., *Macromolecules* **2003**, 36 (11), 3861-3873.
46. Beuermann, S.; Paquet, D. A., Jr.; McMinn, J. H.; Hutchinson, R. A., *Macromolecules* **1997**, 30 (2), 194-197.
47. Cohen, M. D.; Schmidt, G. M. J.; Sonntag, F. I., *J. Chem. Soc.* **1964**, 2000-2013.
48. Bassani, D. M.; Darcos, V.; Mahony, S.; Desvergne, J.-P., *J. Am. Chem. Soc.* **2000**, 122 (36), 8795-8796.
49. Darcos, V.; Griffith, K.; Sallenave, X.; Desvergne, J.-P.; Guyard-Duhayon, C.; Hasenknopf, B.; Bassani, D. M., *Photochem. Photobiol. Sci.* **2003**, 2 (11), 1152-1161.
50. Lewis, F. D.; Quillen, S. L.; Hale, P. D.; Oxman, J. D., *J. Am. Chem. Soc.* **1988**, 110 (4), 1261-1267.

51. Noonan, J. M.; Caccamo, A. F., *ACS Symposium Series (Liq.-Cryst. Polym.)* **1990**, 435, 144-157.
52. Kihara, H.; Miura, T.; Kishi, R.; Yoshida, T.; Shibata, M.; Yosomiya, R., *Liq. Cryst.* **2003**, 30 (7), 799-809.
53. Kihara, H.; Miura, T.; Kishi, R., *Macromol. Rapid Commun.* **2004**, 25 (2), 445-449.
54. Kihara, H.; Miura, T.; Kishi, R.; Kaito, A., *Polymer* **2004**, 45 (18), 6357-6363.
55. Kihara, H.; Miura, T., *Polymer* **2005**, 46 (23), 10378-10382.
56. Udal'tsov, A. V.; Paschenko, V. Z.; Churin, A. A.; Tusov, V. B.; Pshezhetskii, V. S., *J. Photochem. Photobiol., B* **1993**, 21 (1), 87-94.
57. Udal'tsov, A. V., *J. Photochem. Photobiol., B* **1997**, 37 (1-2), 31-39.
58. Ariga, K.; Lvov, Y.; Kunitake, T., *J. Am. Chem. Soc.* **1997**, 119 (9), 2224-2231.
59. Yamauchi, K.; Lizotte, J. R.; Long, T. E., *Macromolecules* **2003**, 36 (4), 1083-1088.
60. Mather, B. D.; Lizotte, J. R.; Long, T. E., *Macromolecules* **2004**, 37 (25), 9331-9337.
61. Chien, L. C.; Cada, L. G., *Macromolecules* **1994**, 27 (14), 3721-3726.
62. Acierno, D.; Amendola, E.; Bugatti, V.; Concilio, S.; Giorgini, L.; Iannelli, P.; Piotta, S. P., *Macromolecules* **2004**, 37 (17), 6418-6423.
63. Alazaroaie, S.; Toader, V.; Carlescu, I.; Kazmierski, K.; Scutaru, D.; Hurduc, N.; Simionescu, C. I., *Eur. Polym. J.* **2003**, 39 (7), 1333-1339.
64. Basu, S.; Vutukuri, D. R.; Shyamroy, S.; Sandanaraj, B. S.; Thayumanavan, S., *J. Am. Chem. Soc.* **2004**, 126 (32), 9890-9891.
65. Arumugam, S.; Vutukuri, D. R.; Thayumanavan, S.; Ramamurthy, V., *J. Am. Chem. Soc.* **2005**, 127 (38), 13200-13206.
66. Mariani, P.; Samori, B.; Sante Angeloni, A.; Ferruti, P., *Liq. Cryst.* **1986**, 1 (4), 327-336.
67. Broer, D. J.; Finkelmann, H.; Kondo, K., *Makromol. Chem.* **1988**, 189 (1), 185-194.
68. Bualek, S.; Zentel, R., *Makromol. Chem.* **1988**, 189 (4), 791-796.
69. Yang, D. K.; Chien, L. C.; Doane, J. W., *Appl. Phys. Lett.* **1992**, 60 (25), 3102-3104.
70. Decher, G., *Science* **1997**, 277 (5330), 1232-1237.
71. Stockton, W. B.; Rubner, M. F., *Macromolecules* **1997**, 30 (9), 2717-2725.
72. Yang, Z.; Cao, T.; Chen, J.; Cao, W., *Eur. Polym. J.* **2002**, 38 (10), 2077-2082.
73. Yang, S. Y.; Rubner, M. F., *J. Am. Chem. Soc.* **2002**, 124 (10), 2100-2101.
74. Zeng, F.; Zimmerman, S. C., *Chem. Rev.* **1997**, 97 (5), 1681-1712.
75. Newkome, G. R.; He, E.; Moorefield, C. N., *Chem. Rev.* **1999**, 99 (7), 1689-1746.
76. Kim, C.; Lee, S. J.; Lee, I. H.; Kim, K. T.; Song, H. H.; Jeon, H.-J., *Chem. Mater.* **2003**, 15 (19), 3638-3642.

Chapter 3: Biomimetic Design and Performance of Polymerizable

Lipids

Reproduced with permission from Accounts of Chemical Research, in press for publication. Unpublished work copyright 2009 American Chemical Society.

3.1 Conspectus

Supported lipid membranes have received significant attention over the past several decades due to their potential application in biological and material sciences. Bilayer lipid membranes (BLMs) consist of two lipid layers arranged with their hydrophilic head region exposed to polar environments and hydrophobic domains in the core. Biological lipid membranes confine and support the cell structure, while selectively controlling the diffusion of ions and proteins between the intra- and extracellular matrix (ECM). Naturally derived lipid monomers spontaneously self-assemble to develop smart gateways that recognize and incorporate desired protein transporters or ion channels. Research interest focuses on using BLMs as models of lamellar lipid assemblies and associated protein receptors in cell membranes. The transport properties of lipid membranes are tuned through careful consideration of the solution medium, transporter functionality, and pH, as well as other environmental conditions. BLMs have received significant interest in the design of biofunctional coatings, controlled release technologies, and biosensors, however, high performance applications require lipid membranes to remain stable at harsh denaturing conditions, and synthetic strategies are often proposed to increase the chemical and mechanical stability of lipid assemblies.

Polymerizing self-assembled lipid structures is a strategy that results in robust biocompatible architectures, and diverse reactive functional groups are available for the synthesis of monomeric lipids. The selection of the polymerizable functionality and its

precise location within the lipid assembly influence the ultimate supramolecular microstructure and polymerization efficiency. The biomimetic potential of polymerized lipids depends on the stability and robustness of the self-assembled membranes, and it is essential the polymerizable functionality not disturb the amphiphilic nature of the lipid to maintain biocompatibility. Innovative applications are the motivational force for the development of durable polylipid compositions. Surface modification with biocompatible polylipids provides the opportunity for specific binding of biological molecules for applications as sensors or controlled release delivery vehicles. Applicability of stable lipid assemblies requires a comprehensive understanding of the mechanism of lipid polymerization in confined supramolecular geometries like the one shown in Figure 3.1. The future is exciting as researchers begin to fully understand the morphology of polylipids in an effort to successfully produce naturally derived sustainable materials. This article highlights recent efforts to covalently stabilize lipid membranes, and emerging applications of mechanically robust self-assembled lipid architectures.

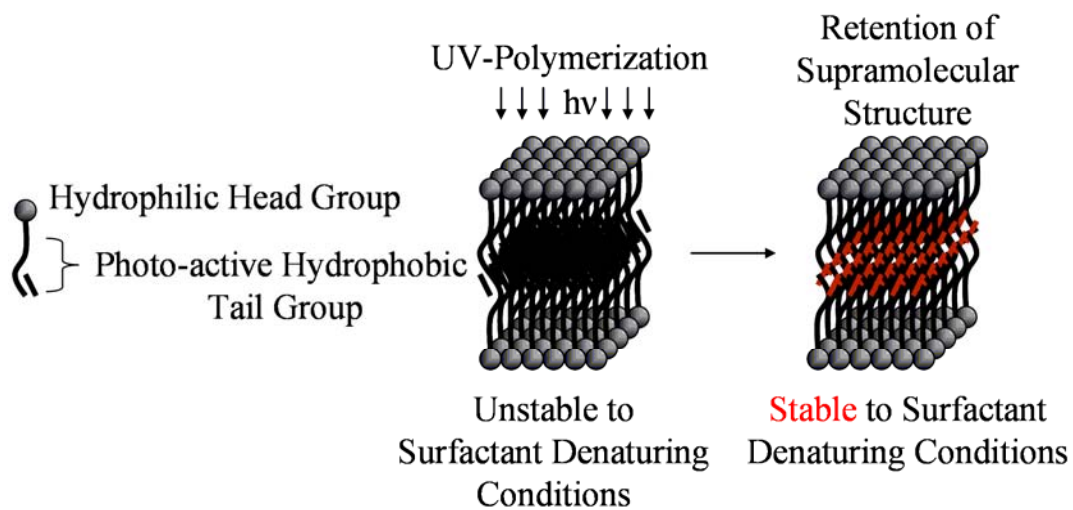


Figure 3.1 Photo-polymerization of a self-assembled lipid bilayer with retention of the bilayer structure.

3.2 Introduction

Self-assembled lipid membranes and coatings offer potential as biosensors, controlled release vehicles, and biofunctional coatings due to their selective permeability and biomimetic properties. Polymerizing lipid assemblies is a strategy used to produce mechanically durable biocompatible architectures, and the choice of the polymerizable functionality influences the self-assembled lipid microstructure and polymerization kinetics. It is important that the polymerizable group not disturb the spontaneous self-assembly of the lipid architecture in order to retain the biomimetic potential of polymerized lipids. The application of polylipids requires a comprehensive understanding of the lipid polymerization mechanism in confined supramolecular geometries, and the influence of polymerization on the lipid membranes interaction with proteins and other biological guests. Innovative controlled release, filtration technologies, and biofunctional coating applications are the motivational force for the enhancement of durable polylipid compositions, and the outlook is exciting as researchers begin to fully comprehend the transitions and morphologies of polylipids in an effort to successfully produce naturally derived sustainable materials. In this article exciting recent efforts to covalently stabilize lipid membranes and emerging applications of mechanically robust self-assembled lipid architectures are highlighted.

3.3 Origin and Self-Assembly of Lipid Membranes

Supported lipid membranes or bilayer lipid membranes (BLMs) have received significant attention over the past several decades due to their potential application in biological and material sciences.¹⁻⁴ Biological lipid membranes confine and support the cell structure, while selectively controlling the diffusion of ions and proteins between the

intra- and extra-cellular matrix (ECM).⁵ Research interest focuses on using BLMs as models of the lamellar assembly of lipids, as shown in Figure 3.2, and associated protein

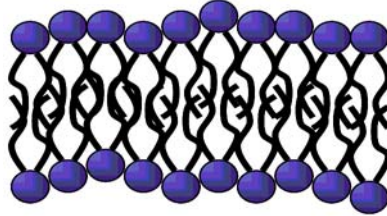


Figure 3.2 Bilayer lipid membrane (BLM)

receptors in cell membranes.⁶⁻⁹ Common procedures for the assembly of BLMs include using either Langmuir-Blodgett-Schaefer (LBS) or vesicle fusion techniques.^{6-8,10} LBS deposition techniques provide precise control over the packing density and composition of the film. Depending upon lipid composition and experimental conditions, LBS techniques allow for control over the lateral organization and membrane asymmetry.¹¹ Vesicle fusion techniques are advantageous due to their more straightforward deposition procedure.¹² However, vesicle fusion techniques only form bilayers from fluid-phase lipids, limiting control of bilayer symmetry and organization.¹³

Amphiphilic lipids are composed of one or more hydrophobic chains covalently linked to a hydrophilic head. Glycerolipids and phospholipids are biologically derived lipids that contain a glycerol group linking the hydrophobic and hydrophilic segments.¹⁴ Unfavorable enthalpic interaction of the hydrophobic tails with the polar medium drives the self-assembly of lipids in aqueous environments, and leads to the spontaneous aggregation of hydrophilic and hydrophobic domains.¹⁵ Self-assembled hydrated lipids are physiochemically, not covalently, bonded and the lipids laterally diffuse in the bilayer with their polar heads oriented at the aqueous interface and hydrophobic tails retained in

the core of the aggregate. The supramolecular phase of hydrated lipids is dependent upon concentration, temperature, pH, and pressure, in addition to the lipid chemical composition, which determines the spontaneous curvature at the lipid-water interface.¹⁶

In biomedical applications as biosensors or in controlled release technologies, assembled membranes have not typically demonstrated sufficient mechanical strength.¹⁷ Researchers have incorporated sugars, cholesterol, and proteins into BLMs in an attempt to increase their mechanical stability.¹⁸⁻²² These additives have not provided sufficient mechanical strength for future applications that require BLMs to survive a range of pressures, temperatures, or harsh chemical conditions. Rangelov and researchers^{23,24} sterically stabilized phosphatidylcholine (PC) liposomes by coating PC vesicles with poly(ethylene glycol) (PEG). PEG was anionically copolymerized with 1-4 repeat units of a lipid monomer, 1,3-didodecyloxy-2-glycidyl-glycerol (DDGG), to produce copolymers with molecular weights between 6000 and 8000 g/mol. The lipid monomer contained di-dodecyl hydrocarbon tails that were covalently attached to an epoxide polymerizable head. In aqueous media, the hydrocarbon chains of the lipid repeat unit self-assembled into the hydrophobic regions of PC liposomes, anchoring PEG to the phospholipid bilayer, as shown in Figure 3.3. Immobilized PEG formed a polymeric coating around the PC liposomes, which inhibited the adsorption of denaturing proteins. Protection from disruptive proteins is critical for polymer-lipid sterically stabilized liposomes to function as drug delivery vehicles.^{25,26}

In order to exploit the biomimetic properties of BLMs, strategies for bilayer stabilization are required that do not coat the lipid membrane, which disrupts desirable associations with the bilayer surface. The polymerization of lipid bilayers represents a

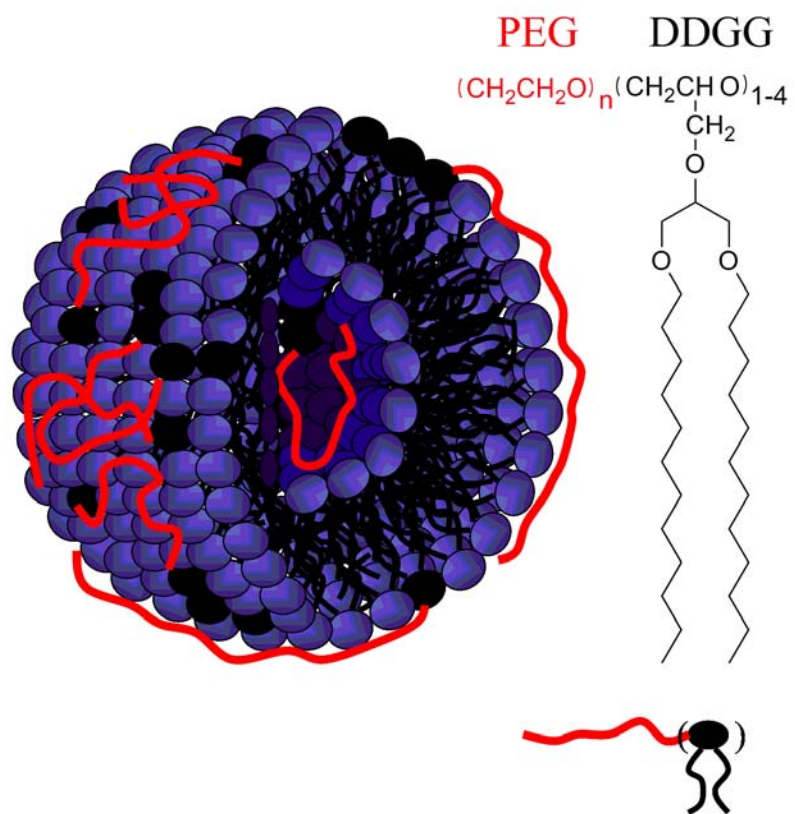


Figure 3.3 Phosphatidylcholine (PC) vesicle sterically stabilized with PEG-DDGG copolymer.

convenient strategy to increase BLM stability, and consequently, the polymerization of lipid membranes has received significant interest since the early 1980s.²⁷⁻²⁹ Diverse synthetic strategies afford the opportunity to incorporate polymerizable functionalities in the head, chain, or tail region of the lipid. Researchers have functionalized lipids with acrylic,^{30,31} styrenic,³² acetylene,³³⁻³⁵ and dienoyl³⁶⁻³⁹ groups. As expected, the location and chemical functionality of the polymerizable group influences the supramolecular structure and polymerization efficiency of monomeric lipids. The polymerizable functionality must not disturb the amphiphilic nature of the lipid to maintain self-assembly, since the biomimetic potential of polymerized lipids depends on the stability and robustness of the self-assembled membranes. Rossi and Chopineau⁴⁰ recently published a review on the biomimetic properties of tethered lipid membranes. Tethered lipid membranes are anchored to a supporting solid surface, and a polymeric coating, receptor/ligand spacer lipid, or functionalized monolayer insulates the lipid from the substrate. Lipid membranes that are tethered to a solid surface provide the opportunity to model and efficiently characterize the interaction of proteins with lipid membranes. Since lipid monomers are not covalently connected to form a polylipid, tethered membranes will not be discussed in this trends article, and readers are referred to Rossi and Chopineau's review of tethered lipid membranes.

3.4 Polymerizable Hydrophobic Regions in Lipid Membranes

Recently, reactive BLMs have received interest for the generation of micropatterned membranes.^{41,42} Morigaki and researchers⁴¹ investigated the stability of photo-polymerized lipid bilayers for the lithographic construction of micropatterned biomimetic membranes. The researchers compared the photo-polymerization properties of two diacetylenic phospholipids on quartz and oxidized substrates. The fluorescence and strong UV-vis absorption properties of polyenynes facilitated characterization using UV-vis absorption and fluorescence spectroscopy. The diacetylenes differed in their composition and degree of functionality, as shown in Figure 3.4. Lipid **1** was a diacetylene containing monoalkyl phosphate, phosphoric acid monohexacosadiynyl ester, and lipid **2** was a bis-diacetylene dialkyl phospholipid, 1,2-bis(10,12-tricosadiynoyl)-*sn*-glycero-3-phosphocholine. The two lipid monomers displayed significantly different photo-reactivities.

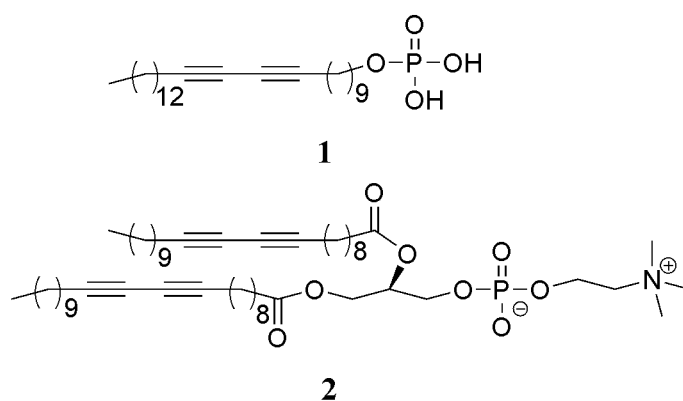


Figure 3.4 Diacetylene monoalkyl phosphate (**1**) and bis-diacetylene phospholipid (DiynePC) (**2**)

The monoalkyl phosphate lipid photo-polymerized at a remarkably faster rate than the dialkyl phospholipid and achieved a higher degree of polymerization. The higher rate and degree of polymerization of **1** was attributed to the efficient packing ability of the monoalkyl amphiphile compared to the dialkyl. Thus, photopolymerization behavior of diacetylenes strongly depends on the molecular packing capabilities. In addition, photopolymerized emission spectra of the amphiphiles displayed substrate dependence. The photo-polymerization of **1** on oxidized silicon and quartz displayed the emission of both red and blue polymers. However, the photo-polymerization on oxidized silicon displayed a stronger blue emission than on quartz. The polymerization efficiency of diacetylene lipids depends on the packing capability and mobility of assembled lipid membranes. Increased interaction between the lipid and substrate can inhibit the lipid chain rearrangement within the bilayer leaflet and encumber the polymerization of diacetylene lipids.⁴³ Lipid chain reconfirmations are necessary to fulfill the topochemical requirements for diacetylene lipid polymerization. The authors suggested that the increased hydrophilicity of the quartz substrate compared to the oxidized silicon produced a less tightly packed arrangement of diacetylene lipids decreasing the polymerization efficiency and resulting in a larger portion of red emitting polyene on quartz. However, another possibility for the decreased polymerization of lipid **1** on quartz could be attributed to the formation of hydrogen bonds between the lipid **1** headgroup and the quartz surface, which limits the freedom of the lipid chains to rearrange and satisfy the diacetylene topochemical polymerization requirements.

The influence of substrate on the photopolymerization behavior of lipid **2** was less pronounced and produced only red emitting polymers on both quartz and oxidized

silicon, however, photopolymerization of lipid **2** on oxidized silicon produced a shorter conjugated polyene chain compared to quartz. The increased degree of polymerization on quartz could have resulted from the decreased packing capabilities of lipid **2** on oxidized silicon, or the less hydrophilic oxidized silicon surface could have promoted intermolecular zwitterionic associations of lipid **2** headgroups. The zwitterionic associations could have limited the mobility of the diacetylene lipid chains to rearrange and fulfill the spatial requirements necessary to achieve diacetylene polymerization.

The difference in polymer backbone configuration distinguished between red and blue emission spectra, and upon UV-polymerization the polydiacetylenes emitted blue light. The polymer shifted to red emissions when the polyene chain length became long enough for the polymer chain to coil-up due to the increased chain mobility provided in the polymer backbone. The emission remained blue if sufficient intermolecular interactions were present to maintain an extended chain. Polymers **1** and **2** were expected to red shift if the amphiphiles were not sufficiently packed on the given substrate.⁴⁴ For quartz and oxidized silicon substrates, **2** displayed a higher amount of red emission than **1**.

Figure 3.5 displays the resulting π -conjugated polydiacetylene of **1** and Figure 3.6 shows the network formation of **2**. Diacetylenes can polymerize in a 1,4-addition mechanism that produces a π -conjugated polymer backbone. The polymerization of diacetylenes requires confined spatial requirements of the monomer units due to the topochemical nature of diacetylene chain addition.⁴⁵ Due to the network formation of the bis-diacetylene, lipid **2** resulted in more mechanically robust bilayers compared to **1**.

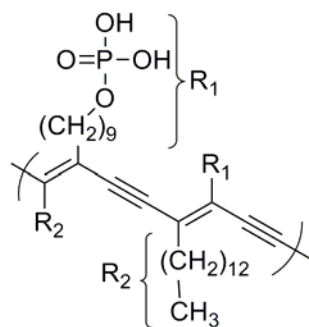


Figure 3.5 Linear π -conjugated polydiacetylene backbone of **1**.

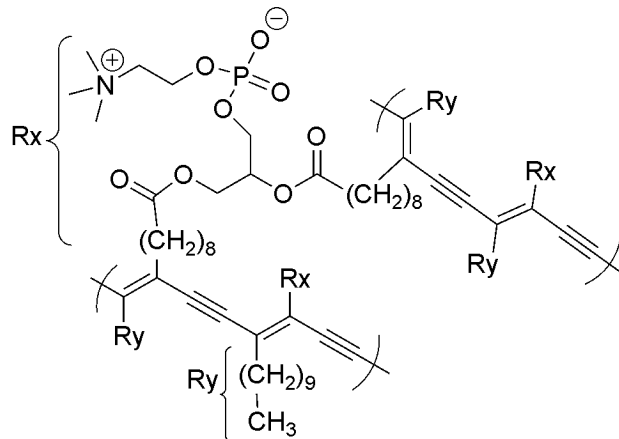


Figure 3.6 Crosslinked π -conjugated polydiacetylene network of **2**.

Polymerized bilayers of **2** did not dissolve in organic solvents and were resistant to surfactant treatment, and in contrast, polymerized bilayers of **1** readily dissolved in water. The increase in stability of **2** was attributed to the higher degree of photo-active functionality that more efficiently produced a crosslinked structure. The mechanical stability of **2** was sufficient to endure the mechanical stress of lithography, however, the packing difficulties prevented the formation of domain boundaries with sharp features.

Morigaki and coworkers⁴⁶ also formed micropatterned lipid membranes containing polymerized and fluid lipid bilayers on glass substrates. Bilayers of **2** were lithographically photo-polymerized on solid substrates, and masks over the substrate produced a patterned surface after the non-irradiated portions were developed, as Figure 3.7 depicts. Phosphocholine (PC) fluid lipid bilayers were incorporated into the developed portions of the substrate from the fusion and reorganization of suspended small unilamellar PC vesicles. The dosage of UV-irradiation controlled the lateral diffusion of the fluid lipid layer, and high UV-dosages produced polymerized bilayers that were impermeable to fluid bilayers. Higher degrees of DiynePC polymerization confined fluid bilayers to defined areas, and lower UV-dosages allowed fluid bilayers to laterally diffuse into polymerized lipid domains.

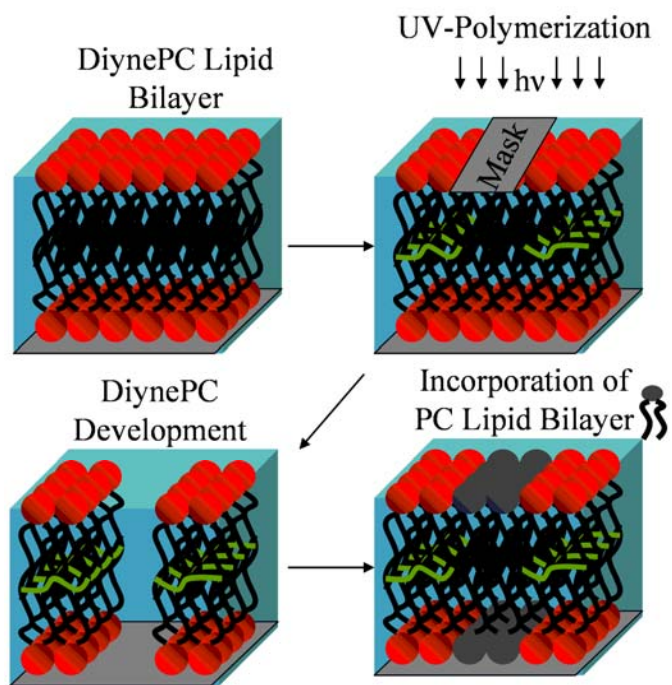


Figure 3.7 Lithographically micropatterned fluid lipid bilayers.

3.5 Polymerizable Hydrophilic Regions in Lipid Membranes

The photo-polymerization of diacetylene groups to stabilize BLMs is a mature field. The topotactic nature of diacetylenelipid photo-polymerization requires efficient chain packing to produce sufficient molecular weights for increased stability.⁴⁷ Lipid diffusion in the fluid phase prevents diacetylenelipids from achieving high degrees of polymerization. Ramakrishnan et al.⁴⁸ synthesized counter-ion polymerizable lipids, as shown in Figure 3.8, containing reactive vinyl groups to increase the applicability of polylipids. Dicyldimethylammonium-4-vinyl benzoate (DDVB) was synthesized from dicyldimethylammonium hydroxide (DDAH) and 4-vinyl benzoic acid, and dicyldimethylammonium-3,5-divinyl benzoate (DDDB) was synthesized from DDAH and 3,5-divinyl benzoic acid. Sonication of solvated lipids resulted in single lamellar

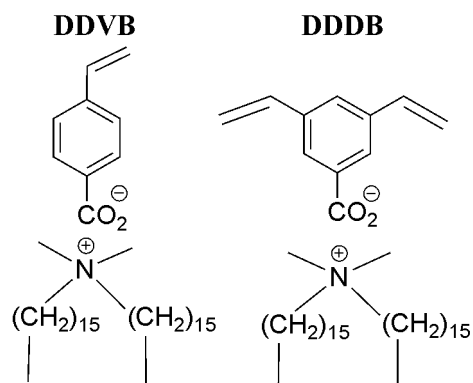


Figure 3.8 Dicyldimethylammonium-4-vinyl benzoate (DDVB) and dicyldimethylammonium-3,5-divinyl benzoate (DDDB)

vesicle dispersions, and exposure to UV-light in the presence of an oil-soluble photoinitiator, 2,2-dimethoxy-2-phenyl acetophenone (DMPA), initiated vesicle polymerization. Vesicular polymerization of DDVB and DDDB resulted in linear and crosslinked polylipids, respectively. The vinyl functionality was not covalently bonded to the lipid, however, the vinyl groups were electrostatically associated to the lipid polar head. Polymerization of the liposomes counter-ion shell provided a durable coating around the lipid bilayer, and the bilayer components retained their monomeric state due to their non-covalent interaction. DMPA was used as the photo-initiator for both DDVB and DDDB vesicle polymerizations, and proved more efficient than water-soluble photoinitiators.

Cetyl trimethylammonium bromide (CTAB) was incrementally added to determine the vesicle stability to lysis, and vesicular light scattering intensity was monitored as a function of CTAB concentration. The scattering intensity of non-polymerized and DDVB poly-vesicles decreased significantly upon the addition of 2 equivalents of CTAB. However, the scattering intensity of DDDB crosslinked vesicles decreased only 10% with the addition of 2 equivalents of CTAB. The small decrease in scattering intensity indicated that the multifunctional lipids produced a more stable vesicle. The researchers examined the stability of vesicles in organic solvents. The light scattering intensity of non-polymerized DDVB and DDDB vesicles continuously decreased due to dissolution of vesicles in ethanol. Linear polymerized DDVB vesicles proved more stable than non-polymerized vesicles. Linear polymerized vesicle scattering intensities sharply increased with increasing ethanol content, until the vesicles precipitated. The scattering intensity of DDDB crosslinked vesicles increased marginally

and precipitation did not occur. The researchers' speculated that the crosslinked rigid network prevented lipid chain reorganization and the semi-rigid crosslinked vesicles did not aggregate and remained suspended in solution.

Katagiri and Caruso⁴⁹ developed robust organoalkoxysilane-based lipid (silane-lipid) coatings on monodisperse colloidal particles. Layer-by-layer (LbL) deposition techniques were used to alternately deposit layers of positively charged poly(diallyldimethylammonium chloride) (PDDA) and negatively charged poly(sodium 4-styrenesulfonate) (PSS) onto a colloidal template. Electrostatic interactions facilitated the silane-lipid deposition onto the polyelectrolyte (PE) multilayer-coated colloidal particles. SEM images of the uncoated melamine formaldehyde (MF) template particles (a), PE multilayer-coated MF particles (b), and silane-lipid coated PE multilayer-coated MF particles (c) are displayed in Figure 3.9. Acidic treatment of the lipid coated particle resulted in the dissolution of the MF core, resulting in hollow lipid coated PE capsules. The alkoxy silane functionalized silane-lipid was pretreated with acid to catalyze the silyl hydrolysis and form the polysiloxane, as shown in Figure 3.10. The silane-lipid produced a stable polysiloxane that was highly resistant to surfactant and ethanol denaturing solutions. The stability of the silane-lipid coating was compared to PE multilayer-coated colloidal particles coated with a non-polymerizable lipid, dimyristoylphosphatidic acid sodium salt (DMPA). Fluorescence measurements indicated that even low surfactant or ethanol concentrations resulted in the decoating of DMPA membranes from the particle surface. The increased silane-lipid stability was attributed to the polysiloxane network.

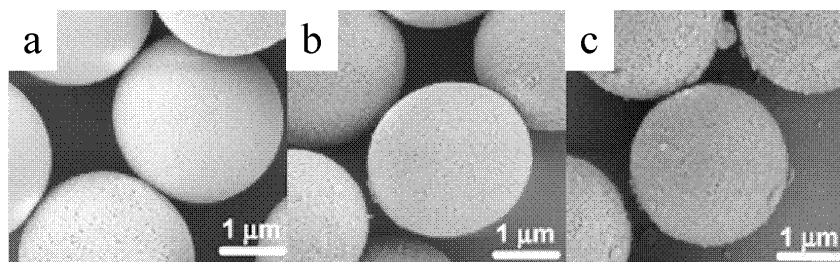


Figure 3.9 (a) MF particle; (b) PE multilayer-coated MF particle; (c) Silane-lipid polysiloxane coated PE-multilayer MF particle. Reprinted with permission from *Macromolecules* 37, 9947-9953 (2004). Copyright 2009 American Chemical Society.

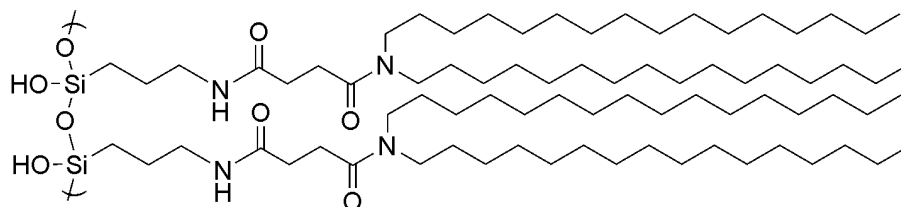


Figure 3.10 Polysiloxane silane-lipid that was deposited onto PE coated monodisperse colloidal particles.

3.6 Polymerization of Nonlamellar Lipid-Cubic Phases

Hydrated lipids also form liquid-crystalline phases depending on their structural composition and concentration.⁵⁰ Marder and coworkers published a review describing cubic liquid-crystalline nanoparticles and discussed their potential application as drug delivery vehicles.⁵¹ Lipid-cubic phases form optically isotropic gels with extremely high surface areas, and are comparable to inorganic zeolites.⁵² Lipid bilayers in cubic liquid-crystalline phases form continuous, three-dimensional cubic-lattice structures in water, as shown in Figure 3.11.⁵³ Lipid-cubic phases are dependent upon their environmental conditions and only form bicontinuous phases within a narrow range of temperatures,

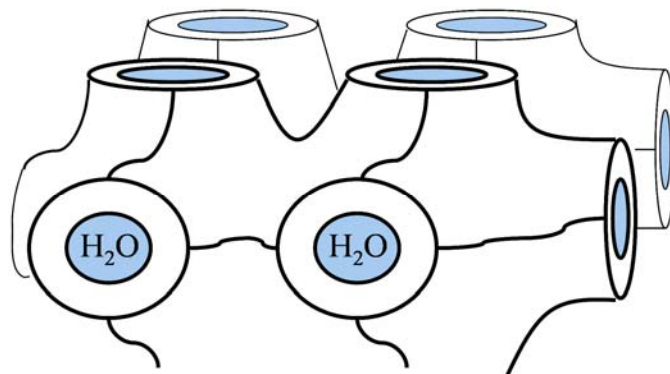


Figure 3.11 Lipid bicontinuous cubic liquid-crystalline phase.

pressures, and lipid concentrations.⁵⁴ The hydrophilic and hydrophobic continuous domains of lipid-cubic phases solubilize lipophilic, hydrophilic, or amphiphilic compounds, making the three-dimensional structures ideal for controlled release drug delivery and separation technologies.^{55,56} Other applications of lipid-cubic phases include templates for the synthesis of nanomaterials^{57,58} and encapsulation of active reagents in cosmetics and packaging technologies.^{59,60}

Due to the limited temperature and concentration ranges for the formation of lipid-cubic phases, a strategy is necessary to increase the stability and application range of liquid-crystalline lipid structures. Stabilization of the cubic phase generates a bicontinuous phase with interpenetrating water channels. Typical aqueous channels in inverted liquid-crystalline lipid phases vary from 3 to 20 nm in diameter depending upon the lipid composition and environmental conditions.^{61,62} Functionalization of the channel surface with chemical host or labels provides a strategy to anchor biological guests or perform separations within the high surface area channeled networks.⁶³⁻⁶⁶

Polymerization of reactive lipids in cubic phases offers a strategy to stabilize lipid liquid-crystalline phases. Thermal, photochemical, or redox initiation mechanisms are efficient strategies for the stabilization of cubic phases.^{61,67} Gin, Noble, and coworkers recently published a review describing the polymerization and crosslinking of nonlamellar phases with retention of their microstructure.⁶⁸ The review discussed the application of polymerized lyotropic liquid-crystalline (LLC) microstructures in the design of novel membrane technologies. Gin and coworkers have tailored the polymerized LLC nano-channeled networks through careful consideration of the lipid composition and environmental conditions to develop robust cubic phases ideal for

nanofiltration membranes,⁶⁹ gas separation membranes,⁷⁰ breathable vapor resistant membranes,⁷¹ and water desalination technologies.⁷² Gin et al. also wrote an earlier review describing the catalytic activity of LLC phases developed from amphiphiles containing photo-active acrylic groups at the terminal of the hydrophobic chains.⁵² Sulfonic acid groups were incorporated in the hydrophilic head portions of the polymerizable amphiphiles that under optimized conditions formed reverse hexagonal phases (H_{II}). Crosslinking the H_{II} microstructures produced robust ordered networks that acid-catalyzed esterification reactions at a higher rate and produced less by-product than commercially available non-ordered sulfonic acid resins.

O'Brien and coworkers synthesized polymerizable monoacylglycerol-*d*₅ (**3**) and crosslinkable 1,2-diacylglycerol (**4**) lipids, as shown in Figure 3.12.⁷³ The monoacylglycerol lipid was deuterated to assist in the NMR characterization of the phase behavior. NMR, along with cross-polarized optical and X-ray diffraction characterization confirmed the formation of an isotropic optically clear lipid cubic phase for a **3**:**4** (9:1

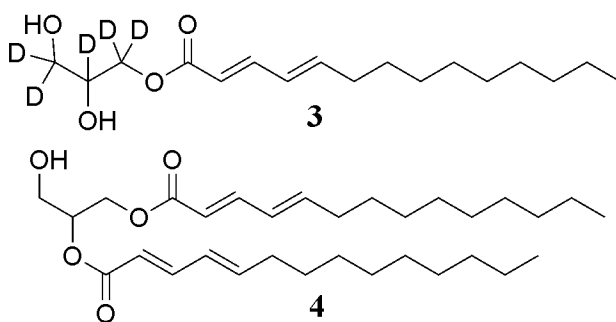


Figure 3.12 Polymerizable monoacylglycerol (**3**) and crosslinkable 1,2-diacylglycerol (**4**)

molar ratio) mixture in water between 5 and 45 °C. Free radical polymerization of the lipid mixture at 45 °C produced a polylipid that was soluble in organic solvents and remained optically clear. The polymerization achieved a high conversion of the dienoate groups as determined with UV-vis spectroscopy and a M_n of 5×10^4 g/mol with a degree of polymerization of approximately 200 was determined using size exclusion chromatography with dichloromethane as the mobile phase. The isotropic nature of the polymerized bicontinuous cubic phase was confirmed with cross-polarized light and X-ray diffraction. The polymerized lipid-cubic phase was thermally stable up to 70 °C, compared to only 45 °C for the cubic phase of the non-polymerized lipid mixture

Marder, O'Brien, and coworkers examined the inverted bicontinuous cubic phase photo-crosslinking of 3-(2,4,13-(*E,E*)-tetradecatrienoyl)-*sn*-glycerol (**5**).⁷⁴ The acylglycerol lipid was mixed with a hydrophobic crosslinking monomer, divinyl benzene (DVB). A 9:1 (**5**:DVB) molar ratio at 25 wt% in water produced an isotropic clear cubic gel that was thermally stable to 45 °C. In the aqueous environment, DVB was internalized into the cubic phase hydrophobic domain containing the polymerizable tetradecatrienoyl tail. The cubic phase was dispersed into cubosomes in the presence of polymeric dispersing agents, and the cubosomes were subsequently photo- and redox-polymerized producing stabilized bicontinuous cubic nanoparticles. Crosslinked cubosomes provide promising bicontinuous cubic phases for applications that require exposure to severe conditions.⁵¹

3.7 Characterizing the Efficiency of Lipid Membrane Polymerization

Morphological characterization of lipid assemblies is typically performed with X-ray diffraction, NMR spectroscopy, differential scanning calorimetry, and transmission and scanning electron microscopy.⁷⁵ Characterization of polymerized lipid layers is often difficult and traditional polymer characterization techniques are not applicable for immobilized lipid membranes. Evaluating the degree of polymerization is desirable to determine the efficiency of initiation and to establish structure-property relationships. Dluhy et al.⁷⁶ utilized near-IR Raman spectroscopy to characterize the photopolymerization of 1-palmitoyl-2-[1,2-(acryloyloxy)dodeca-noyl]-*sn*-glycero-3-phosphocholine (ARPC), which was designed to increase the mechanical integrity of lipid films for biological coatings on polymeric membrane-mimetic films and vascular grafts. ARPC contained a photo-reactive acrylate group at the terminal of one hydrocarbon chain, as shown in Figure 3.13. The researchers formed model lipid films

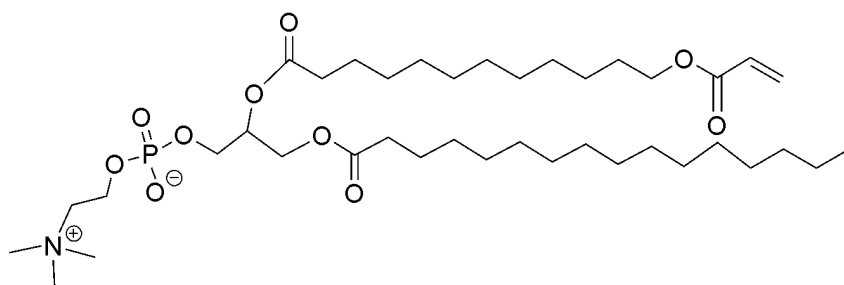


Figure 3.13 1-palmitoyl-2-[1,2-(acryloyloxy)dodeca-noyl]-*sn*-glycero-3-phosphocholine (ARPC)

from the white-light irradiation of hydrated ARPC vesicles using eosin Y (EY) as the photoinitiator, and compared the degree of polymerization as determined from IR and near-IR Raman spectroscopy. IR is the standard method to determine the degree of polymerization, however, IR characterization of lipid films on polyelectrolyte multilayers (PEMs) is difficult due to the relatively weak C=C vibration on multicomponent substrates. Near-IR Raman spectroscopy provides better analysis of homonuclear C=C stretching vibrations in a multicomponent system. The difference in the degree of polymerization between the two methods was less than 0.7%, and indicated near-IR Raman spectroscopy was the preferred characterization method to determine the extent of polymerization on multicomponent substrates. The researchers subsequently used in-situ near-IR Raman microscopy to characterize the formation of lipid membrane films on vascular grafts from the photo-polymerization of ARPC films on PEMs immobilized on the luminal surface of vascular polytetrafluoroethylene (PTFE) grafts, as shown in Figure 3.14. The lipid-coated graft was irradiated with 514.5 nm light for periods up to 300 s, and near-IR Raman microscopy determined the efficiency of polymerization. Photo-polymerization produced a stabilized lipid coated PTFE vascular graft.

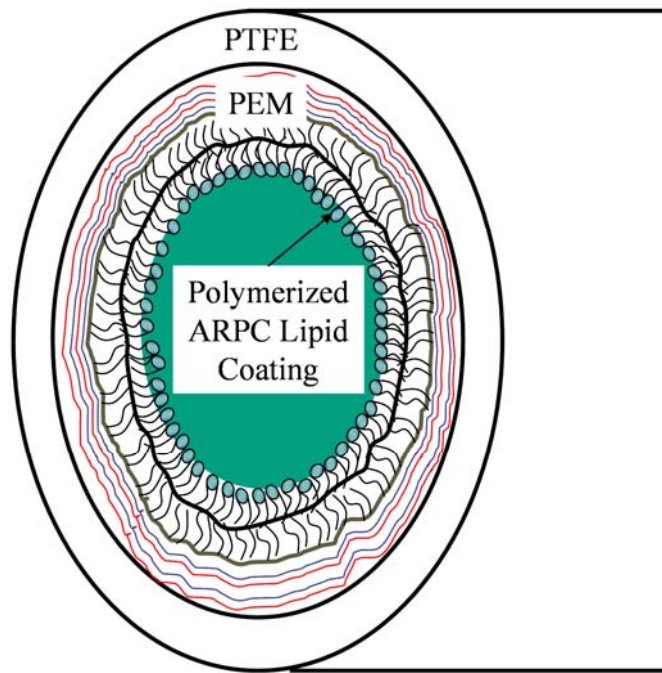


Figure 3.14 Luminal surface of PTFE vascular graft coated with PEM and ARPC poly lipid.

3.8 Biomimetic Properties of Polymerized Lipids

Retention of biomimetic properties remains essential following lipid polymerization. Extensive crosslinking or high molecular weight polylipid membranes can negatively affect the activity of incorporated proteins or transporters, and irradiation can potentially deactivate encapsulated biological molecules. Saavedra and coworkers investigated the activity of bovine rhodopsin (Rho) integrated into a UV-polymerized lipid bilayer.⁷⁷ The lipid bilayer consisted of, 1,2-bis[10-(2',4'-hexadienoyloxy)decanoyl]-*sn*-glycero-3-phosphocholine (bis-SorbPC), as shown in Figure 3.15, which formed a crosslinked network due to the dienoyl functionality of both hydrocarbon chains. Photo-polymerization of bis-SorbPC was initiated with exposure to UVA irradiation and did not require a photo-initiator. The propagating mechanism of bis-SorbPC proceeds from the photo-activated interaction of sorbyl monomer units or the formation of diradicals generated from the photo-excited singlet state.⁷⁸ A combination of 1,2-, 1,4-, and 3,4- additions of the diene are generated during the radical polymerization of bis-SorbPC, as shown in Figure 3.16. The degree of polymerization is lower when photo-initiation occurs at temperatures above the main phase transition, T_m .

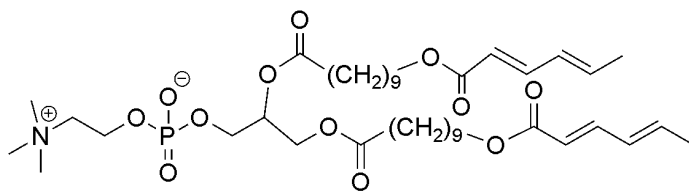


Figure 3.15 1,2-bis[10-(2',4'-hexadienoyloxy)decanoyl]-*sn*-glycero-3-phosphocholine (bis-SorbPC)

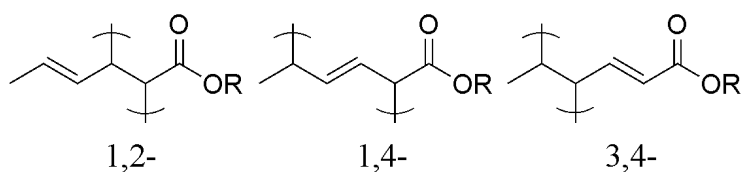


Figure 3.16 The 1,2-, 1,4-, and 3,4- diene addition products of dienoyl polymerization.

Visible light activated the visual photoreceptor, Rho. Plasmon-waveguide resonance (PWR) spectroscopy, which detects the optical properties of thin films, monitored Rho during and post bis-SorbPC polymerization. The lipid bilayer was formed over the resonator surface of the PWR in an aqueous solution, and aliquots of Rho in octylglucoside were introduced to the lipid bilayer formed in the PWR cell. UV-light initiated polymerization through a port in the PWR cell. After photopolymerization, the Rho-lipid bilayer structure was exposed to yellow light and monitored using PWR.

Photo-polymerization of the lipid bilayer produced a crosslinked structure that was stable in the presence of surfactants, and greater than 95% conversion of the lipid monomer was achieved. Characterization of the Rho-lipid bilayer structure during exposure to yellow light indicated that Rho was still photo-active in the polylipid bilayer. The photo-activity of Rho incorporated in the polymerized lipid bilayer was compared to Rho incorporated in a non-polymerized lipid bilayer and comparable photo-activities were obtained. The researchers concluded that the crosslinking of bis-dienoyl phospholipid bilayers did not affect the photo-activity of Rho.

To protect fluorescent tags from unfavorable protein adsorption, Saavedra and researchers⁷⁹ coated the probes with a crosslinked polylipid coating. Rhodamine-

protamine dye molecules were encapsulated in silica nanoparticles (Si NPs) (65-100 nm), and the luminescent Si NPs were coated with crosslinkable bis-SorbPC. Tagged Si NPs are used as fluorescent probes to label cultured cells, however, the silica surface is prone to non-regulated binding in biological media, and the lipid coating was implemented to regulate interactions with the fluorescent Si NPs surface. The lipid coating was photopolymerized achieving 95% monomer conversion, producing a chemically crosslinked polylipid coating that protected the luminescent Si NPs from undesired associations. The nonspecific binding to HeLa cells in the presence of surfactants for Si NPs coated with crosslinked bis-SorbPC was compared to Si NPs coated with a non-polymerizable lipid, 1,2-dioleoyl-*sn*-glycero-3-phosphocholine (DOPC). Before introduction of the surfactant both lipid coatings limited NP interaction with the HeLa cells, however, in the presence of a denaturing surfactant the DOPC bilayers delaminated from the particles surface, resulting in bare Si NPs, which adsorbed to the cells surface. The crosslinked bis-SorbPC coating prevented the adsorption of Si NPs to HeLa cells in the presence of surfactants, proving the stability of the polylipid coating. Retention of the phospholipid bioactivity was demonstrated when biotin was incorporated into the polylipid layer coated on the Si NPs, and biotin functionalized NPs successfully targeted the conjugation to protein receptors.

3.9 Perspective

There are several methods used to increase the stability of lipid assemblies. Polymerization of lipid structures is a strategy used to produce robust biocompatible architectures. There are a wide variety of chemical functionalities available for the synthesis of monomeric lipids. The polymerizable functionality and location within the lipid structure determine the supramolecular microstructure and polymerization efficiency. Lipid monomer conversions of greater than 95% were observed under optimal conditions.^{77,79} Applicability of stable lipid assemblies requires a comprehensive understanding of the lipid polymerization mechanism in confined supramolecular geometries and defects within the self-assembled architectures. Surface modification with biocompatible polylipids provides the opportunity for specific binding of biological molecules for applications as sensors, controlled release delivery vehicles, or in the development of biologically compatible devices. Control of the polymerization kinetics, low monomer conversion, and delamination of the polylipid coating from the substrate are several limitations in the design of polylipid functional materials that future investigations will need to address.

The future is exciting as researchers begin to fully understand the morphology of polylipids in efforts to successfully produce sustainable materials. Innovative applications are the motivational force for the development of novel lipid compositions. Our group has electrospun nonwoven lipid membranes from lecithin solutions to produce high surface area, biocompatible membranes with fibers as small as 2.8 μm .⁸⁰ Above the entanglement concentration (C_e) the lipid wormlike micelles formed entangled couplings similar to polymer coils. Lipid wormlike micelles have contour lengths on the micron

scale.⁸¹ They are flexible, cylindrical rods that display viscoelastic properties in solution. Our current efforts are focused on the *in situ* UV-curing of electrospun fibers of soy-based lipids and synthetic surfactants for the generation of sustainable biocompatible membranes and robust protective amphiphilic coatings. *In situ* UV-curing during electrospinning is a novel process for the development of electrospun lipid membranes with mechanical integrity, and provides environmentally beneficial processing conditions.

3.10 Acknowledgements

This material is based upon work supported in part by the U.S. Army Research Office under grant number W911NF-07-1-0452 Ionic Liquids in Electro-Active Devices (ILEAD) MURI.

3.11 References

1. Huang, W.; Yang, X.; Wang, E., *Anal. Lett.* **2005**, *38*, 3-18.
2. Tanaka, M.; Sackmann, E., *Nature* **2005**, *437*, 656-663.
3. Winter, R.; Dzwolak, W., *Philos. Trans. R. Soc. London, Ser. A* **2005**, *336*, 537-563.
4. Tian, W.-J.; Sasaki, Y.; Fan, S.-D.; Kikuchi, J.-I., *Supramol. Chem.* **2005**, *17* (1-2), 113-119.
5. Hamley, I. W.; Castelletto, V., *Angew. Chem. Int. Ed.* **2007**, *46* (24), 4442-4455.
6. Conboy, J. C.; Liu, S.; O'Brien, D. F.; Saavedra, S. S., *Biomacromolecules* **2003**, *4* (3), 841-849.
7. Ross, E. E.; Rozanski, L. J.; Spratt, T.; Liu, S.; O'Brien, D. F.; Saavedra, S. S., *Langmuir* **2003**, *19* (5), 1752-1765.
8. Ross, E. E.; Spratt, T.; Liu, S.; Rozanski, L. J.; O'Brien, D. F.; Saavedra, S. S., *Langmuir* **2003**, *19* (5), 1766-1774.
9. Tamm, L. K.; McConnell, H. M., *Biophys. J.* **1985**, *47* (1), 105-113.
10. Sackmann, E., *Science* **1996**, *271*, 43-48.
11. Esker, A. R.; Mengel, C.; Wegner, G., *Science* **1998**, *280* (5365), 892-895.
12. Lapinski, M. M.; Castro-Forero, A.; Greiner, A. J.; Ofoli, R. Y.; Blanchard, G. J., *Langmuir* **2007**, *23* (23), 11677-11683.
13. Knoll, W.; Frank, C. W.; Heibel, C.; Naumann, R.; Offenhausser, A.; Ruhe, J.; Schmidt, E. K.; Shen, W. W.; Sinner, A., *Rev. Mol. Biotech.* **2000**, *74* (3), 137-158.
14. Fahy, E., et al., *J. Lipid Res.* **2005**, *46* (5), 839-861.
15. Evans, D. F.; Wennerstrom, H., *The Colloidal Domain: Where Physics, Chemistry, Biology, and Technology Meet*. 2nd ed.; Wiley-VCH: New York, 1999.
16. Katsaras, T.; Gutberlet, T., *Lipid Bilayers: Structure and Interactions*. Springer: New York, 2001.
17. Prashar, J.; Sharp, P.; Scarffe, M.; Cornell, B., *J. Mater. Res.* **2007**, *22* (8), 2189-2194.
18. Bredehorst, R.; Ligler, F. S.; Kusterbeck, A. W.; Chang, E. L.; Gaber, B. P.; Vogel, C. W., *Biochemistry* **1986**, *25* (19), 5693-5698.
19. Crane, J. M.; Tamm, L. K., *Biophys. J.* **2004**, *86* (5), 2965-2979.
20. Mouritsen, O. G.; Zuckermann, M. J., *Lipids* **2004**, *39* (11), 1101-1113.
21. Raffy, S.; Teissie, J., *Biophys. J.* **1999**, *76* (4), 2072-2080.
22. Levy, D.; Briggman, K. A., *Langmuir* **2007**, *23* (13), 7155-7161.

23. Rangelov, S.; Almgren, M.; Tsvetanov, C.; Edwards, K., *Macromolecules* **2002**, *35* (12), 4770-4778.
24. Rangelov, S.; Edwards, K.; Almgren, M.; Karlsson, G., *Langmuir* **2003**, *19* (1), 172-181.
25. Johnsson, M.; Edwards, K., *Biophys. J.* **2003**, *85* (6), 3839-3847.
26. Price, M. E.; Cornelius, R. M.; Brash, J. L., *Biochim. Biophys. Acta* **2001**, *1512* (2), 191-205.
27. Foltynowicz, Z.; Yamaguchi, K.; Czajka, B.; Regen, S. L., *Macromolecules* **1985**, *18* (7), 1394-1401.
28. Hayward, J. A.; Chapman, D., *Biomaterials* **1984**, *5* (3), 135-142.
29. Regen, S. L.; Kirszensztejn, P.; Singh, A., *Macromolecules* **1983**, *16* (2), 335-338.
30. Elbert, R.; Laschewsky, A.; Ringsdorf, H., *J. Am. Chem. Soc.* **1985**, *107* (14), 4134-4141.
31. Regen, S. L.; Czech, B.; Singh, A., *J. Am. Chem. Soc.* **1980**, *102* (21), 6638-6640.
32. Tundo, P.; Kippenberger, D. J.; Klahn, P. L.; Prieto Nelson, E.; Jao, T. C.; Fendler, J. H., *J. Am. Chem. Soc.* **1982**, *104* (2), 456-461.
33. Hub, H. H.; Hupfer, B.; Ringsdorf, H., *Organic Coatings and Plastics Chemistry* **1980**, *42*, 2-7.
34. Lopez, E.; O'Brien, D. F.; Whitesides, T. H., *Biochimica et Biophysica Acta, Biomembranes* **1982**, *693* (2), 437-443.
35. O'Brien, D. F.; Klingbiel, R. T.; Specht, D. P.; Tyminski, P. N., *Ann. N.Y. Acad. Sci.* **1985**, *446*, 282-295.
36. Hupfer, B.; Ringsdorf, H.; Schupp, H., *Macromol. Chem. Phys.* **1981**, *182* (1), 247-253.
37. Liu, S.; O'Brien, D. F., *Macromolecules* **1999**, *32* (17), 5519-5524.
38. Liu, S.; Sisson, T. M.; O'Brien, D. F., *Macromolecules* **2001**, *34* (3), 465-473.
39. Srisiri, W.; Sisson, T. M.; O'Brien, D. F., *J. Am. Chem. Soc.* **1996**, *118* (45), 11327-11328.
40. Rossi, C.; Chopineau, J., *Eur. Biophys. J.* **2007**, *36* (8), 955-965.
41. Morigaki, K.; Baumgart, T.; Jonas, U.; Offenhaeusser, A.; Knoll, W., *Langmuir* **2002**, *18* (10), 4082-4089.
42. Mahajan, N.; Lu, R.; Wu, S.-T.; Fang, J., *Langmuir* **2005**, *21* (7), 3132-3135.
43. Britt, D. W.; Hofmann, U. G.; Moebius, D.; Hell, S. W., *Langmuir* **2001**, *17* (12), 3757-3765.
44. Charych, D. H.; Nagy, J. O.; Spevak, W.; Bednarski, M. D., *Science* **1993**, *261*, 585-588.
45. Sarkar, A.; Okada, S.; Matsuzawa, H.; Matsuda, H.; Nakanishi, H., *J. Mater. Chem.* **2000**, *10*, 819-828.
46. Morigaki, K.; Kiyosue, K.; Taguchi, T., *Langmuir* **2004**, *20* (18), 7729-7735.
47. Jonas, U.; Shah, K.; Norvez, S.; Charych, D. H., *J. Am. Chem. Soc.* **1999**, *121*, 4580-4588.
48. Paul, G. K.; Indi, S. S.; Ramakrishnan, S., *J. Polym. Sci., Part A: Polym. Chem.* **2004**, *42* (20), 5271-5283.
49. Katagiri, K.; Caruso, F., *Macromolecules* **2004**, *37*, 9947-9953.
50. Spicer, P. T., *Curr. Opin. Colloid Interface Sci.* **2005**, *10* (5,6), 274-279.

51. Yang, D.; Armitage, B.; Marder, S. R., *Angew. Chem. Int. Ed.* **2004**, *43*, 4402-4409.
52. Gin, D. L.; Lu, X.; Nemade, P. R.; Pecinovsky, C. S.; Xu, Y.; Zhou, M., *Adv. Funct. Mater.* **2006**, *16* (7), 865-878.
53. Angelov, B.; Angelova, A.; Ollivon, M.; Bourgaux, C.; Campitelli, A., *J. Am. Chem. Soc.* **2003**, *125* (24), 7188-7189.
54. Gruner, S. M., *J. Phys. Chem.* **1989**, *93* (22), 7562-7570.
55. Yaghmur, A.; De Campo, L.; Sagalowicz, L.; Leser, M. E.; Glatter, O., *Langmuir* **2005**, *21* (2), 569-577.
56. Yaghmur, A.; de Campo, L.; Sagalowicz, L.; Leser, M. E.; Glatter, O., *Langmuir* **2006**, *22* (24), 9919-9927.
57. Zhang, F.; Meng, Y.; Gu, D.; Yan, Y.; Yu, C.; Tu, B.; Zhao, D., *J. Am. Chem. Soc.* **2005**, *127* (39), 13508-13509.
58. Liu, T.; Wan, Q.; Xie, Y.; Burger, C.; Liu, L.-Z.; Chu, B., *J. Am. Chem. Soc.* **2001**, *123* (44), 10966-10972.
59. Barauskas, J.; Johnsson, M.; Tiberg, F., *Nano Lett.* **2005**, *5* (8), 1615-1619.
60. Barauskas, J.; Johnsson, M.; Joabsson, F.; Tiberg, F., *Langmuir* **2005**, *21* (6), 2569-2577.
61. O'Brien, D. F.; Armitage, B.; Benedicto, A.; Bennett, D. E.; Lamparski, H. G.; Lee, Y.; Srisiri, W.; Sisson, T. M., *Acc. Chem. Res.* **1998**, *31*, 861-868.
62. Reppy, M. A.; Gray, D. H.; Pindzola, B. A.; Smithers, J. L.; Gin, D. L., *J. Am. Chem. Soc.* **2001**, *123* (3), 363-371.
63. Angelov, B.; Angelova, A.; Garamus, V. M.; Lebas, G.; Lesieur, S.; Ollivon, M.; Funari, S. S.; Willumeit, R.; Couvreur, P., *J. Am. Chem. Soc.* **2007**, *129* (44), 13474-13479.
64. Angelov, B.; Angelova, A.; Papahadjopoulos-Sternberg, B.; Lesieur, S.; Sadoc, J.-F.; Ollivon, M.; Couvreur, P., *J. Am. Chem. Soc.* **2006**, *128* (17), 5813-5817.
65. Hochkoeppler, A.; Landau, E. M.; Venturoli, G.; Zannoni, D.; Feick, R.; Luisi, P. L., *Biotechnol. Bioeng.* **1995**, *46* (2), 93-98.
66. Jeong, S. W.; O'Brien, D. F.; Oraedd, G.; Lindblom, G., *Langmuir* **2002**, *18* (4), 1073-1076.
67. Srisiri, W.; Sisson, T. M.; O'Brien, D. F.; McGrath, K. M.; Han, Y.; Gruner, S. M., *J. Am. Chem. Soc.* **1997**, *119* (21), 4866-4873.
68. Gin, D. L.; Bara, J. E.; Noble, R. D.; Elliott, B. J., *Macromol. Rapid Commun.* **2008**, *29* (5), 367-389.
69. Zhou, M.; Kidd, T. J.; Noble, R. D.; Gin, D. L., *Adv. Mater.* **2005**, *17* (15), 1850-1853.
70. Bara, J. E.; Kaminski, A. K.; Noble, R. D.; Gin, D. L., *J. Membr. Sci.* **2007**, *288* (1+2), 13-19.
71. Lu, X.; Nguyen, V.; Zhou, M.; Zeng, X.; Jin, J.; Elliott, B. J.; Gin, D. L., *Adv. Mater.* **2006**, *18* (24), 3294-3298.
72. Zhou, M.; Nemade, P. R.; Lu, X.; Zeng, X.; Hatakeyama, E. S.; Noble, R. D.; Gin, D. L., *J. Am. Chem. Soc.* **2007**, *129* (31), 9574-9575.
73. Srisiri, W.; Benedicto, A.; O'Brien, D. F.; Trouard, T. P.; Oraedd, G.; Persson, S.; Lindblom, G., *Langmuir* **1998**, *14* (7), 1921-1926.

74. Yang, D.; O'Brien, D. F.; Marder, S. R., *J. Am. Chem. Soc.* **2002**, *124* (45), 13388-13389.
75. Mueller, A.; O'Brien, D. F., *Chem. Rev.* **2002**, *102*, 727-757.
76. Murphy, M. R.; Faucher, K. M.; Sun, X.-L.; Chaikof, E. L.; Dluhy, R. A., *Colloids Surf., B* **2005**, *46* (4), 226-232.
77. Subramaniam, V.; Alves, I. D.; Salgado, G. F. J.; Lau, P.-W.; Wysocki, R. J., Jr.; Salamon, Z.; Tollin, G.; Hruby, V. J.; Brown, M. F.; Saavedra, S. S., *J. Am. Chem. Soc.* **2005**, *127* (15), 5320-5321.
78. Lamparski, H.; O'Brien, D. F., *Macromolecules* **1995**, *28*, 1786-1794.
79. Senarath-Yapa, M. D.; Phimphivong, S.; Coym, J. W.; Wirth, M. J.; Aspinwall, C. A.; Saavedra, S. S., *Langmuir* **2007**, *23* (25), 12624-12633.
80. McKee, M. G.; Layman, J. M.; Cashion, M. P.; Long, T. E., *Science* **2006**, *311*, 353-355.
81. Kalur, G. C.; Frounfelker, B. D.; Cipriano, B. H.; Norman, A. I.; Raghavan, S. R., *Langmuir* **2005**, *21* (24), 10998-11004.

Chapter 4: Gemini Surfactant Electrospun Membranes

Reproduced with permission from *Langmuir*, submitted for publication. Unpublished work copyright 2009 American Chemical Society.

4.1 Abstract

Our research demonstrates for the first time electrospun nonwoven fibrous scaffolds from a low molar mass gemini ammonium surfactant, N,N'-didodecyl-N,N,N',N'-tetramethyl-N,N'-ethanediyl-di-ammonium dibromide (12-2-12). Cryogenic transmission electron microscopy (cryo-TEM) and solution rheological experiments correlated micellar morphological transitions of 12-2-12 with increasing concentration. Ammonium gemini surfactants contain two hydrophobic tails and two hydrophilic ammonium headgroups covalently connected through a spacer. The size of the spacer and composition of the headgroup and hydrophobic tailgroups determine the supramolecular structure and solution behavior of gemini surfactants. The microstructure of 12-2-12 in water transitioned from entangled cylindrical threadlike micelles to branched threadlike micelles and finally a viscoelastic, entangled, highly-branched network of threadlike micelles with increasing concentration. The solution behavior of 12-2-12 in water:methanol (1:1 vol) compared to water produced a drastically different micellar phase. As the 12-2-12 concentration water:methanol increased, the micellar morphology transitioned from partitioned globular micelles into overlapped micelles at an overlap concentration (C^*) of 11 wt%. Electrospinning efforts of 12-2-12 from water did not produce fibers at any concentration, however, electrospinning 12-2-12 in water:methanol at concentrations greater than $2C^*$ produced, hydrophilic continuous fibers with diameters between 0.9 and 7 μm . High surface area scaffolds with hydrophilic surfaces are highly desired and offer potential as charged controlled-release

membranes, tissue engineering scaffolds, and coatings in the discovery of biologically compatible devices.

4.2 Introduction

Electrospinning biologically-derived and low molar mass amphiphiles represents an innovative strategy for biocompatible, high surface area fibers for tissue engineering, drug delivery, and biomedical membrane technologies. Traditionally, electrospun fibers form from viscous, entangled high molecular weight polymers in solution or in the melt, since sufficient viscosities are necessary to withstand the electrostatic forces and whipping instabilities of the charged electrospun jet.¹⁻³ Our laboratories were first to electrospin low molar mass phospholipids based on solutions of asolectin in organic solvents,⁴ and produce high surface area, membranes with fiber diameters as small as 2.8 μm . However, this initial discovery was limited to phospholipids in organic solvents, and the challenge remained to demonstrate the versatility of electrospinning low molar mass amphiphiles in more sustainable aqueous solutions.

Asolectin is a soy-derived natural surfactant mixture composed of charged and neutral lipids, and with increasing concentration in nonpolar solvents, the morphology of asolectin transitions from reverse spherical micelles into elongated worm-like micelles (WLMs). Asolectin WLMs form entanglement couplings above the entanglement concentration, C_e .⁵ In chloroform:*N,N*'-dimethylformamide (7:3 wt:wt), the C_e was measured at 35 wt% for asolectin, and the scaling relationship of specific viscosity (η_{sp}) with concentration transitioned from $\eta_{\text{sp}} \sim C^{2.4}$ at $C < C_e$ to $\eta_{\text{sp}} \sim C^{8.4}$ at $C > C_e$. Above C_e , asolectin WLMs are known to entangle in a manner similar to polymer coils in solution and exhibit contour and persistence lengths of approximately 1 μm and 10 nm,

respectively.⁶ The mass-action law controls the uniaxial growth of WLMs, and as the lipid volume fraction increases, the persistence length becomes sufficiently large for WLMs to behave as flexible dynamic analogs to polymers in solution.^{7,8} Droplets were formed when asolectin was electrospun at $C < C_e$ due to the absence of WLM entanglement couplings, and beaded fibers were collected when electrospun at $C = C_e$. Electrospinning continuous fibers from asolectin solutions required a sufficient solution viscosity in order to suppress the Rayleigh instabilities and prevent breakup of the electrified jet.^{2,9} The three-dimensional entangled asolectin networks at $C > C_e$ provided the viscosity and physical associations necessary to form continuous electrospun fibers from the low molar mass lipids. Electrospinning asolectin scaffolds proved that entangled high molecular weight polymers were not essential to the formation of electrospun fibers; however, some degree of supramolecular association was needed to form continuous fibers from low molar mass precursors.

In this study, we report the aqueous solution behavior and electrospinning of an ammonium gemini surfactant, N,N'-didodecyl-N,N,N',N'-tetramethyl-N,N'-ethanediyl-di-ammonium dibromide (12-2-12), as shown in Figure 4.1. Gemini surfactants, which

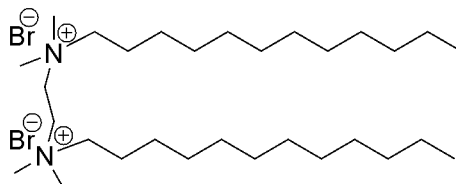


Figure 4.1 N,N'-didodecyl-N,N,N',N'-tetramethyl-N,N'-ethanediyl-di-ammonium dibromide (12-2-12) ammonium gemini surfactant

are also known as dimeric surfactants, are an exceptional class of amphiphiles due to their low critical micelle concentration (CMC) and intriguing supramolecular assemblies in solution.¹⁰⁻¹⁴ Gemini surfactants contain two hydrophobic tails and two hydrophilic headgroups covalently connected with a spacer. Synthetic gemini surfactants include cationic, anionic, zwitterionic, and nonionic functionalities, depending on the incorporated spacer group.¹¹ Moreover, Espert and coworkers¹⁵ verified that the C_{20} concentration, which defines the surfactant concentration necessary to lower the surface tension of water by 0.02 N/m, was two orders of magnitude lower for gemini surfactants compared to conventional monomeric amphiphiles. Thus, they confirmed that dimeric surfactants are more efficient at decreasing the surface tension of water relative to monomeric surfactants. Consequently, gemini surfactants have received significant industrial attention as emulsifiers and dispersants in detergents, cosmetics, personal hygiene products, coatings, and paint formulations.¹⁶⁻¹⁸ Gemini surfactants have also received intense interest as templates for the synthesis of metal nanoparticles,¹⁹⁻²¹ and as novel gene transfection agents due to their superior surface-active properties.^{22,23}

The propensity for supramolecular assembly and WLM growth of gemini surfactants strongly depends on surfactant composition, solution temperature, concentration, and solvent.^{24,25} Zana, Talmon, and Danino explored the influence of spacer group on the self-assembly of quaternary ammonium gemini surfactants, and the resulting aqueous microstructures were examined using cryogenic transmission electron microscopy (cryo-TEM).^{26,27} Ammonium gemini surfactants with shorter spacer lengths, e.g., 2 or 3 methylenes, formed entangled threadlike micelles at exceptionally low concentrations, while gemini surfactants with a spacer length of 4 methylenes formed

spheroidal micelles. Figure 4.2 depicts a cartoon of entangled gemini surfactant threadlike micelles in polar solvents with the headgroups oriented at the interface with a polar environment. The earlier literature has revealed that short spacer lengths covalently restrain the charged ammonium groups at a closer proximity than electrostatic repulsive forces allow for monomeric surfactants. Therefore, ammonium gemini surfactants with short spacers efficiently pack in cylindrical geometries due to a higher packing parameter and lower spontaneous curvature.²⁷ The sphere-to-rod transition occurs if the chemical potential is lower in the cylindrical domain, μ^0_c , than in the spherical region, μ^0_s , and the magnitude of the chemical potential determines the free energy advantage for surfactant molecules to localize in the cylindrical body.²⁸ End-caps of rod-shaped micelles have a hemispherical geometry with a larger diameter than the cylindrical body of the threadlike micelle, and contain a larger number of surfactant molecules than the cylindrical

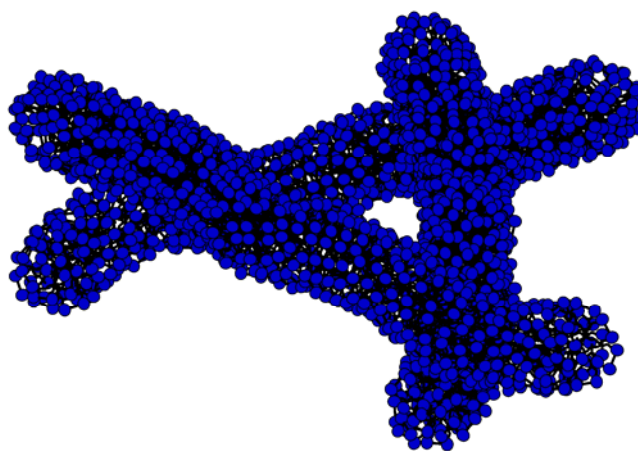


Figure 4.2 Gemini surfactant entangled threadlike micelles in a polar solvent.

portions.^{29,30} End-capping gemini surfactant threadlike micelles is energetically unfavorable because the twin-hydrocarbon tails of gemini surfactants efficiently pack in the cylindrical core of threadlike micelle, leading to the formation of elongated rod-like expansion.³¹

Our cationic ammonium gemini surfactant (12-2-12) was synthesized from the quaternization of 1,2-bis(dimethylamino)ethane with a two-molar equivalent of 1-bromododecane. The supramolecular microstructure of 12-2-12 in water and water:methanol (1:1 vol) was probed with solution rheology and cryo-TEM, and the electrospinning capabilities were investigated for the first time. While others have examined the solution behavior and microstructure of ammonium gemini surfactants in water,^{12,25,31-33} our investigation correlates solution rheology with cryo-TEM for 12-2-12 in water and water:methanol in order to understand the electrospinning performance of low molar mass surfactants for functional hydrophilic membranes.

4.3 Materials and Methods

4.3.1 Materials.

1-Bromododecane (97%), 1,2-bis(dimethylamino)ethane (99%), ethanol (ACS grade anhydrous), ethyl acetate (HPLC grade), ethyl ether (anhydrous), methanol (HPLC grade), and cetyltrimethylammonium bromide (CTAB) (>98%) were purchased from Sigma-Aldrich Chemical Co. 1,2-bis(dimethylamino)ethane and 1-bromododecane were passed through a silica gel column prior to use, and ethanol was distilled from CaH₂ under reduced pressure. Aqueous solutions were made with DI water. All reactions were performed in flame-treated glassware equipped with a magnetic stir bar under argon pressure (6-8 psi), unless otherwise noted.

4.3.2 Instrumentation

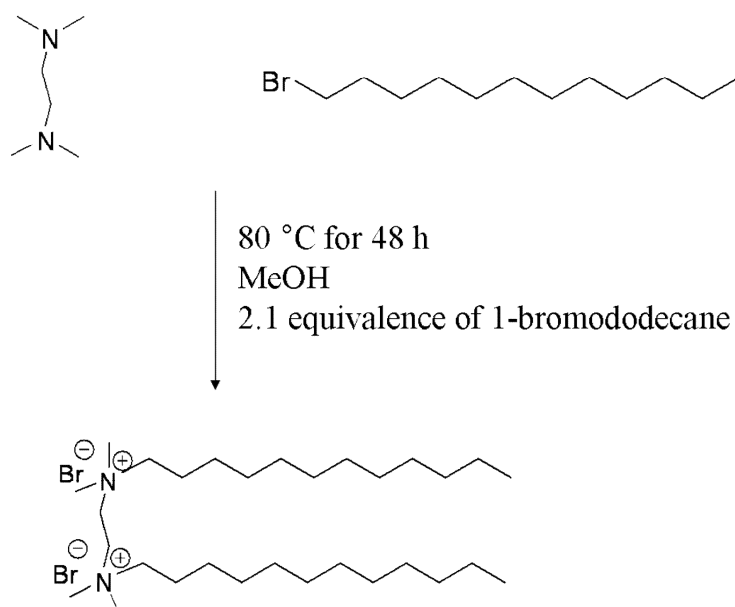
^1H and ^{13}C NMR spectroscopy were performed on a Varian Unity 400 spectrometer at 400 MHz in CDCl_3 . FAB Mass spectrometry was performed on a JEOL HX110 dual focusing mass spectrometer. Strain controlled solution rheology was performed on a TA Instruments AR-G2 rheometer using a concentric cylinder geometry at 25 °C. Steady shear ramp experiments were performed at shear rates between 0.1 and 1000 s^{-1} . The specific viscosity (η_{sp}) was calculated as follows: $\eta_{\text{sp}} = (\eta_o - \eta_s) / \eta_s$, where η_s is the solvent viscosity and η_o the apparent viscosity determined from the Newtonian zero shear region. Samples were thermally equilibrated for 5 min before shearing.

Electrospun fibers were analyzed using a Leo[®] 1550 field emission scanning electron microscope (FESEM). Electrospun fibers were collected on a 1/4" x 1/4" stainless steel mesh, and adhered to a SEM disc. The mounted fibers were sputter-coated with an 8 nm Pt/Au layer to reduce electron charging.

Surface tension measurements were performed using a Kruss (Hamburg, Germany) DSA100 unit. Each pendant drop was created manually and the surface tension measured and recorded, and the drop image was also recorded digitally. The measured surface tension of DI water was 70 mN/m and the surface tension of water:methanol (1:1 vol) was 38 mN/m.

4.3.3 Synthesis of N,N'-didodecyl-N,N,N',N'-tetramethyl-N,N'-ethanediyl-diammonium dibromide (12-2-12)

Zana and coworkers pioneered the synthesis of 12-2-12, as shown in scheme 4.1.²⁵ 1,2-bis(dimethylamino)ethane (0.052 mol, 6.09 g) and 1-bromododecane (0.109 mol, 27.1 g) were dissolved in methanol (0.551 mol, 32.2 mL) in a 250 mL round-



Scheme 4.1 Synthesis of 12-2-12

bottomed flask. A condenser was connected to the reaction flask and the flask was placed in an 80 °C bath for 48 h. The reaction mixture was precipitated into ethyl acetate and a white solid was collected. The white solid was collected and redissolved in chloroform followed by reprecipitation into ethyl ether. The white solid product was isolated and dried at 40 °C under reduced pressure. The yield was 80% and degraded before melting. The product was characterized with ¹H NMR, ¹³C NMR, and mass spectrometry. ¹H NMR is shown in Figure 4.3, (CDCl₃): δ (ppm) 4.72 (4H, N⁺-CH₂-CH₂-N⁺), 3.67 (4H, 2(N⁺-CH₂-CH₂)), 3.50 (12H, 2((CH₃)₂-N⁺)), 1.79 (4H, 2(N⁺-CH₂-CH₂-CH₂)), 1.15-1.40 (36H, 2(N⁺-CH₂-CH₂-(CH₂)₉-CH₃)), 0.830 (6H, 2((CH₂)₉-CH₃))

4.3.4 Cryogenic-TEM

The 12-2-12 solutions were examined on a Tecnai 20 microscope, operated at 200 kV using a Gatan cryo-holder. A small droplet of the suspension (5-10 μL) was placed on a carbon film supported on a TEM copper grid. Following the plunge-freezing technique for sample preparation, the suspension on the TEM grid was blotted and immersed into a liquid ethane reservoir cooled with liquid nitrogen.³⁴ Typical samples were approximately 200 to 400 nm thick in order to avoid multiple scattering peaks of thick samples that diminish image resolution. This thickness range provides a mean free path for elastic scattering of the electron at the corresponding energy.³⁵ The vitrified solutions were transferred to a Gatan 626 cryo-holder and cryo-transfer stage cooled with liquid nitrogen. During observation of the vitrified samples, the cryo-holder temperature was maintained below -175 °C to prevent sublimation of vitreous water. The images were recorded digitally using a Gatan low-dose charge-coupled device (CCD) camera with software package.

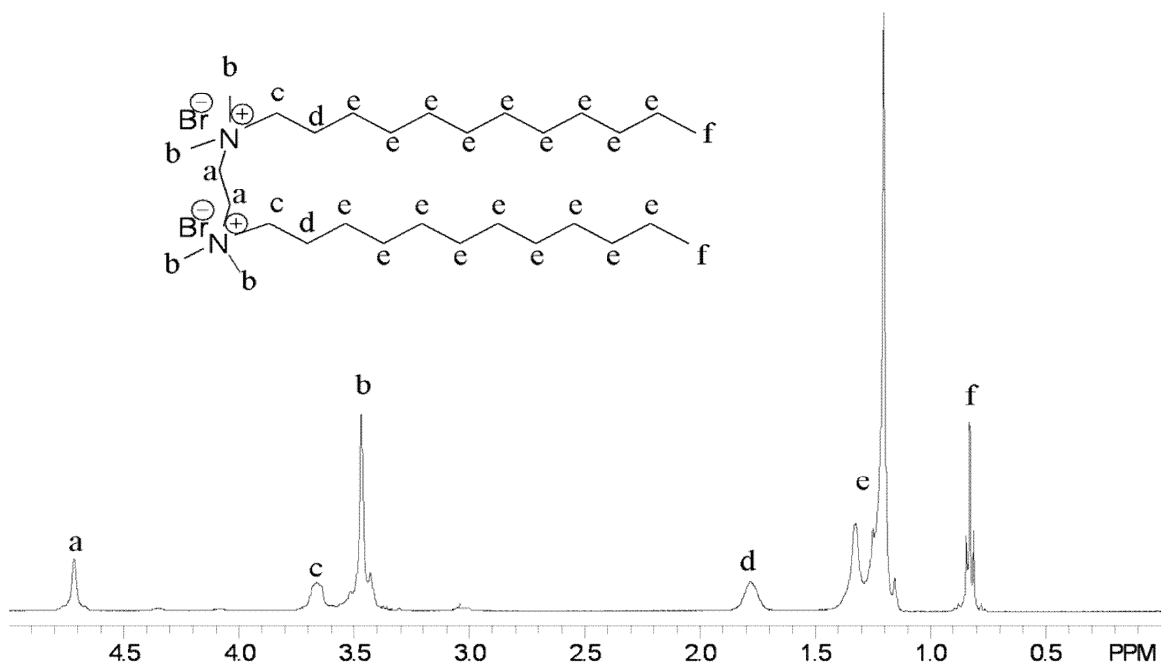


Figure 4.3 ¹H NMR of 12-2-12.

4.3.5 Electrospinning Process

Electrospinning of 12-2-12 from water did not produce fibers at any surfactant concentration. Electrospun fibers of 12-2-12 were collected from water:methanol (1:1vol) solutions following our laboratories electrospinning procedure.^{1,4,36-41} 12-2-12 was dissolved in water:methanol at various concentrations. The solutions were poured into a 20 mL syringe with an 18-gauge needle, and the syringe was mounted in a KD Scientific Inc. syringe pump. The positive lead of a Spellman High Voltage Electronics Corp. CZE1000R high voltage power supply was connected to the syringe needle, and the stainless steel collection target was grounded and placed 12 cm from the needle tip. The fluid was pumped at a constant flow of 5 mL/h, and 25 kV of voltage was applied.

4.4 Results and Discussion

4.4.1 12-2-12 Solution Microstructure in Water

The CMC, surface tension, and interfacial properties of quaternary ammonium gemini surfactants were previously reported.²⁵ In polar solvents, the hydrophilic regions of gemini surfactants are oriented towards the polar environment, with the head groups located at the interface of the hydrophobic tails and polar solvent. Surfactant spherical micelles transition one-dimensionally into threadlike micelles with increasing concentrations under the correct conditions, and the formation of entanglement couplings are observed as shown in Figure 4.2.^{27,30,42} Based upon a theoretical model of micellar growth, Kern and coworkers³³ reported the possibility for three surfactant concentration regimes; (1) a dilute regime of slow increase in the micellar size with increasing concentration, (2) a semidilute regime of rapid micellar growth, and (3) a concentrated regime where the aggregation number depends on the net charge of the end-caps. The transition from the dilute regime to the semidilute regime occurs at the overlap concentration, C^* .⁷ The rate of micellar growth at C^* increases due to the higher concentration of bound ions screening the electrostatic interactions between the headgroups, and the value of C^* decreases as the end-cap energy, E_c , increases, $C^* \sim 1/E_c^2$.^{42,43} Kern and coworkers observed a C^* of 1.55 wt% for 12-2-12 in water at 25 °C, however, the concentrated regime was not easily distinguishable in their plot of zero shear viscosity vs. volume fraction. Bernheim-Groswasser and coworkers³⁰ used cryo-TEM to explore the sphere-to-cylinder transition of 12-2-12 in water at concentrations up to 1.5 wt%. The researchers observed elongated threadlike micelles with a low

concentration of branch points, rings, and end-caps at 1.0 wt%, and a branched threadlike micellar network at 1.5 wt%.

Strain controlled solution rheology determined the zero shear region for 12-2-12 in water at a range of concentrations. Figure 4.4 shows the relationship between η_{sp} and concentration for 12-2-12 in water, where the η_{sp} was calculated from the apparent viscosity in the Newtonian zero shear region.³⁶ The solution rheological scaling behavior was correlated to cryo-TEM micrographs as shown in Figure 4.5 and the microstructural changes were consistent with the observed solution rheological scaling behavior. Although, rheology is a dynamic experiment and cryo-TEM is a static experiment, the visualization of surfactant solutions using cryo-TEM provides an acceptable means to correlate micellar microstructure to rheology. González and Kaler⁴⁴ published a review describing the complimentary techniques of correlating cryo-TEM and solution rheology.

The first transition at 1.5 wt% in Figure 4.4 represents C^* , and this value agreed with the transition that others reported for 12-2-12 in water at 25 °C.^{33,45} The scaling relationship above C^* increased from $\eta_{sp} \sim C^{1.7}$ at $C < C^*$ to $\eta_{sp} \sim C^{4.8}$ at $C > C^*$, indicating a much higher rate of micellar growth. Figure 4.5a depicts the cryo-TEM image of 12-2-12 in water at 1.0 wt%, and indicates the presence of entangled, linear, threadlike micelles with long contour lengths and a low concentration of end-caps. The classical definition of C^* for polymers, which is the concentration when polymeric coils begin to overlap, is ambiguous for the discussion of non-covalent supramolecular assembly of 12-2-12. Clearly, entanglements are present between the threadlike micelles below 1.5 wt%, as shown in Figure 4.5a, and the size of the elongated micelles are concentration dependent. The abrupt change in scaling behavior at C^* is indicative of the

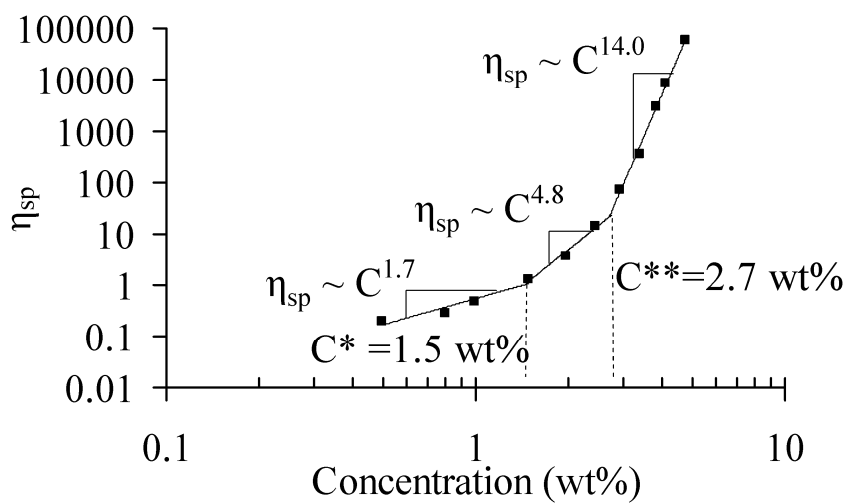


Figure 4.4 η_{sp} vs. concentration for 12-2-12 in water. The surfactant microstructure transitioned from linear threadlike micelles to branched threadlike micelles at 1.5 wt%, and into a highly-branched entangled network at 2.7 wt%.

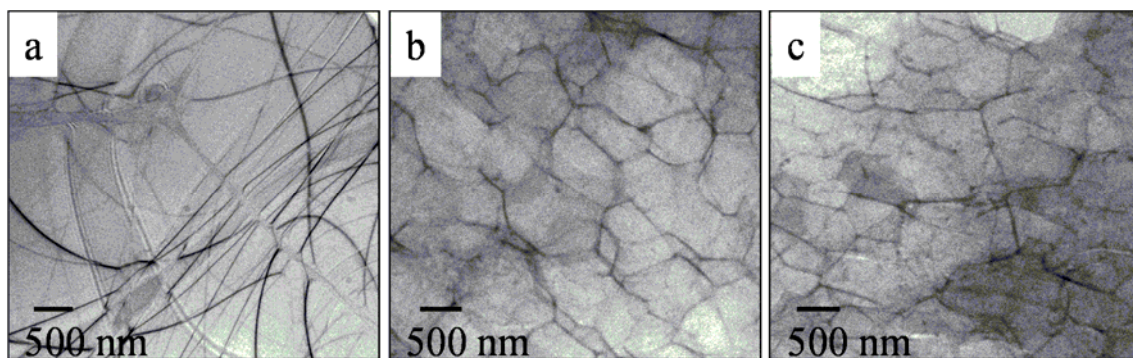


Figure 4.5 Cryo-TEM micrographs of 12-2-12 in water, a) 1.0 wt%, linear entangled threadlike micelles, b) 2.4 wt%, branched threadlike micelles, c) 4.1 wt%, highly-branched entangled threadlike micelles.

transition from the dilute to the semidilute concentration regime, and represents the transition to the regime of increased micellar growth.

Figure 4.5b displays the cryo-TEM micrograph of 12-2-12 in water at 2.4 wt%, $C > C^*$, and the presence of “Y” shaped branch points are distinguished between the threadlike micelles. If the junctions in Figure 4.5b were entanglements, then the contrast darkens from the increased electron density of the overlapping threadlike micelles, however, the contrast does not darken and the junctions are considered branch points.⁴⁴ The second transition in Figure 4.4 at 2.7 wt% represents the transition into the concentrated regime, C^{**} , and the scaling relationship increased from $\eta_{sp} \sim C^{4.8}$ at $C^* < C < C^{**}$ to $\eta_{sp} \sim C^{14.0}$ at $C > C^{**}$. The cryo-TEM in Figure 4.5c displays the formation of a highly-branched network of entangled threadlike micelles at 4.1 wt% of 12-2-12 in water. The microstructure in Figure 4.5c is more difficult to distinguish due to the higher concentration and entangled threadlike micelles. The concentration of cross-links at C^{**} increased, and the microstructure transitioned from a branched structure to an entangled highly-branched network with a higher concentration of threadlike micelles.

The scaling relationship increased in the semidilute and concentrated regimes due to the presence of branch points that formed between the threadlike micelles. Danino and coworkers⁴⁶ observed the network formation of branched threadlike micelles of trimeric ammonium surfactants at a volume fraction of 2.0% in water using cryo-TEM. Drye and Cates⁴⁷ theoretically explored the network formation of “living” cross-linked surfactant solutions. As expected, the degree of branching was dependent upon the free energy relationship between forming a crosslink and forming an end-cap. The crosslinking energy was considerably higher for conventional surfactants than the energy required to

form a hemispherical end-cap. However, the researchers theorized that lowering the micelle curvature provided a strategy to increase the E_c and decrease the crosslink energy. Hemispherical micellar end-caps limit the unfavorable exposure of the hydrophobic micelle core with the surrounding polar media. End-caps are regions of high energy because they require a different spontaneous curvature than the cylindrical domains of the threadlike micelle, and require surfactant headgroups to pack in unfavorable geometries.⁴⁸ Karaborni and coworkers⁴⁹ simulated the aggregation behavior of gemini surfactants, and discovered that branch points formed between threadlike micelles with short spacer groups. The simulations showed that the twin hydrocarbon tails of gemini surfactants preferred a parallel conformation relative to one another in the cylindrical and branched portions of the threadlike micelles. However, gemini surfactants located in the junction points orient their chains perpendicular relative to one another, which forms a 90° angle between the hydrocarbon chains and bridges the cylindrical and branch segments of the threadlike micelles. The flexibility and covalent linkage between the hydrocarbon chains provided an anchor between the branched and cylindrical segments, and served to decrease the free energy of the junction points.

The 12-2-12 gemini surfactant did not require an additional electrolyte to decrease the mean curvature of the growing threadlike micelles. The covalent linkage between the ammonium groups maintained the headgroups at a closer proximity than electrostatic repulsive forces allow for ammonium conventional surfactants. The gemini microstructure grew uniaxially into elongated threadlike micelles that formed entanglement couplings as the 12-2-12 concentration increased. The short covalent linkage between the ammonium sites decreased the area of the gemini headgroup, thereby

lowering the micellar spontaneous curvature and allowing the surfactants to efficiently pack into a cylindrical geometry. As the number of linear threadlike micelles increased, the concentration of cylindrical end-caps increased and branch points formed between the threadlike micelles to minimize the E_c .⁵⁰

Others have observed a decrease in viscosity above a critical surfactant concentration that many have correlated to branching between elongated cylindrical micelles.^{50,51} Candau, Appell, and coworkers^{52,53} observed a decrease in the viscosity and viscosity scaling relationship with concentration as the growth of cetylpyridinium chlorate WLMs increased due to the presence of branching. The dynamic WLM crosslinks provided several new methods of stress relaxation that increased the degrees of freedom and diffusion of the WLMs leading to an increased flow and fluidity of the solution that did not fit the reptation model for the relaxation of entangled cylindrical micelles. Mechanisms for faster relaxation times included the movement of branch points along the cylindrical segments of the WLMs or through the scission and recombination of WLM ghost-like crosslinks, as shown in Figure 4.6 and Figure 4.7, respectively. In the case of 12-2-12 in water at 25 °C, the viscosity continued to increase as the degree of branching increased. The stress relaxation mechanism of the physically cross-linked 12-2-12 network was expected to resemble a network of conventional surfactants with the ability of the branch point to slide along the cylindrical segment, as shown in Figure 4.6. The concentrated regime was not a saturated network⁵³ of threadlike micelles, however, the cryo-TEM image in Figure 4.5c at 4.1 wt% resembled an entangled branched network with a low concentration of end-caps present, and future experimental and modeling experiments are required to understand this phenomenon.

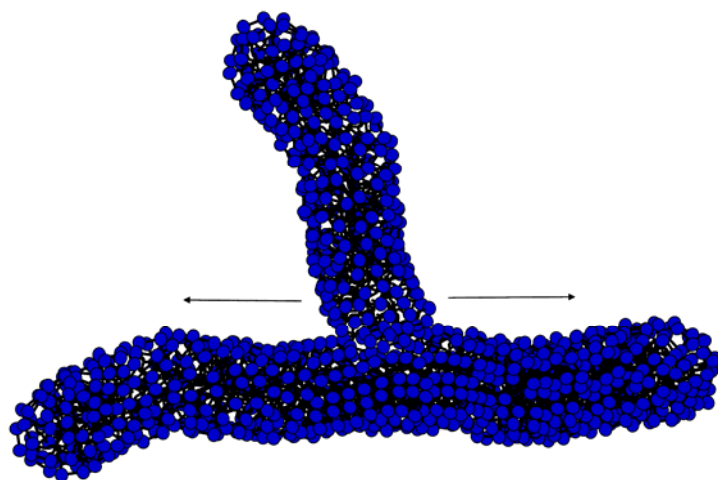


Figure 4.6 Sliding of “Y” shaped branch point along the threadlike micelle.

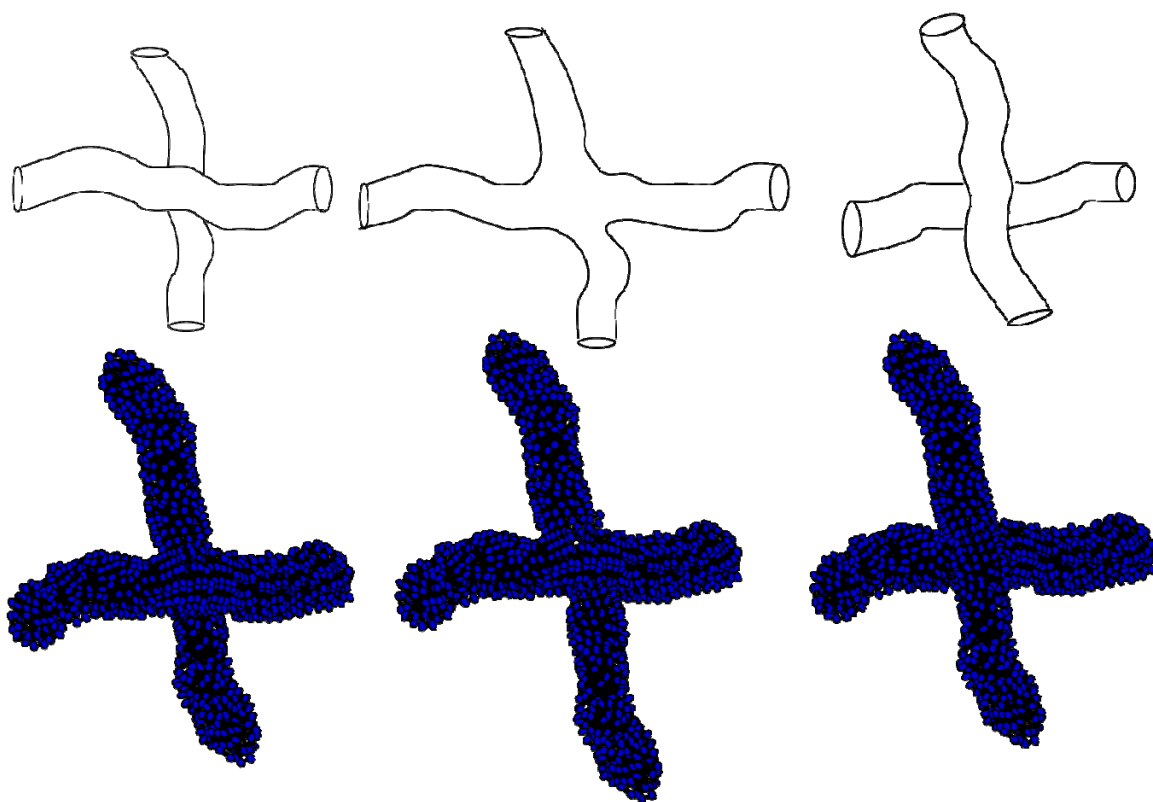


Figure 4.7 Surfactant ghost-like crosslinks.

Others have demonstrated that surfactant solutions exhibit larger scaling relationships than observed for polyelectrolytes⁵⁴ in good solvents in the semi-dilute unentangled regime and semi-dilute entangled regime, $\eta_{sp} \sim C^{0.5}$ and $\eta_{sp} \sim C^{1.5}$, respectively. Magid reported exponents larger than 5.3 for surfactant micellar solutions in the semidilute entangled regime.⁵⁵ Our research group reported scaling relationships of 2.4 and 8.4 for asolectin in the semidilute unentangled and semidilute entangled concentration regimes, respectively.⁴ For comparison, we measured the η_{sp} dependence on concentration for the monomeric surfactant CTAB in water, and observed a power-law exponent of 11.4, which is in good agreement with the reported value by Cappelaere and coworkers.⁵⁶

4.4.2 12-2-12 Solution Microstructure in Water:Methanol

The solution behavior of 12-2-12 in water:methanol was explored for the first time to examine the influence of a solvent mixture on the micellar microstructure and electrospinning behavior 12-2-12. Methanol was chosen as the cosolvent due to a lower surface tension than water, which is beneficial for processing electrospun fibers.⁵⁷ The solution behavior of 12-2-12 in water:methanol demonstrated drastically different microstructures compared to water. The η_{sp} dependence on concentration for 12-2-12 in water:methanol is depicted in Figure 4.8, and two concentration regimes were observed. The micellar morphology transitioned from partitioned globular micelles into overlapped micelles at $C^* = 11$ wt%. Figure 4.9a is a cryo-TEM micrograph of 12-2-12 in water:methanol at 10 wt%, $C < C^*$. Individual irregular globular micelles are distinguished below C^* with an average diameter of 100 nm. The micelles fused together from the overlapping of individual micelles at $C > C^*$, as shown for a 12 wt% solution in

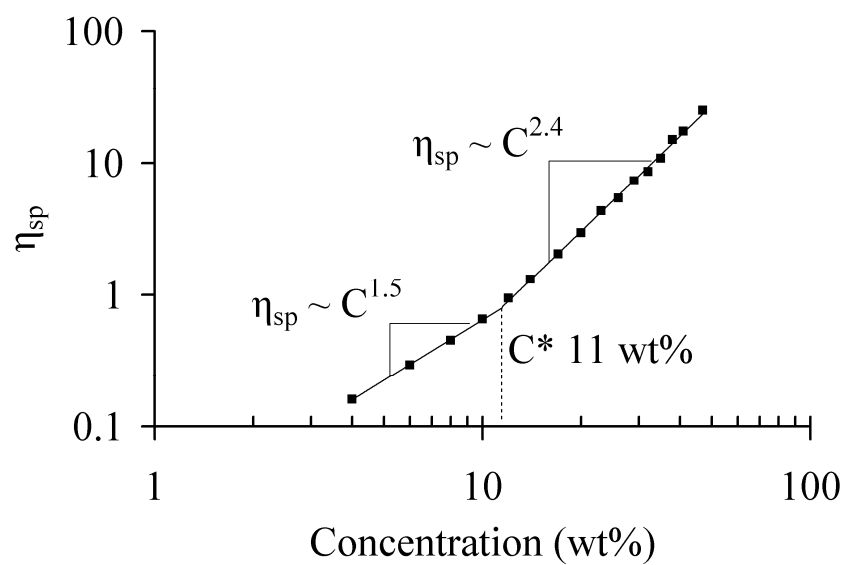


Figure 4.8 η_{sp} vs. concentration for 12-2-12 in water:methanol. Individual globular micelles began to overlap at a surfactant concentration of 11 wt%.

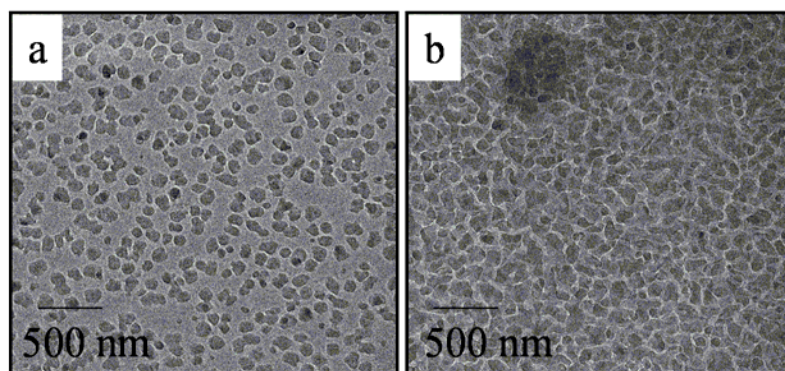


Figure 4.9 Cryo-TEM micrographs of 12-2-12 in water:methanol, a) 10 wt%, individual globular micelles, b) 12 wt%, overlapped micelles.

Figure 4.9b. Cryo-TEM micrographs at concentrations $2C^*$ and $4C^*$ were indistinct due to the high concentration of surfactant microstructures; nonetheless, low resolution threadlike micelles were distinguished at $2C^*$. Low resolution is a common problem of highly concentrated samples because cryo-TEM is more suitable for low concentration solutions where individual microstructures are more clearly observed.³⁴

The solution rheology of CTAB in water:methanol was explored for comparative purposes, and the C^* was measured at 19 wt%. The lower C^* concentration for 12-2-12 in water:methanol compared to CTAB resulted from the increased surface activity of gemini surfactants. The micellization of surfactants in a polar environment involves two competing forces: (1) the interaction of the hydrophobic chains with the polar solvent, which drives the formation of micelles, and (2) the electrostatic repulsive forces between the charged surfactant headgroups, which opposes micellization.⁵⁸ The dual hydrocarbon tails of gemini surfactants provide a larger thermodynamic contribution for micellization compared to single tail monomeric surfactants.¹⁰ Also, gemini surfactants have a smaller headgroup area contribution because the gemini charged groups are covalently confined at a closer proximity than electrostatic repulsive forces allow for single head monomeric surfactants.²⁷

The power law scaling relationships in water:methanol were very similar for both 12-2-12 and CTAB, and were dramatically lower than observed for the surfactants in water. In water:methanol the concentration scaling relationships below and above C^* were 1.5 and 2.4 for 12-2-12, and 1.5 and 2.7 for CTAB, respectively. The decreased scaling relationship in water:methanol compared to water was attributed to the ability of methanol to more efficiently bridge the interface of the surfactant hydrophilic and

hydrophobic domains. This increased the effective headgroup size and decreased the packing parameter, which lead to the formation of globular micelles as shown in Figure 4.9. The larger scaling factors observed for 12-2-12 in water resulted from the optimal volume balance of the head and tail areas of the gemini surfactant, which resulted in the formation of flexible threadlike micelles that were sufficiently long to entangle and form branch points. In contrast, the globular micellar structure in water:methanol did not permit the same degree of intermolecular associations, and lower viscosities and scaling relationships were observed compared to pure water solutions.

4.4.3 Electrospinning Gemini Surfactants

High molecular weight polymers are electrospun from viscous solutions at concentrations typically above C_e or from the melt phase, and chain entanglements for non-associating polymers are necessary to withstand the Raleigh instabilities and stabilize the whipping electrified jet to produce continuous fibers.^{1,2,59,60} The supramolecular microstructure of 12-2-12 in water and water:methanol lead to highly viscous solutions, which prompted us to investigate the possibility for electrospinning. The electrospinning studies were conducted at the same temperature and solvent conditions as the solution rheology experiments in order to ensure similar surfactant microstructures. Moreover, all 12-2-12 solutions were electrospun at 25 kV, 5 mL/h syringe flow rate, and 12 cm tip-to-screen (TTS). Figure 4.10 shows the SEM images of 12-2-12 fibers electrospun from water:methanol. Droplets formed at 20 wt% (Figure 4.10a) as a result of the low solution viscosity destabilizing the electrified jet. When the concentration was increased to $2C^*$ beaded fibers formed as shown in Figure 4.10b at 22 wt%. Figure 4.10c displays the formation of continuous fibers with a low concentration of large beads present and fiber

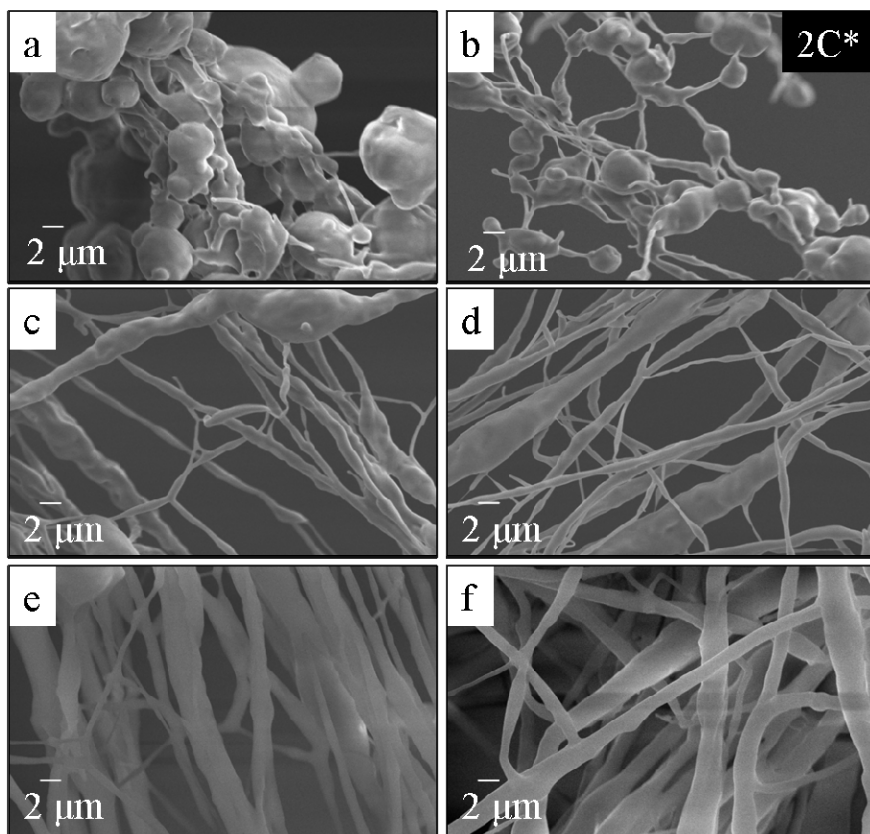


Figure 4.10 FESEM of electrospun fibers of 12-2-12 from water:methanol ($C^*=11$ wt%), electrospun from: a) 20 wt%, b) 22 wt%, c) 28 wt%, d) 30 wt%, e) 42 wt%, d) 44 wt% 12-2-12 gemini surfactant solutions in water:methanol.

diameters ranging from 0.9 μm to 7 μm . Although fibers were continuous without beaded defects at 30 wt%, the fiber morphology was irregular with diameters ranging from 1 μm to 6 μm , as shown in Figure 4.10d. Continuous fibers with average fiber diameters of 4 μm and 5 μm as shown in Figures 4.10e and 4.10f, respectively, were electrospun from 42 wt% and 44 wt% solutions. The threadlike micelle entanglement couplings stabilized the electrospinning jet and resulted in the transition from beads to continuous fibers at concentrations greater than $2C^*$. The 12-2-12 electrospun membranes were completely soluble, and ^1H NMR spectroscopy of the gemini surfactant mats confirmed that the electric field did not alter the chemical structure of the gemini surfactant.

Asolectin was electrospun from CHCl_3/DMF (7/3 wt/wt) where the lipid microstructure formed reverse cylindrical micelles.⁴ Electrospun beads of asolectin were collected at concentrations below C_e and beaded fibers at $C = C_e$. Continuous electrospun fibers of asolectin were collected at $C \geq 1.2C_e$, and the fiber diameter increased with increasing concentration. Electrospun fibers of 12-2-12, as depicted in Figure 4.10, displayed a higher surface roughness than asolectin electrospun fibers. The 12-2-12 fiber diameters also increased with concentration due to the higher degree of micellar growth and entanglements, however, smooth fibers were not observed at any concentration. The irregularities in the 12-2-12 fibers could have resulted from the large applied voltage. Asolectin fibers were electrospun from an applied voltage of 15 kV,⁴ however, 12-2-12 required a voltage of 25 kV to produce fibers. Dietzel and coworkers⁶¹ correlated electrospun fiber morphology to applied voltage, and found that increasing

voltage changed the electrospinning droplet and resulted in a higher concentration of fiber defects.

Electrospinning efforts of 12-2-12 in water did not produce surfactant fibers at any concentration. Greiner and Wendorff⁶² published an electrospinning review and discussed recent electrospinning efforts from aqueous solutions. The electrospinning droplet forms a Taylor cone in the presence of an applied voltage and a jet is ejected from the Taylor cone if the applied voltage is strong enough to overcome the surface tension of the droplet.⁶³ The solution viscosity, surface tension, and conductivity are key solution parameters in forming electrospun fibers.^{59,62,63} Electrospinning from aqueous solutions requires a reduction in the surface tension of water, which is typically accomplished with the addition of surfactants⁵⁷ or cosolvents.^{9,59} In an effort to understand why 12-2-12 did not produce electrospun fibers from water, the solution conductivity and surface tension for 12-2-12 in water and water:methanol were explored for solutions with comparable zero shear viscosities at 25 °C. Electrospun fibers were collected from 42 wt% 12-2-12 water:methanol solutions, which had a surface tension of 26 mN/m and conductivity of 43 mS/cm. Solutions of 2.6 wt% 12-2-12 in water did not produce electrospun fibers, and the solution had a surface tension of 28 mN/m and lower conductivity of 8 mS/cm. The surface tensions and solution conductivities for 12-2-12 solutions with comparable zero shear viscosities in water and water:methanol were within an acceptable range for electrospinning,⁵⁷ however, the 42 wt% water:methanol solution had a higher conductivity due to the much higher concentration of surfactant. Electrospinning low molar mass amphiphiles may require higher solution conductivities

than polymers, or the branched microstructure of 12-2-12 in water may have influenced the electrospinning behavior.

4.5 Conclusions

The micellar morphological transitions of 12-2-12 in water and water:methanol were characterized with cryo-TEM and solution rheology. The 12-2-12 microstructure in water transitioned from linear, entangled, threadlike micelles to branched threadlike micelles at 1.5 wt%, and at 2.7 wt% the microstructure evolved into a viscoelastic, entangled, highly-branched threadlike network. In water:methanol 12-2-12 produced a considerably different micellar microstructure compared to water, and the micellar morphology transitioned from partitioned globular micelles into overlapped micelles at C^* , 11 wt%.

The supramolecular microstructures of 12-2-12 in water and water:methanol lead to highly viscous solutions, and their electrospinning was explored. Electrospinning 12-2-12 in water did not produce surfactant fibers at any concentration. However, for the first time nonwoven fibrous scaffolds were electrospun from gemini surfactants, with fiber diameters between 0.9 and 7 μm with water:methanol as the solvent. The 12-2-12 fiber morphology transitioned from beaded fibers into continuous fibers at concentrations greater than $2C^*$ in water:methanol. The entangled supramolecular structure of the low molar mass surfactant stabilized the electrospinning jet and resulted in continuous fibers. Electrospinning gemini surfactant fibers from polar solvents represents an innovative strategy to develop high surface area scaffolds or membranes with charged hydrophilic surfaces for the development of charged controlled-release membranes, tissue engineering scaffolds, or for biologically compatible coatings.

4.6 Acknowledgments

This material is based upon work supported in part by the U.S. Army Research Office under grant number W911NF-07-1-0452 Ionic Liquids in Electro-Active Devices (ILEAD) MURI.

4.7 References

1. McKee, M. G.; Wilkes, G. L.; Colby, R. H.; Long, T. E., *Macromolecules* **2004**, *37* (5), 1760-1767.
2. Shenoy, S. L.; Bates, W. D.; Frisch, H. L.; Wnek, G. E., *Polymer* **2005**, *46* (10), 3372-3384.
3. Rutledge, G. C.; Fridrikh, S. V., *Adv. Drug Delivery Rev.* **2007**, *59* (14), 1384-1391.
4. McKee, M. G.; Layman, J. M.; Cashion, M. P.; Long, T. E., *Science* **2006**, *311* (5759), 353-355.
5. Schurtenberger, P.; Scartazzini, R.; Magid, L. J.; Leser, M. E.; Luisi, P. L., *J. Phys. Chem.* **1990**, *94* (9), 3695-3701.
6. Shchipunov, Y. A.; Mezzasalma, S. A.; Koper, G. J. M.; Hoffmann, H., *J. Phys. Chem. B* **2001**, *105* (43), 10484-10488.
7. Cates, M. E.; Candau, S. J., *J. Phys.: Condens. Matter* **1990**, *2* (33), 6869-6892.
8. Hunley, M. T., McKee, M.G., Long, T.E., *J. Mater. Chem.* **2007**, *17*, 605-608.
9. Fong, H.; Chun, I.; Reneker, D. H., *Polymer* **1999**, *40* (16), 4585-4592.
10. Hait, S. K.; Moulik, S. P., *Current Science* **2002**, *82* (9), 1101-1111.
11. Menger, F. M.; Keiper, J. S., *Angew. Chem. Int. Ed.* **2000**, *39* (11), 1907-1920.
12. Zana, R., *Adv. Colloid Interface Sci.* **2002**, *97* (1-3), 205-253.
13. In, M.; Zana, R., *J. Dispersion Sci. Technol.* **2007**, *28* (1), 143-154.
14. Layn, K. M.; Debenedetti, P. G.; Prud'homme, R. K., *J. Chem. Phys.* **1998**, *109* (13), 5651-5658.
15. Espert, A.; v. Klitzing, R.; Poulin, P.; Colin, A.; Zana, R.; Langevin, D., *Langmuir* **1998**, *14* (15), 4251-4260.
16. Xia, J.; Zana, R., Applications of Gemini Surfactants. In *Gemini Surfactants : Synthesis, Interfacial and Solution-Phase Behavior, and Applications*, Zana, R.; Xia, J., Eds. Marcel Dekker Inc: New York, 2004; pp 301-321.
17. Chen, L.; Xie, H.; Li, Y.; Yu, W., *Colloids Surf., A* **2008**, *330* (2-3), 176-179.
18. Zhou, M.; Nemade, P. R.; Lu, X.; Zeng, X.; Hatakeyama, E. S.; Noble, R. D.; Gin, D. L., *J. Am. Chem. Soc.* **2007**, *129* (31), 9574-9575.
19. Bakshi, M. S.; Sharma, P.; Banipal, T. S., *Mater. Lett.* **2007**, *61* (28), 5004-5009.
20. Lu, T.; Huang, J.; Li, Z.; Jia, S.; Fu, H., *J. Phys. Chem. B* **2008**, *112* (10), 2909-2914.
21. Bakshi, M. S.; Possmayer, F.; Petersen, N. O., *J. Phys. Chem. C* **2008**, *112* (22), 8259-8265.
22. Kirby, A. J., et al., *Angew. Chem. Int. Ed.* **2003**, *42* (13), 1448-1457.

23. Luciani, P.; Bombelli, C.; Colone, M.; Giansanti, L.; Ryhanen Samppa, J.; Saily, V. M. J.; Mancini, G.; Kinnunen Paavo, K. J., *Biomacromolecules* **2007**, 8 (6), 1999-2003.
24. Rosen, M. J., *Surfactants and interfacial phenomena* 3ed.; Wiley-Interscience: Hoboken, N.J., 2004.
25. Zana, R.; Benraou, M.; Rueff, R., *Langmuir* **1991**, 7 (6), 1072-1075.
26. Zana, R.; Talmon, Y., *Nature* **1993**, 362 (6417), 228-230.
27. Danino, D.; Talmon, Y.; Zana, R., *Langmuir* **1995**, 11 (5), 1448-1456.
28. Camesano, T. A.; Nagarajan, R., *Colloids Surf., A* **2000**, 167 (1-2), 165-177.
29. Eriksson, J. C.; Ljunggren, S., *J. Chem. Soc., Faraday Trans.* **1985**, 81 (8), 1209-1242.
30. Bernheim-Groswasser, A.; Zana, R.; Talmon, Y., *J. Phys. Chem. B* **2000**, 104 (17), 4005-4009.
31. Han, L.; Chen, H.; Luo, P., *Surf. Sci.* **2004**, 564 (1-3), 141-148.
32. Weber, V.; Narayanan, T.; Mendes, E.; Schosseler, F., *Langmuir* **2003**, 19 (4), 992-1000.
33. Kern, F.; Lequeux, F.; Zana, R.; Candau, S. J., *Langmuir* **1994**, 10 (6), 1714-1723.
34. Cui, H.; Hodgdon, T. K.; Kaler, E. W.; Abezgauz, L.; Danino, D.; Lubovsky, M.; Talmon, Y.; Pochan, D. J., *Soft Matter* **2007**, 3, 945-955.
35. Won, Y.-Y., *Korean J. Chem. Eng.* **2004**, 21 (1), 296-302.
36. McKee, M. G.; Hunley, M. T.; Layman, J. M.; Long, T. E., *Macromolecules* **2006**, 39 (2), 575-583.
37. Hunley, M. T.; Harber, A.; Orlicki, J. A.; Rawlett, A. M.; Long, T. E., *Langmuir* **2008**, 24 (3), 654-657.
38. Hunley, M. T.; Long, T. E., *Polym. Int.* **2008**, 57 (3), 385-389.
39. Hunley, M. T.; McKee, M. G.; Long, T. E., *J. Mater. Chem.* **2007**, 17 (7), 605-608.
40. McKee, M. G.; Elkins, C. L.; Long, T. E., *Polymer* **2004**, 45 (26), 8705-8715.
41. McKee, M. G.; Park, T.; Unal, S.; Yilgor, I.; Long, T. E., *Polymer* **2005**, 46 (7), 2011-2015.
42. Oda, R.; Huc, I.; Homo, J.-C.; Heinrich, B.; Schmutz, M.; Candau, S., *Langmuir* **1999**, 15 (7), 2384-2390.
43. MacKintosh, F. C.; Safran, S. A.; Pincus, P. A., *Europhys. Lett.* **1990**, 12 (8), 697-702.
44. Gonzalez, Y. I.; Kaler, E. W., *Curr. Opin. Colloid Interface Sci.* **2005**, 10 (5,6), 256-260.
45. Oelschlaeger, C.; Waton, G.; Candau, S. J.; Cates, M. E., *Langmuir* **2002**, 18 (20), 7265-7271.
46. Danino, D.; Talmon, Y.; Levy, H.; Beinert, G.; Zana, R., *Science* **1995**, 269 (5229), 1420-1421.
47. Drye, T. J.; Cates, M. E., *J. Chem. Phys.* **1992**, 96 (2), 1367-1375.
48. Dreiss, C. A., *Soft Matter* **2007**, 3 (8), 956-970.
49. Karaborni, S.; Esselink, K.; Hilbers, P. A. J.; Smit, B.; Karthaus, J.; van Os, N. M.; Zana, R., *Science* **1994**, 266 (5183), 254-256.
50. Lin, Z., *Langmuir* **1996**, 12 (7), 1729-1737.

51. Khatory, A.; Kern, F.; Lequeux, F.; Appell, J.; Porte, G.; Morie, N.; Ott, A.; Urbach, W., *Langmuir* **1993**, *9* (4), 933-939.
52. Appell, J.; Porte, G.; Khatory, A.; Kern, F.; Candau, S. J., *J. Phys. II* **1992**, *2* (5), 1045-1052.
53. Candau, S. J.; Khatory, A.; Lequeux, F.; Kern, F., *J. Phys. IV* **1993**, *3* (C1), 197-209.
54. Rubinstein, M.; Colby, R. H.; Dobrynin, A. V., *Phys. Rev. Lett.* **1994**, *73* (20), 2776-2779.
55. Magid, L. J., *J. Phys. Chem. B* **1998**, *102* (21), 4064-4074.
56. Cappelaere, E.; Cressely, R.; Decruppe, J. P., *Colloids Surf., A* **1995**, *104* (2/3), 353-374.
57. Nagarajan, R.; Drew, C.; Mello, C. M., *J. Phys. Chem. C* **2007**, *111* (44), 16105-16108.
58. Evans, D. F.; Wennerstrom, H., Solutes and Solvents, Self-Assembly of Amphiphiles. In *The Colloidal Domain Where Physics, Chemistry, Biology, and Technology Meet*, 2 ed.; John Wiley & Sons, Inc: New York, 1999; pp 1-43.
59. Huang, Z.-M.; Zhang, Y.-Z.; Kotaki, M.; Ramakrishna, S., *Compos. Sci. Technol.* **2003**, *63*, 2223-2253.
60. Gupta, P.; Elkins, C.; Long, T. E.; Wilkes, G. L., *Polymer* **2005**, *46* (13), 4799-4810.
61. Deitzel, J. M.; Kleinmeyer, J.; Harris, D.; Tan, N. C. B., *Polymer* **2001**, *42* (1), 261-272.
62. Greiner, A.; Wendorff, J. H., *Angew. Chem. Int. Ed.* **2007**, *46*, 5670-5703.
63. Burger, C.; Hsiao, B. S.; Chu, B., *Annu. Rev. Mater. Res.* **2006**, *36*, 333-368.

Chapter 5: Structure-Property Elucidation of Photo-Polymerizable

Gemini Surfactants

Cashion, Matthew P.; Mohns, Brian R.; Brown, Rebecca H.; Long, Timothy E. *J. Colloid and Interface Science* (submitted).

5.1 Abstract

The thermal and solution properties were explored for a series of ammonium gemini surfactants using differential scanning calorimetry (DSC), polarized light microscopy (PLM), and conductivity experiments. The gemini surfactants were designated as m-s-m, where m represents the number of carbons in the hydrocarbon tails and s denotes the length of the carbon-spacer between ammonium cations. The thermal transitions and Kraft temperatures (T_k) were investigated for model surfactants 12-2-12, 16-2-16, and 18-2-18, which contained only hydrocarbon tails, and polymerizable gemini surfactants Acry-2-Acry and Cinn-2-Cinn, which contained acrylic and cinnamate functionality at the terminal of each tail, respectively. Cin-2-Cinn displayed an isotropic melting temperature at 143 °C, whereas all other surfactants exhibited crystal-to-crystal transitions; liquid crystalline or thermotropic behavior was not observed at temperatures below 160 °C. The T_k was measured in water and water:methanol (1:1 vol) to investigate the influence of solvent on the surfactant solution properties. The T_k in water and water:methanol increased with increasing tail length, however, the T_k was lower for all surfactants in water:methanol compared to water. The addition of a cosolvent represents a strategy to lower the T_k and increase the application temperature range for gemini surfactants.

5.2 Introduction

Gemini surfactants, which are also known as dimeric surfactants, are an exceptional class of amphiphile due to their low critical micelle concentration (CMC) and intriguing supramolecular assemblies.¹⁻⁵ Ammonium gemini surfactants have received significant industrial attention as emulsifiers and dispersants in detergents, cosmetics, personal hygiene products, coatings, and paint formulations.^{4,6,7} Gemini surfactants have also received interest as templates for the synthesis of metal nanoparticles,⁸⁻¹⁰ and as novel gene transfection agents due to their superior surface-active properties.¹¹⁻¹³ Gemini surfactants contain two hydrophobic tails and two hydrophilic headgroups covalently connected with a spacer. Reported hydrophilic headgroups include cationic, anionic, zwitterionic, and nonionic functionality.¹ Ammonium gemini surfactants are designated as m-s-m, where m represents the length of the hydrocarbon tail and s denotes the number of carbons in the headgroup spacer. The size and functionality of the spacer determines the supramolecular microstructure of assembled gemini surfactants. Reported spacer functionalities include: methylenes,¹⁴ stilbenes,¹⁵ biodegradable groups such as amides,¹⁶ esters,¹⁶ and ethylene oxide,¹⁷ and a variety of other spacer groups.³ Wang and coworkers varied the hydrophilicity and flexibility of spacer compositions to investigate their influence on the aggregation properties of quaternary ammonium gemini surfactants.¹⁸ The researchers discovered that highly flexible hydrophilic spacer groups decreased the CMC and ionization degree, while increasing the packing efficiency and micelle aggregation number.

Others have investigated the influence of the tailgroup on the aggregation properties of gemini surfactants, and they discovered that the CMC decreased with

increasing hydrocarbon length.^{5,19,20} Aggregation of hydrophobic segments favors micellization, whereas electrostatic repulsive forces between ionic headgroups opposes surfactant aggregation.²¹ Increasing hydrocarbon chain length facilitates micellization and limits interactions between large hydrophobic tails and the polar solvent. The most common tails in the literature consist of saturated hydrocarbons, however, earlier literature has revealed the synthesis and solution properties of gemini surfactants with fluorinated²²⁻²⁴ and unsaturated hydrocarbon²⁵⁻²⁸ tails.

Polymerizable surfactants have received attention as stabilizers for emulsion polymerization,²⁹ templates for the design of mesoporous materials,³⁰ nanofiltration membranes,³¹ gas separation membranes,³² breathable vapor resistant membranes,³³ water desalination technologies,⁷ and as nanostructured liquid crystalline assemblies.^{34,35} Polymerization of gemini surfactant microstructures provides a strategy to increase the thermal stability and useful temperature range of assembled architectures. Abe and coworkers^{36,37} synthesized a polymerizable ammonium gemini surfactant with a methacrylate group at the terminus of each hydrocarbon chain, $[\text{CH}_2=\text{C}(\text{CH}_3)\text{COO}(\text{CH}_2)_{11}\text{N}^+(\text{CH}_3)_2\text{CH}_2]_2 \cdot 2\text{Br}^-$. Incorporating a small hydrophilic group in the tail might disrupt the surfactant self-assembly and cause the terminal region to migrate to the hydrophilic interface. However, the researchers discovered that the methacrylate groups did not loop to the air/water interface, and the methacryloylundecyl tails behaved very similar to dodecyl hydrocarbon chains. Caillier and coworkers³⁸ synthesized polymerizable ammonium gemini surfactants with fluorinated tailgroups and an acrylate in the spacer between the quaternized ammoniums. The acrylic

functionalized gemini surfactant demonstrated biocidal activity and exhibited superior surface activity.

In this study, model and polymerizable gemini surfactants (Figure 5.1) were synthesized. A kinetic study using *in situ* FTIR spectroscopy was performed to optimize reaction conditions for the gemini surfactants. The synthesis of 12-2-12 and 12-6-12 were monitored with *in situ* FTIR spectroscopy and appearance of the quaternized ammonium C-N⁺ stretch at 908 cm⁻¹ was observed. The thermal transitions and Kraft temperature (T_k) were also measured for the gemini surfactants, 12-2-12, 16-2-16, 18-2-18, and polymerizable gemini surfactants end-capped with cinnamate groups (Cinn-2-Cinn) and acrylate functionality (Acry-2-Acry), as shown in Figure 5.1. T_k values were determined from conductance measurements of surfactant solutions in water and water:methanol (1:1 vol). Differential scanning calorimetry (DSC) was correlated with polarized light microscopy (PLM) to explore the thermal transitions of the gemini surfactant series.

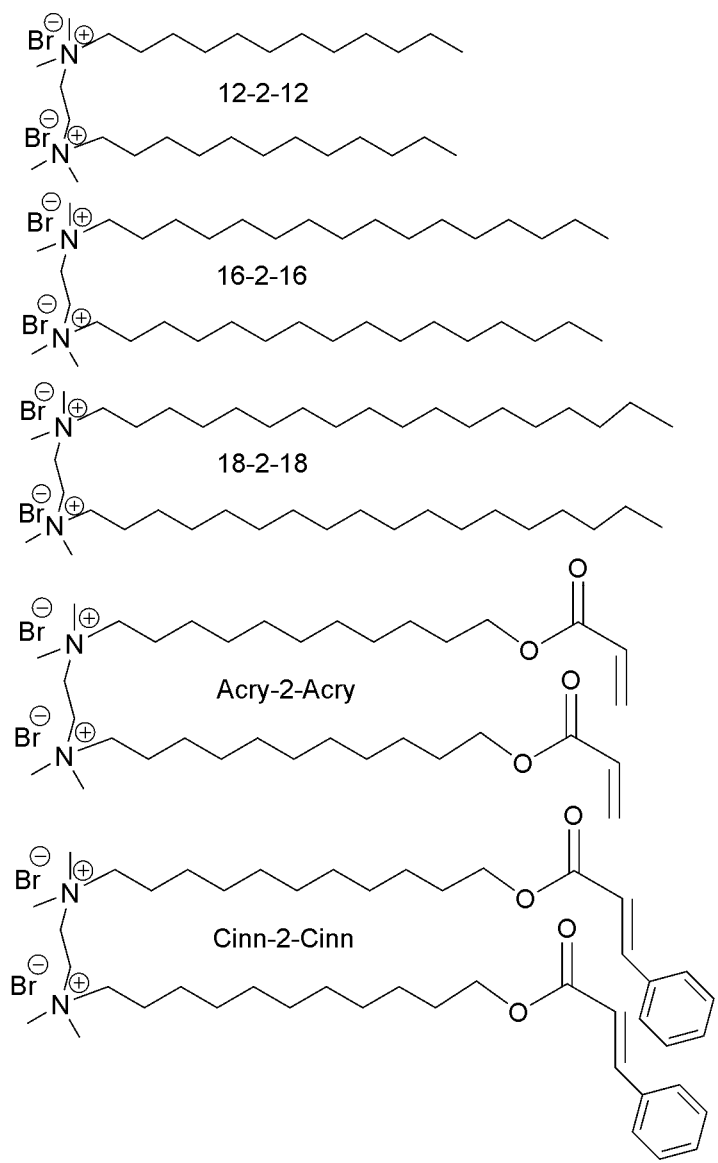


Figure 5.1 Gemini surfactants

5.3 Materials and Methods

5.3.1 Materials

1-Bromododecane (97%), 1-bromohexadecane (97%), 1-bromooctadecane (96%), *N,N,N',N'*-tetramethylethylenediamine (99%), *N,N,N',N'*-tetramethyl-1,6-hexanediamine (99%), cinnamoyl chloride (98%), acryloyl chloride (97%), triethylamine ($\geq 99\%$), hydroquinone (99 %), ethanol (ACS grade anhydrous), ethyl acetate (HPLC grade), ethyl ether (anhydrous), methanol (HPLC grade), dichloromethane (HPLC grade), and cetyltrimethylammonium bromide (CTAB $> 98\%$) were purchased from Sigma-Aldrich Chemical Co. 11-bromoundecanol (97%) was purchased from Alfa Aesar. 1-Bromododecane, 1-bromohexadecane, 1-bromooctadecane, *N,N,N',N'*-tetramethylethylenediamine, and *N,N,N',N'*-tetramethyl-1,6-hexanediamine were passed through a silica gel column prior to use. Ethanol, dichloromethane, and acryloyl chloride were distilled from CaH₂ under reduced pressure prior to use, and cinnamoyl chloride was sublimed to yield white crystals prior to use. Aqueous solutions were made with DI water. All reactions were performed in flame-dried glassware equipped with a magnetic stir bar under argon pressure, unless otherwise noted.

5.3.2 Instrumentation.

¹H and ¹³C NMR spectroscopy were performed on a Varian Unity 400 spectrometer at 400 MHz in CDCl₃. FAB Mass spectrometry was performed on a JEOL HX110 dual focusing mass spectrometer. DSC was performed on a TA Instruments DSC 1000 under a nitrogen flush at a heating rate of 5 °C/min. The transitions were determined as the midpoint of the endotherms of the 2nd heat cycle. Thermogravimetric analysis (TGA) was conducted on a TA Instruments Hi-Res TGA 2950 with a

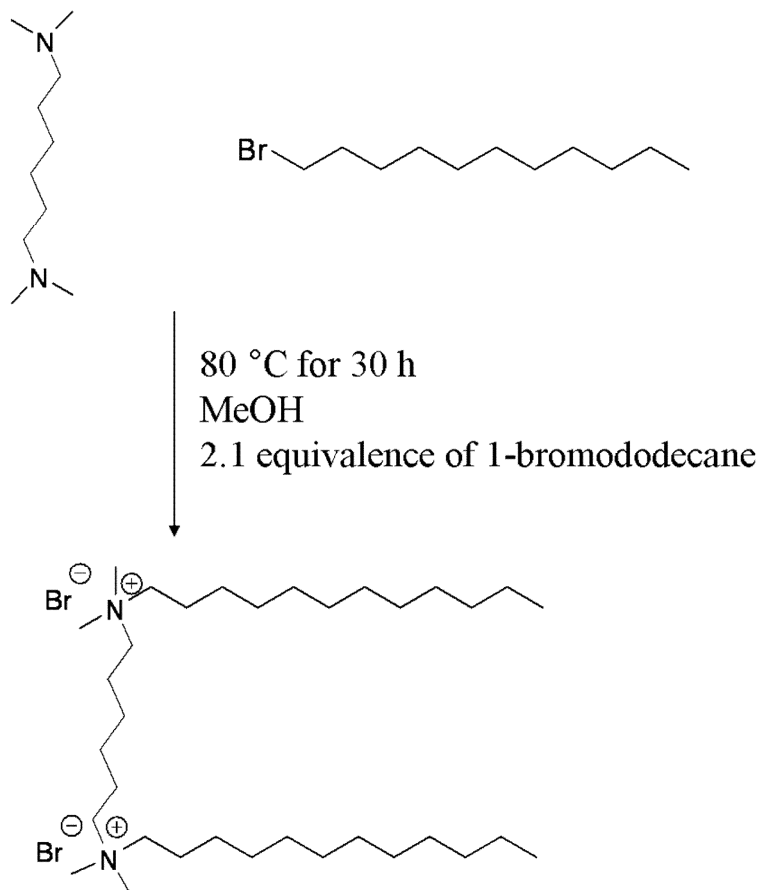
temperature ramp of 5 °C/min under a nitrogen atmosphere. *In situ* FTIR was performed with a Mettler Toledo ReactIR 4000 ATR apparatus equipped with a light conduit and a stainless steel insertion probe with a DiComp (diamond composite) probe tip. Reaction analysis was performed with ReactIR 3.1 software provided by Mettler Toledo.

5.3.3 *In situ* FTIR spectroscopy monitoring the synthesis of N,N'-didodecyl-N,N,N',N'-tetramethyl-N,N'-ethanediyl-di-ammonium dibromide (12-2-12)

The reaction scheme for the synthesis of 12-2-12 is shown in Scheme 4.1. The *in situ* FTIR probe was inserted into a 100-mL, three-necked round-bottomed flask connected with condenser in an 80 °C bath. Methanol (35 mL) was added to the reaction flask. After fifteen minutes 1-bromododecane (0.120 mol, 29.8 g) and *N,N,N',N'*-tetramethylethylenediamine (0.057 mol, 6.72 g) were added to the reaction flask separately and the reaction was monitored for 48 h.

5.3.4 *In situ* FTIR spectroscopy monitoring the synthesis of N,N'-didodecyl-N,N,N',N'-tetramethyl-N,N'-hexanediyl-di-ammonium dibromide (12-6-12)

The reaction scheme for the synthesis of 12-6-12 is shown in Scheme 5.1. The *in situ* FTIR probe was inserted into a 100-mL, three-necked, round-bottomed flask connected with condenser in an 80 °C bath. Methanol (35 mL) was added to the reaction flask. After fifteen minutes 1-bromododecane (0.120 mol, 29.8 g) and *N,N,N',N'*-tetramethyl-1,6-hexanediamine (0.057 mol, 9.82 g) were added to the reaction flask separately and the reaction was monitored for 30 h.



Scheme 5.1 Synthesis of 12-6-12

5.3.5 Synthesis of N,N'-didodecyl-N,N,N',N'-tetramethyl-N,N'-ethanediyl-di-ammonium dibromide (12-2-12)

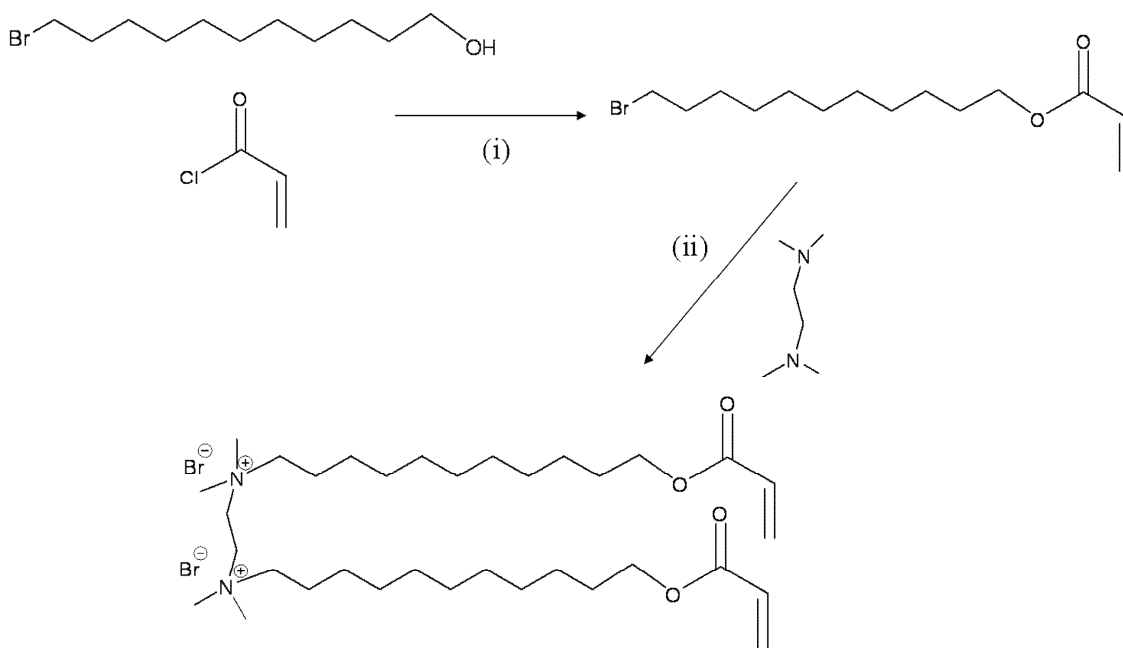
N,N,N',N'-tetramethylethylenediamine (0.052 mol, 6.09 g) and 1-bromododecane (0.109 mol, 27.1 g) were dissolved in methanol (0.795 mol, 32.2 mL) in a 250-mL round-bottomed flask. A condenser was connected to the reaction flask and the flask was placed in an 80 °C bath for 48 h. The reaction mixture was precipitated into ethyl acetate and a white solid was collected. The white solid was redissolved in chloroform and precipitated into ethyl ether. The white solid product was isolated and dried at 40 °C under reduced pressure. The yield was 80% and degraded before melting. The product was characterized with ¹H NMR, ¹³C NMR, and mass spectrometry.

5.3.6 Synthesis of N,N'-dihexadecyl-N,N,N',N'-tetramethyl-N,N'-ethanediyl-di-ammonium dibromide (16-2-16), and N,N'-dioctadecyl-N,N,N',N'-tetramethyl-N,N'-ethanediyl-di-ammonium dibromide (18-2-18)

The synthetic procedure for 12-2-12 was repeated, however, 1-bromohexadecane and 1-bromooctadecane were used as the bromoalkane for the synthesis of 16-2-16 and 18-2-18, respectively.

5.3.7 Synthesis of N,N'-di-(11-(acryloyloxy)undecyl)-N,N,N',N'-tetramethyl-N,N'-ethanediyl-di-ammonium dibromide (Acry-2-Acry)

The synthesis of Acry-2-Acry is shown in Scheme 5.2. 11-Bromoundecanol (0.139 mol, 35.0 g) was dissolved in dichloromethane (139 mL) in a 250-mL two-neck round-bottomed flask and placed in an ice bath. Triethylamine (0.153 mol, 21.4 mL) was added to the reaction flask. Acryloyl chloride (0.153 mol, 12.5 mL) was added dropwise to the reaction flask. The reaction warmed to room temperature over 16 h, at which point



Scheme 5.2 Synthesis of Acry-2-Acry, (i) 0 °C for 16 h, triethylamine, dichloromethane, (ii) 80 °C for 48 h, methanol, hydroquinone.

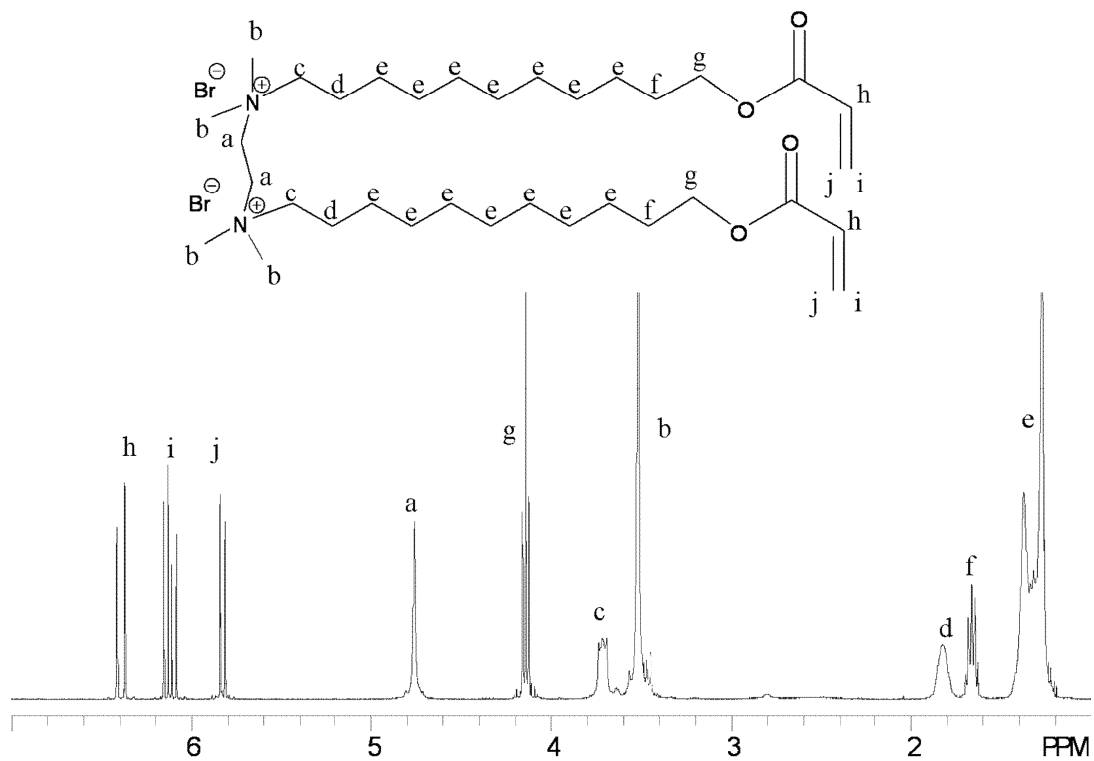


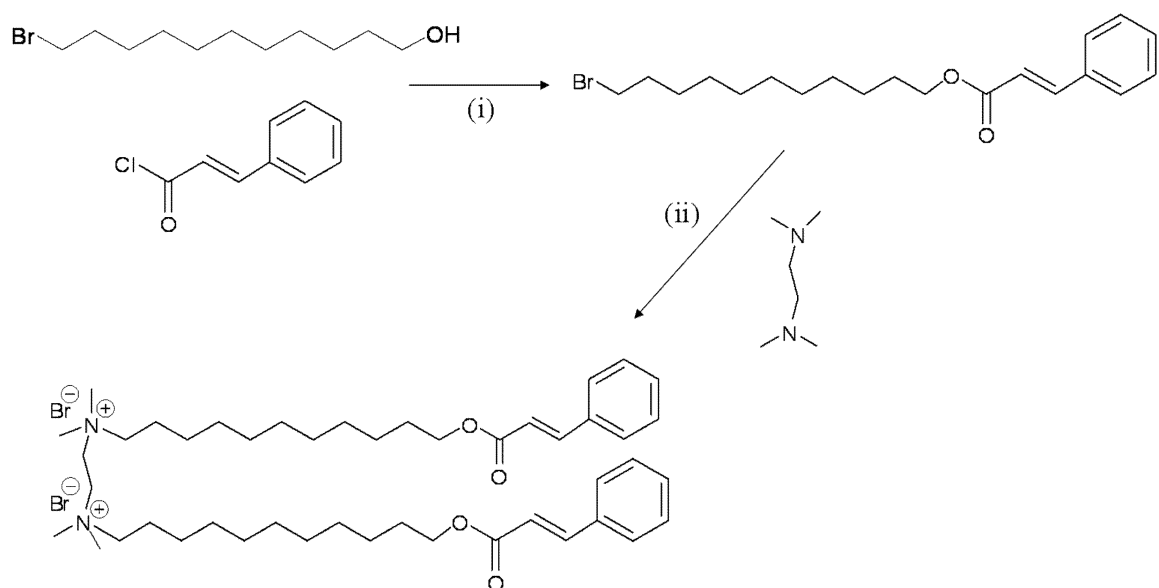
Figure 5.2 ^1H NMR of Acry-2-Acry

the triethylamine salt was filtered off, and the reaction mixture was washed with water twice. The reaction mixture was passed through a silica gel column with dichloromethane as the mobile phase, and the product, 11-bromoundecyl acrylate was collected as a yellow oil, produced a single TLC spot and a yield of 65%.

The quaternization of *N,N,N',N'*-tetramethylethylenediamine (0.026 mol, 3.13 g) with 11-bromoundecyl acrylate (0.057 mol, 17.3 g) was conducted in methanol (16.2 mL) in the presence of hydroquinone (0.182 mmol, 0.020 g). The reaction mixture was heated at 80 °C for 48 h. The reaction mixture was precipitated into ethyl acetate and a white solid was collected. The white solid was redissolved in chloroform and precipitated into ethyl ether. The white solid product was isolated and dried at 25 °C under reduced pressure (yield 78%). The product was characterized with ¹H NMR shown in Figure 5.2, ¹³C NMR, and mass spectrometry.

5.3.8 Synthesis of *N,N'*-di-(11-(cinnamoyloxy)undecyl)-*N,N,N',N'*-tetramethyl-*N,N'*-ethanediyl-di-ammonium dibromide (Cinn-2-Cinn)

The synthesis of Cinn-2-Cinn is shown in Scheme 5.3. 11-Bromoundecanol (0.054 mol, 13.6 g) was dissolved in dichloromethane (54 mL) in a 250-mL two-neck round-bottomed flask and placed in an ice bath. Triethylamine (0.081 mol, 11.3 mL) was added to the reaction flask. Cinnamoyl chloride (0.081 mol, 13.6 g) was dissolved in dichloromethane (13.0 mL) and added dropwise to the reaction flask. The reaction warmed to room temperature over 16 h, at which point the triethylamine salt was filtered off, and the reaction mixture was washed with water twice. The reaction mixture was passed through a silica gel column with dichloromethane as the mobile phase, and the product, 11-bromoundecyl cinnamate, produced a single TLC spot and a yield of 54%.



Scheme 5.3 Synthesis of Cinn-2-Cinn, (i) 0 °C for 16 h, triethylamine, dichloromethane, (ii) 80 °C for 48 h, methanol.

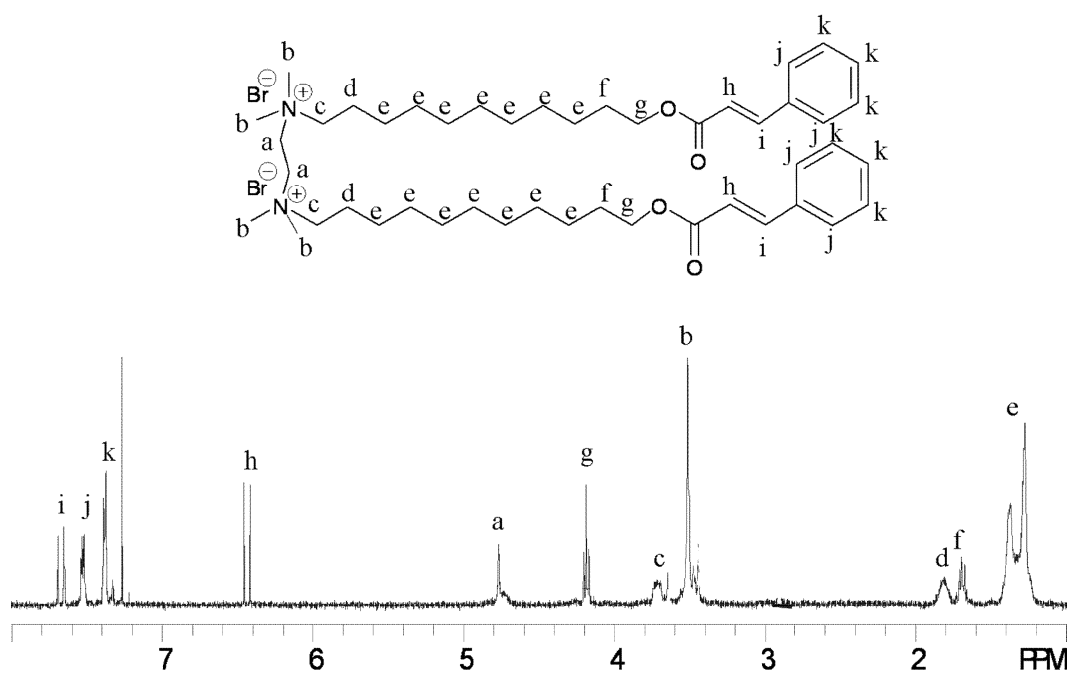


Figure 5.3 ^1H NMR of Cinn-2-Cinn

The quaternization of *N,N,N',N'*-tetramethylethylenediamine (0.014 mol, 1.62 g) with 11-bromoundecyl cinnamate (0.029 mol, 11.1 g) was conducted in methanol (20.0 mL). The reaction mixture was heated at 80 °C for 48 h, at which point the reaction mixture was precipitated into ethyl acetate and a white solid was collected. The white solid was redissolved in chloroform and precipitated into ethyl ether. The white solid product was isolated and dried at 25 °C under reduced pressure (yield 75%). The product was characterized with ¹H NMR shown in Figure 5.3, ¹³C NMR, and mass spectrometry.

5.3.9 Polarized light microscopy (PLM)

PLM was performed on an Olympus BX51 (Center Valley, PA) optical microscope equipped with an Olympus polarizer and analyzer. A Linkam THMS600 heating and freezing stage was mounted, and the microscope was operated in transmitted mode at a heating and cooling rate of 1 °C/min. 12-2-12, 16-2-16, 18-2-18, and the Acry-2-Acry were heated from 80 °C to 120 °C. The Cinn-2-Cinn surfactant was heated from 120°C to 160°C.

5.3.10 T_k conductance measurements

The T_k was measured for the series of gemini surfactants shown in Figure 5.1 in water and water:methanol (1:1 vol). Solutions of 1.0 wt% surfactant were prepared and stored at 1 °C for water solutions and – 28 °C for water:methanol solutions, for one week prior to the conductance measurement to insure precipitation of the surfactants. An Oakton (Vernon Hills, IL) Con 6 conductivity meter was used to measure conductance and temperature of the surfactant solutions. The conductance of DI water was 4.8 μS/cm and water:methanol (1:1 vol) was 9.8 μS/cm at 25 °C. The T_k was determined from the plot of conductance vs. temperature and in agreement with the visual point of

clarification. The conductance of 0.005 wt%, 1.0 wt%, and 2.0 wt% solutions of 12-2-12 in water were measured to investigate the influence of concentration on T_k . All reported T_k values have an error of ± 0.3 °C.

5.4 Results and Discussion

5.4.1 Monitoring the synthesis of 12-2-12 and 12-6-12 with *in situ* FTIR

Our research group has shown *in situ* FTIR spectroscopy as a beneficial spectroscopic technique to monitor reaction progress and determine reaction kinetics.³⁹⁻⁴¹ *In situ* FTIR spectroscopy was used to explore the influence of spacer length on the quaternization reaction rate of gemini surfactant synthesis. The synthesis of 12-2-12 and 12-6-12 was monitored with *in situ* FTIR spectroscopy and growth of the quaternized ammonium C-N⁺ stretch at 908 cm⁻¹ was observed. Gemini surfactant 12-2-12 was synthesized from the quaternization of *N,N,N',N'*-tetramethylethylenediamine with a two-molar equivalent of 1-bromododecane at 80 °C for 48 h in methanol. 12-6-12 was synthesized from the quaternization of *N,N,N',N'*-tetramethyl-1,6-hexanediamine with a two-molar equivalent of 1-bromododecane at 80 °C for 30 h in methanol. Both reactions were conducted in methanol to prevent IR absorbance overlap of the solvent with the C-N⁺ stretch.

The C-N⁺ growth profiles at 908 cm⁻¹ for the synthesis of 12-2-12 and 12-6-12 are shown in Figure 5.4. Synthesis of 12-6-12 was completed after 5 h and displayed an apparent rate constant of 2.1 x 10⁻³ (L/mol*s), whereas the synthesis of 12-2-12 required 40 h and displayed an apparent rate constant of 8.0 x 10⁻⁴ (L/mol*s). For 12-2-12 quaternization, the cationic ammonium withdrew electron density from the unreacted amine, decreasing the nucleophilicity of the second amine. For 12-6-12, the electron donating character of the hexamethylene spacer increased the nucleophilicity of the unreacted amine resulting in a shorter reaction time to achieve complete quaternization. Electron withdrawing contributions were greater for the short ethane spacer due to the

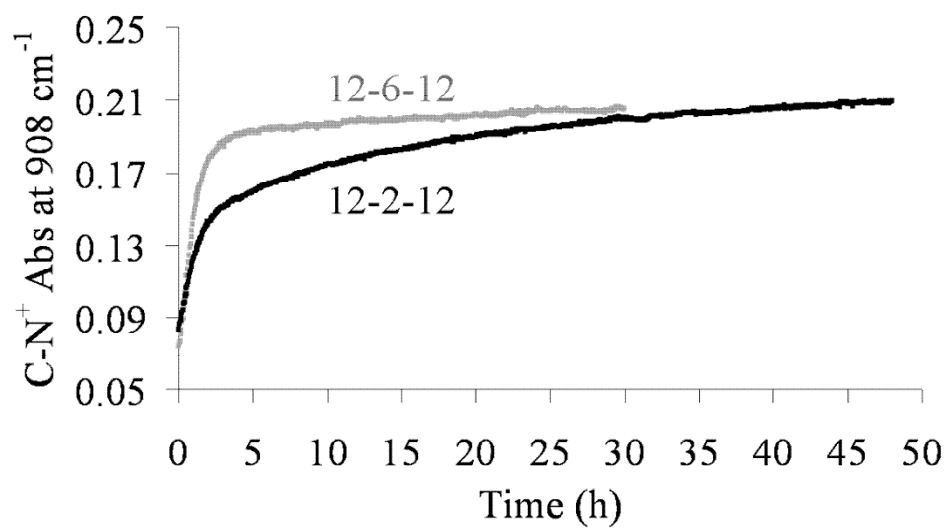


Figure 5.4 Quaternized ammonium growth profile at 908 cm⁻¹ using *in situ* FTIR to monitor the synthesis of 12-6-12 and 12-2-12.

proximity of the amines, therefore, the ethanediamine required a longer reaction time to achieve complete quaternization.

5.4.2 DSC and PLM Correlation

In and Zana published⁴² a review on the phase behavior of gemini surfactants and explored the influence of headgroup and tailgroup functionality on the thermotropic and lyotropic phase behavior of gemini surfactants. Thermotropic behavior was observed for gemini surfactants with alkyl lengths greater than 12 carbons, and was highly dependent upon the spacer length and composition. The thermal transitions of the gemini surfactant series in Figure 5.1 were explored using DSC and PLM, and each transition represented a change in phase or state. Gemini surfactants 12-2-12, 16-2-16, 18-2-18, and Acry-2-Acry were heated from 80 °C to 120 °C at 1 °C/min, and Cinn-2-Cinn was heated from 120 °C to 150 °C at 1 °C/min in PLM experiments. The observed phase transitions were reproducible and independent of thermal history below the thermal decomposition temperature. Quaternized ammoniums are known to thermally degrade and undergo Hoffmann elimination at temperatures above 150 °C.⁴³ Mass loss began at 170 °C for the ammonium gemini surfactant series shown in the TGA curve in Figure 5.5. The degradation temperature of the ammonium surfactants agreed with the reported literature value.^{44,45} Fuller and coworkers⁴⁶ observed thermal decomposition of ammonium gemini surfactants at temperatures above ~170 °C, and reported difficulties reproducing DSC thermal scans due to decomposition. To prevent thermal degradation DSC characterization was limited to 160 °C, and heating traces were reproducible for all surfactants.

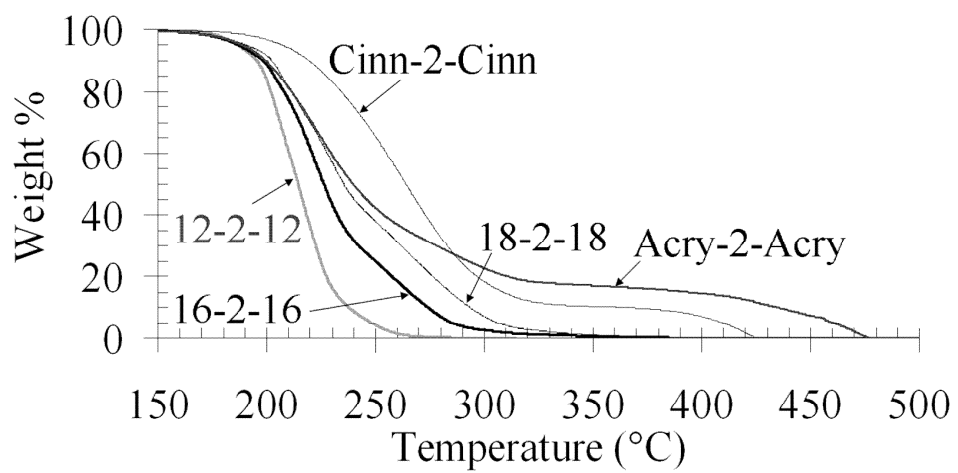


Figure 5.5 TGA analysis of the gemini surfactant series.

Gemini 12-2-12 was the only surfactant that displayed two endothermic transitions at 94 °C and 104 °C. The DSC heating scan of 12-2-12 and PLM images at 90 °C, 100 °C, and 110 °C are shown in Figure 5.6. Both thermal transitions corresponded to crystal-to-crystal transitions, and no liquid crystalline behavior or isotropic melting was observed. The DSC heating scan and PLM images at 90 °C and 110 °C for 16-2-16 are displayed in Figure 5.7. One endothermic transition was observed for 16-2-16 at 104 °C and corresponded to a crystal-to-crystal transition. The shoulder peak at 97 °C in Figure 5.7 did not correspond to any change in PLM, and above 106 °C the crystalline structure was not birefringent as shown in Figure 5.7 at 110 °C. Gemini surfactant 18-2-18 displayed a single endothermic transition at 105 °C. The heating DSC scan and PLM images of 18-2-18 at 90 °C and 110 °C are shown in Figure 5.8. The thermal transition at 105 °C corresponded to a crystal-to-crystal transition, and no thermotropic behavior or isotropic melting was observed.

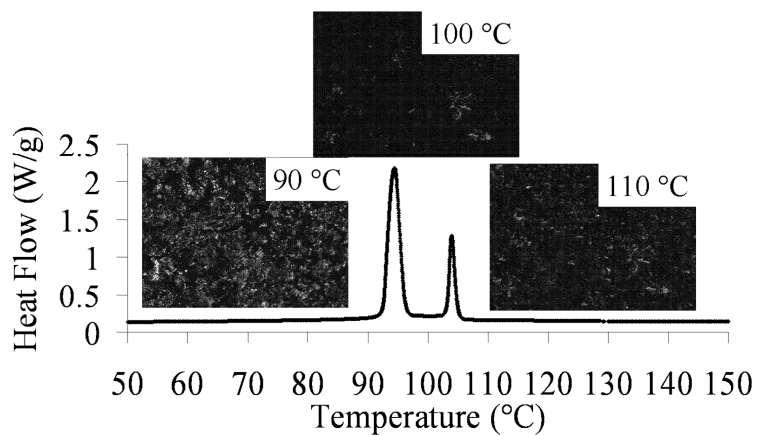


Figure 5.6 DSC of 12-2-12 and PLM images at 90 °C, 100 °C, and 110 °C.

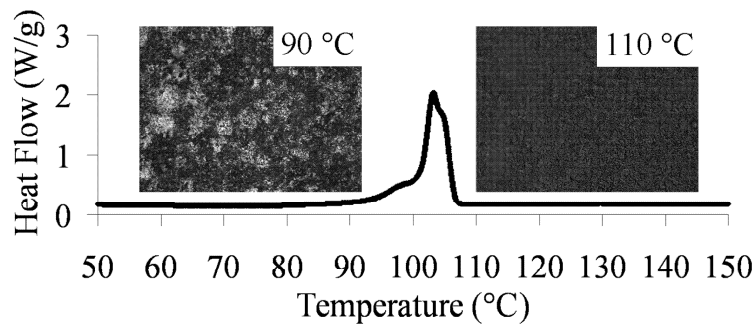


Figure 5.7 DSC of 16-2-16 and PLM images at 90 °C and 110 °C.

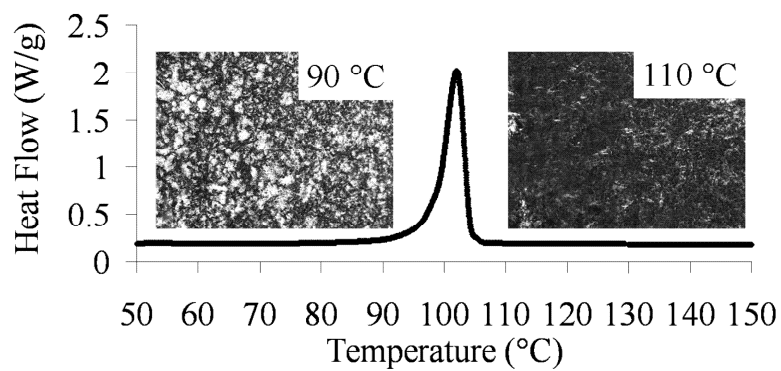


Figure 5.8 DSC of 18-2-18 and PLM images at 90 °C and 110 °C.

A single broad endothermic transition centered at 98 °C was observed for Acry-2-Acry shown in Figure 5.9. The PLM images at temperatures ranging from 80 °C to 110 °C are shown in Figure 5.10. Crystalline structure gradually developed from 80 °C until 104 °C when the structure changed and the crystalline regions subsided. Acry-2-Acry remained solid and did not exhibit any melting or liquid crystalline behavior. Cinn-2-Cinn had the highest endothermic transition at 143 °C shown in Figure 5.11, along with PLM images at 120 °C and 150 °C. The small transition at 95 °C in Figure 5.11 did not correspond to any observed changes in PLM. The thermal transition corresponded to an isotropic melting temperature at 143 °C, and above the clearing temperature no crystalline or liquid crystalline regions were observed, as shown in Figure 5.11 at 150 °C. The higher temperature transition of Cinn-2-Cinn was attributed to the bulkier tailgroups and π - π interactions limiting the mobility of the hydrocarbon tails.

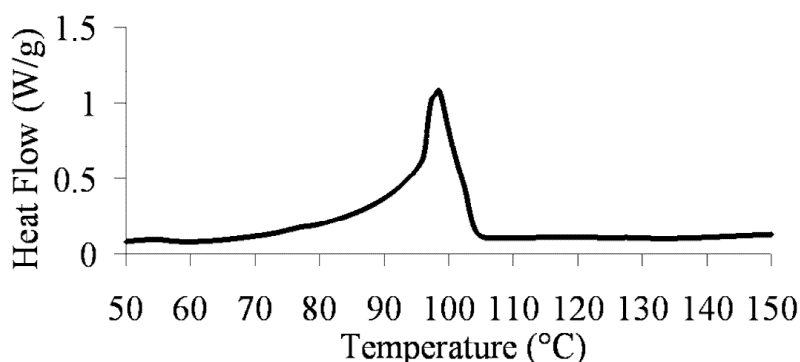


Figure 5.9 DSC heating scan of Acry-2-Acry

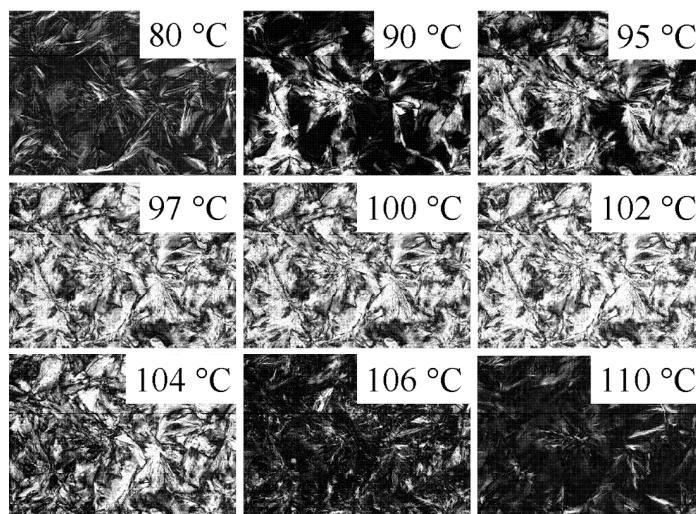


Figure 5.10 PLM images of Acry-2-Acry at 80 °C, 90 °C, 95 °C, 97 °C, 100°C, 102 °C, 104 °C, 106 °C, and 110 °C.

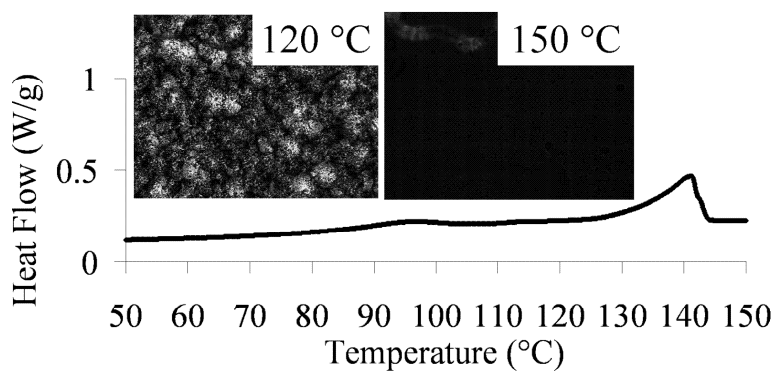


Figure 5.11 DSC of Cinn-2-Cinn and PLM images at 120 °C and 150 °C.

5.4.3 T_k conductance measurements

Conductance experiments measured the T_k values for the gemini surfactant series in Figure 5.1. T_k determines the applicable temperature range for surfactants and is dependent upon the surfactant composition, nature of the headgroup, length of the hydrocarbon tailgroup, and solvent environment.⁴⁷ The surfactant concentration in solution equals the critical micelle concentration (CMC) at T_k , and surfactants precipitate from solution as hydrated crystals at temperatures below T_k .²¹ The enthalpic driving forces overcome the energy barrier to micellization at T_k , turning the solution from cloudy to optically clear as surfactants micellize. A sharp increase in conductance is observed at T_k as surfactants and mobile counterions disperse in solution, and T_k is the temperature at which the conductance increases sharply and the solution becomes clear.

The surfactant concentration in solution equals the CMC at T_k , and theoretically, no T_k is observed at concentrations below the CMC.²¹ To explore the concentrations influence on T_k , the conductance was measured for 12-2-12 at concentrations of 0.005 wt%, 1.0 wt%, and 2.0 wt% in water, as shown in Figure 5.12. For 12-2-12 in water at 25 °C the reported CMC was 0.055 wt%.^{5,48} At 0.005 wt% ($C < \text{CMC}$) the solution was never cloudy and no change in conductance was detected. Below the CMC surfactants localize at the air/water interface to minimize interaction between hydrophobic tailgroups and the polar solvent.²¹ Surfactant concentration in solution did not change at concentrations below the CMC because surfactants were oriented at the air/water interface and not dispersed in solution, therefore, the conductance did not change with increasing temperature. The T_k was 15.8 °C and 15.7 °C for 12-2-12 in water at 1.0 wt% and 2.0 wt%, respectively, as shown in Figure 5.12. The measured T_k for 12-2-12 in

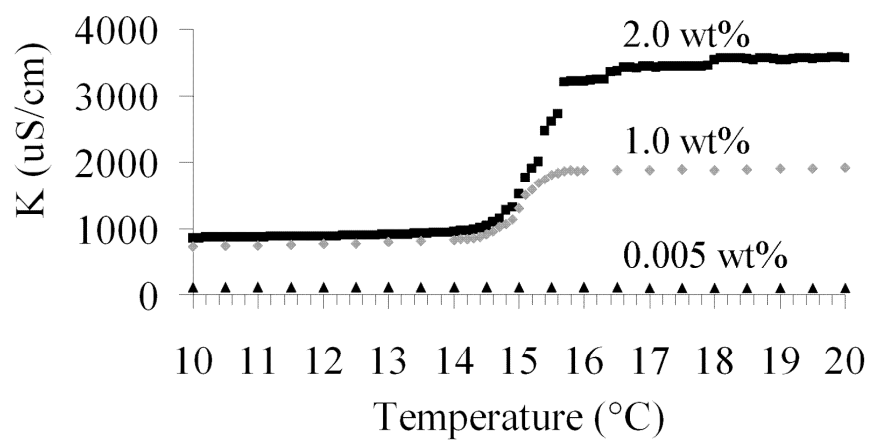


Figure 5.12 Determination of T_k , conductance vs. temperature for 12-2-12 in water at 0.005 wt%, 1.0 wt%, and 2.0 wt%.

water was slightly higher than the reported value of 14.4 °C.^{47,49} However, as expected the T_k was consistent and did not change at concentrations above the CMC. Above the CMC surfactants assemble into micelles at T_k , resulting in an increased conductivity due to the dispersion of ionic groups. The magnitude change in conductivity at T_k was greater for the 2.0 wt% solution due to the higher concentration of dispersed ions.

Table 5.1 lists the T_k values of the gemini surfactant series in water and water:methanol measured at 1.0 wt% for each solution. The cosolvent mixture of water:methanol was studied in an attempt to lower the T_k , and increase the surfactants applicable temperature range. The T_k increased with increasing tailgroup size in water and water:methanol. 12-2-12 displayed the lowest T_k at 15.8 °C and Cinn-2-Cinn the highest at 69.5 °C in water. A similar trend was evident in water:methanol, in which 12-2-12 had the lowest T_k at -17.0 and Cinn-2-Cinn the highest, 46.2 °C. The thermal energy required to disperse the crystalline structure increased as the tailgroup size increased. The bulky end-groups of Cinn-2-Cinn packed efficiently due to the planar cinnamate geometry and phenyl π - π stacking. The T_k was lower for all surfactants in water:methanol compared to water. Adding a cosolvent represents a strategy to increase the applicable temperature range of gemini surfactant solutions. The decreased T_k in water:methanol compared to water was attributed to the ability of methanol to more efficiently localize at the hydrophilic/hydrophobic interface providing more fluidity to the hydrocarbon chains, disrupting the tailgroup crystallinity.

Ammonium Gemini Surfactant	T_k (°C) Water	T_k (°C) Water:Methanol (1:1 vol)
12-2-12	15.8	- 17.0
Acry-2-Acry	26.0	- 2.80
16-2-16	44.4	31.8
18-2-18	57.5	42.9
Cinn-2-Cinn	69.5	46.2

Table 5.1 T_k of the ammonium gemini surfactant series in water and water:methanol (1:1 vol).

5.5 Conclusions

In situ FTIR spectroscopy was used to explore the influence of spacer length on the quaternization reaction rate for the synthesis of 12-2-12 and 12-6-12. Complete quaternization of 12-6-12 was completed after only 5 h, whereas 12-2-12 required 40 h. The electron donating character of hexamethylene increased the nucleophilicity of the unreacted amine, and decreased the reaction time required to complete quaternization.

DSC was correlated with PLM to explore the thermal transitions of the gemini surfactant series in Figure 5.1. DSC and PLM characterization were limited to 160 °C to prevent thermal degradation. Gemini 12-2-12 was the only surfactant that displayed two endothermic transitions at 94 °C and 104 °C. Both thermal transitions corresponded to crystal-to-crystal transitions, meaning 12-2-12 has three crystalline structures. One endothermic transition was observed for 16-2-16 and 18-2-18 at 104 °C and 105 °C, respectively, and each corresponded to a crystal-to-crystal transition. A single broad endothermic transition centered at 98 °C was observed for Acry-2-Acry, and Cinn-2-Cinn had the highest endothermic transition at 143 °C, which corresponded to an isotropic melting transition.

Conductance experiments were utilized to explore the influence of concentration and tailgroup composition on T_k in water and water:methanol. No change in conductance was measured and no T_k was observed for 12-2-12 at concentrations below the CMC. However, the T_k was consistent at concentrations above the CMC. The T_k of the gemini surfactant series was measured in water and water:methanol to explore the influence of solvent on the solution properties. The T_k increased with increasing tailgroup size in water and water:methanol. 12-2-12 displayed the lowest T_k at 15.8 °C and Cinn-2-Cinn

the highest at 69.5 °C in water. A similar trend was evident in water:methanol, in which 12-2-12 had the lowest T_k at -17.0 and Cinn-2-Cinn the highest at 46.2 °C. The T_k was lower for all surfactants in water:methanol compared to water because the cosolvent disrupted the crystalline packing of the gemini tailgroups. The addition of a cosolvent represents a strategy to increase the applicable temperature range for gemini surfactants.

5.6 Acknowledgments

This material is based upon work supported in part by the U.S. Army Research Office under grant number W911NF-07-1-0452 Ionic Liquids in Electro-Active Devices (ILEAD) MURI.

5.7 References

1. Hait, S. K.; Moulik, S. P., *Current Science* **2002**, 82 (9), 1101-1111.
2. Layn, K. M.; Debenedetti, P. G.; Prud'homme, R. K., *J. Chem. Phys.* **1998**, 109 (13), 5651-5658.
3. Menger, F. M.; Keiper, J. S., *Angew. Chem. Int. Ed.* **2000**, 39 (11), 1907-1920.
4. Xia, J.; Zana, R., Applications of Gemini Surfactants. In *Gemini Surfactants : Synthesis, Interfacial and Solution-Phase Behavior, and Applications*, Zana, R.; Xia, J., Eds. Marcel Dekker Inc: New York, 2004; pp 301-321.
5. Zana, R., *Adv. Colloid Interface Sci.* **2002**, 97 (1-3), 205-253.
6. Chen, L.; Xie, H.; Li, Y.; Yu, W., *Colloids Surf., A* **2008**, 330 (2-3), 176-179.
7. Zhou, M.; Nemade, P. R.; Lu, X.; Zeng, X.; Hatakeyama, E. S.; Noble, R. D.; Gin, D. L., *J. Am. Chem. Soc.* **2007**, 129 (31), 9574-9575.
8. Bakshi, M. S.; Sharma, P.; Banipal, T. S., *Mater. Lett.* **2007**, 61 (28), 5004-5009.
9. Lu, T.; Huang, J.; Li, Z.; Jia, S.; Fu, H., *J. Phys. Chem. B* **2008**, 112 (10), 2909-2914.
10. Bakshi, M. S.; Possmayer, F.; Petersen, N. O., *J. Phys. Chem. C* **2008**, 112 (22), 8259-8265.
11. Kirby, A. J.; Camilleri, P.; Engberts, J. B. F. N.; Feiters, M. C.; Nolte, R. J. M.; Soderman, O.; Bergsma, M.; Bell, P. C.; Fielden, M. L.; Garcia Rodriguez, C. L.; Guedat, P.; Kremer, A.; McGregor, C.; Perrin, C.; Ronsin, G.; van Eijk, M. C. P., *Angew. Chem. Int. Ed.* **2003**, 42 (13), 1448-1457.
12. Luciani, P.; Bombelli, C.; Colone, M.; Giansanti, L.; Ryhanen Samppa, J.; Saily, V. M. J.; Mancini, G.; Kinnunen Paavo, K. J., *Biomacromolecules* **2007**, 8 (6), 1999-2003.
13. Vongsetskul, T.; Taylor, D. J. F.; Zhang, J.; Li, P. X.; Thomas, R. K.; Penfold, J., *Langmuir* **2008**, 25 (7), 4027-4035.
14. Zana, R., *J. Colloid Interface Sci.* **2002**, 248 (2), 203-220.
15. Menger, F. M.; Littau, C. A., *J. Am. Chem. Soc.* **1993**, 115 (22), 10083-10090.
16. Pisarcik, M.; Polakovicova, M.; Pupak, M.; Devinsky, F.; Lacko, I., *J. Colloid Interface Sci.* **2008**, 329 (1), 153-159.
17. Wettig, S. D.; Li, X.; Verrall, R. E., *Langmuir* **2003**, 19 (9), 3666-3670.
18. Wang, X.; Wang, J.; Wang, Y.; Yan, H.; Li, P.; Thomas, R. K., *Langmuir* **2004**, 20 (1), 53-56.
19. Camesano, T. A.; Nagarajan, R., *Colloids Surf., A* **2000**, 167 (1-2), 165-177.
20. Li, Y.; Li, P.; Wang, J.; Wang, Y.; Yan, H.; Thomas, R. K., *Langmuir* **2005**, 21 (15), 6703-6706.

21. Evans, D. F.; Wennerstrom, H., Solutes and Solvents, Self-Assembly of Amphiphiles. In *The Colloidal Domain Where Physics, Chemistry, Biology, and Technology Meet*, 2 ed.; John Wiley & Sons, Inc: New York, 1999; pp 1-43.
22. Oda, R.; Huc, I.; Danino, D.; Talmon, Y., *Langmuir* **2000**, *16* (25), 9759-9769.
23. Sakai, K.; Kaji, M.; Takamatsu, Y.; Tsuchiya, K.; Torigoe, K.; Tsubone, K.; Yoshimura, T.; Esumi, K.; Sakai, H.; Abe, M., *Colloids Surf., A* **2009**, *333* (1-3), 26-31.
24. Yoshimura, T.; Ohno, A.; Esumi, K., *Langmuir* **2006**, *22* (10), 4643-4648.
25. Sumida, Y.; Masuyama, A.; Oki, T.; Kida, T.; Nakatsuji, Y.; Ikeda, I.; Nojima, M., *Langmuir* **1996**, *12* (16), 3986-3990.
26. Johnsson, M.; Engberts, J. B. F. N., *J. Phys. Org. Chem.* **2004**, *17* (11), 934-944.
27. Li, X.; Wettig, S. D.; Wang, C.; Foldvari, M.; Verrall, R. E., *Phys. Chem. Chem. Phys.* **2005**, *7* (17), 3172-3178.
28. Gin, D. L.; Bara, J. E.; Noble, R. D.; Elliott, B. J., *Macromol. Rapid Commun.* **2008**, *29* (5), 367-389.
29. Chern, C. S., *Prog. Polym. Sci.* **2006**, *31* (5), 443-486.
30. Lu, Y., *Angew. Chem. Int. Ed.* **2006**, *45* (46), 7664-7667.
31. Zhou, M.; Kidd, T. J.; Noble, R. D.; Gin, D. L., *Adv. Mater.* **2005**, *17* (15), 1850-1853.
32. Bara, J. E.; Kaminski, A. K.; Noble, R. D.; Gin, D. L., *J. Membr. Sci.* **2007**, *288* (1+2), 13-19.
33. Lu, X.; Nguyen, V.; Zhou, M.; Zeng, X.; Jin, J.; Elliott, B. J.; Gin, D. L., *Adv. Mater.* **2006**, *18* (24), 3294-3298.
34. Sievens-Figueroa, L.; Guymon, C. A., *Chem. Mater.* **2009**, *21* (6), 1060-1068.
35. Yan, F.; Texter, J., *Adv. Colloid Interface Sci.* **2006**, *128-130*, 27-35.
36. Abe, M.; Tsubone, K.; Koike, T.; Tsuchiya, K.; Ohkubo, T.; Sakai, H., *Langmuir* **2006**, *22* (20), 8293-8297.
37. Abe, M.; Koike, T.; Nishiyama, H.; Sharma, S. C.; Tsubone, K.; Tsuchiya, K.; Sakai, K.; Sakai, H.; Shchipunov, Y. A.; Schmidt, J.; Talmon, Y., *J. Colloid Interface Sci.* **2009**, *330* (1), 250-253.
38. Caillier, L.; Taffin de Givenchy, E.; Levy, R.; Vandenberghe, Y.; Geribaldi, S.; Guittard, F., *J. Colloid Interface Sci.* **2009**, *332* (1), 201-207.
39. Pasquale, A. J.; Allen, R. D.; Long, T. E., *Macromolecules* **2001**, *34* (23), 8064-8071.
40. Lizotte, J. R.; Long, T. E., *Macromol. Chem. Phys.* **2004**, *205* (5), 692-698.
41. Layman, J. M.; Borgerding, E. M.; Williams, S. R.; Heath, W. H.; Long, T. E., *Macromolecules* **2008**, *41* (13), 4635-4641.
42. In, M.; Zana, R., *J. Dispersion Sci. Technol.* **2007**, *28* (1), 143-154.
43. Xie, W.; Gao, Z. M.; Pan, W. P.; Hunter, D.; Singh, A.; Vaia, R., *Chem. Mater.* **2001**, *13* (9), 2979-2990.
44. Unal, S. Synthesis and characterization of branched macromolecules for high performance elastomers, fibers, and films. Virginia Tech, Blacksburg, VA, 2005.
45. Xie, W.; Xie, R.; Pan, W.-P.; Hunter, D.; Koene, B.; Tan, L.-S.; Vaia, R., *Chem. Mater.* **2002**, *14* (11), 4837-4845.
46. Fuller, S.; Shinde, N. N.; Tiddy, G. J. T.; Attard, G. S.; Howell, O., *Langmuir* **1996**, *12* (5), 1117-1123.

47. Zana, R., *J. Colloid Interface Sci.* **2002**, 252 (1), 259-261.
48. Espert, A.; v. Klitzing, R.; Poulin, P.; Colin, A.; Zana, R.; Langevin, D., *Langmuir* **1998**, 14 (15), 4251-4260.
49. Zhao, J.; Christian, S. D.; Fung, B. M., *J. Phys. Chem. B* **1998**, 102 (39), 7613-7618.

Chapter 6: Influence of Hydrogen Bonding on the Adhesive Properties of Photo-curable Acrylics

Cashion, M.P.; Park, T.; Long, T.E. *Journal of Adhesion* (2009), 85(1), 1-17.

6.1 Abstract

Novel hot melt pressure sensitive adhesives were developed from acrylic terpolymers of 2-ethylhexyl acrylat, 2-hydroxyethyl acrylate (HEA), and methyl acrylate (MA) functionalized with hydrogen bonding and photo-reactive functionalities. The hydrogen bonding and photo-reactive sites were introduced from the reaction of HEA repeat units with cyclohexyl isocyanate and cinnamoyl chloride, respectively. The functionalization reaction conditions were optimized to tailor the degree of urethane and cinnamate groups in order to examine the influence of hydrogen bonding and photo-active groups in low T_g acrylics. The synergy of hydrogen bonding and photo-reactivity resulted in higher peel values and rates of cinnamate photo-reactivity with increasing urethane concentration. The increase in cinnamate photo-reactivity with increasing urethane concentration provides evidence that hydrogen bond associations can promote cinnamate dimerization. Isothermal rheological experiments conducted at 150 °C confirmed the melt stability of the cyclohexyl urethane linkage, cinnamate, and the acrylic composition indicating the potential for hot melt adhesive applications.

6.2 Introduction

Pressure sensitive adhesives (PSAs) bond to a variety of substrates with very low pressure applied for short periods.¹ PSAs are widely used in electronic devices, tapes, labels, medical devices, and the automotive industry.¹⁻³ PSA formulations are soft materials that are inherently tacky at room temperature, and the viscoelastic nature of the adhesive defines the balance between adhesive and cohesive performance. Sufficient adhesive performance requires adequate mechanical strength to resist creep and prevent cohesive failure.

PSAs applied in the molten state in the absence of solvent are termed hot melt pressure sensitive adhesives (HMPSAs).⁴ The exclusion of solvent makes HMPSAs more economically and environmentally advantageous, and furthermore, application in the melt increases production efficiency and eliminates drying steps, reducing energy consumption. HMPSAs are designed to provide tack without the use of activators such as water, solvent, or heat. The bulk properties that make HMPSAs desirable for processing also limit their adhesive performance.⁵ Low viscosities are required at processing temperatures and during application to facilitate spreading and intimate contact with the substrate. Adhesive performance is inferior at molecular weights that are suitable for melt processing due to insufficient chain entanglements. Molecular cohesion is a material's internal resistance to failure, and the mechanical and physical properties of adhesives are dependent upon chain cohesion.^{6,7} Post processing strategies to increase molecular weight and cohesion include covalent crosslinking,^{8,9} physical crosslinking,^{5,10-12} and the addition of tackifiers.¹³

Future strategies are required to incorporate the desirable properties of acrylic HMPSAs exploiting facile synthetic procedures. Acrylics offer a wide application temperature, resistance to oxidation and UV-light degradation, optical clarity, and long term durability.¹⁴ Moreover, acrylic formulations exhibit adhesive properties without the use of additives. This manuscript describes the photo-curing of associated acrylic architectures for HMPSA applications. The association of macromolecules through noncovalent interactions is accomplished through functionality that facilitates the formation of ionic interactions,¹⁰ donor-acceptor complexes,¹⁵ hydrogen bonding,¹⁶ liquid crystalline behavior,¹⁷ and the self-assembly of amphiphilic polymers.¹⁸ Hydrogen bonding is a versatile scaffold for noncovalent associations. Hydrogen bonding functionality is prevalent in biological systems, readily accessible in rational synthesis, and the associations are reversible.

Association of hydrogen bonding groups provides a method to increase the apparent molecular weight after application, and temperatures above the hydrogen bonding dissociation temperature result in low viscosities for melt processing. Poly(acrylic acid) (PAA) is the most published source of hydrogen bonding functionality incorporated in PSA formulations.^{8,19} Hydrogen bonding between carboxylic groups forms cyclic dimers, or linear associations in a *face-on* or lateral fashion.²⁰ However, PAA can thermally crosslink, and intermolecular anhydrides form at temperatures greater than 150 °C.²¹ Crosslinking during processing is not desirable in hot melt applications, and acrylic acids offer only limited utility.

Hydrogen bonding urethane functionality is commonly used for curing PSA precursors.^{22,23} Asahara et al.²⁴ crosslinked poly(ethyl acrylate (EA)-*co*-2-ethylhexyl

acrylate (EHA)-*co*-2-hydroxyethyl methacrylate (HEMA)) random copolymers with an isocyanate end-capped urethane oligomer. Reaction of the primary hydroxyl groups of HEMA with the isocyanate functionalized oligomer developed a network structure. The urethane groups were incorporated exclusively during crosslinking, and the consumption of isocyanate groups correlated to the degree of crosslinking. The peel performance depended upon the duration and temperature of curing, as well as the crosslinker concentration. Asahara and coworkers concluded that lower urethane concentrations yielded higher peel strengths.

Functionality that facilitates electron beam²⁵ or photo-crosslinking²⁶ are popular curing strategies for HMPSAs. Photo-curing is a prevalent crosslinking mechanism that is employed to increase the molecular weight and cohesive strength of HMPSAs. Photo-curing associated macromolecular architectures has received significant interest in the layer-by-layer (LBL) assembly of multilayer thin films,²⁷ formation of supramolecular nanostructures,²⁸ and formation of liquid crystalline polymers.²⁹ Recently, methacrylate photo-active groups were incorporated at the periphery of well-defined four-arm star-shaped poly(D,L-lactide)s and photo-crosslinked producing biologically compatible networked films.^{30,31} Photo-curing offers solvent-free processes, rapid rates of crosslinking, and does not require drying steps, which suggests an economical and efficient process. Crosslinking occurs only during UV-exposure, therefore, controlling the degree of crosslinking with UV-dose. The crosslinker concentration and composition determine the mechanical and adhesive properties of HMPSAs.

Conventional photo-curable strategies employ chain-like reactions initiated with reactive radicals^{6,32} or cations.³³ Chain-like reactive groups typically absorb at high-

energy wavelengths. Photo-initiators that absorb at longer wavelengths are utilized to limit exposure to high energy light and reduce the energy requirements for curing. Homogeneous curing of chain-like photo-crosslinking reactions is difficult due to the limited diffusion of the photo-initiator and oxygen inhibition. In the 1950's, Minsk and coworkers were the first to study the photo-dimerization of cinnamate groups.³⁴ Minsk and researchers reported the photo-initiated crosslinking reaction of cinnamate groups in poly(vinyl cinnamate). The photochemistry of cinnamates involves two photo-reactions upon UV-irradiation, i.e. the trans-cis isomerization and photo-dimerization.³⁵ Photo-dimerization involves the $[2\pi + 2\pi]$ cycloaddition of cinnamates in the head-to-head or head-to-tail configuration to form cyclobutane. Other photo-reactive groups that photo-dimerize in a $[2\pi+2\pi]$ cycloaddition include furans,³⁶ maleimides,³⁷ chalcones,³⁸ and coumarins.³⁹ Since Minsk's initial discovery, the cinnamate functionality has received interest in polymeric and low molar mass reactions as a robust chromophore capable of photo-dimerizing in the presence of oxygen.⁴⁰

In this study, low T_g acrylic random copolymers were functionalized with urethane and cinnamate functionalities to introduce a novel combination of hydrogen bonding and photo-curable substituents, respectively. To the best of our knowledge, there is not a literature precedence describing the use of hydrogen bonding and cinnamate photo-active groups in the development of acrylic HMPSAs. The degree of urethane and cinnamate functionality was varied to systematically study the adhesive and mechanical properties as a function of composition.

6.3 Materials and Methods

6.3.1 Materials

2-Ethylhexyl acrylate (EHA), 2-hydroxyethyl acrylate (HEA), methyl acrylate (MA), azobisisobutyronitrile (AIBN), tetrahydrofuran (THF), ethyl acetate, toluene, cinnamoyl chloride, cyclohexyl isocyanate, and triethylamine were received from Sigma-Aldrich. AIBN was recrystallized twice from methanol. Cinnamoyl chloride was sublimed producing white crystals and cyclohexyl isocyanate was used without further purification. Triethylamine was distilled from CaH₂. Reagent grade THF was passed through a PURE SOLV MD-3 Solvent Purification System (Innovative Technology Inc., Newburyport, MA) immediately prior to use. All reactions were purged with argon and performed under an argon atmosphere in flame-dried glassware.

6.3.2 Instrumentation.

Size exclusion chromatography (SEC) was performed on a Waters (Milford, MA) instrument equipped with 3 in-line Polymer Laboratories PLgel 5 μm MIXED-C columns with a Waters 717 autosampler. SEC characterization was conducted at 40 °C in THF (ACS grade) at a flow rate of 1 mL min⁻¹. A triple detection system included a Waters 2414 refractive index detector, Viscotek (Houston, TX) 270 Dual Detector viscometer, and Wyatt Technologies (Santa Barbara, CA) miniDAWN multiangle laser light scattering (MALLS) detector. Refractive index increments (dn/dc) values were determined online. Reported molecular weights were calculated from light scattering.

¹H NMR spectroscopy was performed on a Varian (Palo Alto, CA) Unity 400 MHz spectrometer in CDCl₃ at 25 °C. Differential scanning calorimetry (DSC) was performed on a TA Instruments (New Castle, DE) DSC 1000 under a nitrogen flush at a

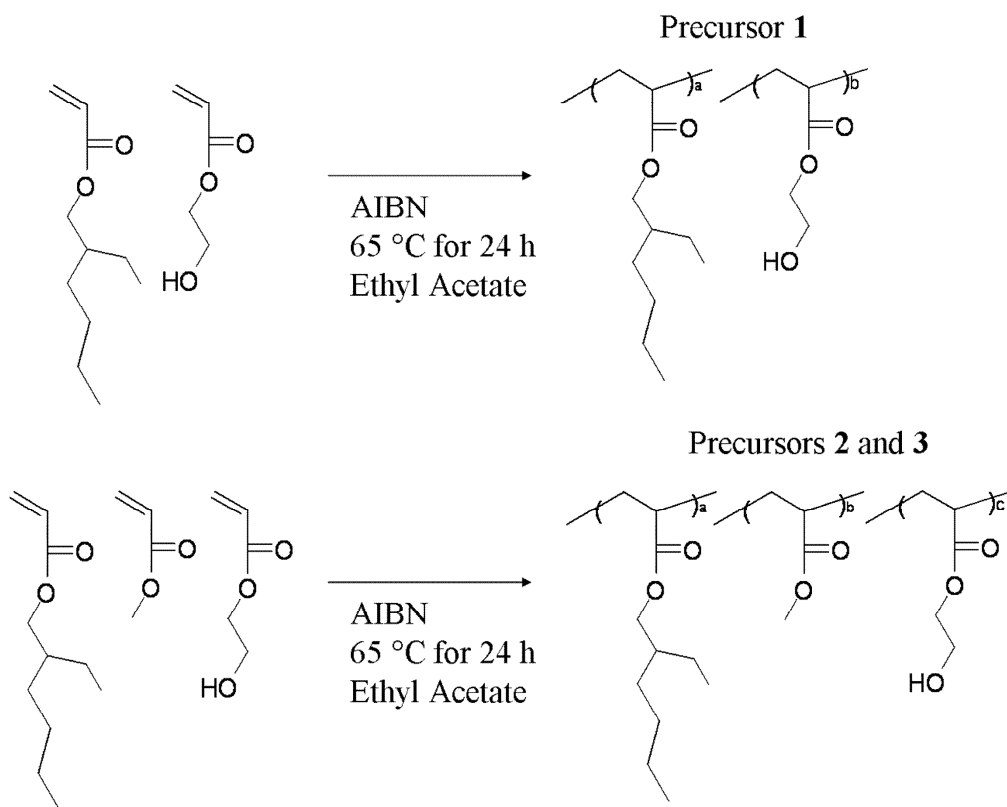
heating rate of 10 °C/min. The glass transition temperature (T_g) was determined as the midpoint of the glass transition endotherm of the 2nd heat cycle. FTIR spectroscopy was performed on a MIDAC M-1700 FTIR (Costa Mesa, CA) with Durascope single bounce diamond ATR. An Analytical Instrument Systems Inc. (Flemington, NJ) UV-spectrometer equipped with fiber optic cables, a DT1000CE light source, and an Ocean Optics USB2000 UV-Vis detector was used to determine the rate of cinnamate photodimerization. Ellipsometry measurements were performed on a phase modulation ellipsometer (Beaglehole Instruments, Wellington, New Zealand) at $\lambda = 632.8$ nm (HeNe laser). The cross section of the laser beam was approximately 1 mm². Measurements were performed in air.

6.3.3 Synthesis of Acrylic Precursor Copolymers 1-3

The synthesis of precursors **1-3** is shown in Scheme 6.1. AIBN (0.80 g, 4.87 mmol) was dissolved in ethyl acetate (133 mL) in a 500-mL, round-bottomed flask equipped with a magnetic stir bar. EHA, HEA, and MA were added to the reaction flask using a degassed syringe. The reaction flask was placed in a 65 °C bath for 24 h. Precipitation into hexanes and subsequent drying afforded the final isolated product. The composition of precursor copolymer **1** contained poly(EHA)-*co*-hydroxyethyl acrylate (HEA) (82-18 mol%). Precursor terpolymer **2** contained poly(EHA-*co*-HEA-*co*-methyl acrylate (MA)) (60-24-16 mol %), and precursor terpolymer **3** contained poly(EHA-*co*-HEA-*co*-MA) (64-14-22 mol%).

6.3.4 Synthesis of Cinn1, Cinn2, and Cinn3: Cinnamate Functionalization of Precursors 1-3

The precursor (15 g) was dissolved in dichloromethane (60 g, 20 wt%) in a two-necked, 250-mL, round-bottomed flask equipped with a magnetic stir bar. Cinnamoyl chloride, in a 1:1 molar equivalence to HEA in the precursor, was added to a 50-mL round-bottomed flask covered with aluminum foil and dissolved in dichloromethane (10



Scheme 6.1 Synthesis of acrylic precursors 1-3.

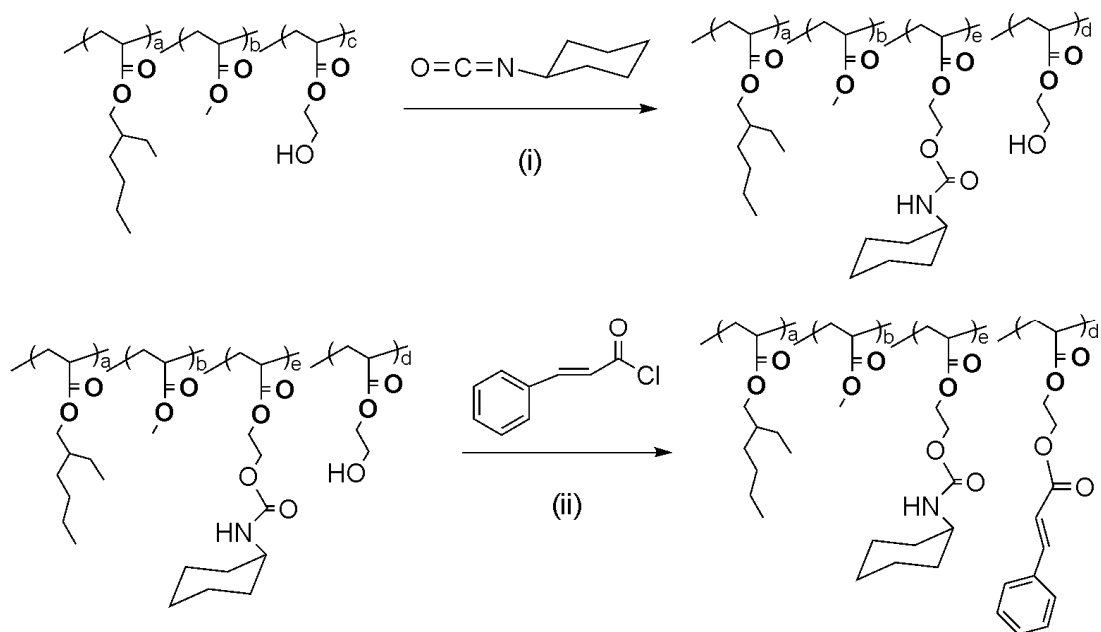
mL). Triethylamine, in a 1:1 molar equivalence to cinnamoyl chloride, was added to the reaction flask using a purged syringe. Next, the reaction flask was covered in aluminum foil and equipped with an addition funnel that was wrapped in aluminum foil. The reaction flask was placed in an ice bath. The cinnamoyl chloride solution was introduced into the addition funnel using a degassed syringe. The cinnamoyl chloride solution was added drop-wise to the reaction flask at 0 °C. The reaction continued to stir at 0 °C for 2 h, and the product was finally precipitated into methanol and vacuum dried. The cinnamate-functionalized copolymers were characterized with ¹H NMR, IR, SEC, and DSC.

6.3.5 Synthesis of Ureth2: Urethane Functionalization of Precursor 2

Precursor **2** (20 g) was dissolved in toluene (30g, 40 wt%) in a 250-mL, round-bottomed flask equipped with a magnetic stir bar. Next, cyclohexyl isocyanate was added in the desired molar ratio compared to HEA, and 0.2 mL of 1 wt% di-*n*-butyltin-dilaurate in toluene was added. The charged molar ratio of cyclohexyl isocyanate to HEA depended on the desired degree of urethane functionalization. A condenser was attached and the reaction was conducted at 50 °C for 8 h. After 8 h, the reaction mixture was precipitated into methanol and the precipitant was vacuum dried. **Ureth2** was characterized with ¹H NMR, IR, SEC, and DSC.

6.3.6 Synthesis of UrethCinn2: Cinnamate Functionalization of Ureth2

Scheme 6.2 displays the urethane and cinnamate functionalization of precursor **2**. **Ureth2** (15 g) was dissolved in dichloromethane (60 g, 20 wt%) in a two-necked, 250-mL, round-bottomed flask equipped with a magnetic stir bar. Cinnamoyl chloride, in a 10:1 molar equivalence to HEA of **Ureth2**, was added to a 50-mL round-bottomed flask



Scheme 6.2 Synthesis of **UrethCinn2**, the urethane, and cinnamate functionalization of precursor 2, (i) 0.2 mL of 1 wt% di-n-butyltin-dilaurate in toluene, 40 wt% solids in toluene, 50 °C, (ii) triethylamine, 20 wt% solids in dichloromethane, 0 °C.

covered with aluminum foil and dissolved in dichloromethane (10 mL). Triethylamine, in a 1:1 molar equivalence to cinnamoyl chloride, was added to the reaction flask using a purged syringe. Next, the reaction flask was covered in aluminum foil and equipped with an addition funnel that was wrapped in aluminum foil. The reaction flask was placed in an ice bath. The cinnamoyl chloride solution was introduced into the addition funnel using a degassed syringe. The cinnamoyl chloride solution was added drop-wise to the reaction flask at 0 °C. The reaction continued to stir at 0 °C for 2 h, and the product was precipitated into methanol and vacuum dried. **UrethCinn2** was characterized with ¹H NMR, IR, SEC, and DSC.

6.3.7 Peel Analysis

The functionalized acrylic (10 g) was dissolved in toluene (15 g, 40 wt %). A foot long strip of 8 in. wide backing paper was cleaned with acetone and isopropanol and heated to 80 °C for 30 min. The functionalized acrylic film was drawn in a controlled manner on the backing paper using a 3 in. wide doctor blade to an average thickness of 21 μm. The film was placed in the oven at 80 °C for 30 min. and ramped to 120 °C for 5 min. Irradiated samples were cured at 10 ft/min. on a Fusion UV (Gaithersburg, MD) model LC-6B benchtop conveyor equipped with a 100 W high pressure mercury lamp. Light intensities were measured using an EIT Inc. (Sterling, VA) UV power puck. UV-dosages were measured at UVA: 0.181±0.013 J/cm² and UVB: 0.147±0.05 J/cm² for 10 s of irradiation. Peel analysis was performed on a ChemInstruments Adhesion/Release Tester AR-1000 (Fairfield, Ohio). Films were cut into 0.75 in. widths, and pressed onto ChemInstrument Inc. 2x8 in. stainless steel plates with a 1 kg rubber roller. The 90° peel test were performed at 25 °C at a rate of 12 in/min. Reported peel values are an average

of five tapes per sample. Peel values are reported in lb_f/in, corresponding to the peeling force per width of tape.

6.3.8 Rate of Cinnamate Photo-dimerization and Gel Fraction Analysis

A quartz slide (1" x 1") was washed with acetone, isopropanol, and THF. The control or urethane sample (0.96 g) was dissolved in toluene (8.64 g) at 10 wt%. The solution was spin cast onto a square quartz slide (1" x 1") at 2000 rpm for 1 min. The UV-vis absorbance of the film was measured before UV-exposure. The coated slide was then irradiated for 10 s, 30 s, 60 s, 90 s, 120 s, 150 s, 180 s, 210 s, 240 s, and 270 s and the UV-vis absorbance was measured after each exposure. Gel fractions were determined for UV-cured and non-cured films. Soxhlet extraction was performed in refluxing THF for 12 h on UV-cured films irradiated for 10 s and non-cured films.

6.4 Results and Discussion

6.4.1 Synthesis and Peel Performance of Cinn1, Cinn2, and Cinn3

The composition of the precursor copolymers included EHA, HEA, and MA. EHA was included to provide a low T_g segment for increased tack, HEA provided a functionalizable site, and MA provided a higher T_g segment to decrease the molecular weight necessary to achieve chain entanglements and provide increased cohesive strength.⁴¹ Table 6.1 compares the composition, molecular weight, and T_g of acrylic precursors **1-3**. The compositions were tailored for a T_g -50 °C and M_w 100,000.

All three precursors were functionalized with cinnamate groups to explore HEA's reactivity as a function of composition. All precursors were functionalized with cinnamate groups from the acid chloride reaction of HEA repeating units with cinnamoyl chloride. Characterization following cinnamate functionalization was performed using NMR spectroscopy, FTIR, DSC, and SEC analysis. ¹H NMR analysis of the cinnamate functionalized precursor confirmed the appearance of cinnamate resonances at 6.51, 7.38, 7.57, and 7.73 ppm. The resonance at 3.78 ppm corresponding to the methylene adjacent to the ester of HEA units diminished, and a new resonance at 4.35 ppm corresponding to the methylene adjacent to the ester of cinnamoyloxyethyl acrylate (CEA) appeared. Following cinnamate functionalization, the FTIR spectrum displayed characteristic cinnamate bands at 1637 cm^{-1} and 980 cm^{-1} , corresponding to the cinnamates vinyl C=C stretching vibration and *trans*-vinylene C-H deformation.⁴² Cinnamate functionalization resulted in an average molecular weight increase of 36%, despite all efforts to avoid spurious light, the molecular weight increase was attributed to premature intermolecular dimerization of the cinnamate sites. As expected, the T_g of all samples increased

Precursor	EHA (mol%)	HEA (mol%)	MA (mol%)	M _w (PDI)	T _g (°C)
1	82	18	-	111,000 (2.81)	-50
2	60	24	16	114,000 (2.59)	-44
3	64	14	22	105,000 (2.04)	-45

Table 6.1 Composition, molecular weight, and T_g comparison of precursors **1-3**.

following cinnamate functionalization due to the incorporation of planar bulky cinnamate groups.

The reactivity of HEA's primary hydroxyl groups was examined as a function of precursor composition. A molar equivalence of cinnamoyl chloride to HEA for each precursor was charged. Precursor **2** achieved the highest degree of functionalization, with 46% of HEA groups reacting to form CEA. Precursor **1** only converted 33% of HEA groups to CEA, corresponding to the lowest degree of functionalization, and 36% of HEA groups in precursor **3** were reacted to form CEA. The degree of HEA functionalization directly correlated to the concentration of bulky EHA units. Precursor **1** contained 82 mol% EHA and **2** possessed 60 mol% EHA, indicating the bulky EHA groups sterically hindered the reactivity of HEA hydroxyl groups.

Table 6.2 displays the UV-cured 90° peel strength of **Cinn1**, **Cinn2**, and **Cinn3**. UV-dosage was held constant for each film, and **Cinn1**, **Cinn2**, and **Cinn3** had average film thicknesses of $20 \pm 3 \mu\text{m}$, $22 \pm 2 \mu\text{m}$, and $21 \pm 4 \mu\text{m}$, respectively. **Cinn2** exhibited the highest peel value of 0.477 lb_f/in, and **Cinn3** exhibited the lowest peel value of 0.167 lb_f/in. All UV-cured samples failed adhesively, and non-cured films failed cohesively. The difference in failure mode between cured and non-cured films indicated intermolecular cinnamate crosslinking occurred during UV-exposure increasing the molecular weight and cohesive strength.

Sample Name	EHA (mol%)	HEA (mol%)	MA (mol%)	CEA (mol%)	M_w (PDI)	UV-Irradiated Peel (lb_f / in)	stdev
Cinn1	82	12	-	6	158000 (3.91)	0.199	0.006
Cinn2	60	13	16	11	141000 (5.18)	0.477	0.006
Cinn3	64	9	22	5	148000 (2.00)	0.167	0.004

Table 6.2 Composition, molecular weight, and UV-cured 90° peel strength of **Cinn1**, **Cinn2**, and **Cinn3**.

6.4.2 Hydrogen Bonding and Photo-active sites in Low T_g Acrylics

Precursor **2** was functionalized with urethane (**2U₂₄**) or cinnamate (**2C₂₄**) groups. **2U₂₄** indicates 100% of HEA groups were functionalized with cyclohexyl isocyanate and **2C₂₄** designates 100% of HEA groups were reacted with cinnamoyl chloride, and NMR spectroscopy confirmed that residual HEA units did not remain in the copolymers. Following complete urethane functionalization (**2U₂₄**) the M_w 145,000 (2.08) and T_g -18 °C. Adhesive **2C₂₄** had a M_w 188,000 (3.08) and T_g -30 °C.

Precursor **2** was functionalized with both urethane and cinnamate groups to investigate the influence of hydrogen bonding sites on the peel performance and cinnamate photo-reactivity. Optimized reaction conditions afforded the opportunity to incorporate cinnamate and urethane groups in the same precursor and control the degree of functionalization, as shown in Scheme 6.2. The composition, molecular weight, and T_g of the urethane series are displayed in Table 6.3. Urethane functionalization was conducted at 50 °C for 8 h, and the molar equivalence of cyclohexyl isocyanate charged determined the degree of urethane functionalization. For example, charging a ten molar excess of cyclohexyl isocyanate relative to HEA achieved 100% functionalization. Cinnamate functionalization was conducted for 2 h at 0 °C, and complete cinnamate functionalization was achieved with a ten molar excess of cinnamoyl chloride to residual HEA units.

Sample Name	EHA (mol%)	MA (mol%)	UEA (mol%)	CEA (mol%)	M _w (PDI)	T _g (°C)
2C ₂₄	60	16	-	24	188,000 (3.08)	-30
2U ₈ C ₁₆	60	16	8	16	129,000 (4.59)	-27
2U ₁₂ C ₁₂	60	16	12	12	152,000 (3.39)	-25
2U ₁₇ C ₇	60	16	17	7	136,000 (3.56)	-23
2U ₂₁ C ₃	60	16	21	3	150,000 (4.30)	-21
2U ₂₄	60	16	24	-	145,000 (2.08)	-18

Table 6.3 Composition, molecular weight, and T_g of the urethane series (UEA: 2-(cyclohexylcarbamoyloxy)ethyl acrylate (urethane ethyl acrylate)).

For hot melt applications, it is essential that the photocrosslinker and PSA composition are melt stable. The cinnamate chromophore is thermally stable to 200 °C.⁴³ Cyclohexyl carbamate was incorporated as hydrogen bonding functionality due to its lack of UV-light absorption and excellent thermal stability. Figure 6.1 displays the isothermal melt rheology of **2U₂₁C₃** at 150 °C for 2 h. The complex viscosity was constant over the entire time range, which indicated the melt stability of the acrylic composition.

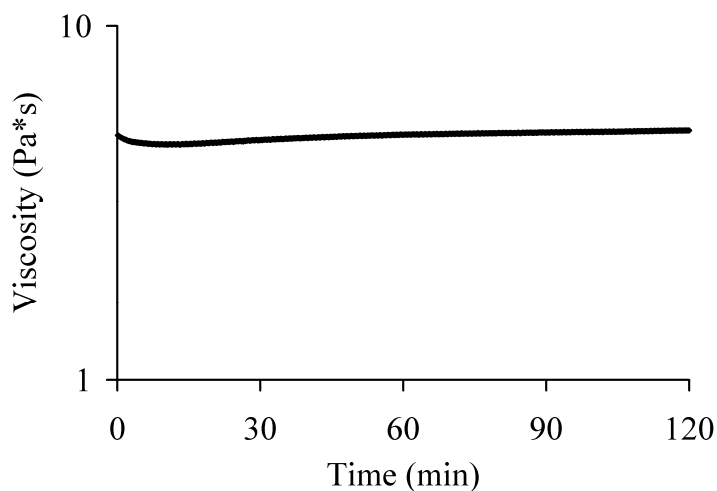


Figure 6.1 Isothermal melt rheology of **2U₂₁C₃** at 150 °C for 2 h.

The UV-cured and non-cured peel analysis and failure modes of the urethane series are displayed in Table 6.4. The UV-cured and non-cured peel strengths of **2U₂₄** were within error at 1.22 ± 0.159 lb_f/in and 1.34 ± 0.147 lb_f/in, respectively, and exhibited the same mode of failure, indicating the cyclohexyl urethane linkage and PSA composition were UV-stable. **2U₂₁C₃** displayed the largest UV-cured and non-cured peel values, 1.03 lb_f/in. and 1.64 lb_f/in., respectively. The UV-cured peel strength decreased as the concentration of cinnamate increased, resulting from an increased crosslink density elevating the modulus and T_g, which prevented the adhesive from spreading on the

Sample Name	UV-Irradiated Peel (lb_f/in)	stdev	Failure Mode	Non-cured Peel (lb_f/in)	stdev	Failure Mode
2C₂₄	0.418	0.016	100 % adhesive	0.844	0.008	100 % cohesive
2U₈C₁₆	0.731	0.014	100 % adhesive	1.59	0.028	85 % cohesive
2U₁₂C₁₂	0.855	0.017	100 % adhesive	1.49	0.021	75% cohesive
2U₂₁C₃	1.03	0.026	100 % adhesive	1.64	0.013	60 % cohesive
2U₂₄	1.22	0.159	50 % cohesive	1.34	0.147	50 % cohesive

Table 6.4 UV-cured and non-cured 90° peel strength of the urethane series.

substrate.⁴⁴ All UV-cured tapes containing cinnamate groups failed 100% adhesively. Complete adhesive failure of the UV-cured films was attributed to the intermolecular dimerization of cinnamate groups leading to an increased molecular weight and network structure formation. The degree of adhesive failure for non-cured tapes was dependent upon the concentration of urethane functionality. As the degree of urethane functionality increased, the percentage of adhesive failure increased. Non-cured **2C₂₄**, which did not contain urethane sites, failed 100% cohesively, and **2U₂₄**, which contained only urethane functionality, exhibited the highest non-cured proportion of adhesive failure, 50%. Increasing adhesive failure with urethane concentration was attributed to an increase in apparent molecular weight resulting from the association of hydrogen bonding urethane groups.

6.4.3 Influence of Hydrogen Bonding Sites on the Rate of Cinnamate Photo-dimerization

Figure 6.2 displays the structure and composition of the urethane and control series. The control series consisted of precursor **2** functionalized only with cinnamate sites, with residual HEA groups remaining. The compositions of the urethane and control series had comparable concentrations of cinnamate groups in order to investigate the influence of hydrogen bonding groups on the rate and efficiency of cinnamate photo-reactivity. Both the urethane and control series contained 60 mol% EHA and 16 mol% MA.

UV-vis spectroscopy was used to investigate the influence of hydrogen bonding associations on the rate of cinnamate photo-reactivity in the solid state. Urethane and control series films were spin coated on quartz slides from 10 wt% solutions in toluene,

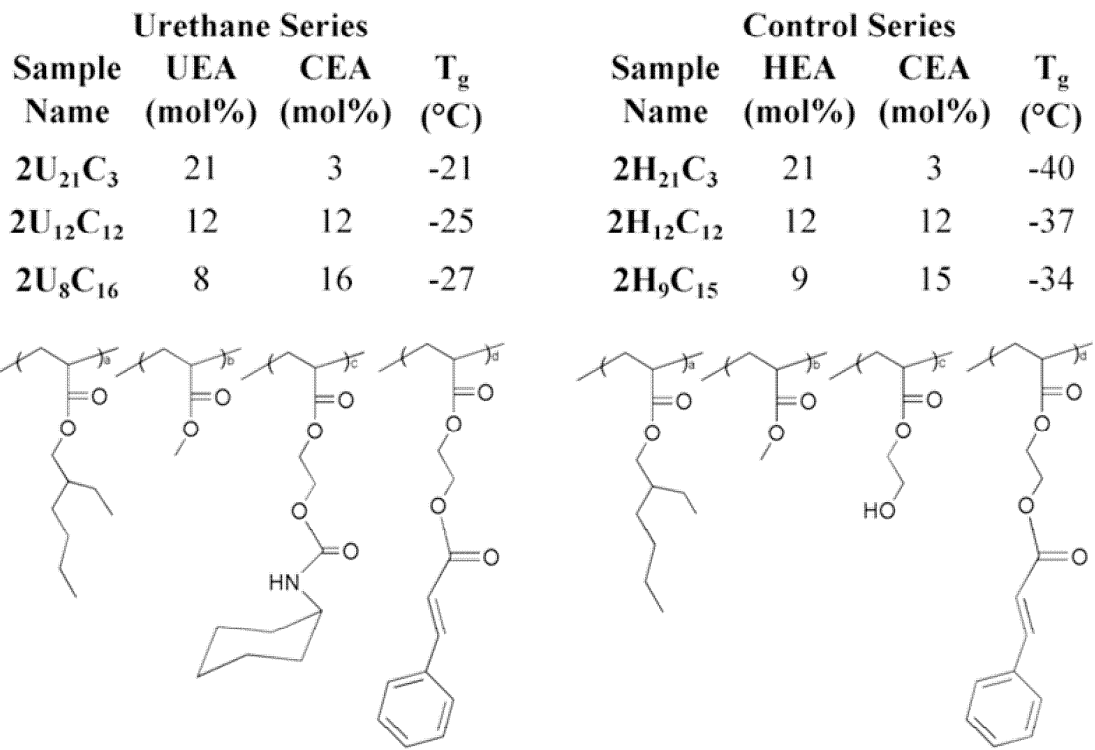


Figure 6.2 Composition and structure of the urethane and control series. Both the urethane and control series contained 60 mol% EHA and 16 mol% MA.

to a thickness of $1.0 \pm 0.14 \mu\text{m}$. The films were spin cast to control film thickness and uniformity. The cinnamate chromophore absorbed 275 nm light, as seen in Figure 6.3 for $2\text{U}_{21}\text{C}_3$. Neither precursor **2** or $2\text{U}_{21}\text{H}_3$, 21 mol% urethane and 3 mol% HEA, absorbed UV-light. Urethane and control films were exposed to UV-light for periods of 10 s, 30 s, 60 s, 90 s, 120 s, 150 s, 180 s, 210 s, 240 s, and 270 s. Decreasing cinnamate UV-absorbance was monitored with an increase in UV-exposure. The decrease in cinnamate absorbance with increasing UV-exposure was attributed to the disappearance of conjugated cinnamate groups that photo-dimerized to form cyclobutane.

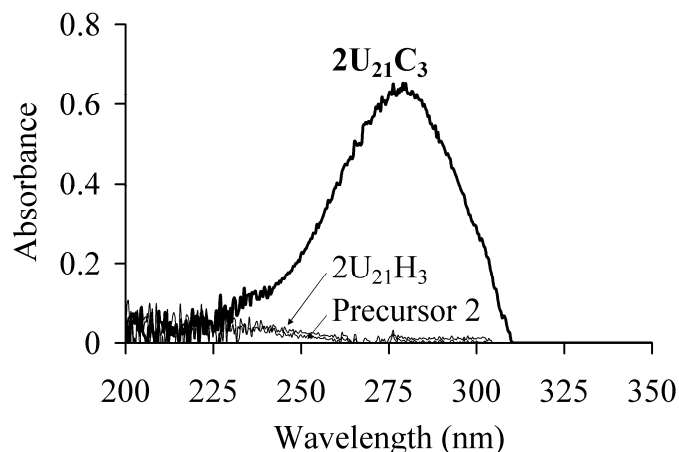


Figure 6.3 UV-vis absorbance of precursor **2** following urethane functionalization ($2\text{U}_{21}\text{H}_3$) and cinnamate functionalization ($2\text{U}_{21}\text{C}_3$).

The rate of cinnamate dimerization was determined from a second order kinetic plot of absorbance versus UV-exposure time, as shown in Figure 6.4. **2U₂₁C₃** contained the largest concentration of urethane groups and exhibited the fastest rate of cinnamate dimerization, 0.314 s^{-1} . The UV-absorbance for **2U₂₁C₃** plateaued after 120 s of irradiation where 90% of cinnamate groups had photo-dimerized, and with increased UV-exposure further change in cinnamate absorbance was not observed. The plateau phenomenon was attributed to a steady-state concentration of cinnamate groups, resulting from the network of intermolecular cinnamate dimers. Confined side chains in the network structure prevented cinnamate groups from rearranging to fulfill the topotactic conformational requirements to achieve cinnamate dimerization.⁴⁵ Control sample, **2H₂₁C₃**, demonstrated the second fastest rate, 0.170 s^{-1} , and required 210 s of irradiation exposure to achieve a steady cinnamate concentration. **2U₈C₁₆** and **2H₉C₁₅** displayed similar rates of cinnamate dimerization, 0.069 s^{-1} and 0.081 s^{-1} , respectively. The cinnamate concentration of the control sample, **2H₉C₁₅**, and urethane sample, **2U₈C₁₆**, reached a steady state after 180 s and 210 s of irradiation exposure, respectively. The increased rate of cinnamate dimerization with increasing concentration of urethane was not a consequence of chain mobility, due to the fact **2U₂₁C₃** had the highest T_g , $-21\text{ }^\circ\text{C}$.

A film of **2U₂₁C₃** was spin cast onto a quartz slide from a 5 wt% toluene solution to examine the influence of film thickness on the rate of cinnamate dimerization. The 5 wt% rate of cinnamate photo-reactivity was compared to **2U₂₁C₃** spin cast from a 10 wt% toluene solution. The influence of film thickness was examined to insure UV-radiation penetrated the entire thickness of the film affording uniform curing, and to explore the concentration effect on the exposure time required to reach a steady state of cinnamate

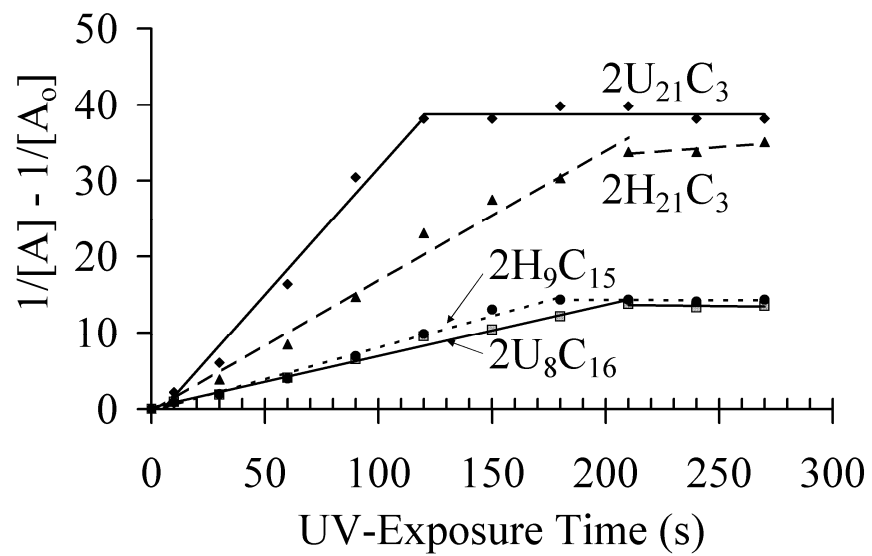


Figure 6.4 Kinetic plot investigating the rate of cinnamate photo-dimerization as a function of cinnamate and urethane concentration.

concentration. The 5 wt% film was $0.18 \pm 0.12 \mu\text{m}$ thick and the 10 wt% film was $1.02 \pm 0.13 \mu\text{m}$ thick. The observed cinnamate dimerization rate of the 5 wt% and 10 wt% films were very similar at 0.382 s^{-1} and 0.341 s^{-1} , respectively. The cinnamate concentration plateaued after 60 s and 120 s of UV-irradiation for the 5 wt% and 10 wt% films, respectively. As expected, the 5 wt% film achieved a steady cinnamate concentration faster because the film was thinner and contained a lower concentration of cinnamate groups.

Sol fraction analysis was conducted on urethane and control series films in refluxing THF. All non-cured films produced no gel fraction, and all UV-cured films were cured for 10 s with a measured UVB-dosage $0.147 \pm 0.05 \text{ J/cm}^2$. UV-cured films of **2U₂₁C₃**, **2U₁₂C₁₂**, and **2U₈C₁₆** produced gel fractions of 25%, 21%, and 18%, respectively. Increasing urethane concentrations correlated to higher gel fractions for the urethane series, indicating the lowest molar concentration of cinnamate produced the highest gel fraction. The opposite effect was evident in the control series. Irradiated films of **2H₂₁C₃**, **2H₁₂C₁₂**, and **2H₉C₁₅** produced gel fractions of 12%, 15%, and 19%, respectively. The gel fraction increased with increasing cinnamate groups for the control series. Increasing gel content with higher cinnamate concentrations was expected for compositions that did not contain hydrogen bonding groups.⁴⁶

6.5 Conclusion

A novel synergy combining hydrogen bonding and photo-reactive groups was developed in low T_g acrylics for application as HMPSAs. Acrylic copolymers of EHA, HEA, and MA were functionalized with urethane and cinnamate groups, and the reaction conditions were optimized to control the degree of functionality and manipulate the relationship between hydrogen bonding and photo-active sites. Hydrogen bonding associations provided strategies to increase the apparent molecular weight post-processing to prevent creep and cohesive failure. Processing above the hydrogen bonding dissociation temperature presents a methodology to maintain viscosities low for melt processing. Isothermal rheological experiments at 150 °C confirmed the melt stability of the cyclohexyl urethane linkage, cinnamate, and the acrylic adhesive composition.

Precursors were functionalized with both urethane and cinnamate groups. The charged molar equivalence of cyclohexyl isocyanate to HEA determined the degree of urethane functionalization. All remaining residual HEA units of the urethane functionalized copolymer were reacted with cinnamoyl chloride introducing cinnamate functionality. The UV-cured peel strength increased as the concentration of urethane increased. Higher concentrations of cinnamates increased the T_g of the UV-cured film, preventing the adhesive from spreading and adequately contacting the substrate. All UV-cured films containing cinnamate groups failed 100% adhesively. Complete adhesive failure was attributed to the network formation from the intermolecular photo-dimerization of cinnamates. The percentage of adhesive failure for non-cured tapes increased as the concentration of urethane units increased. Increasing adhesive failure

with urethane concentration was attributed to an increase in apparent molecular weight resulting from the intermolecular association of hydrogen bonding groups.

A control series was synthesized for comparison to the urethane series to investigate the influence of hydrogen bonding groups on the rate and efficiency of cinnamate photo-reactivity. The control series contained cinnamate groups and residual HEA units, and did not contain any urethane sites. The rate of cinnamate photo-dimerization as a function of composition comparing the urethane and control series was determined from a second order kinetic plot following the disappearance of conjugated cinnamates with UV-exposure, as shown in Figure 6.4. Both the urethane sample, **2U₂₁C₃**, and the control sample, **2H₂₁C₃**, contained three mole percent cinnamate with comparable molecular weights. Sample **2U₂₁C₃** dimerized at a rate of 0.314 s^{-1} and **2H₂₁C₃** at a rate of 0.170 s^{-1} , indicating the presence of urethane groups assisted in the rate of cinnamate dimerization through the formation of intermolecular hydrogen bonds that confined the cinnamate groups in a proximity beneficial for photo-reactivity. The presence of the urethane was not influential when the concentration of the cinnamate group was increased for samples **2U₈C₁₆** and **2H₉C₁₅**. The low concentration of urethane groups did not influence the rate of cinnamate photo-reactivity and the rate of dimerization was very similar for **2U₈C₁₆** and **2H₉C₁₅** at 0.069 s^{-1} and 0.081 s^{-1} , respectively. The relationship between urethane groups and cinnamate photo-reactivity provides evidence that high concentrations of hydrogen bonding associations can increase the efficiency of cinnamate photo-dimerization.

6.6 Acknowledgements

This material is work based upon funding from Avery Dennison Performance Polymers.

6.7 References

1. Benedek, I., *Pressure-sensitive adhesives and applications*. 2nd ed.; Marcel Dekker: New York 2004.
2. Webster, I., *Int. J. Adhes. Adhes.* **1997**, *17* (1), 69-73.
3. Satas, D., *Handbook of pressure sensitive adhesive technology*. 3rd ed.; Satas & Associates: Warwick, RI 1999.
4. Raffy, S.; Teissie, J., *Biophys. J.* **1999**, *76* (4), 2072-2080.
5. O'Connor, A. E.; Macosko, C. W., *J. Appl. Polym. Sci.* **2002**, *86* (13), 3355-3367.
6. Czech, Z., *Polym. Bull.* **2004**, *52* (3-4), 283-288.
7. Sosson, F.; Chateauinois, A.; Creton, C., *J. Polym. Sci., Part B: Polym. Phys.* **2005**, *43* (22), 3316-3330.
8. Czech, Z.; Wojciechowicz, M., *Eur. Polym. J.* **2006**, *42* (9), 2153-2160.
9. Qi, Y.; Meng, X.; Yang, J.; Zeng, Z.; Chen, Y., *J. Appl. Polym. Sci.* **2005**, *96* (3), 846-853.
10. Everaerts, A.; Zieminski, K.; Nguyen, L.; Malmer, J., *J. Adhes.* **2006**, *82* (4), 375-387.
11. Dhal, P. K.; Deshpande, A.; Babu, G. N., *Polymer* **1982**, *23* (6), 937-939.
12. Lim, D. H.; Do, H. S.; Kim, H. J., *J. Appl. Polym. Sci.* **2006**, *102* (3), 2839-2846.
13. Kim, D. J.; Kim, H. J.; Yoon, G. H., *Int. J. Adhes. Adhes.* **2005**, *25* (4), 288-295.
14. Benedek, I., *Pressure-Sensitive Design, Theoretical Aspects*. VSP: Leiden, 2006; Vol. 1.
15. Ariga, K.; Lvov, Y.; Kunitake, T., *J. Am. Chem. Soc.* **1997**, *119* (9), 2224-2231.
16. McKee, M. G.; Elkins, C. L.; Park, T.; Long, T. E., *Macromolecules* **2005**, *38* (14), 6015-6023.
17. Acierno, D.; Amendola, E.; Bugatti, V.; Concilio, S.; Giorgini, L.; Iannelli, P.; Piotta, S. P., *Macromolecules* **2004**, *37* (17), 6418-6423.
18. Arumugam, S.; Vutukuri, D. R.; Thayumanavan, S.; Ramamurthy, V., *J. Am. Chem. Soc.* **2005**, *127* (38), 13200-13206.
19. Gower, M. D.; Shanks, R. A., *J. Polym. Sci., Part B: Polym. Phys.* **2006**, *44* (8), 1237-1252.
20. Dong, J.; Ozaki, Y.; Nakashima, K., *Macromolecules* **1997**, *30* (4), 1111-1117.
21. Maurer, J. J.; Eustace, D. J.; Ratcliffe, C. T., *Macromolecules* **1987**, *20* (1), 196-202.
22. Yaobin, R. H., P.; Longsi, L.; Jianming, X.; Yongqiang, Y., *Polymer-Plastics Technology and Engineering* **2006**, *45*, 495-502.
23. Ansell, C. W. G.; Masters, S. J.; Millan, E. J., *J. Appl. Polym. Sci.* **2001**, *81* (13), 3321-3326.
24. Asahara, J.; Hori, N.; Takemura, A.; Ono, H., *J. Appl. Polym. Sci.* **2003**, *87* (9), 1493-1499.

25. Berejka, A. J., *Adhes. Age* **1997**, *40* (8), 30-32, 35-36.
26. Czech, Z., *Eur. Polym. J.* **2004**, *40* (9), 2221-2227.
27. Yang, S. Y.; Rubner, M. F., *J. Am. Chem. Soc.* **2002**, *124* (10), 2100-2101.
28. Kim, C.; Lee, S. J.; Lee, I. H.; Kim, K. T.; Song, H. H.; Jeon, H. J., *Chem. Mater.* **2003**, *15* (19), 3638-3642.
29. Yang, D. K.; Chien, L. C.; Doane, J. W., *Appl. Phys. Lett.* **1992**, *60* (25), 3102-3104.
30. Karikari, A. S.; Edwards, W. F.; Mecham, J. B.; Long, T. E., *Biomacromolecules* **2005**, *6* (5), 2866-2874.
31. Karikari, A. S.; Williams, S. R.; Heisey, C. L.; Rawlett, A. M.; Long, T. E., *Langmuir* **2006**, *22* (23), 9687-9693.
32. Barwich, J.; Dusterwald, U.; Meyer-Roscher, B.; Wustefeld, R., *Adhes. Age* **1997**, *40* (4), 22-24.
33. Fukui, H.; Ishizawa, H.; Nakasuga, A., *J. Photopolym. Sci. Technol.* **1999**, *12* (1), 169-172.
34. Robertson, E. M.; Van Deusen, W. P.; Minsk, L. M., *J. Appl. Polym. Sci.* **1959**, *2* (No. 6), 308-311.
35. Kimura, T.; Kim, J. Y.; Fukuda, T.; Matsuda, H., *Macromol. Chem. Phys.* **2002**, *203* (16), 2344-2350.
36. Fang, S. W.; Timpe, H. J.; Gandini, A., *Polymer* **2002**, *43* (12), 3505-3510.
37. Gheneim, R.; Perez-Berumen, C.; Gandini, A., *Macromolecules* **2002**, *35* (19), 7246-7253.
38. Zahir, S. A., *J. Appl. Polym. Sci.* **1979**, *23* (5), 1355-1372.
39. Trenor, S. R.; Shultz, A. R.; Love, B. J.; Long, T. E., *Chem. Rev.* **2004**, *104* (6), 3059-3077.
40. Murase, S.; Kinoshita, K.; Horie, K.; Morino, S., *Macromolecules* **1997**, *30* (25), 8088-8090.
41. Aharoni, S. M., *Macromolecules* **1986**, *19* (2), 426-434.
42. Chae, B.; Lee, S. W.; Ree, M.; Jung, Y. M.; Kim, S. B., *Langmuir* **2003**, *19* (3), 687-695.
43. Sung, S.-J.; Cho, K.-Y.; Yoo, J.-H.; Kim, W. S.; Chang, H.-S.; Cho, I.; Park, J.-K., *Chem. Phys. Lett.* **2004**, *394* (4-6), 238-243.
44. Satas, D., *Handbook of Pressure Sensitive Adhesive Technology and Applications*. 3rd ed.; Satas & Associates: Warwick, RI, 1999.
45. Darcos, V.; Griffith, K.; Sallenave, X.; Desvergne, J.-P.; Guyard-Duhayon, C.; Hasenknopf, B.; Bassani, D. M., *Photochem. Photobiol. Sci.* **2003**, *2* (11), 1152-1161.
46. Gupta, P.; Trenor, S. R.; Long, T. E.; Wilkes, G. L., *Macromolecules* **2004**, *37* (24), 9211-9218.

Chapter 7: Photo-rheology of Low T_g Acrylics Functionalized with Hydrogen Bonding and Photo-reactive Groups

7.1 Abstract

Random copolymers of poly(n-butyl acrylate-co-2-hydroxyethyl methacrylate) were functionalized with a novel combination of hydrogen bonding and photo-reactive substituents to explore the photo-curing of associated macromolecular architectures. The influence of urethane hydrogen bonding on the photo-reactivity of cinnamate-functionalized acrylics was investigated with photo-rheology and UV-vis spectroscopy. Photo-rheology was utilized to monitor the viscoelastic changes upon UV-exposure. Cinnamate-functionalized samples displayed an increase in modulus with exposure time, and the percentage increase in modulus decreased as the urethane content increased. This was attributed to a lower concentration of cinnamate groups and lower degree of crosslinking. The rate of cinnamate dimerization was determined from a kinetic analysis utilizing UV-vis spectroscopy. The vinyl cinnamate absorbance at 275 nm decreased as UV-exposure time increased. The decrease in cinnamate concentration was attributed to the loss of conjugated cinnamate groups as cinnamate dimerization formed cyclobutane. The synergy of hydrogen bonding and photo-reactive groups resulted in higher rates of cinnamate photo-reactivity with increasing urethane concentration.

7.2 Introduction

Photo-curable polymers are widely used in lithographic,¹ adhesive,² coating,³ and photonic⁴ applications. Photo-reactions offer solvent-free, environmentally benign strategies, efficient processing, selective reactivity, and fast curing kinetics. Monomers that photo-polymerize with or without the use of photo-sensitizers include (meth)acrylates, dienes, and vinyl groups,⁵⁻⁹ and common photo-reactive oligomers include oligourethane acrylates, epoxyacrylates, and unsaturated polyester acrylates.^{10,11} Photo-reactive monomers and oligomers are extensively applied as surface protective coatings due to an extremely fast rate of photo-initiated crosslinking to form insoluble, mechanically durable polymer networks. Recently, several reviews described the potential of photopolymerization and related emerging technologies.¹²⁻¹⁴

Photo-rheology is an excellent tool to observe the real-time evolution of mechanical and rheological properties as photo-reactive monomers transition from liquid to solid during photo-curing. Photo-rheology monitors the rheological response to *in situ* UV-curing, as shown in Figure 7.1.¹⁵ Khan and coworkers initially introduced photo-curing dynamic rheology, and reported the influence of sample thickness, radiation intensity, and oscillatory shear on the photo-rheological properties of urethane-based thiols.^{16,17} Gasper and coworkers utilized photo-rheology to investigate the viscoelastic properties during photo-curing of urethane-acrylate oligomers and acrylic comonomer coatings.¹⁸ Others have complemented photo-rheology with real time Fourier transform infrared spectroscopy (FTIR) and near infrared spectroscopy (NIR) to monitor the degree of conversion during photo-curing and quantify the photo-curing kinetics of acrylic monomers.^{19,20}

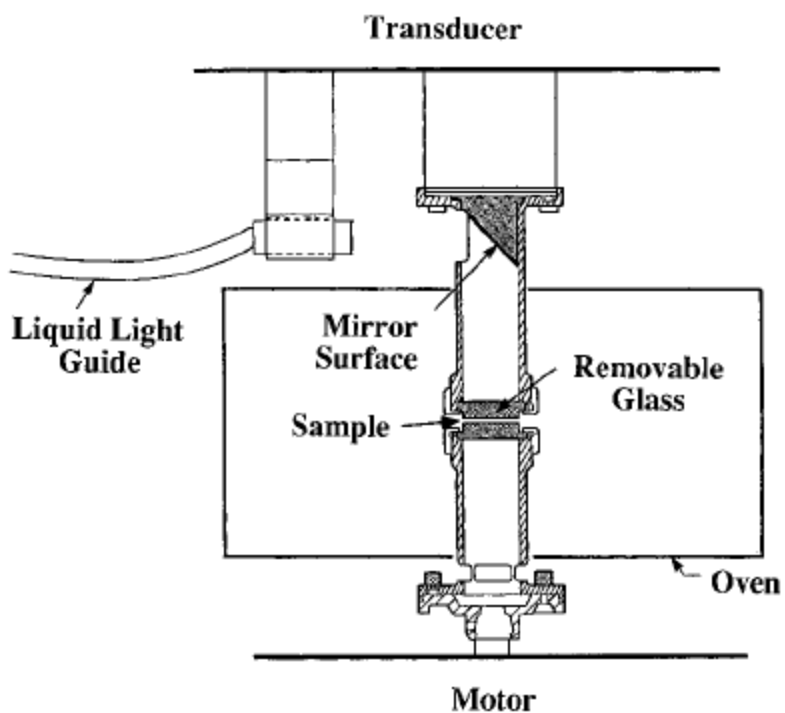


Figure 7.1 Photo-rheometer for rheologically monitoring *in situ* UV-curing. The incident UV beam is reflected from a mirror through the quartz top plate onto the sample film. Reprinted with permission from *Macromolecules* **29**, 5368-5374 (1996). Copyright 2009 American Chemical Society.

Recent photo-rheology literature reports the property evolution of photo-curing monomers and oligomers, however, to the best of our knowledge, photo-rheological studies that describe the photo-curing of polymers functionalized with photo-dimerizable groups are not available in the earlier literature. Our study herein describes the photo-rheology of hydrogen bond containing acrylic random copolymers and the influence of hydrogen bonding associations on the photo-reactivity of cinnamate-functionalized low T_g acrylics. The photo-chemistry of cinnamates involves two photo-reactions upon UV-irradiation, i.e. the initial trans-cis isomerization and subsequent photo-dimerization. Photo-dimerization involves the $[2\pi + 2\pi]$ cycloaddition of cinnamates in the head-to-head or head-to-tail configuration to form cyclobutane isomers.²¹⁻²³

Recently supramolecular polymeric structures have received renewed interest.²⁴⁻²⁶ For example, noncovalent methodologies for the association and self-assembly of macromolecules includes the formation of donor-acceptor complexes,²⁷ hydrogen bonding,²⁸ liquid crystalline behavior,²⁹ and the self-assembly of amphiphilic copolymers.³⁰ Hydrogen bonding functionality is prevalent in biological systems, and the associations are thermo-reversible, therefore, providing a versatile scaffold for noncovalent associations.³¹ Photo-curable, thermoreversible polymers provide orthogonal strategies for the self-assembly and covalent crosslinking of associated polymeric architectures.³² Post-polymerization photo-curing increases the molecular weight and mechanical properties of low viscosity oligomers, providing more facile, solvent-free melt processing. Others have incorporated photo-reactive groups to increase the molecular weight and cohesive strength of low viscosity adhesive formulations for coating applications.^{33,34} Photo-curing of self-assembled architectures has recently

received significant interest in the layer-by-layer (LBL) assembly of multilayer thin films,³⁵ formation of supramolecular nanostructures,³⁶ and formation of liquid crystalline polymers.³⁷

In this study a random copolymer of poly(n-butyl acrylate-*co*-2-hydroxyethyl methacrylate) (poly(nBA-*co*-HEMA)) was synthesized as a reactive polymer precursor, as shown in Scheme 7.1. Primary hydroxyl groups of HEMA repeating units were quantitatively functionalized with urethane and cinnamate groups to introduce a novel combination of hydrogen bonding and photo-reactive substituents, respectively, as shown in Scheme 7.2. The degree of urethane and cinnamate functionality was varied to systematically study the photo-curing behavior as a function of composition. Photo-rheology and UV-vis spectroscopy were used to investigate the influence of hydrogen bonding associations on the photo-reactivity of cinnamate functionalized acrylics.

7.3 Materials and Methods

7.3.1 Materials

Azobisisobutyronitrile (AIBN), tetrahydrofuran (THF), n-butyl acrylate (nBA), 2-hydroxyethyl methacrylate (HEMA), cinnamoyl chloride, triethylamine (TEA), cyclohexyl isocyanate, ethyl acetate, and methanol were purchased from Sigma-Aldrich Chemical Co. AIBN was recrystallized twice from methanol. Reagent grade tetrahydrofuran (THF) was passed through a PURE SOLV MD-3 Solvent Purification System (Innovative Technology Inc.) immediately prior to use. Cinnamoyl chloride was sublimed to produce white crystals. TEA was distilled from CaH_2 . nBA was passed through a neutral alumina column to remove any inhibitor. HEMA (100 g, 0.77 mols) was dissolved in distilled water (400 mL) and hydroquinone (0.10g, 0.90 mmol) was added. The aqueous solution was washed ten times with hexanes to remove any diacrylate present, and NaCl (50 g, 0.90 mol) was added to the final aqueous solution. HEMA was extracted from the aqueous layer with ethyl ether and additional hydroquinone (0.10 g, 0.90 mmol) was added. The organic layer was dried over CaSO_4 and concentrated in vacuum. HEMA was passed over neutral alumina to remove hydroquinone prior to use. Cyclohexyl isocyanate was used without further purification. All reactions were conducted under a nitrogen environment in flame-dried glassware, unless otherwise noted.

7.3.2 Instrumentation

Size exclusion chromatography (SEC) was used to determine molecular weights and polydispersity indices (PDI), M_w/M_n . Molecular weights were determined at 40 °C in tetrahydrofuran (ACS grade) at a flow rate of 1 mL min^{-1} on a Waters GPC equipped

with 3 in-line Polymer Laboratories PLgel 5 μm MIXED-C columns with a Waters 717 autosampler. A triple detection system included a Waters 2414 Refractive Index Detector, Viscotek 270 Dual Detector viscometer, and Wyatt Technologies miniDAWN multiangle laser light scattering (MALLS) detector. The MALLS detector was used to determine absolute weight-average molecular weights with the refractive index increments (dn/dc) determined online.

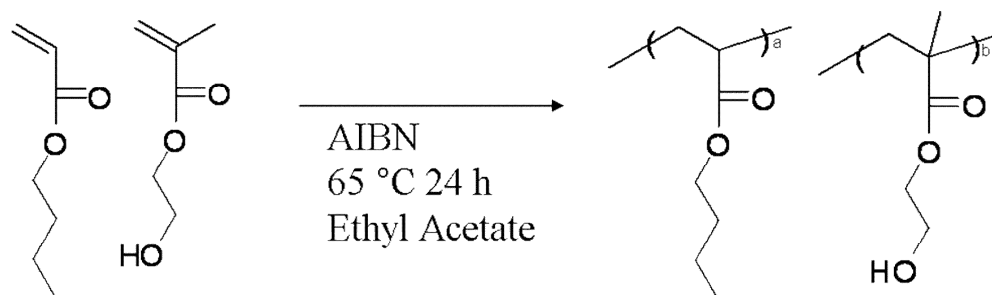
^1H NMR spectroscopy was performed on a Varian Unity 400 spectrometer at 400 MHz in CDCl_3 . Differential scanning calorimetry (DSC) was performed under a nitrogen flush at a heating rate of 10 $^\circ\text{C}/\text{min}$ on a TA Instruments DSC 1000. Data was collected on the 2nd heat cycle. FTIR spectroscopy was performed on a MIDAC M-1700 FTIR with Durascope single bounce diamond ATR. UV-Vis spectroscopy was performed using an Analytical Instrument Systems Inc. spectrometer equipped with fiber optic cables, a DT1000CE light source, and an Ocean Optics USB2000 UV-Vis detector. UV-curing was performed with a Fusion UV Systems Inc. 100 W mercury bulb with a P300MT power supply and an adjustable speed conveyor belt. Light intensities were measured using an EIT Inc. UV power puck. Irradiation for 10 s produced intensities of UVA 1.702 W/cm^2 and UVB 1.446 W/cm^2 . UV-curing rheology was performed on a TA instruments rheometer with a Novacure light source and mercury bulb. Experiments were isothermal at 25 $^\circ\text{C}$ with a 20 mm quartz top plate on a peltier plate, with a gap of 0.3 μm , and conducted at 10 Hz with 3 % strain. Films were irradiated for 55 min with an intensity of 265 mW/cm^2 measured at the peltier plate surface.

7.3.3 Synthesis of Poly(nBA-co-HEMA) Precursor

The synthesis of the poly(nBA-co-HEMA) precursor is shown in Scheme 7.1. AIBN (0.80 g, 4.87 mmol) was dissolved in ethyl acetate (133 mL) in a 500-mL, round-bottomed flask equipped with a magnetic stir bar. nBA (36.0 g, 1.98 mol) and HEMA (4.00 g, 0.031 mol) were added to the reaction flask using a degassed syringe. The reaction flask was placed in a 65 °C bath for 24 h. Precipitation into hexanes and subsequent drying afforded the final isolated product. 76 mol% nBA, 24 mol% HEMA, M_w 40,000, PDI 1.91, T_g -27 °C. ATR-IR: (C=O) 1714 cm^{-1} , (C-H) 2800-2950 cm^{-1} , (C-O) 1000-1260 cm^{-1} . ^1H NMR, (CDCl_3): δ (ppm) 4.07 (2H, C(O)-O-CH₂-CH₂ (nBA)) and (2H, C(O)-O-CH₂-CH₂ (HEMA)), 3.80 (2H, CH₂-CH₂-OH (HEMA)), 0.90 (3H, CH₂-C(-CH₃)(-C(O)-O-) (HEMA)). The chemical shifts of all the protons in the polymer backbone were between 2.50 and 1.00 ppm.

7.3.4 Urethane Functionalization of the Acrylic Precursor

A 10% molar excess of cyclohexyl isocyanate to HEMA repeating units achieved 100% urethane functionalization. The molar ratio of urethane to pendant hydroxyl groups was varied to influence the degree of functionalization. The precursor (6.30 g, 0.016 mol HEMA) was dissolved in toluene (9.45 g) in a 100-mL, round-bottomed flask equipped with a magnetic stir bar. Cyclohexyl isocyanate (2.21 g, 0.018 mol) was added to the reaction flask using a degassed syringe. Di-n-butyltindilaurate (0.20 mL, 1 wt % in toluene) was added to the reaction flask as a catalyst. The reaction flask was placed in a 50 °C bath for 8 h. Precipitation into hexanes and subsequent drying afforded the final isolated product. Yield 75%. ATR-IR: (N-H) 3200-3500 cm^{-1} , urethane (C=O) 1535 cm^{-1} . ^1H NMR, (CDCl_3): δ (ppm) 4.21 (2H, C(O)-O-CH₂-CH₂-O-C(O)-NH (UEMA)),

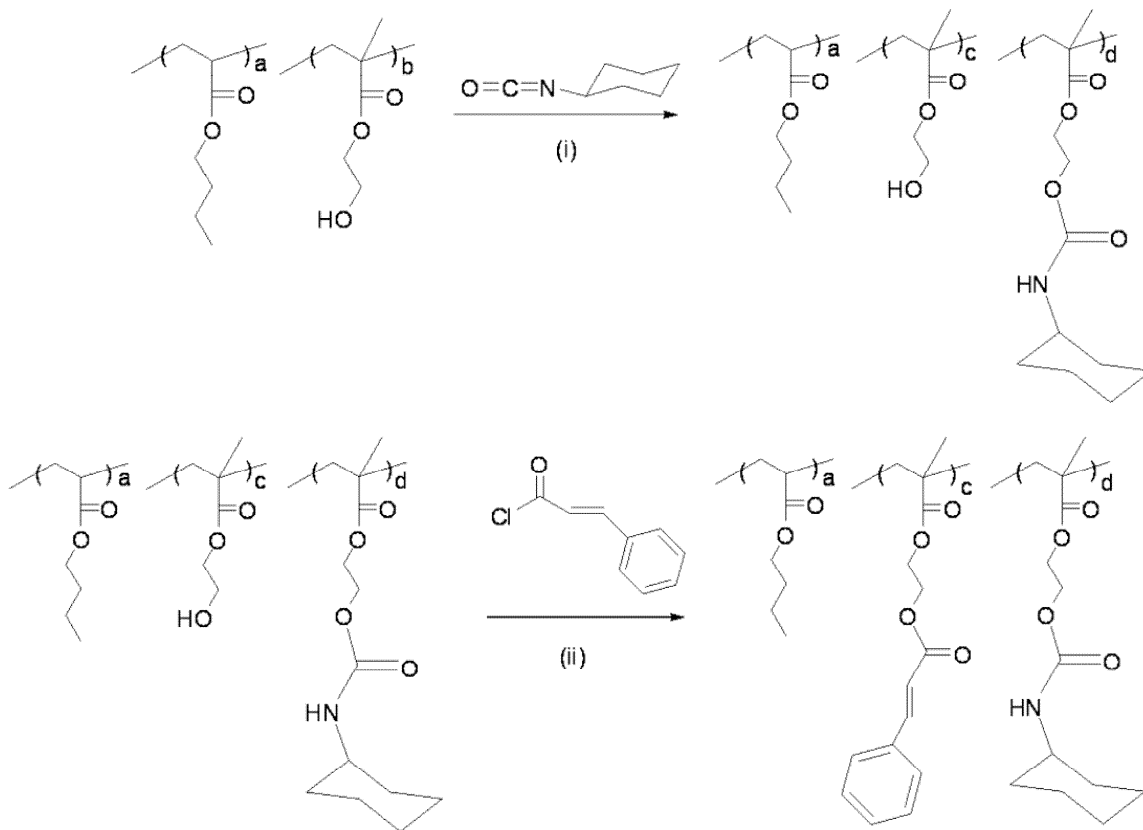


Scheme 7.1 Synthesis of the poly(nBA-co-HEMA) precursor.

4.07 (2H, C(O)-O-CH₂-CH₂ (nBA)), 4.00 (2H, C(O)-O-CH₂-CH₂ (UEMA)), 3.45 (1H, NH-CH-(CH₂)₂ (UEMA)), 0.90 (3H, CH₂-C(-CH₃)(-C(O)-O-) (HEMA)). The chemical shifts of all the protons in the polymer backbone were between 2.50 and 1.00 ppm.

7.3.5 Cinnamate Functionalization of the Precursor and Urethane Functionalized Acrylic

Urethane and cinnamate functionalization of the poly(nBA-*co*-HEMA) precursor is depicted in Scheme 7.2. A five-molar excess of cinnamoyl chloride achieved 100% cinnamate functionalization. The precursor (5.78 g, 0.015 mol HEMA) or urethane functionalized sample was dissolved in dichloromethane (42.9 g) in a 250-mL, two-necked, round-bottomed flask equipped with a magnetic stir bar and addition funnel. The solution was cooled to 0 °C and TEA (7.55 g, 0.075 mol) was added to the reaction flask using a degassed syringe. Cinnamoyl chloride (12.5 g, 0.075 mol) was dissolved in dichloromethane (16.0 g) and added drop-wise to the reaction flask. The reaction was stirred at 0 °C for 2 h. Precipitation into methanol and subsequent drying afforded the final isolated product. Yield 65%. ATR-IR: cinnamate (C=C, vinyl) 1637 cm⁻¹, (C=C, Aromatic) 1500 cm⁻¹. ¹H NMR, (CDCl₃): δ (ppm) 7.75 (1H, *trans* O-C(O)-CH=CH-Ar (CEMA)), 7.57 (2H, Ar H (CEMA)), 7.38 (3H, Ar H (CEMA)), 6.48 (1H, *trans* CO₂-CH=CH-Ar (CEMA)), 4.40 (2H, C(O)-O-CH₂-CH₂ (CEMA), 4.21 (2H, C(O)-O-CH₂-CH₂ (UEMA)) and (2H, C(O)-O-CH₂-CH₂ (CEMA)), 4.07 (2H, C(O)-O-CH₂-CH₂ (nBA)), 4.00 (2H, C(O)-O-CH₂-CH₂-O-C(O)-NH (UEMA)), 3.45 (1H, NH-CH-(CH₂)₂ (UEMA)), 0.90 (3H, CH₂-C(-CH₃)(-C(O)-O-) (CEMA and UEMA)). The chemical shifts of all the protons in the polymer backbone were between 2.50 and 1.00 ppm.



Scheme 7.2 Urethane and cinnamate functionalization of poly(nBA-co-HEMA) precursor, (i) 0.2 mL of 1 wt% di-n-butyltin-dilaurate in toluene, 40 wt% solids in toluene, 50 °C, (ii) triethylamine, 20 wt% solids in dichloromethane, 0 °C.

7.3.6 UV-Vis Characterization of UV-Irradiated Films

The sample was dissolved in toluene at 10 wt%. The solution was spin-cast onto a square quartz slide (1" x 1") at 2000 rpm for 1 min. The UV-Vis absorbance of the film was measured. The coated slide was then irradiated for 10 s, 30 s, 60 s, 90 s, 120 s, 150 s, and 180 s periods and the UV-Vis absorbance measured after each exposure period. Cinnamate samples were spin coated on quartz slides to a thickness of 0.79 ± 0.03 μm , 1.05 ± 0.04 μm , 0.98 ± 0.03 μm , and 1.00 ± 0.04 μm for U_{20}C_4 , $\text{U}_{11}\text{C}_{13}$, U_5C_{19} , and C_{24} , (which are defined in Table 7.1) respectively.

7.4 Results and Discussion

7.4.1 Synthesis and Functionalization of the Poly(nBA-co-HEMA) Precursor with Hydrogen Bonding and Photo-reactive Groups

nBA was incorporated into the precursor copolymer to tailor the glass transition temperature to below room temperature, and HEMA was incorporated as a functionalization site for the subsequent incorporation of urethane and cinnamate groups. The random copolymer precursor contained 76 mol% nBA and 24 mol% HEMA as determined using ^1H NMR shown in Figure 7.2. The precursor had a M_w 40,000 (M_w/M_n 1.91) and T_g -27 °C.

To investigate the effect of functionalization on the thermal and rheological properties, complete conversion of HEMA groups to cinnamate or urethane functionality was necessary. A 10% molar excess of cyclohexyl isocyanate to HEMA repeat units achieved 100% urethane (incorporation of 24 mol% 2-[(cyclohexylamino)carbonyl]oxyethyl methacrylate) functionalization, U_{24} . The ^1H NMR of U_{24} is shown in Figure 7.3. The HEMA peak at 3.80 ppm completely disappeared, while the C-H connecting the cyclohexyl to the urethane linkage appeared at 3.45 ppm. The 100% urethane functionalized copolymer had a M_w 52,300 (M_w/M_n 2.16) and T_g -12 °C. The T_g increase was attributed to the increase in apparent molecular weight due to the association of intermolecular urethane hydrogen bonds. A five-molar excess of cinnamoyl chloride to HEMA repeat units achieved 100% cinnamate (incorporation of 24 mol% 2-cinnamoyloxyethyl methacrylate) functionalization, C_{24} . The ^1H NMR of C_{24} is shown in Figure 7.4 and the HEMA peak at 3.80 ppm completely disappeared, while the cinnamate peaks appeared at 7.75 ppm,

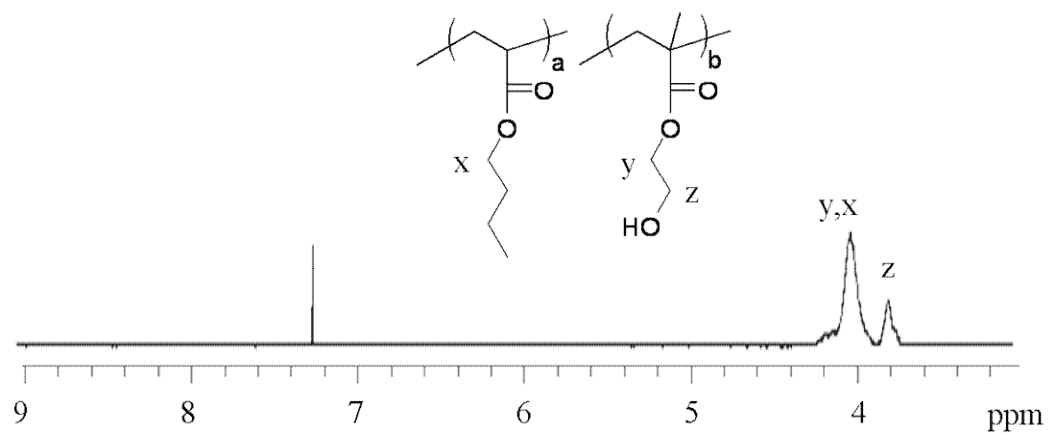


Figure 7.2 ^1H NMR of poly(nBA-co-HEMA) precursor.

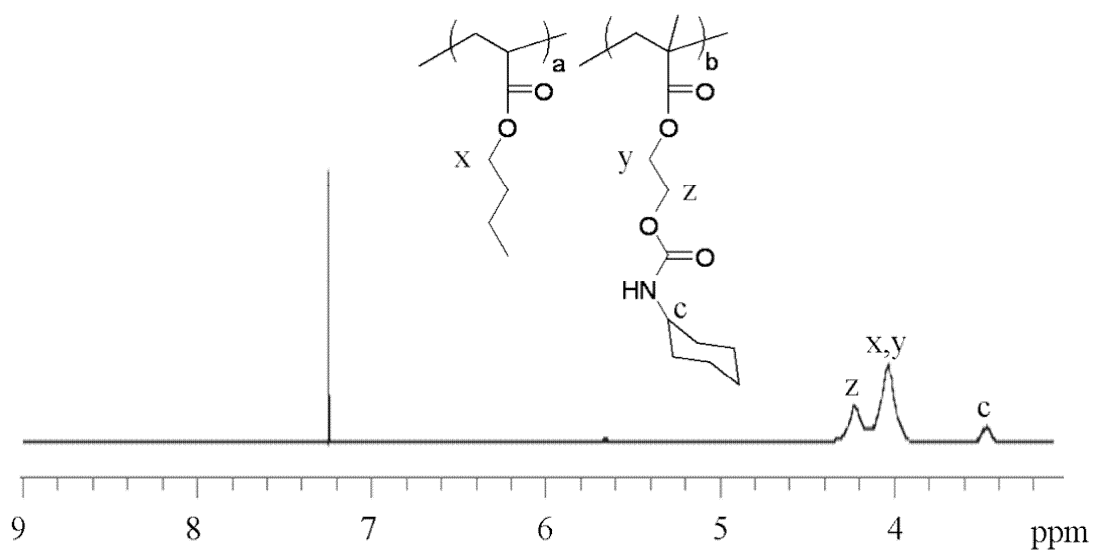


Figure 7.3 ^1H NMR of U_{24} .

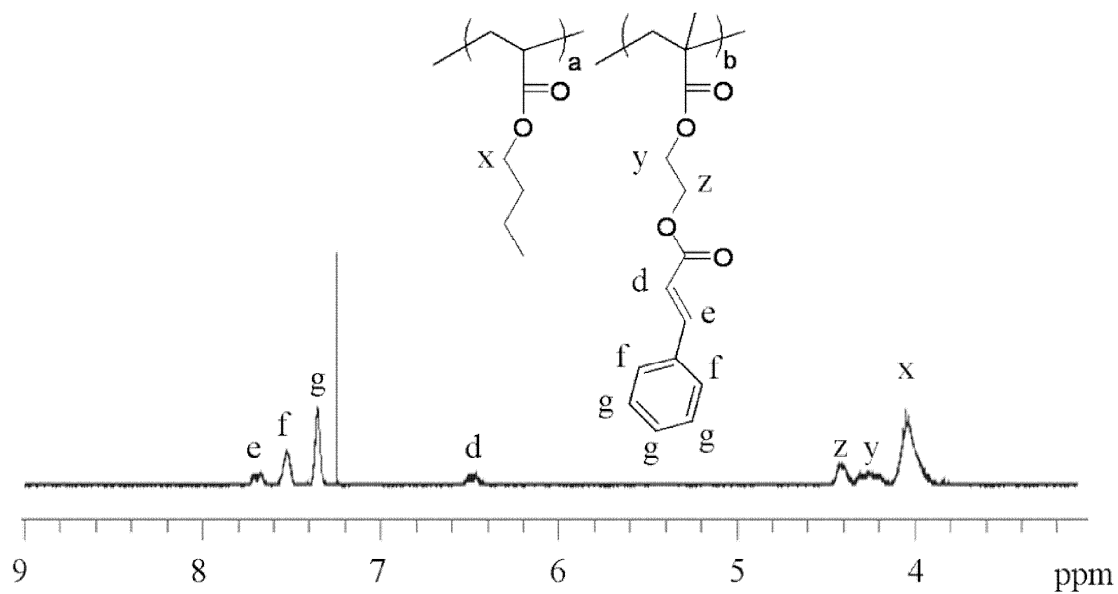


Figure 7.4 ^1H NMR of C_{24} .

7.57 ppm, 7.38 ppm, and 6.48 ppm. The 100% cinnamate-functionalized copolymer had a M_w 53,400 (M_w/M_n 2.16) and T_g -17 °C. The T_g increase was attributed to the incorporation of bulky cinnamate pendent groups.

The precursor was functionalized with varying degrees of urethane and cinnamate functionality, as summarized in Table 7.1. Urethane functionality was introduced in the first synthetic step to limit premature crosslinking during cinnamate functionalization. Within the reaction period the ratio of cyclohexyl isocyanate to HEMA repeat units determined the degree of urethane functionalization. Following urethane functionalization, cinnamoyl chloride was charged in a five-molar excess to the residual HEMA groups. UV-vis spectroscopy and photo-curing rheology were used to determine the influence of hydrogen bonding sites on the efficiency of cinnamate photo-reactivity and rheological properties.

Sample Name	nBA mol%	HEMA mol%	Ureth EMA* mol%	Cinn EMA* mol%	M _w (PDI)	T _g (°C)
Precursor	76	24	-	-	40,000 (1.91)	-27
U ₂₄	76	-	24	-	52,300 (2.16)	-12
U ₂₀ C ₄	76	-	20	4	54,000 (1.46)	-12
U ₁₁ C ₁₃	76	-	11	13	50,200 (2.06)	-17
U ₅ C ₁₉	76	-	5	19	52,100 (1.93)	-22
C ₂₄	76	-	-	24	52,400 (2.16)	-17

Table 7.1 Composition, molecular weight, and T_g comparison of the precursor, urethane- and cinnamate-functionalized series of acrylic copolymers (*EMA: ethyl methacrylate).

7.4.2 Photo-rheology of the Urethane and Cinnamate Functionalized Acrylics

The photo-rheology of the precursor and functionalized melt films are shown in Figure 7.5. The films were allowed to initially equilibrate under shear for 420 s, and the UV-light was subsequently activated initiating distinguishable changes in the melt viscosities. As expected, the steady state viscosities prior to irradiation increased as the concentration of urethane groups increased. Copolymer **U₂₄** had the highest and **C₂₄** had the lowest initial viscosity of functionalized samples, which was attributed to the concentration of urethane units. All functionalized samples had comparable weight-average molecular weights, ranging from 50,200 to 54,000.

The melt viscosity of cinnamate-functionalized films increased upon UV-exposure. The increase in viscosity was attributed to the intermolecular crosslinking reaction of cinnamate photo-dimerization. During photo-curing, the viscosity of **C₂₄** increased over 300%. A viscosity increase of only 26% was achieved for **U₂₀C₄**. The percentage increase in viscosity decreased as the urethane content increased, which was attributed to a lower concentration of cinnamate groups achieving a lower degree of crosslinking.

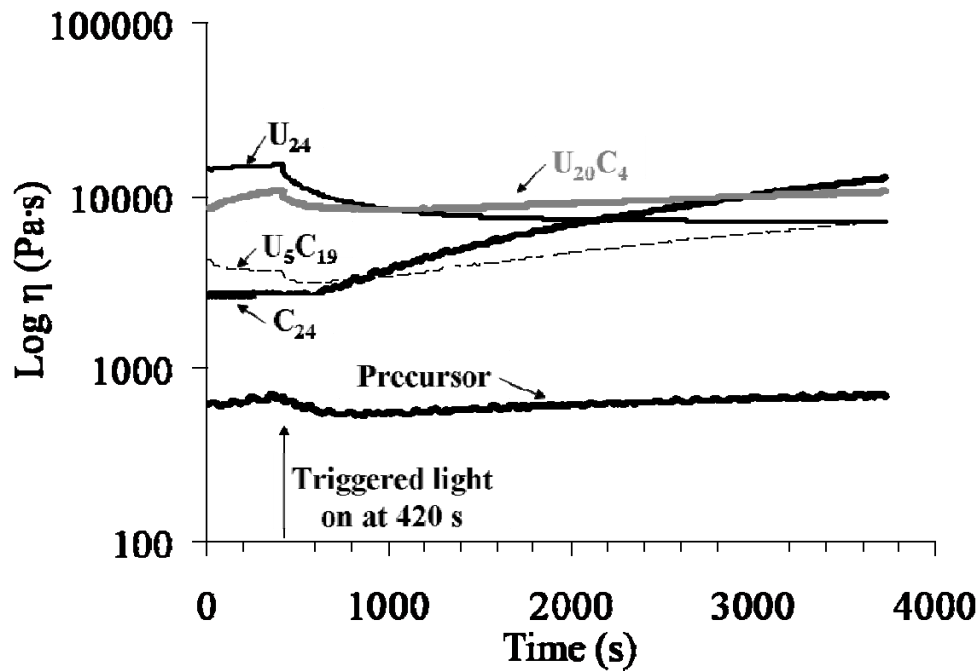


Figure 7.5 Photo-rheology of the precursor, urethane- and cinnamate-functionalized copolymers. Films were equilibrated for 420 s, at which point the UV-light was actuated.

7.4.3 Influence of Composition on the Rate of Cinnamate Photo-reactivity

The influence of composition on the rate of cinnamate dimerization was investigated using UV-vis spectroscopy. Cinnamate samples were spin-coated on quartz slides to a thickness of $0.79\pm 0.03\ \mu\text{m}$, $1.05\pm 0.04\ \mu\text{m}$, $0.98\pm 0.03\ \mu\text{m}$, and $1.00\pm 0.04\ \mu\text{m}$ for U_{20}C_4 , $\text{U}_{11}\text{C}_{13}$, U_5C_{19} , and C_{24} , respectively. The rate of cinnamate dimerization was determined from a second order kinetic plot of absorbance versus UV-exposure time. The cinnamate absorbance peak at 275 nm decreased as UV-exposure time increased, as shown in Figure 7.6 for U_{20}C_4 . The decrease in cinnamate concentration was attributed to the loss of conjugated cinnamate groups as cinnamate dimerization occurred.

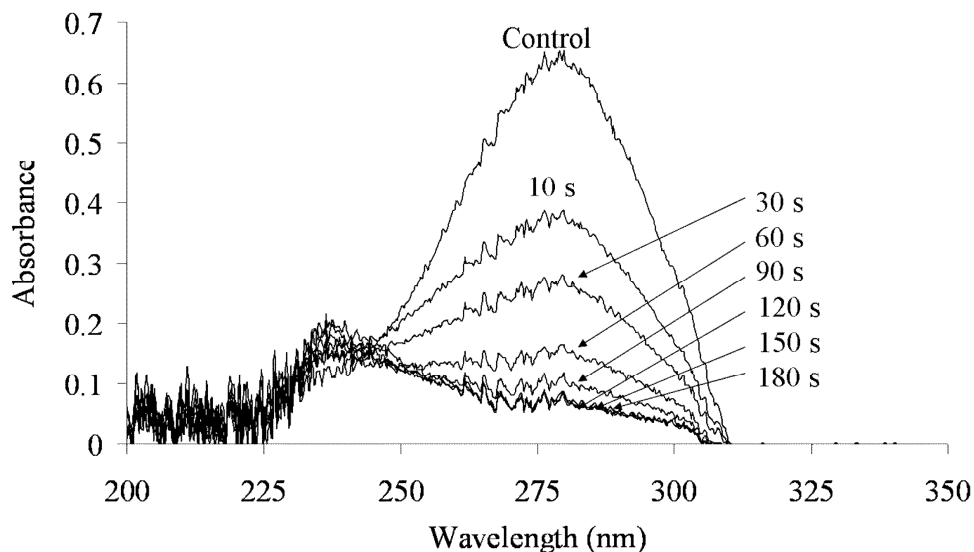


Figure 7.6 Decrease in cinnamate UV-absorbance at 275 nm with increasing UV-exposure time for U_{20}C_4 .

Figure 7.7 displays a second order kinetic plot of absorbance versus UV-exposure time for the cinnamate functionalized series. The precursor and **U₂₄** were not included in the kinetic study because they contained no photo-reactive cinnamate groups. **C₂₄** contained the highest molar percentage of cinnamate and displayed the slowest rate of cinnamate dimerization, 0.05 s^{-1} . The rate of cinnamate dimerization increased as the concentration of urethane increased. **U₂₀C₄** displayed the fastest rate of cinnamate photo-dimerization at 0.17 s^{-1} , while possessing the highest T_g , $-12 \text{ }^\circ\text{C}$. Therefore, the correlation between urethane concentration and the rate of cinnamate dimerization was not attributed to a glass transition temperature effect. **U₁₁C₁₃** and **U₅C₁₉** displayed similar rates of cinnamate dimerization at 0.10 s^{-1} and 0.09 s^{-1} , respectively.

The cinnamate absorbance of **U₂₀C₄** did not change after 120 s of UV-irradiation. A change in cinnamate absorbance was not detected following 150 s of irradiation in all other films. The absorbance plateau was attributed to the equilibration of cinnamate concentration. Network formation prevented necessary chain mobility to satisfy the topochemical requirements of cinnamate dimerization. As expected, the required UV-exposure time to achieve cinnamate equilibration was concentration dependent. **U₂₀C₄** was also coated from a 5 wt% solution to produce a $0.16 \pm 0.03 \text{ }\mu\text{m}$ thick film. The 5 wt% and 10 wt% films exhibited nearly identical rates of cinnamate photo-reactivity at 0.16 s^{-1} and 0.17 s^{-1} , respectively. However, only 90 s of UV-irradiation was required to equilibrate the 5 wt% film compared to 120 s for the 10 wt% film. The 5 wt% film equilibrated faster due to a lower concentration of cinnamate groups.

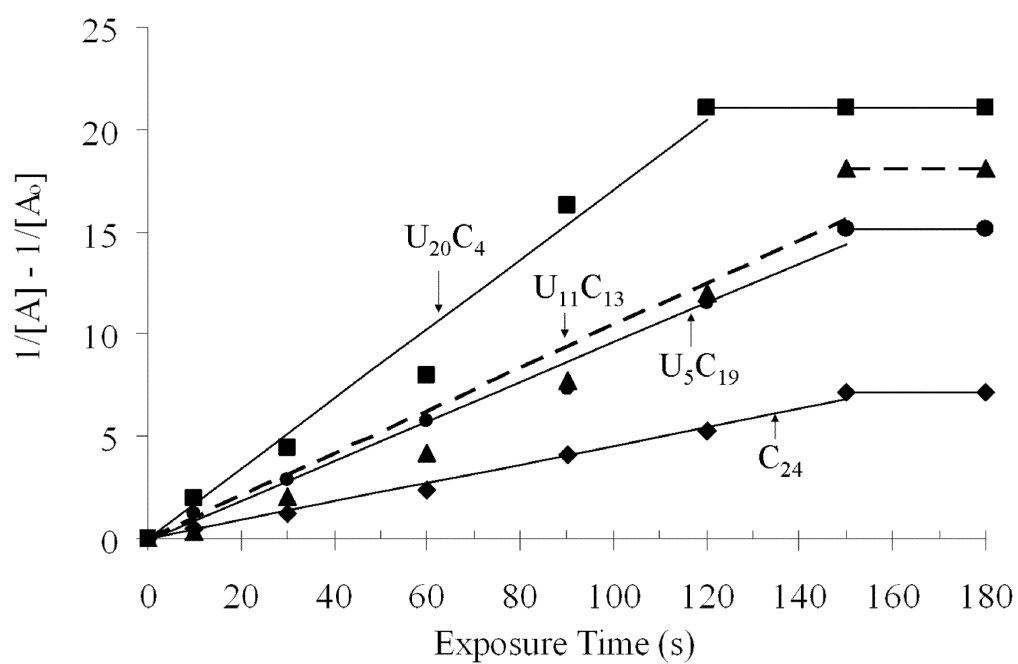


Figure 7.7 Kinetic plot investigating the rate of cinnamate dimerization versus UV-exposure time as a function of cinnamate and urethane concentration.

7.5 Conclusions

A random copolymer of poly(nBA-*co*-HEMA) was functionalized with cinnamate and urethane groups to introduce a novel combination of hydrogen bonding and photo-reactive sites, respectively. The reaction conditions were optimized to control the degree of functionality and a series of urethane and cinnamate containing copolymers were synthesized with comparable molecular weights. Photo-rheology was utilized to monitor the viscoelastic changes in material properties with UV-exposure. Cinnamate functionalized samples displayed an increase in viscosity with exposure time. The change in viscosity was attributed to the intermolecular crosslinking dimerization of cinnamates. The percentage increase in viscosity during photo-curing decreased as the urethane concentration increased. This was attributed to a lower concentration of cinnamate groups and lower degree of crosslinking.

UV-vis spectroscopy was utilized to determine the concentration of conjugated cinnamate groups following segmented irradiation periods. Conjugated cinnamate absorbance at 275 nm decreased as UV-exposure time increased and a side band at 240 nm attributed to the presence of cyclobutane appeared. The rate of cinnamate dimerization increased as the concentration of urethane increased, suggesting that hydrogen bonding sites promoted cinnamate dimerization.

7.6 Acknowledgements

This material is work based upon funding from Avery Dennison Performance Polymers, Pasadena, CA.

7.7 References

1. Tey, J. N.; Soutar, A. M.; Priyadarshi, A.; Mhaisalkar, S. G.; Hew, K. M., *J. Appl. Polym. Sci.* **2007**, *103* (3), 1985-1991.
2. Chang, E.; Holguin, D., *J. Adhes.* **2005**, *81* (5), 495-508.
3. Karatas, S.; Hosgor, Z.; Menciloglu, Y.; Kayaman-Apohan, N.; Gungor, A., *J. Appl. Polym. Sci.* **2006**, *102* (2), 1906-1914.
4. Song, B. J.; Park, J. K.; Kim, H. K., *J. Polym. Sci., Part A: Polym. Chem.* **2004**, *42* (24), 6375-6383.
5. Gu, H.; Snavelly, D. L., *J. Appl. Polym. Sci.* **2003**, *90* (2), 565-571.
6. Yoshitaka, O., *Polym. Photochem.* **1986**, *7*, 109.
7. Vermeil, C.; Matheson, M.; Leach, S.; Muller, F., *J. Chem. Phys.* **1964**, *61* (4), 596-606.
8. Eskins, K.; Dintzis, F. R.; Friedman, M., *J. Macromol. Sci., Pure Appl. Chem.* **1971**, *5* (3), 541-546.
9. Shim, S. E.; Jung, H.; Lee, H.; Biswas, J.; Choe, S., *Polymer* **2003**, *44* (19), 5563-5572.
10. Makovetskii, A. A.; Milyavskii, Y. S.; Averina, L. M.; Zamyatin, A. A., *J. Appl. Spectrosc.* **2004**, *71* (6), 916-921.
11. Lee, S. S.; Luciani, A.; Månson, J.E., *Prog. Org. Coat.* **2000**, *38*, 193-197.
12. Khudyakov, I. V.; Turro, N. J., *Photochem. UV-Curing* **2006**, 241-251.
13. Clapper, J. D.; Sievens-Figueroa, L.; Guymon, C. A., *Chem. Mater.* **2008**, *20* (3), 768-781.
14. Baroli, B., *J. Chem. Technol. Biotechnol.* **2006**, *81* (4), 491-499.
15. Chiou, B.-S.; English, R. J.; Khan, S. A., *Macromolecules* **1996**, *29* (16), 5368-5374.
16. Khan, S. A.; Plitz, I.M.; Frantz, R.A., *Rheol. Acta* **1992**, *31*, 151-160.
17. Khan, S. A., *J. Rheol.* **1992**, *36* (4), 573-587.
18. Gasper, S. M.; Schissel, D.N.; Baker, L.S.; Smith, D.L.; Youngman, R.E.; Wu, L.; Sonner, S.M.; Hancock, R.R.; Hogue, C.L.; Givens, S.R., *Macromolecules* **2006**, *39*, 2126-2136.
19. Botella, A.; Dupuy, J.; Roche, A.; Sautereau, H.; Verney, V., *Macromol. Rapid Commun.* **2004**, *25*, 1155-1158.
20. Schmidt, L. E.; Leterrier, Y.; Vesin, J.; Wilhelm, M.; Manson, J.E., *Macromol. Mat. Eng.* **2005**, *290*, 1115-1124.
21. Mahy, R. B.; Oulmidi, A.; Challioui, A.; Derouet, D.; Brosse, J.C., *Eur. Polym. J.* **2006**, *42*, 2389-2397.
22. Cashion, M. P.; Park, T.; Long, T. E., *J. Adhes.* **2009**, *85* (1), 1-17.
23. Minsk, L. M.; Smith, J. G.; Van Deusen, W. P.; Wright, J. F., *J. Appl. Polym. Sci.* **1959**, *2* (6), 302-307.

24. de Greef, T. F. A.; Meijer, E. W., *Nature* **2008**, *453* (7192), 171-173.
25. Schexnaider, P.; Schmidt, G., *Colloid Polym. Sci.* **2009**, *287* (1), 1-11.
26. Kim, H.-J.; Lim, Y.-B.; Lee, M., *J. Polym. Sci., Part A Polym. Chem.* **2008**, *46* (6), 1925-1935.
27. Dobrawa, R.; Wuerthner, F., *J. Polym. Sci., Part A: Polym. Chem.* **2005**, *43* (21), 4981-4995.
28. Bosman, A. W.; Brunsveld, L.; Folmer, B. J. B.; Sijbesma, R. P.; Meijer, E. W., *Macromol. Symp.* **2003**, *201* (Mission and Challenge of Polymer Science and Technology), 143-154.
29. Lehn, J.-M., *Polym. Int.* **2002**, *51* (10), 825-839.
30. Hillmyer, M. A., *Science* **2007**, *317* (5838), 604-605.
31. Brunsveld, L.; Folmer, B. J. B.; Meijer, E. W.; Sijbesma, R. P., *Chem. Rev.* **2001**, *101* (12), 4071-4097.
32. O'Reilly, R. K.; Hawker, C. J.; Wooley, K. L., *Chem. Soc. Rev.* **2006**, *35* (11), 1068-1083.
33. Barwich, J.; Dusterwald, U.; Meyer-Roscher, B.; Wustefeld, R., *Adhes. Age* **1997**, *40* (4), 22-24.
34. Czech, Z., *Polym. Bull.* **2004**, *52* (3-4), 283-288.
35. Yang, S. Y.; Rubner, M. F., *J. Am. Chem. Soc.* **2002**, *124* (10), 2100-2101.
36. Kim, C.; Lee, S. J.; Lee, I. H.; Kim, K. T.; Song, H. H.; Jeon, H.-J., *Chem. Mater.* **2003**, *15* (19), 3638-3642.
37. Yang, D. K.; Chien, L. C.; Doane, J. W., *Appl. Phys. Lett.* **1992**, *60* (25), 3102-3104.

Chapter 8: *In situ* Photo-crosslinking Electrospun Fibers of Cinnamate Functionalized Low T_g Acrylics

8.1 Abstract

Electrospun fibers were *in situ* photo-crosslinked to develop fibrous membranes from cinnamate-functionalized low T_g acrylics. Poly(n-butyl acrylate-*co*-2-hydroxyethyl methacrylate) (poly(nBA-*co*-HEMA)) precursor was functionalized with 6 mol% cinnamate functionality. The photo-reactive cinnamates were introduced from the reaction of HEMA repeat units with cinnamoyl chloride. Electrospinning was conducted approximately 55 °C above the T_g of the cinnamate acrylate and the electrospun fibers did not retain their fibrous morphology without photo-curing. Electrospinning without photo-curing produced an adhesive coating resulting from the bulk flow of the low T_g acrylic, and the surface of the collection substrate became tacky. However, electrospun fibers were collected that retained their fibrous morphology and resisted flow when *in situ* photo-cured during electrospinning. The intermolecular photo-dimerization of cinnamates resulted in a network formation that prevented the low T_g acrylic from flowing, and the photo-cured membrane contained a gel fraction of 74 ± 5%. *In situ* photo-curing represents a strategy to broaden the available polymer architectures to electrospin high surface area fibrous membranes for applications in medical bandages, filtration membranes, and protective clothing.

8.2 Introduction

Photo-reactive polymers are widely used in liquid crystalline,¹ drug delivery,² tissue engineering,³ adhesive,⁴ lithographic,⁵ coating,⁶ and photonic⁷ applications. Photo-reactions offer solvent-free environmentally beneficial strategies, efficient processing, selective reactivity, and fast curing kinetics.⁸ Photo-reactive monomers and oligomers are extensively applied as surface protective coatings due to an extremely fast rate of photo-crosslinking to form insoluble, mechanically durable networks.^{1,9,10} In the 1950's Minsk and coworkers were the first to study the photo-dimerization of cinnamate groups.^{11,12} Minsk and researchers reported the photo-crosslinking reaction of cinnamate groups in poly(vinyl cinnamate). Cinnamates are thermally stable below 200 °C¹³ and known to photo-dimerize without a photo-sensitizer through a $[2\pi + 2\pi]$ cycloaddition to form cyclobutane.¹⁴ Since Minsk's initial discovery the cinnamate functionality has received interest in polymeric and small molecules as a photo-reactive crosslinker.¹⁵⁻¹⁹ In the present study a low T_g cinnamate functionalized acrylate was electrospun in the presence of UV-irradiation to develop insoluble fibrous membranes.

Electrospinning is a strategy to develop nanostructured materials of nonwoven fibrous membranes with fiber diameters ranging from nanometers to microns with high surface areas.²⁰⁻²³ An external electric field is applied to a solution or melt traditionally containing entangled high molecular weight polymers. The solution or melt droplet becomes unstable in the presence of an electric field, and a submicron jet is ejected from the droplet and travels towards a grounded substrate.²⁴ As the jet travels toward the grounded substrate it becomes unstable and demonstrates a whipping motion. The whipping-like motion accounts for solvent evaporation and thinning of single fibers

resulting in submicron fiber diameters.²¹ The electrospun mat is collected as a disordered three-dimensional nonwoven fibrous membrane with a high specific surface area and submicron degree of porosity.²⁵ Traditionally, the formation of electrospun fibers requires viscous, entangled, high molecular weight polymers in solution or in the melt, since sufficient physical associations are necessary to withstand electrostatic forces and whipping instabilities of the charged electrospun jet.²⁰⁻²³ Solutions of low viscosity fluids without sufficient physical associations breaks up during electrospinning resulting in electrospraying.^{26,27} Electrospun fibers have received significant attention as filtration membranes, vascular grafts, drug delivery vehicles, and tissue scaffolds.²⁸⁻³¹

Electrospinning is typically conducted at room temperature and requires a polymer with a T_g above room temperature to prevent bulk flow of the electrospun membrane. However, thermal curing,³² UV-curing,³³ and chemical treatment³⁴ are strategies reported in the literature to crosslink electrospun fibers and increase their mechanical stability. Reported crosslinking mechanisms are applied post-electrospinning when the fiber has already formed and crosslinking increases the mechanical properties and decreases the membranes solubility.³²⁻³⁵ Gupta and coworkers³⁶ introduced a photo-curing technique to *in situ* photo-crosslink electrospun fibers of cinnamate functionalized poly(methyl methacrylate (MMA)-*co*-2-hydroxyethyl acrylate (HEA)). The electrospun jet was exposed to UV-irradiation while in flight to the grounded target. The cinnamate acrylates had T_g 's greater than 90 °C and no morphological difference was observed between the fibers electrospun with and without *in situ* photo-curing. However, the *in situ* photo-cured fibers produced insoluble crosslinked membranes and the non-cured membranes remained completely soluble. Kim and coworkers³⁷ were the first to *in situ*

photo-cure electrospun fibers of oligomeric precursors. Conventional free radical polymerization was used to synthesis prepolymers of 2-hydroxyethyl methacrylate (HEMA) and ethylene glycol dimethacrylate (EGDMA). Short polymerization times of 3-4 min at 70 °C were utilized to keep the oligomeric branched acrylates soluble. A photoinitiator was incorporated and the prepolymer solution was electrospun and *in situ* photo-cured, producing crosslinked electrospun HEMA hydrogels.

We report a strategy to electrospin low T_g polymers and develop insoluble crosslinked membranes. Our group's traditional electrospinning procedure^{21,38-44} was modified to UV-irradiate the electrospinning jet as it traveled to the grounded substrate, and Figure 8.1 displays the electrospinning setup with *in situ* photo-curing. Random copolymers of poly(n-butyl acrylate (nBA)-*co*-HEMA) were synthesized as a reactive macromolecular precursor. The precursor acrylate was functionalized with cinnamates to incorporate a photo-crosslinker that did not require a photo-sensitizer. HEMA repeating units of the precursor were functionalized with cinnamate groups from the acid chloride reaction with cinnamoyl chloride. The influence of *in situ* photo-curing during electrospinning was investigated, and the cinnamate acrylate electrospun membranes were characterized with SEM, FTIR spectroscopy, and gel fraction analysis.

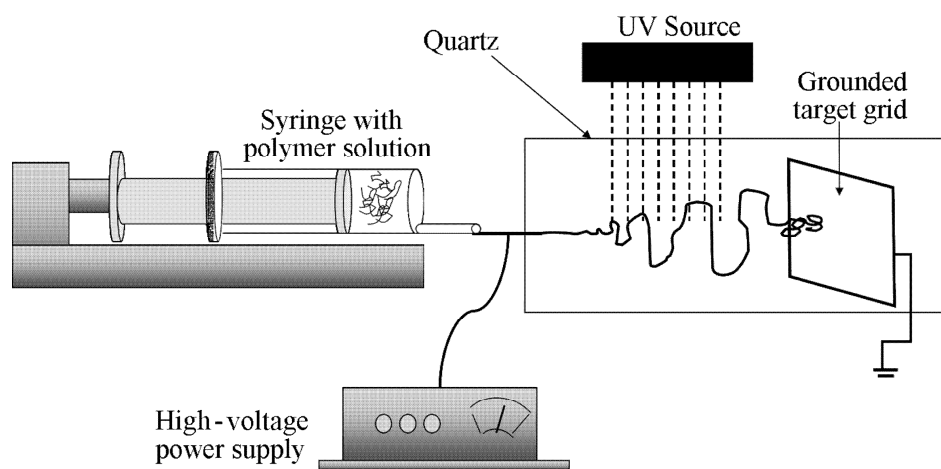


Figure 8.1 Electrospinning setup with *in situ* photo-curing.

8.3 Materials and Methods

8.3.1 Materials

Azobisisobutyronitrile (AIBN 98%), n-butyl acrylate ($\geq 99\%$), 2-hydroxyethyl methacrylate ($\geq 99\%$), cinnamoyl chloride (98%), triethylamine (TEA, $\geq 99\%$), hydroquinone (99%), ethyl acetate (HPLC), tetrahydrofuran (THF, HPLC), dichloromethane (HPLC), N,N-dimethylformamide (DMF, HPLC), chloroform, and methanol (HPLC) were purchased from Sigma-Aldrich Chemical Co. AIBN was recrystallized twice from methanol. THF was passed through a PURE SOLV MD-3 Solvent Purification System (Innovative Technology Inc.) immediately prior to use. Cinnamoyl chloride was sublimed and produced white crystals that melted between 35-37 °C. TEA was distilled from CaH_2 . nBA was passed through a neutral alumina column to remove any inhibitor. The purification of HEMA was modified from the literature procedure.⁴⁵ HEMA (100 g, 0.77 mols) was dissolved in distilled water (400 mL) and hydroquinone (0.10g, 0.90 mmol) was added. The aqueous solution was washed ten times with hexanes to remove any diacrylate present, and NaCl (50 g, 0.90 mol) was added to the final aqueous solution. HEMA was extracted from the aqueous layer with ethyl ether and additional hydroquinone (0.10 g, 0.90 mmol) was added. The organic layer was dried over CaSO_4 and concentrated in vacuum. HEMA was passed over neutral alumina to remove hydroquinone prior to use. All reactions were conducted under an argon environment in flamed-dried glassware, unless otherwise noted.

8.3.2 Instrumentation

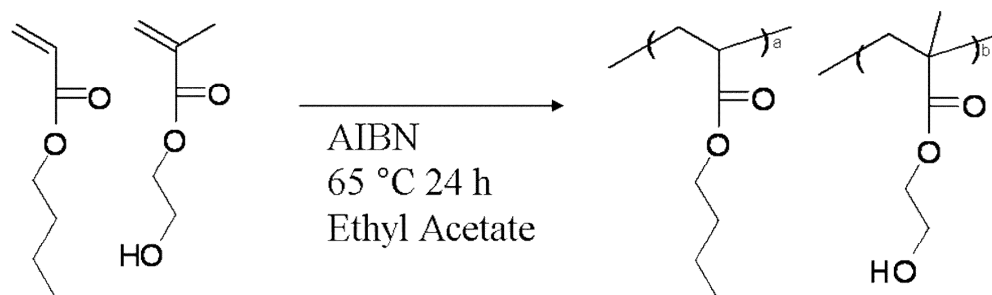
Size exclusion chromatography (SEC) was used to determine molecular weights and polydispersity indices (PDI), M_w/M_n . Molecular weights were determined at 40 °C

in tetrahydrofuran (ACS grade) at a flow rate of 1 mL min⁻¹ on a Waters GPC equipped with 3 in-line Polymer Laboratories PLgel 5 μm MIXED-C columns with a Waters 717 autosampler. A triple detection system included a Waters 2414 Refractive Index Detector, Viscotek 270 Dual Detector viscometer, and Wyatt Technologies miniDAWN multiangle laser light scattering (MALLS) detector. The MALLS detector was used to determine absolute weight-average molecular weights with the refractive index increments (dn/dc) determined online.

¹H NMR spectroscopy was performed on a Varian Unity 400 spectrometer at 400 MHz in CDCl₃. Differential scanning calorimetry (DSC) was performed under a nitrogen flush at a heating rate of 10 °C/min on a TA Instruments DSC 1000. Data was collected on the 2nd heat cycle. FTIR spectroscopy was performed on a MIDAC M-1700 FTIR with Durascope single bounce diamond ATR. UV-Vis spectroscopy was performed using an Analytical Instrument Systems Inc. spectrometer equipped with fiber optic cables, a DT1000CE light source, and an Ocean Optics USB2000 UV-Vis detector. UV-curing was performed with a Fusion UV Systems Inc. 100 W mercury bulb with a P300MT power supply. Light intensities were measured using an EIT Inc. UV power puck. Irradiation for 10 s produced intensities of UVA 0.326 W/cm² and UVB 0.262 W/cm².

8.3.3 Synthesis of Poly(nBA-co-HEMA) Precursor

Scheme 8.1 displays the reaction scheme for the synthesis of poly(nBA-co-HEMA) precursor. AIBN (0.504 g, 3.07 mmol) was dissolved in ethyl acetate (85.0 mL) in a 500-mL, round-bottomed flask equipped with a magnetic stir bar. nBA (43.5 g, 0.339 mol) and HEMA (6.84 g, 0.060 mol) were added to the reaction flask using a

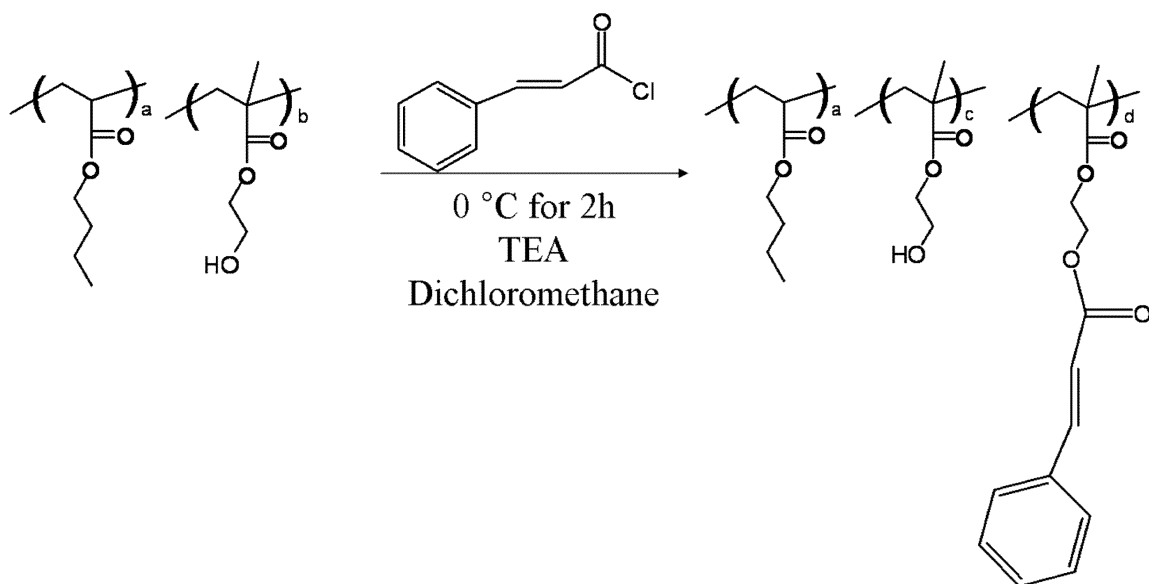


Scheme 8.1 Synthesis of the poly(nBA-*co*-HEMA) precursor.

degassed syringe. The reaction flask was placed in a 65 °C bath for 24 h. The reaction was precipitated into hexanes and vacuum dried under reduced pressure. 79 mol% nBA, 21 mol% HEMA, M_w 231,000, PDI 2.51, T_g -38 °C. ATR-IR: (C=O) 1714 cm^{-1} , (C-H) 2800-2950 cm^{-1} , (C-O) 1000-1260 cm^{-1} . ^1H NMR, (CDCl_3): δ (ppm) 4.07 (2H, $\text{CO}_2\text{-CH}_2\text{-CH}_2$ (nBA)) and (2H, $\text{CO}_2\text{-CH}_2\text{-CH}_2$ (HEMA)), 3.80 (2H, $\text{CH}_2\text{-CH}_2\text{-OH}$ (HEMA)), 0.90 (3H, $\text{CH}_2\text{-C(-CH}_3\text{)(-C(O)-O-)}$ (HEMA)). The chemical shifts of all the protons in the polymer backbone were between 2.50 and 1.00 ppm.

8.3.4 Cinnamate Functionalization of the Acrylic Precursor

Scheme 8.2 displays the reaction scheme for the cinnamate functionalization of the acrylic precursor. The precursor (7.55 g, 0.013 mol HEMA) was dissolved in dichloromethane (20.0 mL) in a 250-mL, two-necked, round-bottomed flask equipped with a magnetic stir bar and addition funnel. The solution was placed in an ice bath and triethylamine (3.19 g, 0.032 mol) was added to the reaction flask using a degassed syringe. Cinnamoyl chloride (5.25 g, 0.032 mol) was dissolved in dichloromethane (6 mL) and added drop-wise to the reaction flask. The reaction was stirred in an ice bath for 2 h. The reaction was precipitated into hexanes and vacuum dried under reduced pressure. 79 mol% nBA, 15 mol% HEMA, 6 mol% cinnamoyloxyethyl methacrylate (CEMA), M_w 254,000, PDI 2.25, T_g -30 °C. ATR-IR: cinnamate (C=C, vinyl) 1637 cm^{-1} , (C=C, Aromatic) 1500 cm^{-1} . ^1H NMR, (CDCl_3): δ (ppm) 7.75 (1H, $\text{CO}_2\text{-CH=CH-Ar}$ (CEMA)), 7.57 (2H, Ar H (CEMA)), 7.40 (3H, Ar H (CEMA)), 6.51 (1H, $\text{CO}_2\text{-CH=CH-Ar}$ (CEMA)), 4.40 (2H, C(O)-O- $\text{CH}_2\text{-CH}_2$ (CEMA)), 4.21 (2H, $\text{CO}_2\text{-CH}_2\text{-CH}_2$ (CEMA)), 4.07 (2H, $\text{CO}_2\text{-CH}_2\text{-CH}_2$ (nBA)) and (2H, $\text{CO}_2\text{-CH}_2\text{-CH}_2$ (HEMA)), 3.80 (2H, $\text{CH}_2\text{-CH}_2\text{-OH}$ (HEMA)), 0.90 (3H, $\text{CH}_2\text{-C(-CH}_3\text{)(-C(O)-O-)}$ (HEMA)).



Scheme 8.2 Cinnamate functionalization of the acrylic precursor.

OH (HEMA)), 0.90 (3H, CH₂-C(-CH₃)(-CO₂) (HEMA)). The chemical shifts of all the protons in the polymer backbone were between 2.50 and 1.00 ppm.

8.3.5 *In situ* Photo-curing Electrospun Fibers

The cinnamate functionalized acrylate was dissolved in DMF/CHCl₃ (3/1 vol) at concentrations of 15 wt%, 25 wt%, and 35 wt%. Electrospun fibers of the cinnamate functionalized acrylate were collected following our groups electrospinning procedure,^{21,38-44} which was adapted to include *in situ* photo-curing, as shown in Figure 8.1. The solutions were transferred to a 20-mL syringe with an 18-gauge needle, and the syringe was mounted in a KD Scientific Inc. syringe pump. The positive lead of a Spellman High Voltage Electronics Corp. CZE1000R high voltage power supply was connected to the syringe needle, and the stainless steel collection target was grounded and at a tip to screen (TTS) distance of 15 cm. The fluid was pumped at a constant flow of 5 mL/h, and 15 kV of voltage was applied. The electrospinning jet was exposed to a F300M Fusion UV System with H-bulb and intensity in the UVB of 0.245 W/cm². The same setup was used to electrospin a 25 wt% cinnamate acrylic solution in DMF/THF (3/1 vol) without UV-irradiation. Electrospun fibers were analyzed using a Leo[®] 1550 field emission scanning electron microscope (FESEM). Electrospun fibers were collected on a ¼" x ¼" stainless steel mesh, and adhered to a SEM disc. The mounted fibers were sputter-coated with an 8 nm Pt/Au layer to reduce electron charging. Gel fractions were determined for *in situ* photo-cured electrospun fibers and non-cured controls. Soxhlet extractions were performed in refluxing THF for 16 h.

8.4 Results and Discussion

8.4.1 Synthesis and Functionalization of Poly(nBA-co-HEMA) with Photo-reactive Cinnamate

nBA was incorporated into the precursor copolymer to provide a low T_g segment, and HEMA was incorporated as a functionalization site for the subsequent incorporation of cinnamate groups. The acrylic precursor contained 79 mol% nBA and 21 mol% HEMA and a M_w 231,000, PDI 2.51, and T_g -38 °C. The precursor copolymer was functionalized with cinnamates to incorporate a photo-crosslinker. HEMA repeating units of the precursor were functionalized with cinnamate groups from the acid chloride reaction with cinnamoyl chloride. Characterization following cinnamate functionalization was performed using NMR spectroscopy, FTIR spectroscopy, DSC, and SEC analysis. ^1H NMR analysis of the cinnamate functionalized precursor confirmed the appearance of cinnamate resonances at 6.51, 7.40, 7.57, and 7.75 ppm. The resonance at 3.80 ppm corresponding to the methylene adjacent to the hydroxyl of HEMA diminished, and a new resonance at 4.40 ppm corresponding to the methylene adjacent to the ester of cinnamoyloxyethyl methacrylate (CEMA) appeared. The cinnamate functionalized acrylate contained 79 mol% nBA, 15 mol% HEMA, and 6 mol% CEMA and a M_w 254,000, PDI 2.25, and T_g -30 °C. As expected, the T_g increased following cinnamate functionalization due to the incorporation of planar bulky cinnamate groups. The UV-vis characterization of the precursor and cinnamate functionalized films are shown in Figure 8.2. The precursor did not absorb in the UV region, however, the cinnamate chromophore of the functionalized acrylic absorbed at 275 nm.

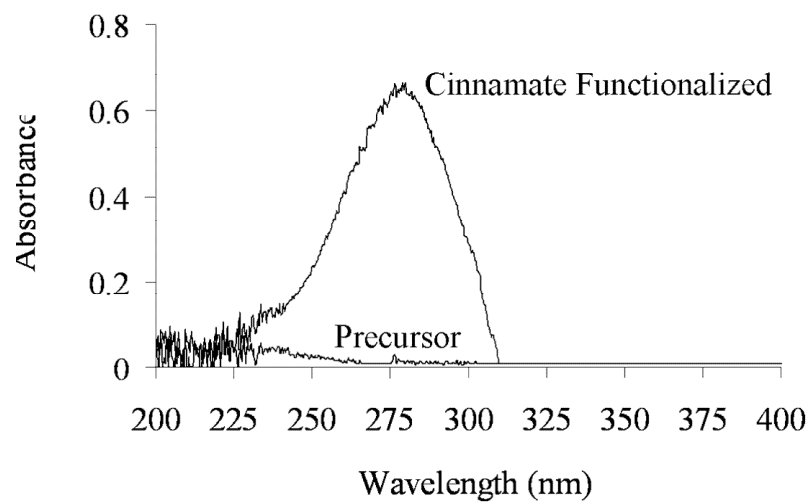


Figure 8.2 UV-vis absorbance of the acrylic precursor and cinnamate functionalized acrylate.

8.4.2 Electrospinning Cinnamate Functionalized Low T_g Acrylic Without UV-curing

Cinnamate functionalized acrylic electrospun fibers did not retain their fibrous morphology without *in situ* photo-crosslinking. The T_g of the cinnamate functionalized acrylate was $-30\text{ }^\circ\text{C}$ and electrospinning experiments were conducted at room temperature, approximately $55\text{ }^\circ\text{C}$ above the T_g . An electrospun jet originated from the Taylor cone of the electrospinning droplet and the cinnamate functionalized acrylate did electrospin fibers without *in situ* photo-curing. However, the low T_g acrylic fibers flowed and did not retain their fibrous structure. Electrospinning without *in situ* photo-curing resulted in a low T_g acrylic coating on the collection substrate as shown in the SEM image in Figure 8.3. The surface of the collection grid became tacky due to the low T_g acrylic coating, and the acrylic was easily removed from the substrate when washed with THF. Choi and coworkers⁴⁶ observed the flow of polybutadiene (T_g $-80\text{ }^\circ\text{C}$) electrospun fibers that were not crosslinked, and UV-curing post-electrospinning was necessary to retain the polybutadiene fiber morphology.

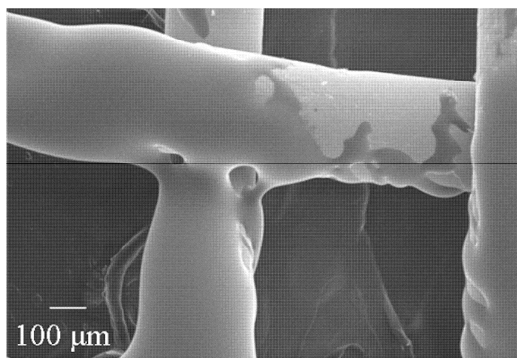


Figure 8.3 SEM of cinnamate functionalized acrylic electrospun without *in situ* photo-curing, which resulted in an acrylic coating on the collection substrate.

8.4.3 *In situ* Photo-crosslinking Electrospun Cinnamate Functionalized Low T_g Acrylic Fibers

The literature reports many examples of high molecular weight polymers electrospun from viscous solutions at concentrations typically above C_e or from the melt phase, and chain entanglements are necessary to withstand the Raleigh instabilities and stabilize the whipping electrified jet to produce continuous fibers.^{20,21,23,47} Traditionally polymers with a T_g greater than room temperature are electrospun to prevent polymer flow and retain the fiber morphology, however, thermal curing,³² UV-curing,³³ and chemical treatment³⁴ are strategies reported in the literature to crosslink electrospun fibers. Reported crosslinking mechanisms are applied post-electrospinning when the fiber has already formed and crosslinking increases the mechanical properties and decreases the membranes solubility.³²⁻³⁵ We report a strategy to electrospin low T_g polymers and develop insoluble crosslinked membranes.

Electrospun fibers were *in situ* photo-crosslinked to develop fibrous membranes of cinnamate functionalized low T_g acrylates. The electrospun jet generated from the Taylor cone of the electrospinning droplet was UV-irradiated as it proceeded to the collection substrate as shown in Figure 8.1. The UV-light was irradiated through a quartz plate onto the electrospinning jet to prevent the collection of electrospun fibers on the UV-light. As shown in Figure 8.2 the cinnamate chromophore absorbs 275 nm light in the UVB region. The UVB intensity measured through the quartz plate at a distance of 20 cm from the UV-lamp was 0.245 W/cm² with an energy dose of 2.48 J/cm² for 10 s.

Cinnamate functionalized acrylic electrospun fibers retained their fibrous morphology when *in situ* photo-cured. DMF/THF (3/1 vol) was chosen as the

electrospinning solvent to balance the solvents volatility and optimize the electrospinning procedure. DMF (bp 153 °C) was incorporated as a low vapor pressure solvent to provide mobility to the cinnamate side chains in the electrospun jet. Upon UV-irradiation vinyl cinnamate groups require a center to center distance $\leq 4.2 \text{ \AA}$ to promote photo-dimerization.⁴⁸ Sufficient chain mobility was required to arrange cinnamates in a conformation beneficial for photo-dimerization. The low volatility of DMF increased the polymer chain mobility in the electrospinning jet, and provided the fluidity necessary for cinnamates to photo-dimerize. THF (bp 66 °C) was incorporated as a good solvent for the cinnamate functionalized acrylic and as a volatile portion to prevent solvent accumulation in the collected fibers.

Figure 8.4 displays the *in situ* photo-cured cinnamate acrylate electrospun fibers at different electrospinning concentrations. Droplets formed at 15 wt% (Figure 8.4a) as a result of the low solution viscosity destabilizing the electrified jet. Sufficient solution viscosities were necessary to withstand the electrostatic forces and whipping instabilities of the charged electrospun jet.²⁰⁻²³ When the concentration was increased to 25 wt% smooth continuous fibers formed with diameters ranging from 5 μm to 10 μm , as shown in Figure 8.4b. The increased solution viscosity stabilized the electrospinning jet and resulted in the transition from droplets to continuous fibers at 25 wt%. Figure 8.4c displays the formation of continuous fibers with larger diameters ranging from 20 μm to 60 μm when electrospun from 35 wt%.

The FTIR spectra of the cinnamate acrylate and *in situ* photo-cured electrospun membrane are displayed in Figure 8.5. The cinnamate C=C absorbance at 1637 cm^{-1} for the cinnamate acrylate disappeared in the photo-cured electrospun membrane. The

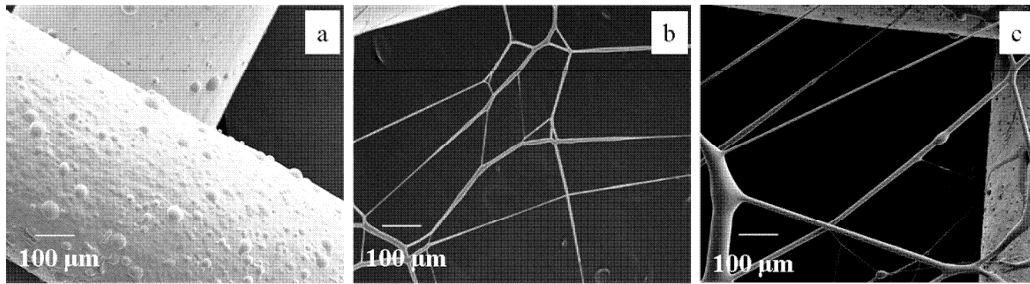


Figure 8.4 SEM of the *in situ* photo-cured cinnamate acrylate electrospun fibers from concentrations of a) 15 wt% b) 25 wt% c) 35 wt% in DMF/THF (3/1 vol).

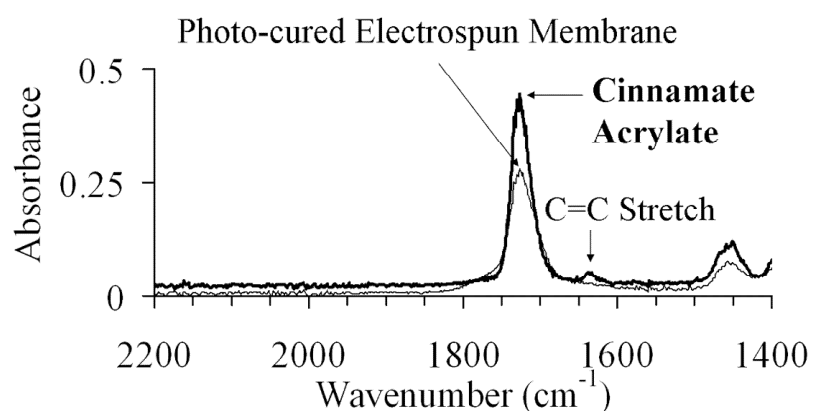


Figure 8.5 FTIR spectroscopy of the cinnamate acrylate and *in situ* photo-cured electrospun membrane. The cinnamate C=C stretch decreased following photo-curing.

decrease in vinyl concentration was attributed to cinnamate photo-dimerization resulting from the $[2\pi + 2\pi]$ cycloaddition of conjugated cinnamates. The gel fraction analysis was conducted on control films of non-cured cinnamate acrylate and *in situ* photo-cured electrospun membranes in refluxing THF. The non-cured control films contained no gel fraction due to their linear topology and solubility in THF. However, the photo-cured electrospun membranes contained gel fractions of $74 \pm 5\%$ due to the network architecture formed from the intermolecular photo-dimerization of cinnamates.

8.5 Conclusion

Electrospun fibers were *in situ* photo-crosslinked to develop fibrous membranes from cinnamate functionalized low T_g acrylics. The random acrylic precursor contained 79 mol% nBA, 21 mol% HEMA and T_g -38 °C. The precursor acrylic was functionalized with cinnamates to incorporate a photo-crosslinker that was thermally stable and did not require a photo-initiator. HEMA repeating units of the precursor were functionalized with cinnamate groups from the acid chloride reaction with cinnamoyl chloride. The cinnamate functionalized acrylic contained 79 mol% nBA, 15 mol% HEMA, and 6 mol% CEMA and T_g -30 °C. *In situ* photo-curing was required to electrospin continuous fibers that retained their fibrous morphology. Electrospinning was conducted approximately 55 °C above the T_g of the cinnamate acrylate, and electrospinning without *in situ* photo-curing resulted in bulk flow of the fibers and acrylic coating on the collection substrate. Fibrous membranes were collected of the low T_g cinnamate acrylate in the presence of *in situ* photo-curing. The electrospun jet generated in the presence of an electric field was UV-irradiated as it proceeded to the collection substrate. The photo-cured electrospun jet facilitated the formation of photo-dimers due to the rapid rate of cinnamate photo-

reactivity, and the intermolecular network prevented bulk polymer flow and stabilized the fiber structure. The cinnamate C=C absorbance at 1637 cm^{-1} decreased in the photo-cured electrospun membrane indicating the disappearance of conjugated cinnamate groups from the formation of photo-dimers. The *in situ* photo-cured electrospun membranes produced gel fractions of $74 \pm 5\%$, and represented a strategy to develop robust nonwoven membranes from low T_g macromolecules.

8.6 Acknowledgements

We would like to acknowledge Brian R. Mohns of Virginia Tech for constructing the *in situ* photo-curing electrospinning setup. This material is work based upon funding from Avery Dennison Performance Polymers.

8.7 References

1. Clapper, J. D.; Sievens-Figueroa, L.; Guymon, C. A., *Chem. Mater.* **2008**, *20* (3), 768-781.
2. Van Tomme, S. R.; Storm, G.; Hennink, W. E., *Int. J. Pharm.* **2008**, *355* (1-2), 1-18.
3. Ifkovits, J. L.; Burdick, J. A., *Tissue Eng.* **2007**, *13* (10), 2369-2385.
4. Chang, E.; Holguin, D., *J. Adhes.* **2005**, *81* (5), 495-508.
5. Tey, J. N.; Soutar, A. M.; Priyadarshi, A.; Mhaisalkar, S. G.; Hew, K. M., *J. Appl. Polym. Sci.* **2007**, *103* (3), 1985-1991.
6. Karatas, S.; Hosgor, Z.; Menciloglu, Y.; Kayaman-Apohan, N.; Gungor, A., *J. Appl. Polym. Sci.* **2006**, *102* (2), 1906-1914.
7. Song, B. J.; Park, J. K.; Kim, H. K., *J. Polym. Sci., Part A: Polym. Chem.* **2004**, *42* (24), 6375-6383.
8. Kaur, M.; Srivastava, A. K., *J. Macromol. Sci., Polym. Rev.* **2002**, *C42* (4), 481-512.
9. Khudyakov, I. V.; Turro, N. J., *Photochem. UV-Curing* **2006**, 241-251.
10. Baroli, B., *J. Chem. Technol. Biotechnol.* **2006**, *81* (4), 491-499.
11. Robertson, E. M.; Van Deusen, W. P.; Minsk, L. M., *J. Appl. Polym. Sci.* **1959**, *2* (6), 308-311.
12. Minsk, L. M.; Smith, J. G.; Van Deusen, W. P.; Wright, J. F., *J. Appl. Polym. Sci.* **1959**, *2* (6), 302-307.
13. Sung, S.-J.; Cho, K.-Y.; Yoo, J.-H.; Kim, W. S.; Chang, H.-S.; Cho, I.; Park, J.-K., *Chem. Phys. Lett.* **2004**, *394* (4-6), 238-243.
14. Kimura, T.; Kim, J.-Y.; Fukuda, T.; Matsuda, H., *Macromol. Chem. Phys.* **2002**, *203* (16), 2344-2350.
15. Cashion, M. P.; Park, T.; Long, T. E., *J. Adhes.* **2009**, *85* (1), 1-17.
16. Visconte, L. L. Y.; Andrade, C. T.; Azuma, C., *J. Appl. Polym. Sci.* **1998**, *69* (5), 907-910.
17. Coleman, M. M.; Hu, Y.; Sobkowiak, M.; Painter, P. C., *J. Polym. Sci., Part B Polym. Phys.* **1998**, *36* (9), 1579-1590.
18. Murase, S.; Kinoshita, K.; Horie, K.; Morino, S., *Macromolecules* **1997**, *30* (25), 8088-8090.
19. Andreopoulos, F. M.; Roberts, M. J.; Bentley, M. D.; Harris, J. M.; Beckman, E. J.; Russell, A. J., *Biotechnol. Bioeng.* **1999**, *65* (5), 579-588.
20. Gupta, P.; Elkins, C.; Long, T. E.; Wilkes, G. L., *Polymer* **2005**, *46* (13), 4799-4810.

21. McKee, M. G.; Wilkes, G. L.; Colby, R. H.; Long, T. E., *Macromolecules* **2004**, *37* (5), 1760-1767.
22. Rutledge, G. C.; Fridrikh, S. V., *Adv. Drug Delivery Rev.* **2007**, *59* (14), 1384-1391.
23. Shenoy, S. L.; Bates, W. D.; Frisch, H. L.; Wnek, G. E., *Polymer* **2005**, *46* (10), 3372-3384.
24. Burger, C.; Hsiao, B. S.; Chu, B., *Annu. Rev. Mater. Res.* **2006**, *36*, 333-368.
25. Deitzel, J. M.; Kleinmeyer, J.; Harris, D.; Tan, N. C. B., *Polymer* **2001**, *42* (1), 261-272.
26. Fong, H.; Chun, I.; Reneker, D. H., *Polymer* **1999**, *40* (16), 4585-4592.
27. Shenoy, S. L.; Bates, W. D.; Wnek, G., *Polymer* **2005**, *46* (21), 8990-9004.
28. Dalton, P. D.; Joergensen, N. T.; Groll, J.; Moeller, M., *Biomed. Mater.* **2008**, *3* (3), 1-11.
29. Greiner, A.; Wendorff, J. H., *Angew. Chem. Int. Ed.* **2007**, *46*, 5670-5703.
30. Casper, C. L.; Yamaguchi, N.; Kiick, K. L.; Rabolt, J. F., *Biomacromolecules* **2005**, *6* (4), 1998-2007.
31. Ner, Y.; Grote, J. G.; Stuart, J. A.; Sotzing, G. A., *Soft Matter* **2008**, *4* (7), 1448-1453.
32. Li, L.; Hsieh, Y. L., *Nanotechnology* **2005**, *16* (12), 2852-2860.
33. Liu, Y. R.; Bolger, B.; Cahill, P. A.; McGuinness, G. B., *Mater. Lett.* **2009**, *63* (3-4), 419-421.
34. Ignatova, M.; Manolova, N.; Markova, N.; Rashkov, I., *Macromol. Bio.* **2009**, *9* (1), 102-111.
35. Tan, A. R.; Ifkovits, J. L.; Baker, B. M.; Brey, D. M.; Mauck, R. L.; Burdick, J. A., *J. Biomed. Mater. Res. A* **2008**, *87A* (4), 1034-1043.
36. Gupta, P.; Trenor, S. R.; Long, T. E.; Wilkes, G. L., *Macromolecules* **2004**, *37* (24), 9211-9218.
37. Kim, S. H.; Kim, S.-H.; Nair, S.; Moore, E., *Macromolecules* **2005**, *38* (9), 3719-3723.
38. Hunley, M. T.; Harber, A.; Orlicki, J. A.; Rawlett, A. M.; Long, T. E., *Langmuir* **2008**, *24* (3), 654-657.
39. Hunley, M. T.; Long, T. E., *Polym. Int.* **2008**, *57* (3), 385-389.
40. Hunley, M. T.; McKee, M. G.; Long, T. E., *J. Mater. Chem.* **2007**, *17* (7), 605-608.
41. McKee, M. G.; Elkins, C. L.; Long, T. E., *Polymer* **2004**, *45* (26), 8705-8715.
42. McKee, M. G.; Hunley, M. T.; Layman, J. M.; Long, T. E., *Macromolecules* **2006**, *39* (2), 575-583.
43. McKee, M. G.; Layman, J. M.; Cashion, M. P.; Long, T. E., *Science* **2006**, *311* (5759), 353-355.
44. McKee, M. G.; Park, T.; Unal, S.; Yilgor, I.; Long, T. E., *Polymer* **2005**, *46* (7), 2011-2015.
45. Coca, S.; Jasieczek, C. B.; Beers, K. L.; Matyjaszewski, K., *J. Polym. Sci., Part A Polym. Chem.* **1998**, *36* (9), 1417-1424.
46. Choi, S. S.; Hong, J. P.; Seo, Y. S.; Chung, S. M.; Nah, C., *J. Appl. Polym. Sci.* **2006**, *101* (4), 2333-2337.

47. Huang, Z.-M.; Zhang, Y.-Z.; Kotaki, M.; Ramakrishna, S., *Compos. Sci. Technol.* **2003**, *63*, 2223-2253.
48. Cohen, M. D.; Schmidt, G. M. J.; Sonntag, F. I., *J. Chem. Soc.* **1964**, 2000-2013.

Chapter 9: Overall Conclusions

The synthesis and characterization of photo-reactive low molar mass surfactants and macromolecules was described. First, the micellar morphology of gemini surfactant, 12-2-12, was investigated to fundamentally understand the solution properties of ammonium gemini surfactants. The solution microstructure in water and water:methanol was characterized with cryo-TEM and solution rheology. The cosolvent mixture of water:methanol was investigated to explore the solvents role in self-assembly and electrospinning. The 12-2-12 microstructure in water transitioned from linear, entangled, threadlike micelles to branched threadlike micelles at 1.5 wt%, and at 2.7 wt% the microstructure evolved into a viscoelastic, entangled, highly-branched threadlike network. In water:methanol 12-2-12 produced a considerably different micellar microstructure compared to water, and the micellar morphology transitioned from partitioned globular micelles into overlapped micelles at $C^* = 11$ wt%.

The supramolecular microstructures of 12-2-12 in water and water:methanol lead to highly viscous solutions, and their electrospinning was explored. Electrospinning 12-2-12 in water did not produce surfactant fibers at any concentration. However, for the first time nonwoven fibrous scaffolds were electrospun from gemini surfactants, with fiber diameters between 0.9 and 7 μm with water:methanol as the solvent. The 12-2-12 fiber morphology transitioned from beaded fibers into continuous fibers at concentrations greater than $2C^*$ in water:methanol. The entangled supramolecular structure of the low molar mass surfactant stabilized the electrospinning jet and resulted in continuous fibers. Electrospinning gemini surfactant fibers from polar solvents represents an innovative

strategy to develop high surface area scaffolds or membranes with charged hydrophilic surfaces for the development of charged controlled-release membranes, tissue engineering scaffolds, or biologically compatible coatings.

In situ FTIR spectroscopy was used to explore the influence of spacer length on the quaternization reaction rate for the synthesis of 12-2-12 and 12-6-12. Complete quaternization of 12-6-12 was completed after only 5 h, whereas 12-2-12 required 40 h. The electron donating character of hexamethylene increased the nucleophilicity of the unreacted amine, and decreased the reaction time required to complete quaternization.

DSC was correlated with PLM to explore the thermal transitions of model and photopolymerizable gemini surfactants. DSC and PLM characterization were limited to 160 °C to prevent thermal degradation of the quaternized ammonium surfactants. Gemini 12-2-12 was the only surfactant that displayed two endothermic transitions at 94 °C and 104 °C. Both thermal transitions corresponded to crystal-to-crystal transitions, meaning 12-2-12 has three crystalline structures. One endothermic transition was observed for 16-2-16 and 18-2-18 at 104 °C and 105 °C, respectively, and each corresponded to a crystal-to-crystal transition. A single broad endothermic transition centered at 98 °C was observed for Acry-2-Acry, and Cinn-2-Cinn had the highest endothermic transition at 143 °C, which corresponded to an isotropic melting transition.

Conductance experiments were utilized to explore the influence of concentration and tail composition on T_k in water and water:methanol. No change in conductance was measured and no T_k was observed for 12-2-12 at concentrations below the CMC. However, the T_k was consistent at concentrations above the CMC. The T_k of the gemini surfactant series was measured in water and water:methanol to explore the influence of

solvent on the solution properties. The T_k increased with increasing tail size in water and water:methanol. 12-2-12 displayed the lowest T_k at 15.8 °C and Cinn-2-Cinn the highest at 69.5 °C in water. A similar trend was evident in water:methanol, in which 12-2-12 had the lowest T_k at -17.0 and Cinn-2-Cinn the highest at 46.2 °C. The T_k was lower for all surfactants in water:methanol compared to water because the cosolvent disrupted the crystalline packing of the gemini tails. The addition of a cosolvent represents a strategy to increase the applicable temperature range for gemini surfactants.

The influence of hydrogen bonding associations on the photo-reactivity of cinnamate functionalized macromolecular architectures was studied. A novel synergy combining hydrogen bonding and photo-reactive groups was developed in low T_g acrylics for application as hot melt pressure sensitive adhesives. Acrylic copolymers of 2-ethylhexyl acrylate (EHA), 2-hydroxyethyl acrylate (HEA), and methyl acrylate (MA) were functionalized with urethane and cinnamate groups, and the reaction conditions were optimized to control the degree of functionality and manipulate the relationship between hydrogen bonding and photo-active sites. Hydrogen bonding associations provided strategies to increase the apparent molecular weight post-processing to prevent creep and cohesive failure. Processing above the hydrogen bonding dissociation temperature presents a methodology to maintain viscosities low for melt processing. Isothermal rheological experiments at 150 °C confirmed the melt stability of the cyclohexyl urethane linkage, cinnamate, and the acrylic adhesive composition.

Low T_g acrylic precursors were functionalized with both urethane and cinnamate groups. The charged molar equivalence of cyclohexyl isocyanate to HEA determined the degree of urethane functionalization. All remaining residual HEA units of the urethane

functionalized acrylic were reacted with cinnamoyl chloride introducing cinnamate functionality. The UV-cured peel strength increased as the concentration of urethane increased. Higher concentrations of cinnamates increased the T_g of the UV-cured film, preventing the adhesive from spreading and adequately contacting the substrate. All UV-cured films containing cinnamate groups failed 100% adhesively. Complete adhesive failure was attributed to the network formation from the intermolecular photo-dimerization of cinnamates. The percentage of adhesive failure for non-cured tapes increased as the concentration of urethane units increased. Increasing adhesive failure with urethane concentration was attributed to an increase in apparent molecular weight resulting from the intermolecular association of hydrogen bonding groups.

A control series was synthesized for comparison to the urethane series to investigate the influence of hydrogen bonding groups on the rate and efficiency of cinnamate photo-reactivity. The control series contained cinnamate groups and residual HEA units, and did not contain any urethane sites. The rate of cinnamate photo-dimerization as a function of composition comparing the urethane and control series was determined from a second order kinetic plot following the disappearance of conjugated cinnamates with UV-exposure. The urethane sample, **2U₂₁C₃**, and the control sample, **2H₂₁C₃**, contained three mole percent cinnamate with comparable molecular weights. Sample **2U₂₁C₃** dimerized at a rate of 0.314 s^{-1} and **2H₂₁C₃** at a rate of 0.170 s^{-1} , indicating the presence of urethane groups assisted in the rate of cinnamate dimerization through the formation of intermolecular hydrogen bonds that confined the cinnamate groups in a proximity beneficial for photo-reactivity. The presence of the urethane was not influential when the concentration of the cinnamate group was increased for samples

2U₈C₁₆ and **2H₉C₁₅**. The low concentration of urethane groups did not influence the rate of cinnamate photo-reactivity and the rate of dimerization was very similar for **2U₈C₁₆** and **2H₉C₁₅** at 0.069 s⁻¹ and 0.081 s⁻¹, respectively. The relationship between urethane groups and cinnamate photo-reactivity provides evidence that high concentrations of hydrogen bonding associations can increase the efficiency of cinnamate photo-dimerization.

Photo-rheology was introduced to explore the influence of hydrogen bonding associations on the photo-reactivity of cinnamate functionalized low T_g acrylic precursors. A random copolymer of poly(nBA-co-HEMA) was functionalized with cinnamate and urethane groups to introduce hydrogen bonding and photo-reactive sites, respectively. The reaction conditions were optimized to control the degree of functionality and a series of urethane and cinnamate containing acrylics were synthesized with comparable molecular weights. Photo-rheology was utilized to monitor the viscoelastic changes in material properties with UV-exposure. Cinnamate functionalized samples displayed an increase in viscosity with exposure time. The change in viscosity was attributed to the intermolecular dimerization of cinnamates. The percentage increase in viscosity during photo-curing decreased as the urethane concentration increased. This was attributed to a lower concentration of cinnamate groups and lower degree of crosslinking.

UV-vis spectroscopy was utilized to determine the concentration of conjugated cinnamate groups following segmented irradiation periods. Conjugated cinnamate absorbance at 275 nm decreased as UV-exposure time increased. The rate of cinnamate

dimerization increased as the concentration of urethane increased, suggesting that hydrogen bonding sites promoted cinnamate dimerization.

For the first time electrospun fibers were *in situ* photo-crosslinked to develop fibrous membranes from cinnamate functionalized low T_g acrylics. The random acrylic precursor contained 79 mol% nBA, 21 mol% HEMA and T_g -38 °C. The precursor acrylic was functionalized with cinnamates to incorporate a photo-crosslinker that was thermally stable and did not require a photo-initiator. HEMA repeating units of the precursor were functionalized with cinnamate groups from the acid chloride reaction with cinnamoyl chloride. The cinnamate functionalized acrylic contained 79 mol% nBA, 15 mol% HEMA, and 6 mol% CEMA and T_g -30 °C. *In situ* photo-curing was required to electrospin continuous fibers that retained their fibrous morphology. Electrospinning was conducted approximately 55 °C above the T_g of the cinnamate acrylate, and electrospinning without *in situ* photo-curing resulted in bulk flow of the fibers and acrylic coating on the collection substrate. Fibrous membranes were collected of the low T_g cinnamate acrylate in the presence of *in situ* photo-curing. The electrospun jet generated in the presence of an electric field was UV-irradiated as it proceeded to the collection substrate. The photo-cured electrospun jet facilitated the formation of photo-dimers due to the rapid rate of cinnamate photo-reactivity, and the intermolecular network prevented bulk polymer flow and stabilized the fiber structure. The cinnamate C=C absorbance at 1637 cm^{-1} decreased in the photo-cured electrospun membrane indicating the disappearance of conjugated cinnamate groups from the formation of photo-dimers. The *in situ* photo-cured electrospun membranes produced gel fractions of $74 \pm 5\%$, and

represented a strategy to develop robust nonwoven membranes from low T_g macromolecules.

Chapter 10: Suggested Future Work

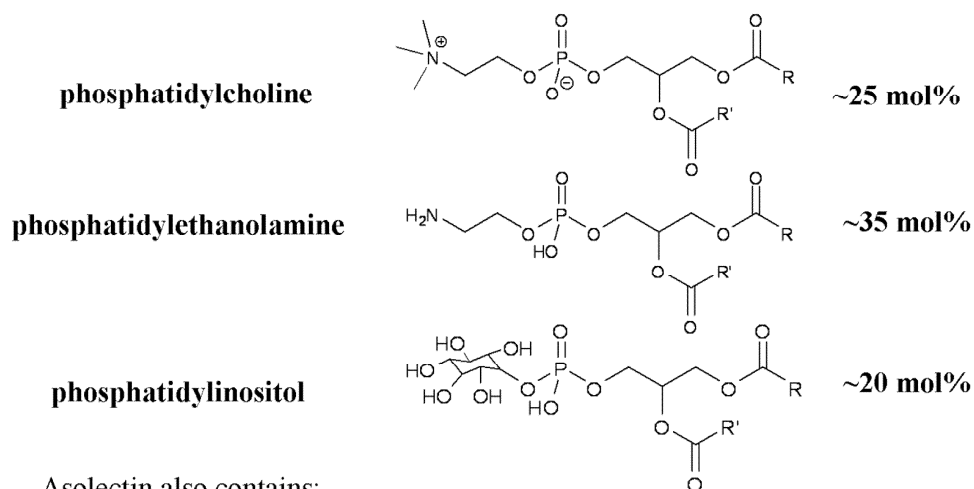
10.1 Photopolymerizable Gemini Surfactant Lyotropic Liquid Crystals

Explore the lyotropic liquid crystalline (LLC) behavior of photopolymerizable Acry-2-Acry and Cinn-2-Cinn gemini surfactants in water. Gin and coworkers¹ synthesized a phosphonium gemini surfactant with diene groups at the terminal of each hydrocarbon tail. The phosphonium gemini surfactants formed hexagonal (H_I), bicontinuous cubic (Q_I), and lamellar (L_α) phases in water. A photoinitiator was necessary to photopolymerize the LLC phases with retention of the self-assembled architectures. The polymerized LLC phases resulted in a crosslinked microstructure that was insoluble and thermally stable. Ammonium gemini surfactants Acry-2-Acry and Cinn-2-Cinn are novel surfactant compositions that are not reported in the literature. The smaller size of the ammonium headgroup compared to phosphonium would increase the packing parameter, and allow LLC phases to form at lower surfactant concentrations. Acry-2-Acry would require a photoinitiator to polymerize the self-assembled architecture, however, Cinn-2-Cinn would not require a photoinitiator. Crosslinked gemini surfactant hexagonal and bicontinuous cubic phases offer potential as drug-delivery vehicles,² nanofiltration membranes for the purification of water,³ and as nanoreactors for the synthesis of novel nanostructured materials.⁴

10.2 Photo-reactive Asolectin Electrospun Membranes

Our research group was the first to electrospin nonwoven membranes from low molar mass lipids.⁵ The electrospun lipid membrane was soluble and not mechanically stable because the lipids were physically associated and not covalently coupled.

Asolectin is a mixture of phospholipids with a variety of charged and uncharged headgroup compositions shown in Figure 10.1. The tails of the lipid mixture are composed of 24% saturated fatty acids, 14% mono-unsaturated fatty acids, and 62%



Asolectin also contains:

- Minor amounts of other phospholipids, polar lipids, and ~3 mol% H₂O
- Approximately 24% saturated fatty acids, 14% mono-unsaturated and 62% poly-unsaturated fatty acids

Figure 10.1 Mixture of lipids that compose asolectin. Referenced from Sigma-Aldrich.

poly-unsaturated fatty acids. Preliminary experiments indicated asolectin absorbs in the UV-region from 270 nm to 320 nm as shown in Figure 10.2. Asolectin films were UV-irradiated to explore the photopolymerizable behavior of the unsaturated asolectin lipids. Bulk films of asolectin were cast from 40 wt% solutions in chloroform containing 0 wt%, 0.1 wt%, and 1.0 wt% 2,2-dimethoxy-2- phenylacetophenone photoinitiator. The UV-cured asolectin films received a UV-dose of UVA 3.87 J/cm², UVB 2.99 J/cm², and UVC 0.412 J/cm² and resulted in a self-standing lipid film that remained completely soluble.

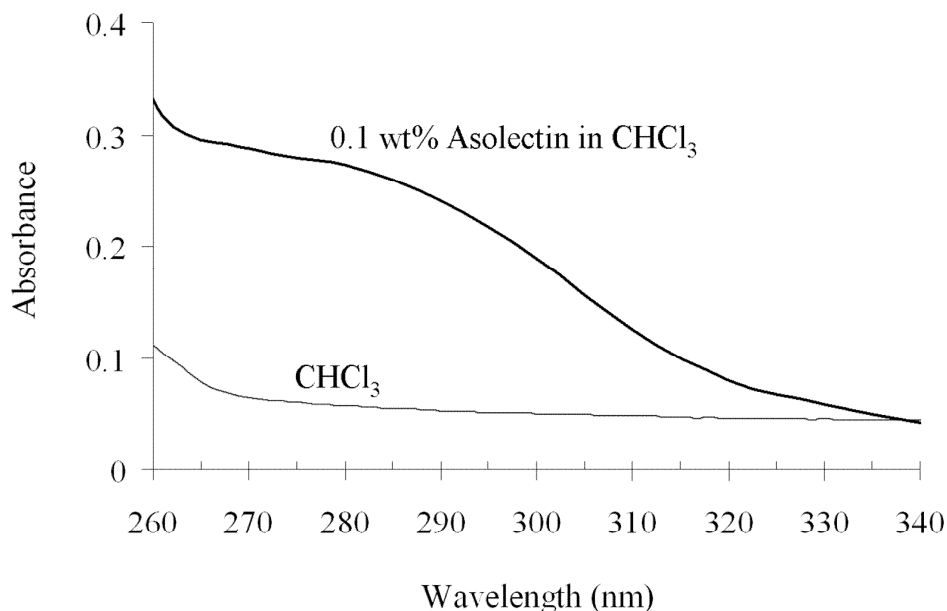


Figure 10.2 UV-vis characterization of asolectin at 0.1 wt% in chloroform and chloroform.

TGA analysis shown in Figure 10.3 indicated no change in the thermal degradation temperature between the UV-irradiated films and a non-irradiated asolectin control. Figure 10.4 depicts the melt rheology at 110 °C for the UV-irradiated and non-irradiated control films. UV-irradiated films had a storage modulus approximately two-orders of magnitude higher than the non-irradiated control, however, the concentration of photoinitiator did not influence the modulus. Molecular weight characterization of the asolectin films was not possible due to the highly charged nature of the lipid mixture, however, it was speculated that the increase in modulus was attributed to the increase in

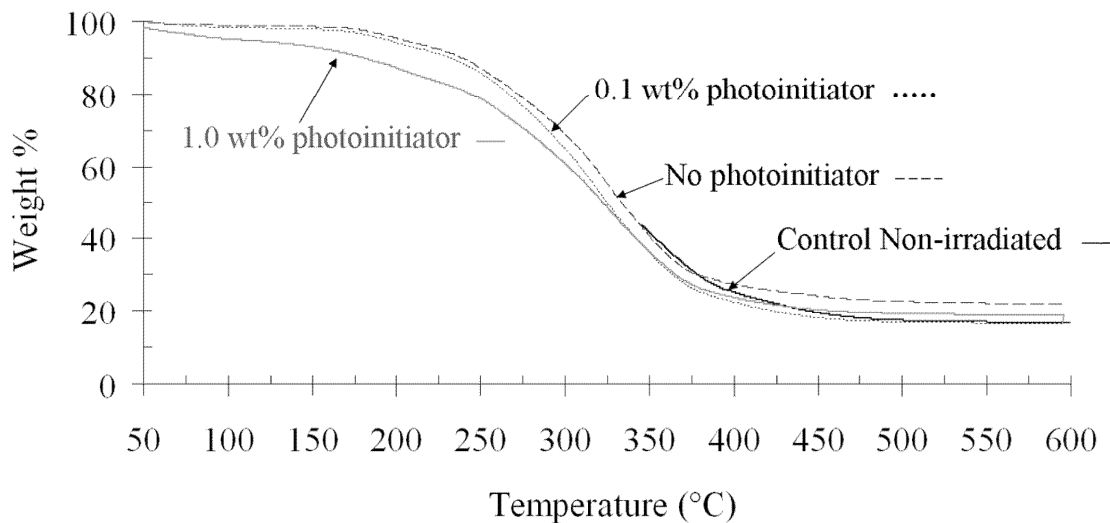


Figure 10.3 TGA analysis of the UV-irradiated asolectin films with 0 wt%, 0.1 wt%, and 1.0 wt% photoinitiator and a non-irradiated control film.

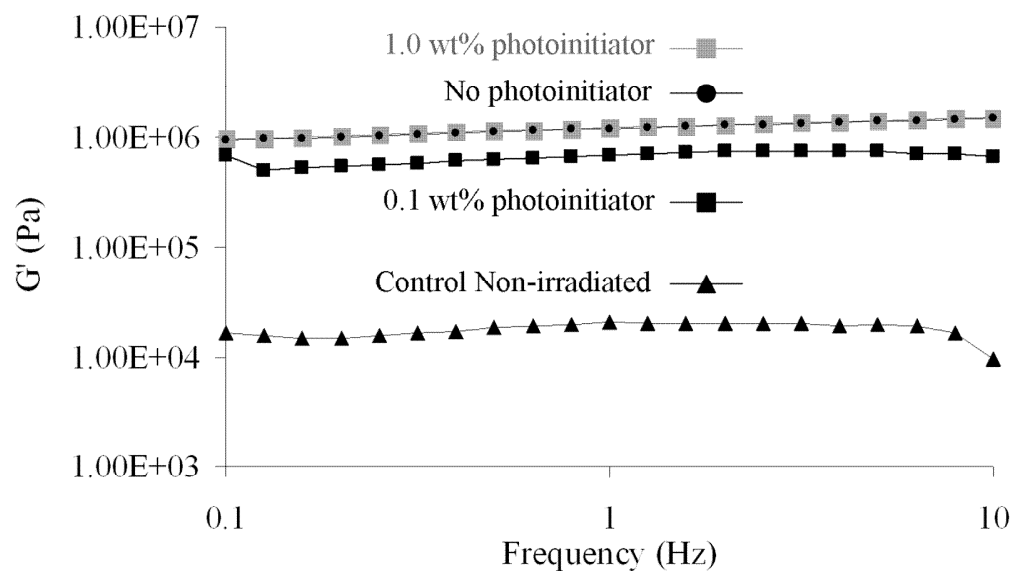


Figure 10.4 Storage modulus of UV-irradiated asolectin films with 0 wt%, 0.1 wt%, and 1.0 wt% photoinitiator and non-irradiated control film. Melt rheology conditions: 8 mm parallel plates, 2% strain, 110 °C, and 1 mm gap.

molecular weight from the photoinitiated reaction of unsaturated lipid tails. These initial experiments indicate asolectin is photo-reactive and offers the potential to develop mechanically stable electrospun lipid membranes. UV-irradiated electrospun lipid membranes will not result in crosslinked photo-cured scaffolds, however, UV-irradiating could increase the tensile properties and durability of the electrospun lipid membranes.

10.3 Designer Electrospinnable Photo-reactive Amphiphiles

Electrospinning low molar mass amphiphiles represents a strategy to develop three-dimensional biocompatible nonwoven membranes from phospholipids and other sustainable resources. However, electrospun membranes of low molar mass amphiphiles are not mechanically robust and strategies are required to increase the stability of amphiphilic membranes. Incorporating photo-reactive polymerizable groups in the surfactant architecture represents a methodology to polymerize electrospun membranes *in situ* or post-electrospinning. It is well documented and my research confirms that the solution properties and supramolecular architecture are highly dependent on the surfactant composition. Altering the composition of the surfactant will influence the self-assembled structure, and electrospinning low molar mass surfactants requires the formation of elongated cylindrical micelles to stabilize the electrospinning jet.

The solution properties and electrospinning of Acry-2-Acry were explored in an attempt to electrospin a polymerizable gemini surfactant. Acry-2-Acry had a T_k below room temperature (-2.80 °C) and formed optically clear dispersed solutions at room temperature. Cinn-2-Cinn had a T_k of 46.2 °C and therefore precipitated from solution at room temperature, and was not suitable for electrospinning. The solution rheology of

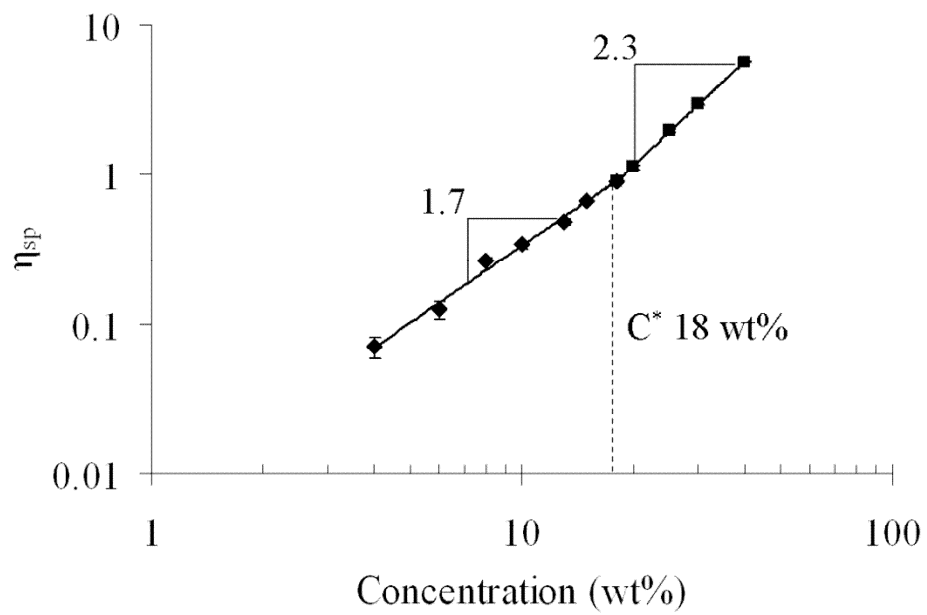


Figure 10.5 Solution rheology of Acry-2-Acry in water:methanol (1:1 vol).

Acry-2-Acry in water:methanol (1:1 vol) revealed a $C^* = 18 \text{ wt}\%$, as shown in Figure 10.5. The scaling relationships were very similar for Acry-2-Acry ($n_{sp} \sim C^{1.7}$ at $C < C^*$ and $n_{sp} \sim C^{2.3}$ at $C > C^*$) and 12-2-12 ($n_{sp} \sim C^{1.5}$ at $C < C^*$ and $n_{sp} \sim C^{2.4}$ at $C > C^*$) in water:methanol in the dilute and semidilute concentration regimes. Electrospinning Acry-2-Acry at 70 wt% in water:methanol produced surfactant droplets, as shown in the SEM image in 10.6a. *In situ* photo-curing the Acry-2-Acry electrospun jet did not stabilize the fibers and also resulted in droplets as shown in Figure 10.6b. Acry-2-Acry did not disperse in water:methanol at concentrations above 70 wt%.

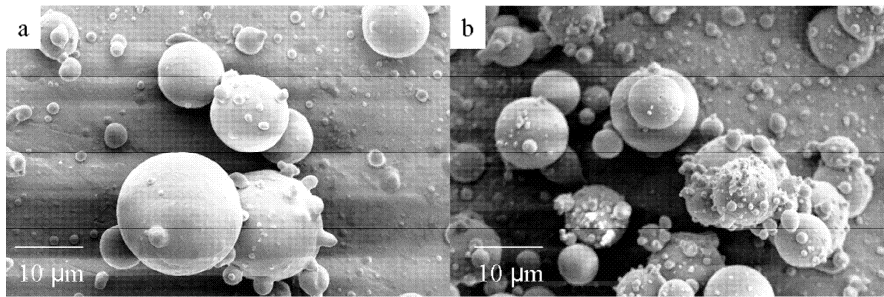


Figure 10.6 SEM of Acry-2-Acry electrospun from 70 wt% in water:methanol (1:1 vol), a) without *in situ* photo-curing, b) *in situ* photo-cured.

Incorporating a longer tail and larger hydrophobic content is recommended to increase the surfactant solution viscosity and stabilize the electrospinning jet to produce continuous polymerizable surfactant fibers. For surfactants with polymerizable tails, it is recommended to design ammonium gemini surfactants with a spacer of two carbons and a 12 carbon tail functionalized with methacrylate polymerizable groups, as shown in Figure 10.7. Increasing the tail length beyond 12 or 14 carbons could increase the T_k value to above room temperature, which would inhibit electrospinning. Also, it is recommended to explore gemini surfactants with polymerizable headgroups, like the designer gemini in Figure 10.7, however, the tail length should be increased to 14 carbons to balance the headgroup and tail volume contributions to satisfy the required packing parameter to form cylindrical micelles.

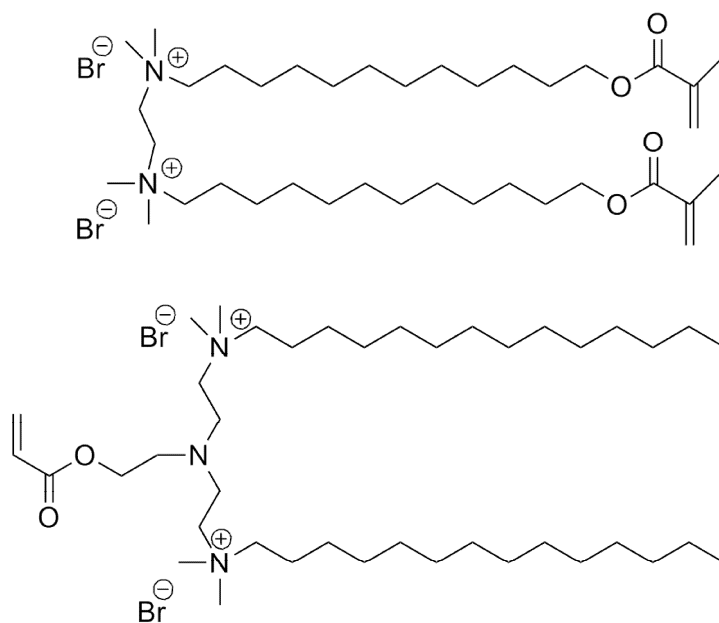


Figure 10.7 Polymerizable gemini surfactants.

10.4 References

1. Pindzola, B. A.; Jin, J. Z.; Gin, D. L., *J. Am. Chem. Soc.* **2003**, *125* (10), 2940-2949.
2. Gin, D. L.; Bara, J. E.; Noble, R. D.; Elliott, B. J., *Macromol. Rapid Commun.* **2008**, *29* (5), 367-389.
3. Zhou, M.; Nemade, P. R.; Lu, X.; Zeng, X.; Hatakeyama, E. S.; Noble, R. D.; Gin, D. L., *J. Am. Chem. Soc.* **2007**, *129* (31), 9574-9575.
4. Gin, D. L.; Gu, W. Q.; Pindzola, B. A.; Zhou, W. J., *Acc. Chem. Res.* **2001**, *34* (12), 973-980.
5. McKee, M. G.; Layman, J. M.; Cashion, M. P.; Long, T. E., *Science* **2006**, *311* (5759), 353-355.

Appendix A: Surfactant Scaling Relationships in Water and Water:Methanol

	C* (wt%)	C** (wt%)	C<C*	C*<C<C**	C**<C
12-2-12	1.5	2.7	$\eta_{sp} \sim C^{1.7}$	$\eta_{sp} \sim C^{4.8}$	$\eta_{sp} \sim C^{14.0}$
CTAB*	11	N/A	$\eta_{sp} \sim C^{1.8}$	$\eta_{sp} \sim C^{10.4}$	N/A

Table A.1 Scaling relationships in water at 25 °C. *CTAB has a Kraft Temperature of 26 °C in water and the solution rheology was run at 30 °C.

	C* (wt%)	C<C*	C*<C
12-2-12	11	$\eta_{sp} \sim C^{1.8}$	$\eta_{sp} \sim C^{2.4}$
CTAB	19	$\eta_{sp} \sim C^{1.5}$	$\eta_{sp} \sim C^{2.7}$
Acry-2-Acry	18	$\eta_{sp} \sim C^{1.7}$	$\eta_{sp} \sim C^{2.3}$

Table A.2 Scaling relationships in water:methanol (1:1 vol) at 25 °C.